

A Thesis Submitted for the Degree of PhD at the University of Warwick

Permanent WRAP URL:

<http://wrap.warwick.ac.uk/150346>

Copyright and reuse:

This thesis is made available online and is protected by original copyright.

Please scroll down to view the document itself.

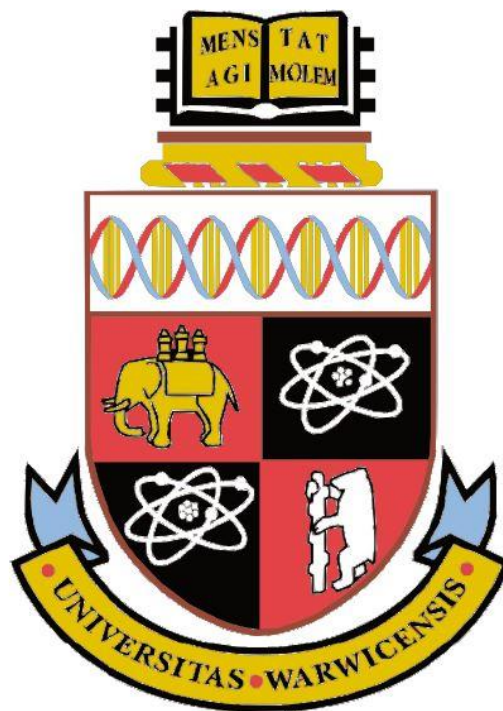
Please refer to the repository record for this item for information to help you to cite it.

Our policy information is available from the repository home page.

For more information, please contact the WRAP Team at: wrap@warwick.ac.uk

In-Situ and Correlative Study of Recrystallization and Precipitation in Cold-Rolled-Annealed Microalloyed Steels

Ishwar Kapoor



*A thesis submitted in partial fulfilment of the requirements for
the degree of Doctor of Philosophy in Engineering*

University of Warwick, WMG, September 2019

Table of Contents

Table of Contents	i
List of Tables	v
List of Figures	vi
Acknowledgements	xiv
Declaration of Originality	xvi
Abstract	xviii
Nomenclature	xx
Abbreviations	xxv
1. Introduction	1
1.1. General introduction	1
1.2. Thesis structure	3
2. Literature Review	5
2.1. Automotive steel	5
2.2. Process route to produce cold-rolled annealed low-carbon steel	7
2.2.1. Continuous casting process	8
2.2.2. Hot-rolling	8
2.2.3. Cold-rolling	10
2.3. Cold-rolled texture	11
2.4. Process route for cold-rolled and continuously-annealed steel	11
2.5. Phase diagram	13
2.6. Defects	14
2.7. Strengthening mechanisms of ferritic steels	15
2.7.1. Solid solution strengthening	15
2.7.2. Grain size effect on strengthening	17
2.7.3. Dispersion or Precipitation strengthening	17
2.7.4. Work hardening	18
2.8. Annealing	19
2.8.1. Recovery	19
2.8.2. Recrystallization	20

2.8.3. Grain growth	23
2.9. Precipitation	23
2.10. Recrystallization kinetics	27
2.10.1. Driving force for recrystallization (stored energy of deformation).....	29
2.10.2. Effect of grain size on recrystallization kinetics	30
2.10.3. Impeding force against recrystallization	31
2.11. Recrystallization fraction evaluation	33
2.12. Texture development during annealing of cold-rolled steel	34
2.13. Mechanical properties of low-carbon steel	35
3. Research questions, hypotheses and objectives	38
3.1. Research questions.....	38
3.2. Research hypotheses	39
3.2.1. Overall working hypothesis	39
3.2.2. Further hypotheses explored in this PhD research are as follows.....	40
3.3. Research objectives.....	40
3.3.1. Main objectives of this PhD project are as follows.....	40
4. Methodology	42
4.1. Materials investigated	42
4.2. Details of laboratory processed hot-rolled and cold-rolled steel.....	43
4.3. Experimental procedures to study microstructure properties of cold-rolled annealed samples.....	43
4.3.1. Muffle furnace annealing and EBSD investigation of steel grades	44
4.3.2. Texture study of bulk furnace annealed sample using EBSD.....	46
4.3.3. Texture study using XRD	47
4.3.4. Hot stage <i>quasi</i> in-situ EBSD	47
4.3.5. Post processing of EBSD data	48
4.3.6. FIB-lift Out and TEM investigation of steel grades.....	49
4.3.7. Dilatometry	50
4.4. Mechanical testing	50
4.4.1. Nanoindentation experiment.....	50
4.4.2. Hardness measurement	51
4.4.3. Tensile testing	51
5. Results.....	53
5.1. As-received hot-rolled state	53
5.2. As-received cold-rolled state	55
5.3. Identification of ferrite to austenite phase transformation temperature	56
5.4. EBSD study of muffle furnace annealed samples.....	58

5.5. Recrystallization (%) and JMAK equation	65
5.6. <i>Quasi</i> in-situ analysis of geometrically necessary dislocation density in α - fibre and γ -fibre after annealing at 700 °C 0 s; 800 °C 0 s and 800 °C 2 min	69
5.7. Texture analysis of muffle annealed samples	72
5.8. Precipitate study of muffle furnace annealed samples	75
5.9. Mechanical properties	82
5.9.1. Nanoindentation analysis of muffle furnace annealed samples	82
5.9.2. Microhardness and Uniaxial tensile measurements	85
6. Discussion	88
6.1. EBSD and STEM analysis of the as-received and muffle furnace annealed steel grades	88
6.1.1. Initial precipitate state in the hot-rolled steel grades.....	88
6.1.2. Difference in grain size in hot-rolled steel grades	89
6.1.3. Recrystallization and precipitation behaviour of the muffle furnace annealed base, Ti+ and Ti+Mn+ steel grades.....	90
6.1.4. Effect of different hot-rolled grain sizes on the recrystallization kinetics	99
6.1.5. Evaluation of recrystallization fraction.....	100
6.1.6. Development of texture of furnace annealed samples	100
6.2 Mechanical properties	103
6.2.1. Correlation between variation of nanoindentation hardness and GND density of muffle furnace annealed samples	103
6.2.2. Combined strength evaluation for the base, Ti+ and Ti+Mn+ grades for the annealing condition of 800 °C 2 min.....	104
6.2.3. Strength and ductility of the bulk annealed samples for different Tata Steel industrial designed cycles: A, B and C	106
6.3. Hot stage <i>quasi</i> in-situ EBSD study of the Ti+ grade steel.....	108
6.3.1. Role of alpha and gamma fibres during annealing.....	108
6.3.2. Reliability of hot stage <i>quasi</i> in-situ EBSD	112
7. Further work.....	115
7.1. Academic insight	115
7.2. Industrial perspective	115
8. Conclusions.....	117
8.1. Recrystallization and textural behaviour.....	117
8.2. Hot-stage <i>quasi</i> in-situ EBSD	117
8.3. Industrial implications	118
8.4. Development of the Methodology	118
9. Supplementary information	120
9.1. Calculation of geometrically necessary dislocation (GND) density	120

9.2. Solute drag parameter calculation.....	124
9.3 Selection of areas for STEM-EDS analysis	125
9.4. ImageJ post-processing of STEM images.....	126
9.5. Verification of MatCalc model	131
9.6 Sensitivity of GND analysis to certain EBSD parameters	132
References.....	134

List of Tables

Table 2.1-1 Classification of automotive steel (adapted from Demeri [48] and Hall [49])	5
Table 2.1-2 Approximate relative cost of different grades of steel (adapted from Demeri [48])	6
Table 4.1- 1: Chemical composition in weight (%) for the three grades of steel investigated in this study	42
Table 5.3-1 Ferrite to austenite phase transformation starting (T_s) and finishing (T_f) temperatures evaluated using Dilatometry (heating rate ~ 25 °C/s) and Thermo-Calc using TCFE9 database (equilibrium state) for base, Ti+ and Ti+Mn+ grades of steel.....	57
Table 5.5-1 Vickers hardness (HV/1) measurements of base, Ti+ and Ti+Mn+ grades of steel for different conditions	68
Table 6.1-1 Parameters for MatCalc simulation of precipitate size and volume fraction.....	91
Table 6.3-1 Average GND density of cold-rolled alpha and gamma fibres and un- recrystallized and recrystallized matrix of alpha and gamma fibres at different annealing conditions.....	111
Table 9.2- 1 Parameters for solute drag force calculation after Clark [46], Gladman [58], Zurob et al. [112,182], Cahn [203] Xu [305] and Wicaksono and Militzer [313].....	125
Table 9.3-1 Precipitate size and volume fraction information obtained from Fig. 9.3-1 and Fig. 9.3-2	131
Table 9.4-1 Parameters for MatCalc simulation of precipitate size and volume fraction....	132

List of Figures

Fig. 2.1-1 Graphical representation of different types of steels (including AHSS-III) (taken from Hall [49]).....	6
Fig. 2.1-2 Automotive steel grades used in 2015 Ford Edge car model in BIW applications (taken from Hall and Fekete [52] and adapted from Reed [53]).....	7
Fig. 2.2-1 Process route of low-carbon steel strip production (taken from Llewellyn and Hudd [59])	9
Fig. 2.2-2 Intermediate stages in Hot-Strip Mill 2 plant of Tata Steel Europe: pre-heat furnace (a), rougher and edger (b), finishing mill (c) and coiler (d) (permission from Tata Steel Europe)	9
Fig. 2.2-3 Continuous-Cooling-Transformation (CCT) diagram. Notation ‘F’ stands for ferrite, ‘P’ stands for pearlite, ‘B’ stands for bainite and ‘Ms’ stands for martensite (a); Cooling-Coiling strategies to achieve different final microstructures. ‘Ms’ stands for martensite (b) (taken from Rodriguez-Ibabe [60]).....	10
Fig. 2.2-4 Product flow and different stages in Hot-Strip Mill 2 plant in Tata Steel IJmuiden (permission from Tata Steel Europe)	10
Fig. 2.3-1 ODF on the section $\phi_2 = 45^\circ$: cold-rolled low-carbon steel deformed to 50% (a), 74% (b) and 95% (c) (adapted from Hutchinson [63] and Schläfer and Bunge [66]).....	11
Fig. 2.4-1 Schematic layout of Radiant Tube Furnace (RTF) of a continuous annealing line for cold-rolled steel strip in Tata Steel IJmuiden. Notations #1, #2, #3 etc. are mechanical inputs and outputs for various functions such as gas flow, temperature, pressure measurement etc. (taken from Wu et al. [77]).....	12
Fig. 2.4-2 Diagrammatic representation of product flow and different stages in continuous annealing line in Tata Steel Europe (adapted after Marga Zuijderwijk, from Tata Steel Europe, personal communication, April 15, 2019)	12
Fig. 2.5-1 Equilibrium iron-carbon phase diagram (adapted from Callister and Rethwisch [79])	13
Fig. 2.6-1 Dislocation movement from one grain to another (taken from Callister and Rethwisch [79]).....	14
Fig. 2.7-1 Plot of ferrite matrix hardness versus wt. (%) of substitutional alloying elements (taken from Maalekian [98] and adapted from Thelning [99])	16
Fig. 2.8- 1 Progress of grain recovery (taken from Humphreys and Hatherly [96]).....	19
Fig. 2.8-2 XRD result of annealing texture at 1000 K of 90% cold rolled low carbon steel, 5s (a), 6s (b), and 7s (c) (taken from Raabe [108] and adapted from Raabe and Lücke [111]) .	20

Fig. 2.8-3 Local misorientation profile in {001} alpha fibre grain orientation and {111} gamma fibre grain orientation of a 70 % cold-rolled low-carbon steel (taken from Raabe [108] and adapted from Thomas et al. [120])	22
Fig. 2.9-1 Solubility product of different microalloying elements in austenite and ferrite phase. Very low solubility of TiN and high solubility of VC in austenite phase. Solubility of microalloying elements in ferrite are lower than austenite phase (taken from Gladman [58])	24
Fig. 2.12-1 ODF on the section $\phi_2=45^\circ$: bulk texture evaluated from XRD (a) - (d), recrystallized texture (e) – (g) and un-recrystallized texture (h) – (j) evaluated from EBSP of a steel for recrystallization (%) of 0%, 24%, 66% and 100% (taken from Hutchinson [259])	35
Fig. 2.13-1 Diagrammatic sketch of engineering stress versus engineering strain curve of mild steel. Notation ‘A’ represents starting of tensile test, ‘B’ represents upper yield stress, ‘C’ represents lower yield stress and starting of Luder band formation, ‘D’ represents lower yield stress and completion of Lüders band spread across sample and ‘E’ represents failure of sample (taken from Sylwestrowicz and Hall [264])	36
Fig. 4.3-1 Tata Steel industrial annealing cycles, A, B and C (permission from Tata Steel Europe).....	44
Fig. 4.3-2 Muffle furnace based in WMG. Thermocouple records surface temperature of metal block and feeds back to data logger equipment	45
Fig. 4.3-3 Tata Steel industrial annealing cycles, A, B and C and temperature versus time plots recorded by data logger for annealing conditions of 700 °C 0 s, 800 °C 0 s, 800 °C 2 min and 800 °C 5 min. Tata Steel Industrial annealing cycles are shown after permission from Tata Steel Europe.....	45
Fig. 4.3-4 Parameters for Standard noise reduction function (taken from Channel 5 Oxford Instruments manual [288]).....	46
Fig. 4.3-5 Gatan Murano 525 heating stage for hot-stage In-situ EBSD experiment (taken from GATAN, Murano and Microtest In-situ Stages [293])	48
Fig. 4.3- 6 Tata Steel industrial annealing cycles, A, B and C and temperature versus time plots recorded by thermocouple in contact with the sample placed in hot-stage for annealing conditions of 700 °C 0 s, 800 °C 0 s, 800 °C 2 min and 800 °C 5 min. Tata Steel Industrial annealing cycles are shown after permission from Tata Steel Europe.....	48
Fig. 4.3-7 Sample geometry for Hot Stage quasi In-situ EBSD (left) and EBSD, Nanoindentation and FIB-lift out TEM (right) investigation.....	50

Fig. 4.4-1 Dog bone shaped tensile sample of ISO/EM A50 size. L_c , L_o , S_o , w and t are parallel length, original gauge length, original cross-sectional area of the parallel length, original width of the parallel length of test sample, original thickness of test sample respectively..... 52

Fig. 5.1-1 Normal Direction Inverse Pole Figure (ND-IPF) map of hot-rolled low-carbon microalloyed steel (as-received) for the TD section of the base grade sample..... 53

Fig. 5.1-2 STEM bright field (BF) image and EDS chemical maps of carbo-nitrides of Vanadium V(C/N) decorated along grain boundary and carbo-nitrides of Titanium and Vanadium (Ti,V)(C/N) present in ferrite matrix of hot-rolled condition of low-carbon microalloyed steel (as-received) of three different grades, base (a), Ti+ (b) and Ti+Mn+ (c). Arrows mark the precipitates present in ferrite matrix of hot-rolled base, Ti+ and Ti+Mn+ grades..... 54

Fig. 5.2-1 Normal Direction Inverse Pole Figure (ND-IPF) and ODF on the section $\varphi_2=45^\circ$ maps of cold-rolled low-carbon microalloyed steel (as-received) for the TD cross-section of the Ti+ grade sample. Arrows mark the alpha and gamma fibres and random oriented sub-grains/grains in the cold-rolled state. A = {001}{110}; B = {121}{110}; C = {111}{110} and D = {111}{121} grain orientation 56

Fig. 5.3-1 Dilatometry trace with respect to temperature and time of 0 s to 50 s (a) and 620 s to 660 s (b) of the ferrite to austenite phase transformation for base, Ti+ and Ti+Mn+ grades of steel. Maximum heating temperature of 1000 °C at 25 °C/s for a dwell time of 10 min and air cooled to room temperature. Sample temperature is maintained at 1000 °C for time of 40 s to 640 s and therefore dilatometry trace plot for time, 50 s to 620 s is not shown 57

Fig. 5.3-2 Variation of volume fraction of ferrite phase (a) and austenite phase (b) with increase in temperature from 600 °C to 1000 °C for base, Ti+ and Ti+Mn+ grades of steel in equilibrium condition evaluated from ThermoCalc using TCFE9 database..... 57

Fig. 5.4-1 Normal Direction Inverse Pole Figure (ND-IPF) maps of low-carbon microalloyed steel of base grade after annealing at 700 °C 0 s (a), 800 °C 0 s (b), 800 °C 2 min (c), 800 °C 5 min (d), 800 °C 15 min (e), 800 °C 30 min (f), 800 °C 1 hr (g) and 800 °C 2 hrs (h)..... 59

Fig. 5.4-2 Normal Direction Inverse Pole Figure (ND-IPF) maps of low-carbon microalloyed steel of Ti+ grade after annealing at 700 °C 0 s (a), 800 °C 0 s (b), 800 °C 2 min (c), 800 °C 5 min (d), 800 °C 15 min (e), 800 °C 30 min (f), 800 °C 1 hr (g) and 800 °C 2 hrs (h)..... 60

Fig. 5.4-3 Normal Direction Inverse Pole Figure (ND-IPF) maps of low-carbon microalloyed steel of Ti+Mn+ grade after annealing at 700 °C 0 s (a), 800 °C 0 s (b), 800 °C 2 min (c), 800 °C 5 min (d), 800 °C 15 min (e), 800 °C 30 min (f), 800 °C 1 hr (g) and 800 °C 2 hrs (h).... 61

Fig. 5.4-4 Normal Direction Inverse Pole Figure (ND-IPF) map of low-carbon microalloyed steel of Ti+Mn+ grade after annealing at 800 °C 0 s at high magnification of x5k. Arrows 'A'

and 'B' indicate nucleation of recrystallized grains along HAGB of alpha/gamma fibre and higher misorientation region between alpha fibre and random grain orientations respectively

.....	62
Fig. 5.4-5 Relative frequency (%) of grain size with aspect ratio greater than 2.6 of base grade for different annealing conditions: 800 °C 0 s; 800 °C 2 min; 800 °C 5 min; 800 °C 15 min; 800 °C 30 min; 800 °C 1 hr and 800 °C 2 hrs.....	63
Fig. 5.4-6 Relative frequency (%) of grain size with aspect ratio greater than 2.6 of Ti+ (a) and Ti+Mn+ (b) grades for different annealing conditions: 800 °C 2 min; 800 °C 5 min; 800 °C 15 min; 800 °C 30 min; 800 °C 1 hr and 800 °C 2 hrs	64
Fig. 5.4-7 Average grain size with aspect ratio greater than 2.6 of base, Ti+ and Ti+Mn+ grades (a) and Ti+ and Ti+Mn+ grades (b) for different annealing conditions: 800 °C 0 s; 800 °C 2 min; 800 °C 5 min; 800 °C 15 min; 800 °C 30 min; 800 °C 1 hr and 800 °C 2 hrs.....	65
Fig. 5.5-1 Recrystallization (%) measurements using three different methods: local average misorientation (LAM), aspect ratio (AR) and Vickers hardness (HV/1) of base (a), Ti+ (b) and Ti+Mn+ (c) grades of steel for different conditions: cold-rolled; 700 °C 0 s; 800 °C 0 s; 800 °C 2 min; 800 °C 5 min; 800 °C 15 min; 800 °C 30 min; 800 °C 1 hr and 800 °C 2 hrs.....	67
Fig. 5.5-2 Local average misorientation (LAM) map (a) and (b) and plots (c) and (d) before and after annealing of low-carbon microalloyed steel at 800 °C 0 s	68
Fig. 5.5-3 Logarithmic plot of recrystallization fraction and time of Ti+ and Ti+Mn+ grades of steel for annealing temperature of 800 °C	69
Fig. 5.6-1 Normal Direction Inverse Pole Figure (ND-IPF) maps of low-carbon microalloyed steel before annealing (a) and after annealing at 700 °C 0 s (b). In Fig. 5.6-1a, the alpha fibre region is marked as 1 and the gamma fibre region is marked as 2 for the cold-rolled state. In Fig. 5.6-1b, a bulged portion of the alpha fibre region is marked as 3 for the annealed sample. Arrows marked as A, B and C in Fig. 5.6-1b are recrystallized nucleus after annealing	70
Fig. 5.6-2 Normal Direction Inverse Pole Figure (ND-IPF) maps for two annealing conditions: before (a) and after (c) annealing at 800 °C 0 s, and before (b) and after (d) annealing at 800 °C 2 min. For 800 °C 0 s annealing condition, site specific local average misorientation (LAM), log of geometrically necessary dislocation (GND) density and log of stored energy (SE) map is shown for the un-recrystallized and recrystallized matrix of annealed sample.....	71
Fig. 5.7-1a ODF on the section $\varphi_2=45^\circ$ texture maps of base grade steel.....	72
Fig. 5.7-1b ODF on the section $\varphi_2=45^\circ$ texture maps of Ti+ grade steel.....	73
Fig. 5.7-1c ODF on the section $\varphi_2=45^\circ$ texture maps of Ti+Mn+ grade steel.....	74
Fig. 5.8-1 STEM bright field (BF) image (a) and EDS chemical maps (b) and (c) of carbonitrides of Titanium and Vanadium (Ti,V)C precipitates pinned to a sub-grain boundary at	

700 °C 0 s for Ti+ grade steel at two different FIB-lift out samples after bulk-furnace annealing	76
Fig. 5.8-2 STEM high-angle annular dark-field (HAADF) image superimposed with Vanadium EDS chemical map (a), bright field (BF) image (b) and EDS chemical maps of carbo-nitrides of Titanium and Vanadium (Ti,V)C precipitates (c) and (d) pinned to a sub-grain boundary at 700 °C 0 s for Ti+Mn+ grade steel at two different FIB-lift out samples after bulk-furnace annealing.....	77
Fig. 5.8-3 EDS chemical maps (left) and diffraction pattern (right) of one of the (Ti,V)(C/N) precipitates suspended in carbon replica film (shown with a pink arrow) of Ti+ grade sample treated at 800 °C 5 min annealing condition	78
Fig. 5.8-4 STEM bright field (BF) image and EDS chemical maps of carbo-nitrides of Vanadium V(C/N) precipitates for base (a) and carbo-nitrides of Titanium and Vanadium (Ti,V)C precipitates for Ti+ (b) and Ti+Mn+ (c) grades of steel annealed at 800 °C 2 min condition at two different FIB-lift out samples for each grade after bulk-furnace annealing	79
Fig. 5.8-5 STEM bright field (BF) image and EDS chemical maps of carbo-nitrides of Vanadium V(C/N) precipitates for base (a) and carbo-nitrides of Titanium and Vanadium (Ti,V)C precipitates for Ti+ (b) and Ti+Mn+ (c) grades of steel annealed at 800 °C 5 min condition at two different FIB-lift out samples for each grade after bulk-furnace annealing	80
Fig. 5.8-6 Relative frequency (%) of precipitate size of base (a), Ti+ (b) and Ti+Mn+ (c) grades of steel for different annealing conditions: 700 °C 0 s; 800 °C 0 s; 800 °C 2 min and 800 °C 5 min	81
Fig. 5.8-7 Average precipitate size of base (a), Ti+ (b) and Ti+Mn+ (c) grades of steel for different annealing conditions: 700 °C 0 s; 800 °C 0 s; 800 °C 2 min and 800 °C 5 min	82
Fig. 5.8-8 Precipitate number density of base, Ti+ and Ti+Mn+ grades of steel for different conditions: hot-rolled; 700 °C 0 s; 800 °C 0 s; 800 °C 2 min and 800 °C 5 min	82
Fig. 5.9-1 Band contrast (BC) map (centre) of Ti+ grade steel with 90 nanoindents after bulk furnace annealing at 800 °C 2 min condition. Normal direction inverse pole figure (ND-IPF) maps (left and right) and geometrically necessary dislocation (GND) density maps (top and bottom) of corresponding regions, numbered as 1, 2, 3 and 4 in white colour. Circles mark the dislocation pile up near the indents introduced during nanoindentation.....	83
Fig. 5.9-2 Average geometrically necessary dislocation (GND) density of base, Ti+ and Ti+Mn+ grades of steel for different conditions: cold-rolled; 700 °C; 800 °C 0 s and 800 °C 2 min	84
Fig. 5.9-3 Average nanoindentation hardness of base, Ti+ and Ti+Mn+ grades of steel for different conditions: cold-rolled; 700 °C; 800 °C 0 s and 800 °C 2 min	84

Fig. 5.9-4 Average Vickers hardness of base, Ti+ and Ti+Mn+ grades of steel for different conditions: 700 °C 0 s; 800 °C 0 s; 800 °C 2 min; 800 °C 5 min; 800 °C 15 min; 800 °C 30 min; 800 °C 1 hr and 800 °C 2 hrs.....	86
Fig. 5.9-5 Comparison of Yield strength at 0.2 % strain ($R_{0.2}$) and empirical yield strength (YS) of base, Ti+ and Ti+Mn+ grades of steel for different conditions: cold-rolled; 700 °C 0 s; 800 °C 0 s; 800 °C 2 min; 800 °C 5 min.....	86
Fig. 5.9-6 Tensile strength (TS) of base, Ti+ and Ti+Mn+ grades of steel for different conditions: cold-rolled; 700 °C 0 s; 800 °C 0 s; 800 °C 2 min; 800 °C 5 min.....	87
Fig. 5.9-7 Elongation, EL (%) of base, Ti+ and Ti+Mn+ grades of steel for different conditions: cold-rolled; 700 °C 0 s; 800 °C 0 s; 800 °C 2 min; 800 °C 5 min	87
Fig. 6.1-1 STEM bright-field (BF) image superimposed with Carbon EDS chemical map (a) bright field (BF) image (b) and EDS chemical map of C (c), Ti (d) and V (e). Iron-carbide along sub-grain boundary in the hot-rolled Ti+ grade. Arrows mark the iron-carbide in C chemical map and carbo-nitride of titanium in Ti chemical map	89
Fig. 6.1-2 Variation of experimentally evaluated (solid dot) and numerically evaluated, radius of precipitate (top) and precipitate volume fraction (%) (bottom) with increase in annealing time of the base (a) and the Ti+ (b) grades of steel. Annealing conditions: 700 °C 0 s, 800 °C 0 s, 800 °C 2 min and 800 °C 5 min correspond numerically to time: 13 s, 25 s, 145 s and 325 s respectively.....	93
Fig. 6.1-3 Variation of numerically evaluated Zener pinning force with increase in annealing time of the base and Ti+ grades of steel (a), ND-IPF maps of base (b) and Ti+ (c) grades for annealing condition of 800 °C 0 s, 800 °C 5 min, 800 °C 15 min and 800 °C 1 hr . Annealing conditions: 800 °C 0 s, 800 °C 5 min, 800 °C 15 min and 800 °C 1 hr correspond numerically to time: 25 s, 325 s, 925 s and 3625 s respectively	94
Fig. 6.1-4 Experimental value of Zener pinning force in the base and Ti+ grades for three different cases. Three different cases are explained in the above paragraph.....	95
Fig. 6.1-5 STEM bright field (BF) (a), high-angle annular dark-field (HAADF) (b) images and EDS chemical map of Mn (c) of the Ti+Mn+ grade of steel annealed under the 800 °C 0 s condition	96
Fig. 6.1-6 Variation of effective drag i.e. combined solute drag (SD) and intrinsic boundary friction (IBF) with increase in grain boundary velocity during annealing for the Ti+ and Ti+Mn+ grades of steel.....	97
Fig. 6.1-7 Variation of volume fraction of precipitates with increase in temperature 500 °C to 1000 °C for the base, Ti+ and Ti+Mn+ grades of steel in equilibrium condition evaluated from ThermoCalc using TCFE9 database	99

Fig. 6.1-8 Variation in orientation density of alpha fibre grains with increase in Φ from 0° to 90° for constant $\varphi_2 = 45^\circ$ for the cold-rolled low-carbon microalloyed steel of base, Ti+ and Ti+Mn+ grades	101
Fig. 6.1-9 ODF on the section $\varphi_2=45^\circ$ texture map of the Ti+ grade steel annealed at the 800°C 2 hrs condition	102
Fig. 6.2-1 Effective yield strength (combination of inherent, solid solution, grain size, dislocation, precipitation strength) and yield strength from the tensile test for the base, Ti+ and Ti+Mn+ grades of steel for the annealing condition of 800°C 2 min.....	105
Fig. 6.2-2 Variation of precipitation strengthening with increase in precipitate size from 0 nm to 50 nm for cold-rolled annealed at 800°C 2 min products, base and Ti+ grades of steel and Tata Steel's commercial hot-rolled products, XPF 800 and XPF 1000 grades of steel [10]. Notation 'f' stands for volume fraction of precipitates	106
Fig. 6.2-3 Tata Steel industrial annealing cycles, A, B and C (permission from Tata Steel Europe).....	107
Fig. 6.2-4 Plot of elongation (%) and tensile strength properties of the base, Ti+ and Ti+Mn+ steel grades annealed for industrially simulated cycles, A, B and C in Continuous Annealing Simulator (CASim) on a AHSS elongation (%) versus tensile strength diagram. AHSS elongation (%) versus tensile strength diagram is reproduced after Hall [49])	108
Fig. 6.3-1 Average GND density plot for cold-rolled alpha and gamma fibres and recrystallized and un-recrystallized matrix (grains) of alpha and gamma fibres at different annealing conditions (a). Fig. 6.3-1b shows recrystallization (%) of alpha and gamma matrix (grains) at different annealing conditions for low-carbon microalloyed steel of Ti+ grade	110
Fig. 6.3-2 Normal Direction Inverse Pole Figure (ND-IPF) maps of interior microstructure of hot stage quasi in-situ samples of Ti+ grade steel for three annealing conditions: 700°C 0 s (a), 800°C 0 s (b) and 800°C 2 min (c). Fraction recrystallized (%) (d) and recrystallized grain size (μm) (e) quantified on surface and interior microstructure of hot stage quasi in-situ samples for cold-rolled state and annealed states obtained at different annealing conditions	113
Fig. 9.1-1 Normal Direction Inverse Pole Figure (ND-IPF) map of annealed sample of Ti+ grade for 800°C 0 s condition obtained from MTEX toolbox available in MATLAB R2016b (http://mtex-toolbox.github.io/). Red rectangle diagram is drawn to extract misorientation data from the area of interest in the EBSD image.....	121
Fig. 9.1-2 Pixels of different square filter type. Blue colour for 3×3 filter type, green colour for 5×5 filter type, orange colour for 7×7 filter type, violet colour for 9×9 filter type and red colour for 11×11 filter type. Notation 'u' indicates step size used for EBSD scan	122

Fig. 9.1-3 Average local average misorientation (LAM) versus different filter types (3 x 3, 5 x 5, 7 x 7, 9 x 9 and 11 x 11) for three different sites (1, 2 and 3) of deformed ferrite matrix of Ti+ grade sample for annealing condition of 800 °C 0 s.....	122
Fig. 9.3-1 STEM high-angle annular dark-field (HAADF) image superimposed with Vanadium EDS chemical map. Pink coloured rectangular box in Fig. 9.3-1a and 9.3-1b represents site of interest at higher magnification.....	126
Fig. 9.4-2 STEM -EDS chemical map of carbo-nitrides of Vanadium precipitates pinned to a sub-grain boundary at 700 °C 0 s for the Ti+ grade steel at two different FIB-lift out samples after bulk-furnace annealing (a), post-processed images from ImageJ software, bandpass filter (BPF) and threshold (THD) (b) and (c) respectively	127
Fig. 9.4-3 STEM-EDS chemical map of carbo-nitrides of Vanadium precipitates at 800 °C 2 min for the Ti+ grade steel at two different FIB-lift out samples after bulk-furnace annealing (a), post-processed images from ImageJ software, bandpass filter (BPF) and threshold (THD) (b) and (c) respectively	127
Fig. 9.5-1 Comparison of TEM experimental and MatCalc simulation results of V_4C_3 precipitate size (a) and volume fraction (b) in Fe-V-C martensitic steel tempered at 600 °C. Experimental results are taken from Yamasaki and Bhadeshia paper [322].....	132
Fig. 9.6-1 Distribution of local average misorientation for Hough Resolution of 30, 60 and 100 of a Si single crystal (taken from a Aztec European EBSD user meeting in Frankfurt 2019) [365].....	133

Acknowledgements

I would like to thank my academic supervisors, Dr Vit Janik, Dr Zushu Li and Dr Geoff West and industrial supervisors Dr Yongjun Lan and Dr Arjan Rijkenberg for their immense help and guidance for my PhD research.

I would like to especially thank Dr Vit Janik for teaching me right from the start of my academic internship in WMG in summer 2015. He has taught me to interpret and relate research findings to the applied automotive engineering aspect. He has always motivated me to learn new characterisation machines such as EBSD, FIB-lift out, TEM and APT. I still remember one sentence of his, “EBSD is more than a colour map as it tell almost everything about a material”.

I would like to especially thank Dr Zushu Li for teaching me about the writing and presentation skills and Dr Geoff West for teaching me FIB-lift out and TEM. They have always motivated me to look for the question in deep and try to find answer in more than one way. I am also thankful to Dr Zushu Li, Dr Geoff West and Dr Claire Davis for giving me opportunity to attend various research conferences to learn new ideas in EBSD and recrystallization.

I would like to especially thank Dr Yongjun Lan for teaching me about precipitate modelling and mechanism of the interaction between recrystallization and precipitation process. He has always ready to give his valuable scientific support to me whenever I required for my PhD research. I would also especially like to thank Dr Arjan Rijkenberg for motivating me to look deeper to my research problem and also providing me with the required materials and data for my PhD research. He has also showed me around R&D of Tata Steel Europe and explained me the industrial process of hot-rolling and continuous annealing of cold-rolled steel.

I would like to thank current and previous WMG staff or visiting staff members, Dr Samuel Mark for teaching me some TEM practical aspects, Dr Scott Taylor for his valuable inputs in my PhD thesis writings, Dr Samuel Clark for teaching me about MTEX toolbox in MATLAB, Dr Hiren Kotadia and Dr Martha Indriyati for arranging accessories for muffle furnace.

I would also like to thank staff members from Tata Steel UK and Europe, Numan Aslam for helping me with dilatometry experiment setup, Marga Zuiderwijk for teaching me about the practical knowledge of continuous annealing line cycle of cold-rolled steel and group of staff members who were involved in the preparation of hot-rolled and cold-rolled samples, Ben Voskamp (casting), Leen Visser (hot and cold rolling), Nick Ontijt (hot rolling), Brian Du Pont (hot rolling), Daphne van de Giesen (hot rolling), Jack Kuijk (sampling/cutting). I would also like to thank Ron van Leeuwen for assisting me with tensile testing and Richard Brandon with CASim.

I would like to thank my parents and family for everything.

Declaration of Originality

This thesis is submitted to the University of Warwick, UK as part of my PhD research work carried out both in WMG, University of Warwick and Tata Steel based in UK and Europe. This thesis has been written by myself based on my supervisors' teaching and guidance and not been submitted to any previous academic degrees.

The work presented in this thesis was carried out by the author, I. Kapoor (myself) except in some of the cases as mentioned below:

The Hot-stage *quasi* in-situ EBSD experiment to understand recrystallized alpha and gamma texture development using geometrically necessary dislocation (GND) analysis in chapters 5 and 6 was co-performed with Dr Vit Janik, assistant professor in Coventry University, UK. Analysis of GND evaluation in MATLAB R2016b was taught by Dr Samuel Clark, post-doctoral research associate in UCL, London, UK. The experimental setup and post-processing and interpretation of all EBSD data was carried out by myself.

The MatCalc simulation to calculate precipitate size, volume fraction and Zener pinning force in chapter 6 was co-performed with Dr Yongjun Lan, principal researcher in Tata Steel, UK. Simulation design, analysis and interpretation was carried out by myself.

The dilatometry experiment to determine starting and finishing of ferrite to austenite phase transformation temperatures in chapter 5 were co-performed with Dr Yongjun Lan, principal researcher in Tata Steel UK and Numan Aslam, research assistant in Tata Steel UK. Experimental design, analysis and interpretation of results was carried out by myself.

Bulk texture of cold-rolled and annealed steel using XRD in chapters 5 and 6 was co-performed with Dr Stefan Melzer, principal scientist in Tata Steel Europe. Experimental design and interpretation of results was carried out by myself.

Uniaxial tensile tests of cold-rolled and annealed steel grades in chapters 5 and 6 was co-performed with Ron Van Leeuwen, technical staff in Tata Steel Europe. Annealing of steel grades in Continuous Annealing Simulator (CASim) in chapters 5 and 6 was co-performed by Richard Brandon, technical staff in Tata Steel Europe. Experimental design, analysis and interpretation of results was carried out by myself.

The part of the thesis includes texts from the following published article by the author, I. Kapoor (myself) arising from this PhD Thesis work

I. Kapoor, Y. Lan, A. Rijkenberg, Z. Li, V. Janik, *Quasi* in-situ analysis of geometrically necessary dislocation density in α -fibre and γ -fibre during static recrystallization in cold-rolled low-carbon Ti-V bearing microalloyed steel, *Mater. Charact.* 145 (2018) 686–696. doi:<https://doi.org/10.1016/j.matchar.2018.09.032>.

Information obtained from the published and unpublished research work has been acknowledged and referenced in the text of this thesis.

Abstract

This thesis presents the research work carried out to fundamentally understand the recrystallization behaviour, evolution of precipitates and their interaction with recrystallization process in three novel cold-rolled low-carbon microalloyed steel grades (base grade containing V as microalloying element; Ti+ grade containing Ti as microalloying element in base grade; and Ti+Mn+ grade containing additional Mn in Ti+ grade) during sub-critical annealing.

Cold-rolled steel grades are annealed at different annealing conditions: 700 °C 0 s, 800 °C 0 s, 800 °C 2 min, 800 °C 5 min, 800 °C 15 min, 800 °C 30 min, 800 °C 1 hr and 800 °C 2 hrs at the heating rate of ~ 10 °C/s inside muffle furnace. Effect of titanium and vanadium carbonitride precipitates and manganese solute atoms on recrystallization behaviour, recrystallized texture development and recrystallization and precipitation interaction are studied using Electron Backscatter Diffraction (EBSD) and Scanning transmission electron microscopy (STEM). The average geometrically necessary dislocation (GND) density and average nanoindentation hardness values of the un-recrystallized ferrite matrix are evaluated for different conditions: cold-rolled, 700 °C 0 s, 800 °C 0 s, 800 °C 2 min to study difference in softening behaviour among three different steel grades. Experimental results of EBSD, STEM and nanoindentation and numerical calculations of precipitate pinning and solute drag effect on recrystallization process suggest that recrystallization kinetics is highest in base grade. For Ti+ grade, fine (< 15 nm) precipitates of (Ti,V)(C/N) are significant enough to interfere with the grain boundary motion and result in sluggish recrystallization kinetics. While for base grade, precipitation is much slower than the recrystallization process. Recrystallization behaviour of Ti+ and Ti+Mn+ grades is similar for dwell time of 2 min and longer at annealing temperature of 800 °C and suggests that solute drag effect of Mn solute atoms is negligible for those conditions.

Hot-stage *quasi* in-situ EBSD is performed for three conditions: 700 °C 0 s, 800 °C 0 s, 800 °C 2 min at heating rate of ~ 10 °C/s to study onset and evolution of recrystallization process and texture development on sample surface of cold-rolled low-carbon steel. For the lower annealing temperature of 700 °C with no dwell, almost no recrystallization is observed and microstructure resembles the as-received deformed material with the exception of occasional sub-micron sized nuclei. For the annealing conditions of 800 °C 0 s and 800 °C 2 min, onset and evolution of recrystallization is observed in-situ as a function of the initial as-cold rolled texture. Slower recovery rate of alpha fibre than gamma fibre is observed and confirmed by lower drop in average geometrically necessary dislocation (GND) density for un-recrystallized alpha fibres ($1.1\text{E}+14\text{ m}^{-2}$ for 700 °C 0 s, $1.4\text{E}+14\text{ m}^{-2}$ for 800 °C 0 s and $4.5\text{E}+14\text{ m}^{-2}$ for 800 °C 2 min) than for un-recrystallized gamma fibre grains ($3.0\text{E}+14\text{ m}^{-2}$ for 700 °C 0 s,

6.2E+14 m⁻² for 800 °C 0 s and 9.8E+14 m⁻² for 800 °C 2 min) during annealing. Strong gamma texture in recrystallized matrix is found for dwell time of 0 s and longer at annealing temperature of 800 °C.

Vickers hardness and uniaxial tensile tests are performed on cold-rolled and muffle furnace annealed bulk samples to correlate microstructural observations with bulk mechanical properties and compare with automotive steel grades. Although Ti+ and Ti+Mn+ steel grades are lower on strength and ductility balance compared to DP and CP steels, cold-rolled annealed partially recrystallized Ti+ and Ti+Mn+ steel grades of high strength (750 – 880 MPa) with moderate ductility (2 – 10 %) have the potentiality to be used in light-weighting automotive body structures where high strength and moderate ductility are required.

Nomenclature

Symbol	Description	Chapters
T	Absolute temperature	2
T_m	Absolute metal melting point temperature	2
Ac_1	Start temperature of austenite phase formation	2
Ac_3	Finish temperature of austenite phase formation	2
ρ_{GND}	Geometrically necessary dislocation density	2, 9
θ	Misorientation angle	2, 9
b	Burgers vector	2, 6, 9
u	Unit length	2
$\Delta\sigma_z$	Increase in yield stress due to the presence of solute atoms	2
k_z	Strengthening coefficient of individual solute atoms	2
c_z	Solute atom concentration in terms of wt.%,	2
σ_y	yield stress	2, 5, 6
σ_i	lattice friction stress	2
k_y	Strength coefficient	2
d	Grain size	2, 5, 6
d	Precipitate size	2, 5, 6
r	Radius of precipitate (assume spherical shaped precipitate)	2, 6
r^*	Critical radius of precipitate for precipitate coalescence (assume spherical shaped precipitate)	2

$\Delta\sigma_{pp}$	Yield stress contribution attributed to precipitates	2
f	Volume fraction of precipitates	2, 6
X	Precipitate size in μm	2
σ_d	Dislocation density strength	2, 6
α	Constant	2, 6
M	Average Taylor factor	2, 6
μ	Shear modulus	2, 6
e	True strain	2
D	Instantaneous average grain size	2
D_o	Initial average grain size	2
k	Growth constant which is dependent upon temperature	2
n	Growth exponent	2
t	Time	2
$X(t)$	recrystallized volume fraction at time, t	2, 5
n	JMAK exponent	2, 5
k	constant dependent on grain nucleation and growth rate	2, 5
\dot{N}	Grain nucleation rate	2
\dot{G}	Grain growth rate	2
ΔG_{SE}	Stored energy as a function of dislocation density	2, 6
ρ	dislocation density	2, 6
μ	Shear modulus	2, 6
b	Burgers vector	2, 6

V_m	Molar volume	2, 6
E	Stored energy as a function of subgrain size and misorientation angle	2
K	constant dependent upon subgrain shape	2
γ_s	Subgrain boundary energy	2
γ_m	maximum grain boundary energy	2
θ_m	maximal misorientation angle	2
ΔG_{pin}	Zener precipitate pinning force	2, 6
σ	energy of grain boundaries	2, 6
ΔG_{sd}	Solute drag force	2, 6
C_o	concentration of solute atom	2, 6
N_v	molar volume	2, 6
k	Boltzmann constant	2, 6
δ	grain boundary thickness	2, 6
E_o	grain boundary interaction energy with atom	2, 6
X	bulk diffusion constant	2, 6
v	grain boundary velocity	2, 6
α	Solute drag force parameter as a function of molar volume, Boltzmann constant, temperature, grain boundary thickness, grain boundary interaction energy and bulk diffusion constant	2, 6
β^2	Solute drag force parameter as a function of α , molar volume, Boltzmann constant, temperature, grain boundary thickness, grain boundary interaction energy and bulk diffusion constant	2, 6
ΔG_{IBF}	Intrinsic drag force	2, 6

M_i	Intrinsic grain boundary mobility	2, 6
ΔG_{RX}	Net driving force for recrystallization	2
L_c	Parallel length of dog bone shaped tensile sample	2
L_o	Original gauge length of dog bone shaped tensile sample	2
S_o	Original cross-sectional area of the parallel length of dog bone shaped tensile sample	2
w	Original width of the parallel length of dog bone shaped tensile sample	2
t	Original thickness of dog bone shaped tensile sample	2
Ar_3	Austenite-ferrite transformation temperature	5
T_s	Ferrite to austenite phase transformation starting temperature	5
T_f	Ferrite to austenite phase transformation finishing temperature	5
T_{nr}	Non-recrystallization temperature	6
$R_{0.2}$	Proof strength (yield strength at 0.2 % strain)	5, 6
D_V^α	Diffusivity of V in ferrite phase	6, 9
D_{Ti}^α	Diffusivity of Ti in ferrite phase	6
φ_2	Bunge Euler angles	2, 5, 6
Φ	Bunge Euler angles	2, 6
σ_p	Precipitation strengthening	6
x_o	Co-ordinate of the rectangle drawn over BD-IPF EBSD map	9
y_o	Co-ordinate of the rectangle drawn over BD-IPF EBSD map	9

L	Dimension of the rectangle drawn over BD-IPF EBSD map	9
W	Dimension of the rectangle drawn over BD-IPF EBSD map	9
u	Step size during EBSD scan	9
n	Represent 1 st , 2 nd , 3 rd , 4 th and 5 th neighbour square filters of EBSD map	9

Abbreviations

APT – Atom Probe Tomography

AR – Aspect Ratio

AUST SS - Austenitic-Stainless-Steel

BA - Batch-Annealing

BC – Band Contrast

BCC – Body-Centred Cubic

BF – Bright-Field

BH - Bake-Hardenable

BIW – Body-In-White

BPF – Band Pass Filter

CA – Continuous-Annealing OR Continuously-Annealed

CCT - Continuous-Cooling-Transformation

C-Mn - Carbon-Manganese

CP – Complex-Phase

CR – Cold-Rolled

CT – Coiling Temperature

DFE – Direct-Fired Furnace

DP – Dual Phase

EBSD – Electron Backscatter Diffraction

EV – Electric Vehicle

EL – Elongation

EDS – Energy-Dispersive X-ray Spectroscopy

FCC – Face-Centred Cubic

FEG- Field Emission Gun

FIB – Focussed Ion Beam

GAM - Grain Average Misorientation

GB – Grain Boundary

GG – Grain Growth

GND – Geometrically Necessary Dislocation

GP - Guinier – Preston

HAADF – High-Angle Annular Dark-Field

HAGB – High Angle Grain Boundary

HR – High Resolution

HSLA – High-Strength-Low-Alloy

HSS – High-Strength-Steel

HV - Vickers hardness

IBF – Intrinsic Boundary Friction

IF – Interstitial-Free

IPF – Inverse Polar Figure

JMAK - Johnson-Mehl-Avrami-Kolmogorov

LAGB – Low Angle Grain Boundary

LAM – Local Average Misorientation

LC – Low-Carbon

L-IP - Lightweight-Induced-Plasticity

LYS - Lower Yield Strength OR Lower Yield Stress

MS – Mild-Steel

ND – Normal Direction

ODF – Orientation Distribution Function

PHF – Pre-Heating Furnace

PSN – Particle Stimulated Nucleation

RD – Rolling Direction

RTF – Radiant-Tube Furnace

RV – Recovery

RX – Recrystallization

SD – Solute Drag

SDD - Silicon Drift Detectors

SEM – Scanning Electron Microscopy

SIBM – Strain Induced Boundary Migration

SSD - Statistically Stored Dislocations

STEM – Scanning Transmission Electron Microscopy

TD – Transverse Direction

THD - Threshold

TRIP – Transformation-Induced-Plasticity

TS – Tensile Strength

TWIP - Twinning- Induced-Plasticity

UHSS – Ultra-High-Strength-Steel

UYS - Upper Yield Strength OR Upper Yield Stress

XPF – Extra Process Formability

XRD – X-ray Diffraction

YS - Yield Strength

1. Introduction

1.1. General introduction

Development of light-weighting automotive body structures is crucial nowadays in automotive industry to minimise fuel consumption and emissions [1–5]. The 2017 UK greenhouse gas annual report revealed that transport sector accounts for ~ 34 % of the total CO₂ emissions. Passenger cars within road transport section are the most significant source of CO₂ emissions [6]. In order to minimise CO₂ emissions from cars, countries such as Norway, Sweden and the UK are working on shifting petrol and diesel automotive powertrain to a complete zero emissions Electric Vehicle (EV) powertrain [7]. Moreover incorporation of lithium batteries and related gadgets in electric, hybrid, solar or hydrogen driven cars, requires light-weighting of automotive structures to offset weight gain from added safety and/or luxury or added power source and extra weight of added energy storage [4]. Therefore, at present, vehicle light-weighting (including petrol, diesel or electric vehicles) is one of the top priorities in automotive industries and various alternative materials for car bodies are being investigated such as aluminium [8], magnesium [9], steel [10], polymers and polymer-based or carbon-based composites [11], and their combinations (hybrid materials) [12].

Among engineering materials, steel is widely used in automobiles because of its abundance, cost effectiveness and ease in manufacturing capability as compared to other materials [3,13]. Mayyas et al. [14] performed total life cycle energy and CO₂ emission analysis for different body-in-white (BIW) materials. For the lifetime of vehicle of 200,000 miles, aluminium and magnesium intensive BIW structures result in lowest energy consumption and least CO₂ emission. While, for lifetime of vehicle less than 100,000 miles, steel intensive BIW structures are better in performance than aluminium and magnesium intensive BIW structures. Energy consumption and CO₂ emission associated with material extraction, shaping and manufacturing phase is significantly lower for steel intensive as compared to aluminium and magnesium BIW structures.

Hot rolled dual-phase (DP) and complex-phase (CP) steels are exhaustively used for chassis and suspension systems because of their high strength and elongation (%) properties [15–17]. In case of multiphase steels, ferrite with large second phase particles such as pearlite, bainite or martensite are significant in terms of providing high strength, but limits the formability and flexibility of these materials during shaping etc. [10,18–22]. To resolve stress accumulation failure issues during plastic deformation, single phase ferrite matrix with nanometre-sized precipitates has been developed mainly for chassis and suspension applications with excellent stretch flange formability [10,21]. For Body In White (BIW) applications, cold-rolled annealed multiphase steels (tensile strength, TS > 600 MPa) such as DP, CP, transformation-

induced-plasticity (TRIP), bainitic/martensitic and ultra-high-strength-steel (UHSS) and cold-rolled annealed high-strength-low-alloy (HSLA) steel grades (TS ~ 600 MPa) are extensively used [5,19,23–25]. Microalloying content of Nb, Ti, V or Mo in these HSLA grades is limited to avoid inhibition of recrystallization and maintain precipitation strengthening [24–31]. Static recrystallization and precipitation behaviour of cold-rolled low-carbon microalloyed steel during sub-critical annealing is relatively less understood. Therefore, cold-rolled continuously-annealed (CA) low-carbon microalloyed steel (TS > ~ 600 MPa) with single ferrite phase matrix containing nanometre-sized precipitates for BIW applications is a new concept and requires further investigation.

Cold-rolled continuously-annealed (CA) [24] thin (thickness ~ 1 mm) steel sheet is advantageous for light-weighting automotive parts. Cold-rolled steel has efficient surface finish because of minima chances of surface oxidation with excellent yield strength of about 1000 MPa due to work hardening [32,33]. During cold-rolling of steel, grains are elongated in rolling direction and develop anisotropic mechanical properties which is not suitable for automotive manufacturing (for example door panels) because of poor elongation (< 3 %) [30]. In order to obtain optimum combination of strength and ductility, cold-rolled steel sheet is inter-critically [34,35] or sub-critically annealed [29,36]. Annealing of cold-rolled low-carbon microalloyed steel is a complex phenomenon which involves recovery and recrystallization of cold-rolled textures with varied stored energy along with the interaction of precipitates with microstructural defects [35,37–44].

The concept of single phase ferrite steel with nanometre-sized precipitates has been explored previously in hot-rolled condition for chassis and suspension applications [10,21,45]. Funakawa et al. [21] developed hot-rolled steel of single phase ferrite matrix with 4-6 nanometre-sized precipitates of (Ti, Mo)C which provides additional strength of about 300 MPa from nano-precipitation hardening. Hai-long et al. [45] investigated Ti-V-Nb microalloyed single phase ferrite matrix hot-rolled steel. Because of the cumulative strengthening from precipitation (~ 250 MPa); dislocation (~ 145 MPa) and ferrite base matrix (~ 315 MPa), hot-rolled steel of average yield strength of about 710 MPa is achieved [45]. Similarly, Rijkenberg et al. [10] has developed hot-rolled steel with single phase ferrite matrix microalloyed with V-Nb-Mo elements, commercially known as XPF 650; XPF 800 and XPF 1000 grades (where XPF stands for eXtra Processing Formability). A combination of random and fine (~ 3 nm) interphase precipitates of V; NbV and NbVMo carbon-nitrides leads to enhanced precipitation strengthening in XPF 650 (~ 200 MPa); XPF 800 (~ 250 MPa) and XPF 1000 (~ 450 MPa) steel grades [10]. In previous PhD thesis work on XPF grade [46], Clark investigated interphase precipitation mechanism during cooling of hot-rolled low-carbon single phase ferrite steel microalloyed with vanadium and showed that during phase

transformation at 700 °C, a negligible amount of C is consumed at gamma/alpha interphase boundary for interphase precipitation and carbon distribution in gamma phase is not reduced significantly.

The purpose of this PhD research is to fundamentally understand the recrystallization behaviour and evolution of the recrystallized texture by analysing geometrically necessary dislocation (GND) density in alpha and gamma texture fibres present in three novel cold-rolled low-carbon microalloyed steel grades (base grade containing V as microalloying element; Ti+ grade containing Ti as microalloying element in base grade; and Ti+Mn+ grade containing additional Mn in Ti+ grade) during sub-critical annealing, and to describe the precipitation evolution and their interaction with recrystallization during annealing. This thesis is related to the new product concept of Tata Steel Europe R&D in the area of cold-rolled continuously-annealed low-carbon microalloyed steel for automotive BIW applications which is a continuation of the hot-rolled XPF grade concept.

Additionally, in this thesis correlative and *quasi* in-situ material characterisation techniques are developed using hot stage *quasi* in-situ EBSD, nanoindentation and FIB-lift out STEM methods to fundamentally understand the above mentioned processes and answer the research questions. To further correlate microstructural observations with bulk mechanical properties, Vickers hardness and tensile properties are evaluated from a muffle furnace annealed bulk samples and compared with conventional automotive multiphase (such as DP and CP) steel grades.

1.2. Thesis structure

This thesis is divided into 9 chapters as summarised below:

1. Introduction as mentioned above. This chapter discusses the motivation behind this PhD research work.
2. Literature Review on understanding the recrystallized texture development and precipitation interaction with recrystallization kinetics during sub-critical annealing of cold-rolled low-carbon microalloyed steel is presented. The effect of precipitation on recrystallized kinetics and combined effect of recrystallization and precipitation on mechanical properties of cold-rolled annealed steel is reviewed.
3. Research questions, hypotheses and objectives chapter discusses the unanswered questions based upon literature review, and the subsequent research hypotheses and objectives are proposed to answer these questions.

4. Methodology chapter discusses the experimental techniques utilised to understand the evolution microstructure and mechanical properties of the cold-rolled low-carbon microalloyed steel grades during the annealing process.
5. Results chapter describes the findings and observations from microstructural and mechanical experiments. It includes EBSD, STEM and nanoindentation analysis to understand recrystallization behaviour among base, Ti+ and Ti+Mn+ grades during sub-critical annealing. Hot-stage *quasi* in-situ EBSD results are presented to show both qualitatively and quantitatively alpha/gamma texture development on surface. Hardness and uniaxial tensile test properties are presented for three grades to support microstructural observations.
6. Discussion chapter interprets the recrystallization and precipitation behaviour, texture development and mechanical properties of base, Ti+ and Ti+Mn+ grades of steel for sub-critical annealing conditions. It also includes the quantification of recrystallization behaviour of alpha/gamma fibre and discusses the reliability of the microstructural features forming on the surface during hot stage quasi in-situ analysis of Ti+ grade.
7. Further work chapter proposes what could be carried out in near future to explore certain areas of research based on the findings presented in this thesis.
8. Conclusions chapter summarises the main points from the results and discussion.
9. Supplementary chapter with additional information.

2. Literature Review

2.1. Automotive steel

For automotive body construction, there are various structural materials, such as aluminium [8], magnesium [9], steel [10], carbon fibre-reinforced materials [11], etc. Among them steel is the most widely used and in increasing volumes because of its attractive properties at low cost [47], such as high elastic modulus of 210 GPa, easily modified strength and ductility via annealing, good appearance when painted [13]. There are various types of steels that can be classified, based on its strength and elongation, as shown in Table 2.1-1.

Table 2.1-1 Classification of automotive steel (adapted from Demeri [48] and Hall [49])

Category	Types	Tensile Strength (TS) in MPa and Elongation, EL (%)
Low-Carbon (LC)	Interstitial-Free (IF), Low-Carbon (LC), Mild-Steel (MS)	TS < ~ 300 MPa ~ 30 < EL < ~ 60 (%)
Conventional or Traditional High-Strength-Steel (HSS)	IF-HS, Bake-Hardenable (BH), Carbon-Manganese (C-Mn), High-Strength-Low-Alloy (HSLA)	~ 300 < TS < ~ 750 MPa ~ 10 < EL < ~ 45 (%)
Advanced-High-Strength-Steel - 1 st Generation (AHSS-I)	Dual-Phase (DP), Complex-Phase (CP), Transformation-Induced-Plasticity (TRIP), Martensitic-Steel (MS)	TS > ~ 500 MPa ~ 5 < EL < ~ 30 (%)
Advanced-High-Strength-Steel - 2 nd Generation (AHSS-II)	Lightweight-Induced-Plasticity (L-IP), Austenitic-Stainless-Steel (AUST SS), Twinning-Induced-Plasticity (TWIP)	TS > ~ 900 MPa ~ 45 < EL < ~ 70 (%)
Advanced-High-Strength-Steel - 3 rd Generation (AHSS-III)	Low cost steel under research	Under research TS > ~ 1000 MPa EL > ~ 30 (%)

AHSS-I microstructure is composed of ferrite matrix and other phases such as martensite or bainite which enhances steel strength [13]. Martensite phase within ferrite matrix raises the tensile strength up to 1000 MPa [50].

AHSS-II is the advanced generation of steel after AHSS-I, it consists of twinning-induced-plasticity (TWIP), lightweight-induced-plasticity (L-IP), and austenite-stainless-steel (AUST SS). This group of steels provide high tensile strength greater than ~ 900 MPa and formability greater than $\sim 50\%$ as shown in Fig. 2.1-1. Unlike HSS or AHSS-I, which consists of ferrite base, AHSS-II grain morphology is austenite matrix across the whole temperature processing range consisting of a high levels of Mn about ~ 20 wt. % and with ~ 0.6 wt. % of C. Disadvantages of AHSS-II are increased cost due to the addition of high wt. % Mn as compared to other grades of steel and also segregation of Mn [13,51]. The high level of manganese makes traditional thermal process problematic and leads to increased production costs [17,51]. Table 2.1-2 represents relative cost of different types of steels.

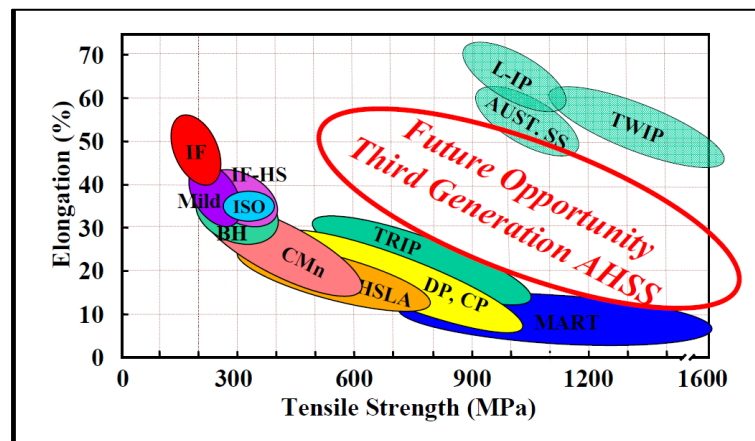


Fig. 2.1-1 Graphical representation of different types of steels (including AHSS-III) (taken from Hall [49])

Table 2.1-2 Approximate relative cost of different grades of steel (adapted from Demeri [48])

Steel grade	~ Relative cost
Cold rolled	1.00
HSLA	1.15
DP	1.40
Martensitic	1.50
AUST SS	5.70

In the case of LC and HSS there is a drop in elongation with increased strength. In the case of AHSS-I (e.g. TRIP) however, at a similar tensile strength AHSS-I has a higher elongation than HSLA, but still far less than AHSS-II which reaches up to ~ 50 % elongation in case of TWIP. AHSS-II offers higher elongation at high strength of ~ 900 MPa but still it is not preferable because of its high cost. These factors led researchers to look into the development of a new generation of AHSS called AHSS-III to fill the gap in between AHSS-I and AHSS-II. The aim is to have steel of similar or higher strength and higher formability as compared to AHSS-I whilst keep cost as effective as AHSS-I [13]. Techniques such as grain refinement or optimization of processing (annealing) cycle allow AHSS-III to achieve strength of ~ 1000 MPa and elongation of 30 % [17]. Fig. 2.1-2 shows the usage of different steel grades in 2015 Ford Edge car model [52,53]. Approximately 50 % of AHSS-I generation (DP or martensitic) and 20 % of HSS grades are used to optimize car body weight and strength to withstand high impact crash [52,53].

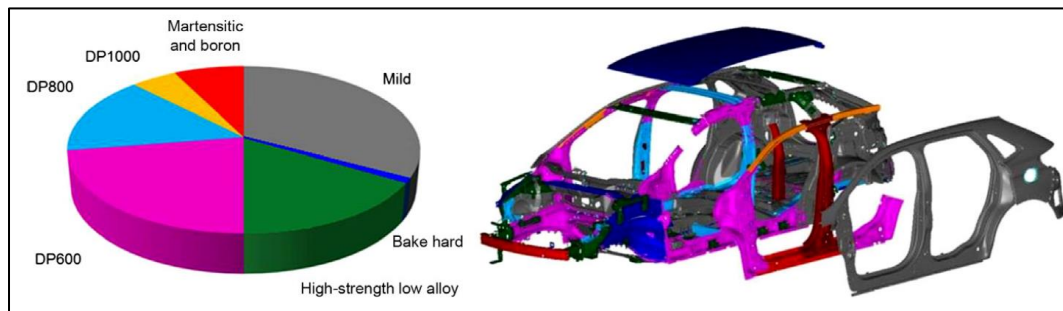


Fig. 2.1-2 Automotive steel grades used in 2015 Ford Edge car model in BIW applications (taken from Hall and Fekete [52] and adapted from Reed [53])

AHSS-I generation steel grades, especially DP, TRIP and CP steels have been investigated to develop steel of higher strength and elongation (%) for automotive applications. By altering carbon weight (%), annealing cycle parameters [54], different ratios of complex phases are formed which leads to enhancement in strength [17]. Multiphase steels include large second phase particles of pearlite, bainite or martensite which make dislocations pile up along interfaces during elongation and thus increase the chance of material failure and reduce stretch-flange formability [10,18,19,21,22]. Development of single phase ductile ferrite matrix and dispersed nanometre-sized precipitates for precipitation strengthening provides improved formability [10,21]. Addition of microalloying elements such as Ti or V or Nb or Mo consume most of the carbon present in solid solution to form precipitates and hence reduces the chances of coarse cementite particles [46].

2.2. Process route to produce cold-rolled annealed low-carbon steel

There are several processes involved during production of cold-rolled annealed low-carbon steel and each process plays a significant role in the development of the final product as shown

in Fig. 2.2-1. Continuous annealing is one of the final processes for cold-rolled annealed low-carbon steel development. There are three main manufacturing processes involved before continuous annealing is carried out in Tata Steel Europe:

2.2.1. Continuous casting process – Molten steel is poured into a reservoir (called ‘tundish’), which further flows to a water cooling mould for solidification. After that, steel is passed through multiple rolls and subsequent water sprays to ensure that steel becomes fully solidified and develops into desired shape which at the end is cut into required length and size using Gas torch [55]. Slabs are then directly sent to hot-strip mill for further hot-rolling process.

2.2.2. Hot-rolling – Slabs (thickness ~ 230 mm) are first re-heated in a furnace (Fig. 2.2-2a) to red hot ($T \sim 1250$ °C) [55] [56], then passed through de-scalers to remove iron oxide layer using scale breakers and water jets [57]. The slabs are then passed to reverse roughing mill (Fig. 2.2-2b) to reduce the thickness of the slab; typically from 230 mm to 35 mm. Thinned slabs are then passed to finish rolling (Fig. 2.2-2c) which is comprised of 7 rolling stands in Hot Strip Mill 2 in Tata Steel Europe for final required thickness typically between 1.5 mm to 25 mm [56]. Hot-rolled steel undergoes controlled cooling to avoid interphase precipitation [58] and simultaneously to ensure that all austenite grains are transformed to ferrite grains. Steel is coiled (Fig. 2.2-2d) at coiling temperature ~ 600 °C and cooled down to room temperature maintaining supersaturated ferrite matrix suitable to undergo further cold-rolling. Fig. 2.2-3a and Fig. 2.2-3b represent the diagrammatic sketch of cooling and coiling process respectively. A pyrometer is used to measure the temperature of the slab located at different sections of rolling mill. The pre-set rolling temperature is achieved through adjustment of rolling speed and the quantity of cooling water by comparing the pyrometer temperature to the nominal rolling temperature (Jos Mosk, Senior Process Engineer at the Hot-Strip Mill 2 in Tata Steel Europe, personal communication, April 15, 2019). Fig. 2.2-4 represents hot-rolling process flow of Hot-strip mill 2 at Tata Steel Europe plant.

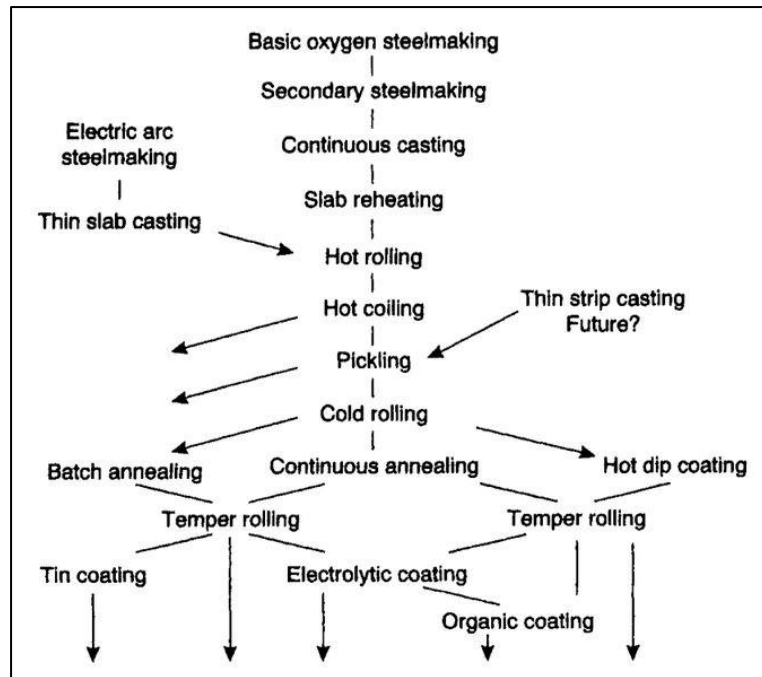


Fig. 2.2-1 Process route of low-carbon steel strip production (taken from Llewellyn and Hudd [59])



a



b



c



d

Fig. 2.2-2 Intermediate stages in Hot-Strip Mill 2 plant of Tata Steel Europe: pre-heat furnace (a), rougher and edger (b), finishing mill (c) and coiler (d) (permission from Tata Steel Europe)

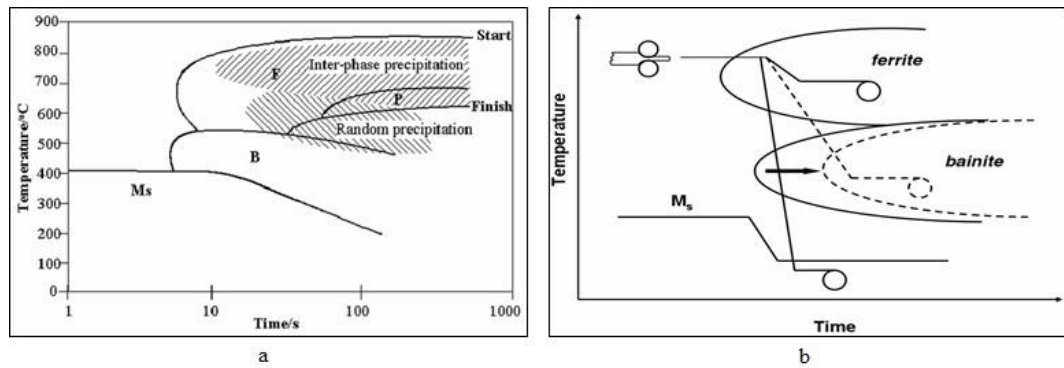


Fig. 2.2-3 Continuous-Cooling-Transformation (CCT) diagram. Notation ‘F’ stands for ferrite, ‘P’ stands for pearlite, ‘B’ stands for bainite and ‘Ms’ stands for martensite (a); Cooling-Coiling strategies to achieve different final microstructures. ‘Ms’ stands for martensite (b) (taken from Rodriguez-Ibabe [60])

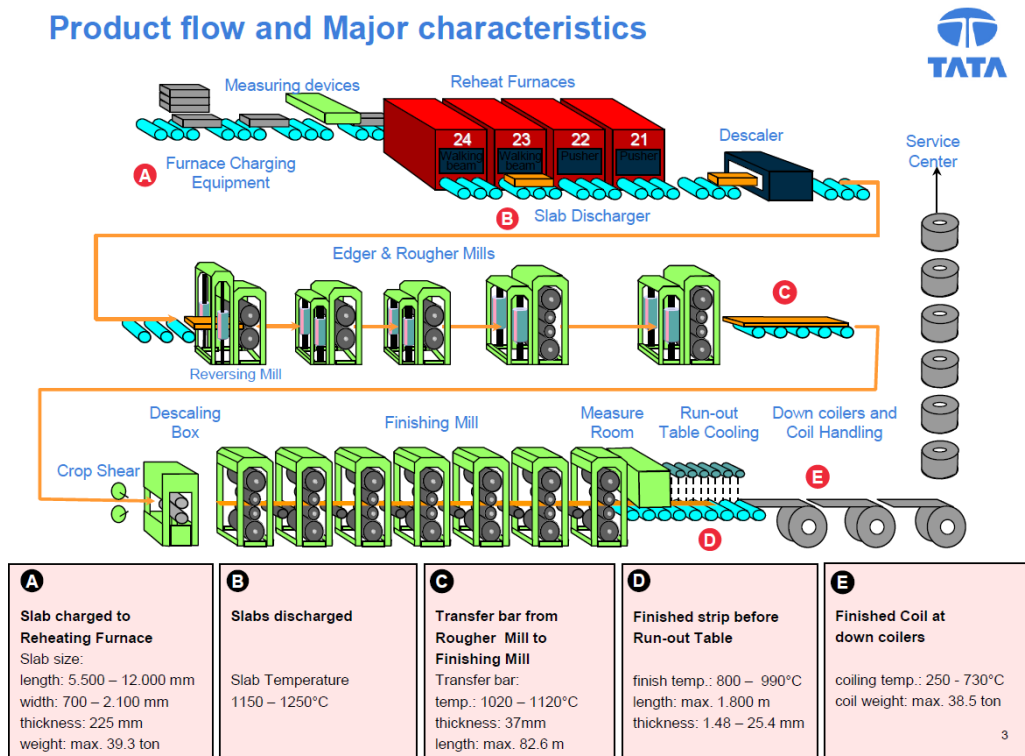


Fig. 2.2-4 Product flow and different stages in Hot-Strip Mill 2 plant in Tata Steel IJmuiden (permission from Tata Steel Europe)

2.2.3. Cold-rolling - For further reduction of thickness, hot-rolled steel is cold-rolled at temperature, $T < \sim 0.3T_m$ (T_m is absolute metal melting point) [61], where steel is uncoiled and passed through rolling mills, which decreases its thickness further about 1 mm (thickness reduction $\sim 50\%$ to 90%). After cold rolling, strip is coiled back again.

2.3. Cold-rolled texture

During cold-rolling of hot-rolled low-carbon steel, grains are oriented in certain directions with respect to sample co-ordinate system and form a typical cold-rolling texture; coordination system conventionally referred as RD for rolling direction, TD for transverse direction and ND for normal direction. Texture introduces anisotropic material properties such as elastic modulus, ductility etc. [62]. In cold-rolled steel, two main texture families are formed: $\langle 110 \rangle$ parallel to rolling direction (alpha fibre), and $\langle 111 \rangle$ parallel to normal direction (gamma fibre) [63,64]. Alpha fibre contains grains of mainly three orientations ($\{001\}\langle 110 \rangle$, $\{112\}\langle 110 \rangle$, and $\{111\}\langle 110 \rangle$) and gamma fibre contains grains of mainly two orientations ($\{111\}\langle 110 \rangle$, and $\{111\}\langle 121 \rangle$) [62,64,65]. Fig. 2.3-1 represents 2D Orientation density function (ODF) plot ($\varphi_2 = 45^\circ$) of low-carbon cold-rolled steel texture deformed at 50 %, 74 % and 95 % [63,66]. With increased cold-rolling reduction (%), texture intensity of alpha and gamma fibres is increased as shown in Fig. 2.3-1. Cold-rolled annealed low-carbon steel texture is reviewed next in subsection 2.12.

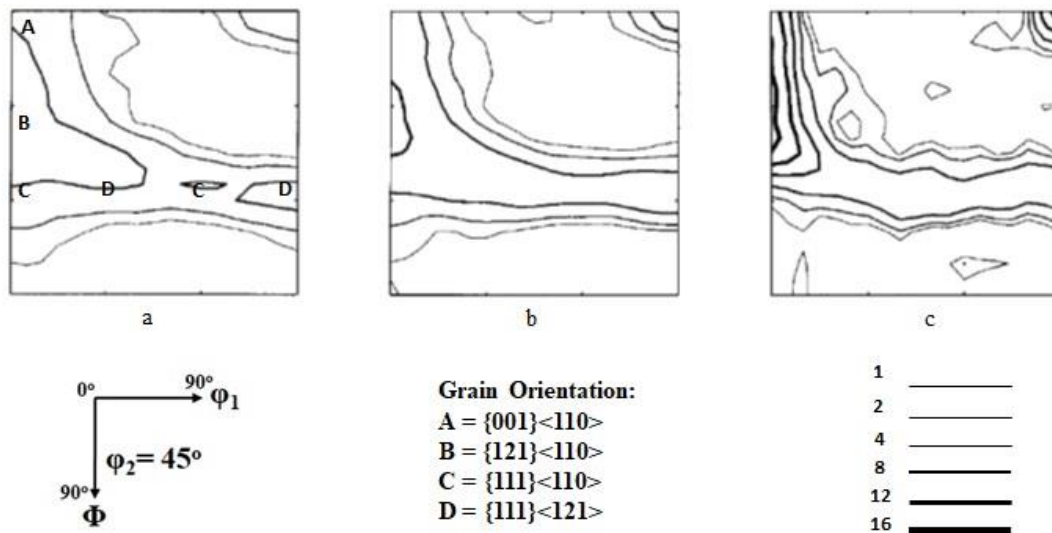


Fig. 2.3-1 ODF on the section $\varphi_2 = 45^\circ$: cold-rolled low-carbon steel deformed to 50% (a), 74% (b) and 95% (c) (adapted from Hutchinson [63] and Schläfer and Bunge [66])

2.4. Process route for cold-rolled and continuously-annealed steel

Cold-rolled annealed steel is developed either via batch-annealing (BA) or continuous-annealing (CA) route. Continuous-annealing is the preferred route compared to batch annealing in the modern steel industry, as it involves shorter annealing time, smooth surface finishing and more uniform mechanical properties [67–70]. Cold-rolled steel strips are welded to one another and passed through a Pre-heating furnace (PHF). Steel strip is then directed to Direct-fired furnace (DFF) [71–74] for heating at specified temperature (e.g. $T \sim 700^\circ\text{C}$) in an open flame environment at faster heating rate ($\sim 25^\circ\text{C/s}$). A combustible atmosphere of gas mixture ($\text{N}_2 + \text{air/O}_2$) is injected in DFF at dew point $\sim 59^\circ\text{C}$ (Marga Zuijderwijk, from

Tata Steel Europe, personal communication, April 15, 2019) for flame ignition. Once the specified temperature is achieved, steel strip is directed to Radiant-tube furnace (RTF) [73,75] for further annealing at slower heating rate $\sim 10^\circ\text{C}/\text{s}$ for a shorter period of time ~ 60 s and isothermally held at target temperature (e.g. $T \sim 800^\circ\text{C}$) for 0 s to 2 min. About 95 % of heat radiated through the tube is utilised to heat the steel strip as shown in Fig. 2.4-1 [76]. RTF is filled with a protective gas mixture of $\text{N}_2 + \text{H}_2$ to avoid oxidation of steel at elevated temperature [77]. Once the target temperature and dwell time are achieved, steel strip is cooled down to galvanising temperature ($T > 450^\circ\text{C}$) [78] inside RTF. Strip is dipped inside hot-dip galvanizing tub for zinc (Zn) coating and slow air cooled to room temperature. Fig. 2.4-2 represents schematic figure of cold-rolled annealing process flow.

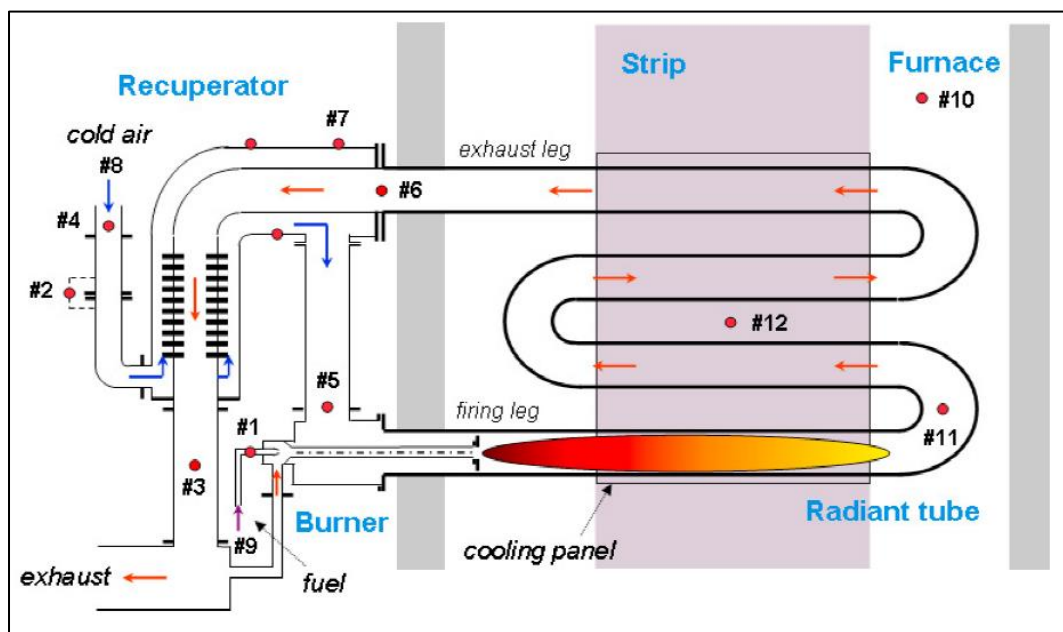


Fig. 2.4-1 Schematic layout of Radiant Tube Furnace (RTF) of a continuous annealing line for cold-rolled steel strip in Tata Steel IJmuiden. Notations #1, #2, #3 etc. are mechanical inputs and outputs for various functions such as gas flow, temperature, pressure measurement etc. (taken from Wu et al. [77])

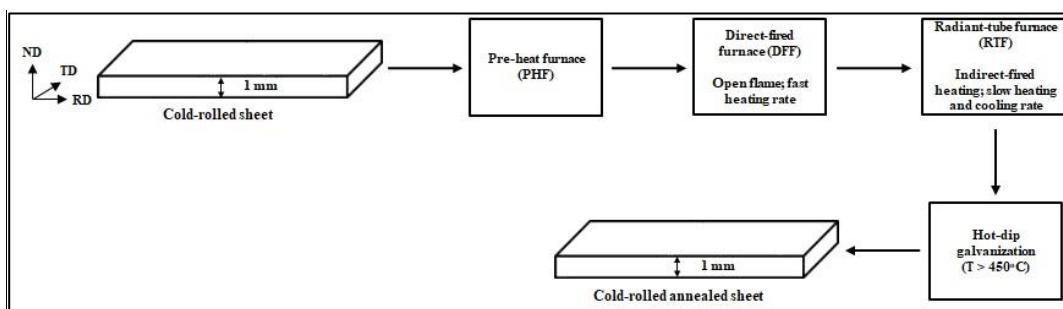


Fig. 2.4-2 Diagrammatic representation of product flow and different stages in continuous annealing line in Tata Steel Europe (adapted after Marga Zuijderwijk, from Tata Steel Europe, personal communication, April 15, 2019)

2.5. Phase diagram

The well-known iron-carbon equilibrium phase diagram (Fig. 2.5-1) provides significant insight into the effect of C on the physical-metallurgical state of the steel at certain temperatures. Depending upon temperature, rate of heating and cooling and carbon content, steel can undergo phase transformation from austenite to ferrite [79]. With an increase in heating rate (for example, 0.1 °C/s to 1 °C /s for low carbon steel [80] and 5 °C /s to 200 °C /s for martensite steel [81]) critical temperatures, A_{c1} (start temperature of austenite phase formation) and A_{c3} (finish temperature of austenite phase formation) increase and could favour stable ferrite microstructure at higher temperature ($T \sim 850^{\circ}\text{C}$) [82]. For a virtually pure iron-carbon alloy, maximum solubility of carbon in ferrite matrix is ~ 0.022 wt. % at 727°C [79]. Addition of carbide forming elements (such as Ti, V, Mo, Nb), promoting fast controlled cooling after hot-rolling process and maintaining low coiling temperature ($T \sim 600^{\circ}\text{C}$) promotes ductile single phase ferrite matrix with negligible coarse cementite particles [46].

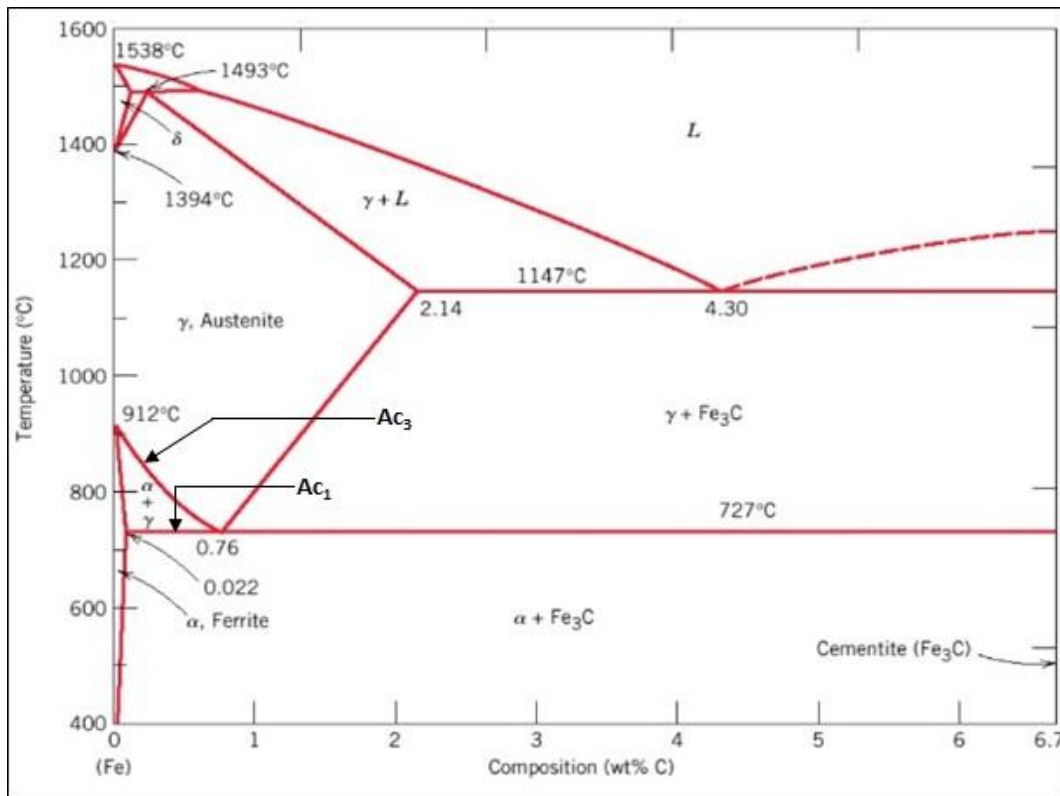


Fig. 2.5-1 Equilibrium iron-carbon phase diagram (adapted from Callister and Rethwisch [79])

During metal processing, defects within the crystal structure are introduced which are an inherent property. Defects are important from an application point of view such as enhancing the strength of steel. Defects also affect fine recrystallized grain distribution by interfering with grain boundary movement during annealing. In the following section different types of defects and their role on steel properties are discussed.

2.6. Defects

Steel is a polycrystalline material and has defects classified in terms of dimensions: point (vacancy, interstitial and substitutional atoms), linear (dislocations), planar (grain boundary), and volumetric (shear bands, dislocation bands, and transition bands) defects. Point defects come under the category of atomic defects, and have three different types: vacancies, substitutional, and interstitial atoms. A vacancy is a missing atom in a crystal lattice [83], a substitutional atomic defect is a foreign atom replacing parent's atom within a lattice site and creates inhomogeneity. In case of the iron lattice, Mn atoms occupy some of iron lattice sites as substitutional atoms since its atomic size is similar to iron atoms, and in the case of interstitial type, C and N occupy interstitial atomic positions within the iron lattice (ferrite phase) as their size is smaller than iron atoms [84].

Line defects are dislocations created by insertion of an extra half plane, or shearing of cubic lattice [83]. Dislocations form during metal's thermo-mechanical processing and then further multiply when the lattice is distorted during rolling, for instance. Interaction of dislocations and second phase particles or grain boundaries is significant during deformation. During deformation dislocations pile up against grain boundaries as shown schematically in Fig. 2.6-1 or form loops around second phase particles [85] which creates strain accumulation.

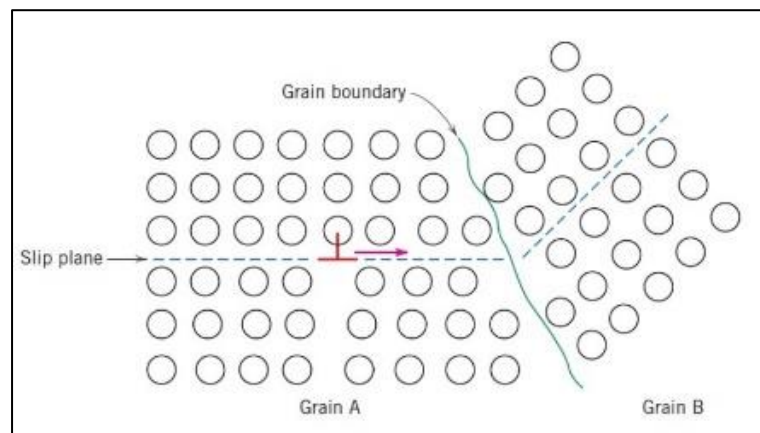


Fig. 2.6-1 Dislocation movement from one grain to another (taken from Callister and Rethwisch [79])

Upon plastic deformation, dislocations move, interact and multiply. Dislocations are not uniformly distributed throughout a material's thickness. Density of dislocations on the surface is different from the inner layers. Upon plastic deformation, the density of dislocations on the surface layer increases and chances of interactions among each other also increases. As the deformation is continued, dislocations also start appearing in the inner volume (depth ~ 80 μm) when the stress reaches the elastic limit [86]. In the stage of strain hardening, formation

of cellular structures (size ~ 0.5 to 1.8 μm) take place due to the increase in dislocation density [86].

Dislocations are comprised of geometrically necessary dislocations (GND) and statistically stored dislocations (SSD); GNDs are dislocations with the same signs which are formed in the strain gradient region and satisfy the geometrical constraints with a net non-zero Burgers vector, whereas SSDs constitute random dislocations formed by mutual trapping process with a net zero Burgers vector during plastic deformation [87–91]. According to Ashby's model for homogenous deformation of a single crystal, SSDs have the dominant role in work hardening. While in the case of non-homogenous deformation of polycrystalline materials, both SSDs and GNDs are generated but the rate of GND generation is higher which makes the density of GNDs higher than the density of SSDs and thus has a significant role in work hardening phenomena [88,91]. Quantification of SSD density is possible using Transmission Electron Microscopy (TEM), but it is a time consuming process with limited statistical significance and reduced accuracy due to artefacts created during TEM sample preparation [87,91–93]. On the other hand, from the local average misorientation map obtained from EBSD data, GND density can easily be evaluated [92] using the relation given by Kubin and Mortensen [94] relating misorientation angle ' θ ' and GND density ' ρ_{GND} ' based on the strain gradient model as proposed by Gao et al. [95],

$$\rho_{\text{GND}} = \frac{2\theta}{ub} \quad (2.6-1)$$

where b is scalar value of Burgers vector and u is the unit length.

Grain boundaries (GB) are one of the planar defects, separating two grains of different crystallographic orientations. When misorientation between two adjacent grains is high ($> 10^\circ$) [61] then the GB is termed as a high angle grain boundary (HAGB) otherwise, as a low angle grain boundary (LAGB). During cold-rolling grains elongate in rolling direction; following further deformation ($> \sim 50\%$) shear bands are formed which pass across multiple grains. Within a grain, deformation bands are formed having different orientations compared to each other, and within two deformation bands there is a sharp lattice curvature region of high local distortion termed as transition bands. Ferritic steel has high stacking fault energy [96] and favours slip as a deformation mechanism. In BCC-iron common slip planes are $\{110\}$, $\{211\}$, and $\{321\}$ and slip direction is $\langle 111 \rangle$ [83].

2.7. Strengthening mechanisms of ferritic steels

2.7.1 Solid solution strengthening

Strengthening is imparted by inhibiting the movement of dislocations during deformation, in case of solid solution strengthening by either interstitial or substitutional mechanisms. C and

N occupy octahedral interstitial sites in the iron lattice and form a tetrahedral irregular geometry which leads to the generation of strain energy due to lattice distortion. C and N atoms bind on dislocation lines and make external deformation harder thus increasing the strength [84,97]. While Mn, Ni and Cr have atomic sizes close to the atomic size of iron atoms, these atoms occupy substitutional sites within the lattice of iron [84]. Dislocation movement is prevented by the presence of substitutional atoms, which thus strengthens the material. With increases in wt. % of solute elements (Mn, P, S etc.), hardness of the ferrite matrix increases. Hardness increases due to increased wt. % of solute elements is highest for P and least for Cr as shown in Fig. 2.7-1. Mn is one of the most common elements in steels which has a vital contribution in hardness of ferrite matrix [98]. For microalloyed steels, yield strength is directly proportional to solute concentration (wt. (%)) as given by equation 2.7-1.

$$\Delta\sigma_z = \sum_z k_z \cdot c_z \quad (2.7-1)$$

Where, k_z is the strengthening coefficient of individual solute atoms, c_z is solute atom concentration in terms of wt.%, and $\Delta\sigma_z$ is increase in yield stress due to the presence of solute atoms [58].

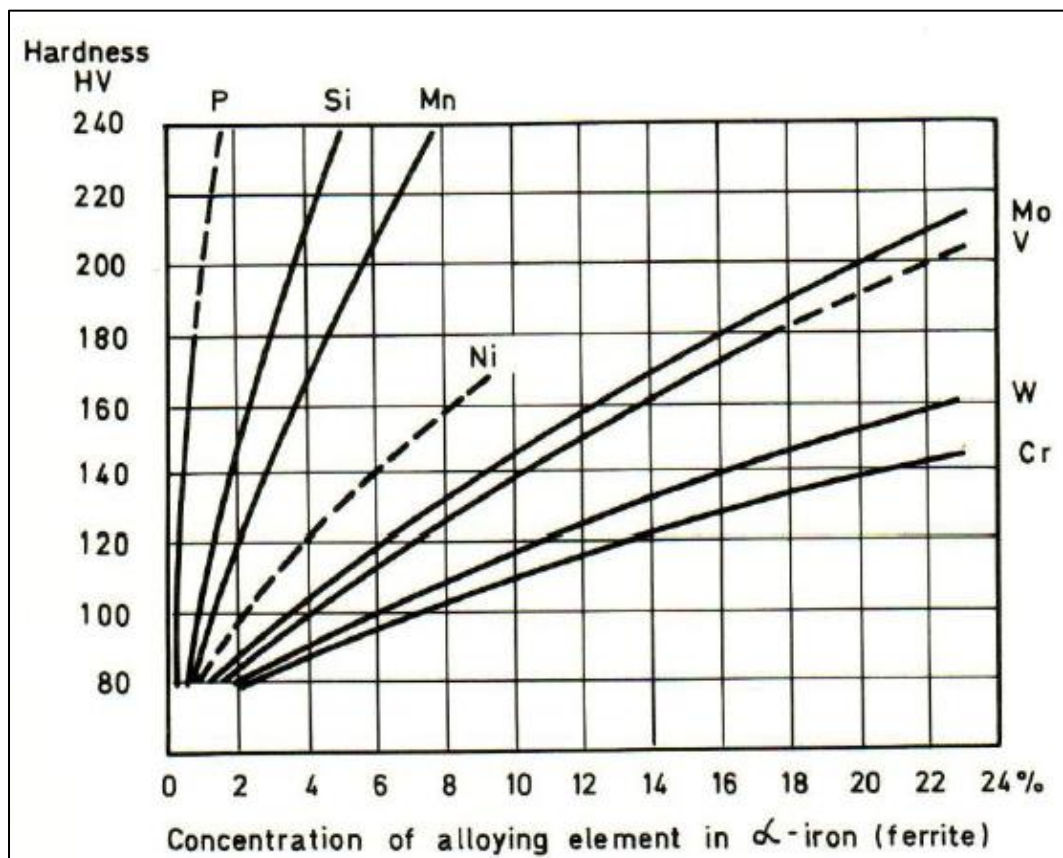


Fig. 2.7-1 Plot of ferrite matrix hardness versus wt. (%) of substitutional alloying elements (taken from Maalekian [98] and adapted from Thelning [99])

2.7.2. Grain size effect on strengthening

Controlling grain size is key to optimising strength and toughness of structural steels [100]. According to the Hall-Petch relationship (equation (2.7-2)) which is valid for steel and other non-ferrous alloys, for finer grains yield stress (σ_y) will be higher [58,84].

$$\sigma_y = \sigma_i + k_y d^{-0.5} \quad (2.7-2)$$

Where, σ_i is a constant termed as lattice friction stress, d is grain diameter, k_y is a constant termed as strength coefficient and defined as slope of σ_y vs $d^{-0.5}$ [58].

Development of fine grains in cold-rolled ferritic steel via recrystallization depends upon factors such as annealing cycle parameters, and fine particle distribution. Fine particles are effective in pinning grain boundaries and resist their further motion during grain growth. While coarse particles larger than the critical particle size are ineffective in pinning and result in coarsening of grains. Critical particle size is dependent upon atomic number of the ferrite matrix and growing grains, and the volume fraction of particles [100,101]. For the development of fine grains, Ti [41], and V are added to form carbides, nitrides or carbonitrides and act as pinning particles for grain boundary movement during recrystallization [100]. At higher temperatures there is a higher chance for particle coalescence which results in particle size reaching critical size r^* , and thus facilitates grain growth and grain size strengthening falls down [101].

2.7.3. Dispersion or Precipitation strengthening

Carbides of Ti are not only used for grain refinement but also to provide precipitation strengthening. During deformation, dislocations move and interact with second phase particles i.e. precipitates. On coming into contact with particles, dislocations either form loops around them and escape or cut through them. For microalloyed steel, yield stress, volume fraction, and particle size are related by the Ashby-Orowan equation given as [58]

$$\Delta\sigma_{pp}(MPa) = \left(\frac{10.8f^{0.5}}{X}\right)\left(\ln\left(\frac{X}{6.125 \times 10^{-4}}\right)\right) \quad (2.7-3)$$

Where, $\Delta\sigma_{pp}$ is yield stress contribution attributed to precipitates, X is particle size in μm , and f is volume fraction of particles within the microstructure. For the case of fine dispersed particles, distances between the particles are very small which makes it difficult for dislocations to bypass through them during deformation. Mathematically it has been shown in the Ashby-Orowan equation that on decreasing X i.e. for fine particles, higher yield stress is required for plastic yielding as $1/X$ is dominant over the logarithmic term.

2.7.4. Work hardening

Increase in dislocation density during deformation leads to an increase in applied stress as shown mathematically [102]

$$\sigma_d = \alpha M \mu b \rho^{0.5} \quad (2.7-4)$$

Where, σ_d is yield stress contribution attributed to dislocations, α is a constant, M is average Taylor factor, μ is shear modulus, b is magnitude of the Burger's vector and ρ is dislocation density. On further deformation, rate of formation and annihilation of dislocations is balanced and work hardening is saturated. Strengthening via deformation is achieved at the cost of toughness and ductility [84].

On combining the effect of solid solution strengthening, grain size strengthening, dispersed or precipitation strengthening, work hardening and lattice friction stress, one gets a generalised expression for microalloyed steels, given by [58]

$$\sigma_y(MPa) = \sigma_i + \sum k_i \cdot c_i + k_y \cdot d^{-0.5} + \left(\frac{10.8f^{0.5}}{X}\right) \left(\ln\left(\frac{X}{6.125 \cdot 10^{-4}}\right)\right) + \alpha M \mu b \rho^{0.5} \quad (2.7-5)$$

Precipitation strengthening is one of the crucial components in providing strength for steels developed for automotive body applications. Size of precipitates is very important in controlling precipitation strengthening. For example, very fine nanometre-sized precipitates ($X < 3$ nm) of volume fraction value $\sim 4.35 \times 10^{-3}$ provide precipitation strengthening almost greater than 300 MPa in hot-rolled steel for chassis applications [21]. Lower concentration of nitrogen ($N < 0.005$ wt. %) reduces the chance of coarse TiN precipitate formation and promotes fine (< 10 nm) nanometre-sized carbide precipitates of Ti and Mo [21]. While, higher concentration of nitrogen ($N \sim 0.022$ wt.%) favours coarse Ti-V nitride precipitate formation in austenite and ferrite phase and reduces precipitation strengthening [103]. On increasing titanium (%), strength of steel is increased and finer precipitates of TiC (30 - 100 nm) are effective in precipitation strengthening as compared to coarser particles ($\sim 1 \mu\text{m}$) of TiN and $\text{Ti}_4\text{C}_2\text{S}_2$ [104]. While, with increased Mn concentration (wt. $> \sim 1\%$) austenite grain size is refined and also austenite to ferrite transformation temperature is lowered which favours the formation of fine precipitates of TiC.

Therefore, dislocation strengthening due to high dislocation density, grain refinement strengthening due to fine ferrite grains, solid solution strengthening due to high concentration of Mn, and finally precipitation strengthening due to fine precipitates of TiC are the main contributors to the strength of high strength steels [105]. Since the distance between fine particles is small, during deformation dislocations are blocked in-between them. With further deformation, dislocation density is increased and leads to increases in strength of steel [106]. Particle spacing not only affects the strength of steel but also hardness. Contribution of

precipitates to hardness is significant in low-carbon and microalloyed steels as studied by Moon et al. Microalloy steels containing Ti and Nb have smaller interparticle spacing ($\sim 12 \mu\text{m}$) as compared to steel containing only Ti ($\sim 14 \mu\text{m}$), which leads to increased hardness on indentation [107].

2.8. Annealing

During cold-rolling steel gains strength and hardness at the expense of ductility. For use within automotive bodies both optimum strength and ductility are required. Therefore, steel is subjected to a heating process where grains undergo microstructural changes to optimize the steel properties in terms of its ductility and strength [108]. An annealing heating cycle is designed [79,83,108] which includes heating at a specific heating rate, then holding the sample at fixed elevated temperature for a fixed duration of time (dwell time) and then cooled down to room temperature. Steel could be either inter-critically [34,35] or sub-critically annealed [29,36], depending upon the final required annealed microstructure. During annealing recovery (RV), recrystallization (RX) and grain coarsening or grain growth (GG) take place [108,109]. Moreover, in the case of low-carbon microalloyed steel, microalloying elements such as Ti and V form carbides or carbo-nitrides in austenite and ferrite matrices and affect recovery and recrystallization kinetics during annealing [58].

2.8.1. Recovery

Recovery involves dislocation rearrangement, annihilation and point defect annihilation to lower the stored energy within grains which the material has gained during cold-rolling [96,110]. It occurs prior to recrystallization and does not involve high angle grain boundary movement, only the internal grain structure is altered leaving original grain boundaries unaltered. Recovery occurs at lower temperature as compared to recrystallization, and it starts as soon as thermal energy is sufficient for dislocations and point defects to mobilise and form subgrain structures within deformed grains as shown in Fig. 2.8-1 [96]. During recovery, texture of annealed samples is almost unchanged to that of the as-received condition, since recovery only involves alteration of the internal grain substructure, original grain boundaries are un-changed as shown in Fig. 2.8-2 [108,111].

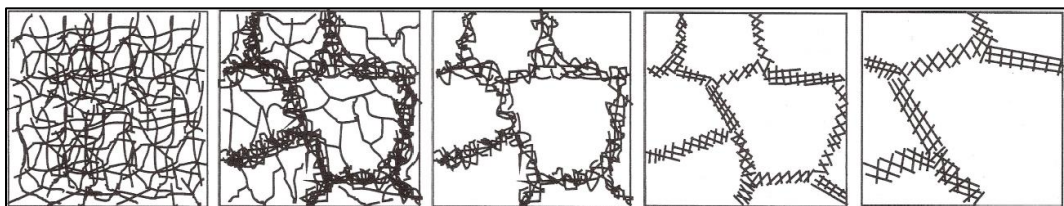


Fig. 2.8- 1 Progress of grain recovery (taken from Humphreys and Hatherly [96])

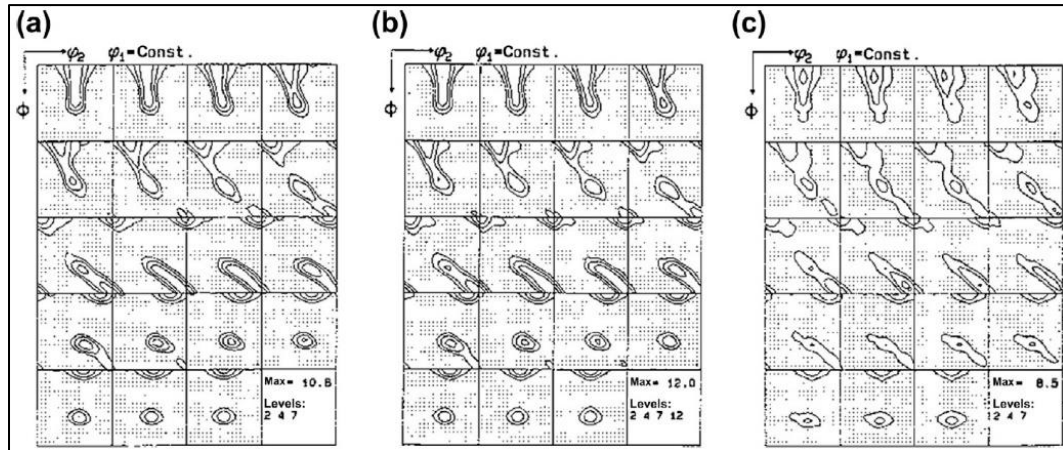


Fig. 2.8-2 XRD result of annealing texture at 1000 K of 90% cold rolled low carbon steel, 5s (a), 6s (b), and 7s (c) (taken from Raabe [108] and adapted from Raabe and Lücke [111])

Since recovery involves dislocation movement, the effect of fine second phase particles or solute atoms is vital in determining the rate of recovery, as they pin dislocations and resist their further movement, which hampers the formation of subgrains. Annealing parameters such as heating rate and heating temperature affects the rate of the recovery mechanism. Since recovery also involves consumption of stored energy, there will be a lower driving force for recrystallization in case recovery is developed [109] [112]. For very slow heating rates, the recovery process is extended and could even suppresses recrystallization processes [108].

2.8.2. Recrystallization

Recrystallization in a cold-rolled steel is a thermally activated process, characterized by formation and motion of high angle grain boundaries transforming deformed grains to strain free grains. Recrystallization has two stages, nucleation and grain growth [109]. Nucleation involves formation and migration of subgrain boundaries within a deformed matrix [113] and it is completed when grain boundary misorientation angles reaches $10^\circ - 15^\circ$. The grain growth stage of recrystallization is characterised by subsequent increases of grain boundary angles [96].

Nucleation can happen by migration of already existing high angle grain boundaries from a region of low to high dislocation density within a deformed matrix. It is also termed as strain induced boundary migration (SIBM) by Beck and Sperry in 1950 [114]. During SIBM, the orientation of strain free grains is as that of previous grains [96,113]. Another way for nucleation to happen is by migration of low angle grain boundaries studied by Beck [115], Cahn [116], and Cottrell [117]. Once subgrain formation is completed, subgrains start to grow by consuming their surrounding deformed matrix. During subgrain growth, misorientation of subgrains increases due to absorption of dislocations on its boundaries. Recovery involves subgrain growth by migration of low angle grain boundaries, therefore the recovery process

also plays a significant role in the nucleation process for recrystallization [96,112]. Belyakov et al. [118] investigated two different cold-rolled ferritic steels deformed at a lower strain of 2 and higher strain of 4.4. During annealing ($T \sim 600$ °C) of lower strained cold-rolled steel, recovery precedes recrystallization forming strain free subgrains which led to the development of recrystallized nuclei. While in the case of higher strained cold-rolled steel, deformed microstructures are dominated by high angle subgrain/grain boundaries. Therefore, during annealing a rapid recovery process takes place and promotes faster softening kinetics in the recovery stage as compared to lower strained condition [96,118]. Alternatively, nucleation also happens via subgrain coalescence [113].

Recrystallized nuclei originate in deformed matrices. Some common nucleation sites such as high angle grain boundaries, shear-, deformation- and transition bands [119,120] (which are the regions of high local misorientation), and regions near large particles [121]. Thomas et al. [120] performed high resolution-electron backscatter diffraction (HR-EBSD) to identify sites of nucleation for the recrystallization process in IF steel. Higher local misorientations within the deformed regions of gamma fibre (shown in Fig. 2.8-3) and microstructural regions containing lots of randomly oriented grains (other than alpha and gamma fibre orientation) form the potential sites for nucleation to proceed and further grow to recrystallized grains during annealing [120]. Presence of large particles in a matrix, create locally deformed regions which form favourable sites for nucleation via particle stimulated nucleation (PSN) [109,122].

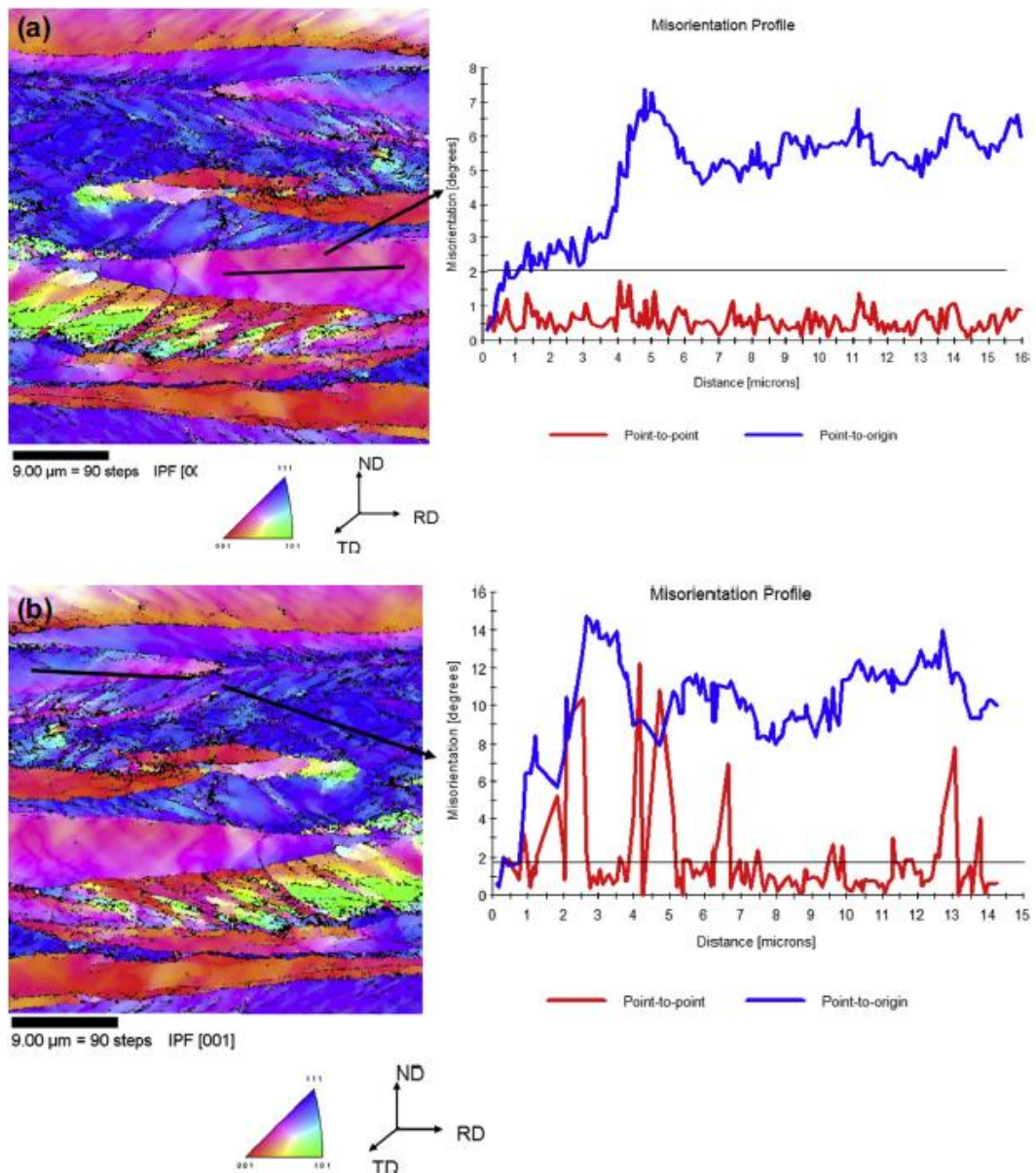


Fig. 2.8-3 Local misorientation profile in {001} alpha fibre grain orientation and {111} gamma fibre grain orientation of a 70 % cold-rolled low-carbon steel (taken from Raabe [108] and adapted from Thomas et al. [120])

With the advancement of hot stage EBSD it is possible to study instantaneously the microstructural changes during annealing [123–132]. Kerisit et al. [133] studied microstructural evolution in Ta-alloy to evaluate nucleation rate, grain growth rate and grain boundary velocity by generating EBSD scans at certain time intervals during in-situ annealing. By comparing the EBSD IPF maps taken from the same sample location and at the same magnification before and after the annealing, so called *quasi* in-situ EBSD [134] allows us to understand the role of particular microstructural components upon the kinetics of the ongoing microstructural changes. The role of twins [135] or shear bands [134] on the development of recrystallized texture during annealing has been recently studied in Mg-alloy WE43. The role

of strain-induced boundary migration (SIBM) on the amount of recrystallization for Al-alloy deformed at low (strain, $e < 0.7$) and high (strain, $e > 1.4$) strains have been previously analysed using in-situ EBSD [136]. Therefore, from hot stage quasi in-situ EBSD investigation, it is possible to locate nucleation sites and understand further development of fully recrystallized grains which is not feasible in case of ex-situ post-mortem EBSD analysis on the microstructure of muffle furnace annealed bulk samples [123].

2.8.3. Grain growth

Grain growth occurs once recrystallization is completed. During grain growth surface energy associated with grain boundaries is released and acts as the driving force for grain boundary movement. Overall grain boundary area is decreased with increases in average grain size and decrease in relative frequency (%) [96,137]. In general, grain growth with respect to time can be expressed as:

$$D^n - D_o^n = kt \quad (2.8-1)$$

Where, D is instantaneous average grain size, D_o is initial average grain size, k is growth constant which is dependent upon temperature, n is growth exponent and t is time [138,139]. Depending upon microstructural environment, grain growth could happen continuously (normal grain growth) or non-continuously (abnormal grain growth). Normal grain growth involves homogenous grain size distribution, while abnormal grain growth involves non-homogenous distribution of fine and coarse grain size. Abnormal grain growth could possibly occur due to large misorientation sites near coarse second phase particles within matrix [108] or free surface energy [140].

In this thesis, mainly the recovery and recrystallization of low-carbon steels is investigated. For more detailed information on grain growth processes, the reader is referred to the review book “Recrystallization and Related Annealing Phenomena” by Humphreys and Hatherly [96].

2.9. Precipitation

The main reason to have fine precipitates in a hot- or cold-rolled annealed steel is to compensate for the loss of initial strength by work hardening by means of precipitation strengthening; and to control recrystallized grain size development for higher grain size strengthening [58]. Hot- and cold-rolled low-carbon steel microalloyed with carbide forming elements such as Ti or V [141–144] form precipitates during annealing [145]. Fine precipitates (~ 3 nm) with high volume fraction (~ 0.0082), provide precipitation strengthening ~ 500 MPa in hot-rolled automotive steel grades [10]. Therefore, controlling the size and amount of precipitates in the automotive steel is important. During the hot-rolling process, regulating the coiling temperature to control precipitate size and amount in hot-rolled microalloyed steel is

a comparatively easy and economical step. Higher coiling temperatures ($T > 600\text{ }^{\circ}\text{C}$) promote a high volume fraction of precipitates, while lower coiling temperatures ($T < 600\text{ }^{\circ}\text{C}$) promote microalloying elements to remain in solution. Therefore, during continuous annealing of cold-rolled low-carbon microalloyed steel, samples coiled with low temperature yield higher amounts and more uniform fine precipitates [70,146–149].

Microalloying elements such as Mo, Nb, Ti and V [106,150,151] provide strengthening to steel by precipitation hardening and grain refinement. The cost of Ti is lower than other competitive precipitating elements [104]. Higher solubility of V (Fig. 2.9-1) in austenite phase favours fine precipitation of V(C/N) in ferrite phase and precipitation hardening during annealing of steel [142,149,152,153]. Precipitates could exist as a complex entity (such as carbides and nitrides of $\text{Ti}_x\text{V}_{1-x}$) in microalloyed steel with multiple precipitating elements (Ti, V, Nb etc). The carbides and nitrides of Ti and V are mutually soluble among each other as they have the same crystal structure (FCC) and similar lattice parameters [142,154]. Due to low solubility of Ti, carbides and nitrides of Ti precipitate out earlier in austenite phase (Fig. 2.9-1) and at later stage V co-precipitate on pre-existing Ti precipitates in ferrite phase. Pre-existing carbide and nitride of Ti forms favourable nucleation site for V precipitation [58,142,155–158].

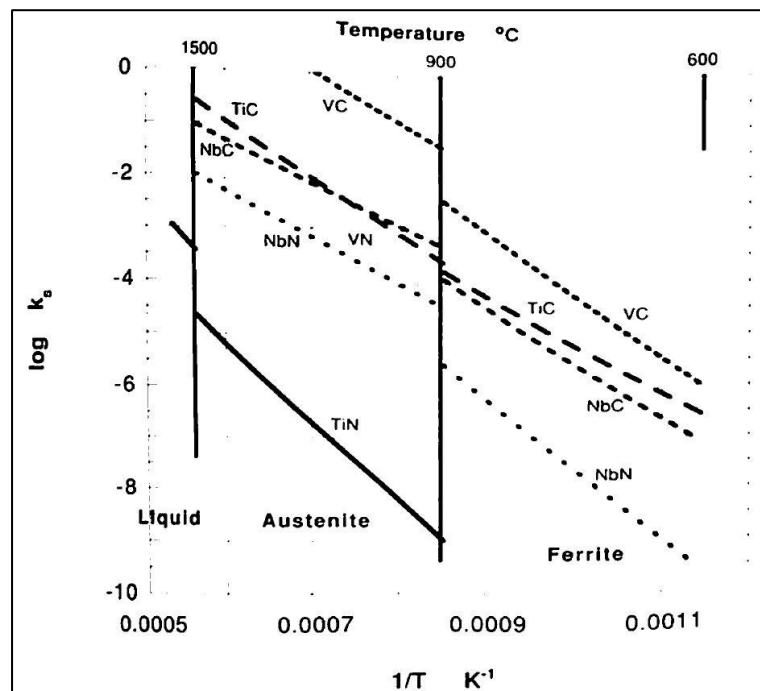


Fig. 2.9-1 Solubility product of different microalloying elements in austenite and ferrite phase. Very low solubility of TiN and high solubility of VC in austenite phase. Solubility of microalloying elements in ferrite are lower than austenite phase (taken from Gladman [58])

Information about amount, size, location and distribution of precipitates within a matrix is important, as these properties effect recovery/recrystallization kinetics and final mechanical properties of a material [159]. During cooling of hot-rolled microalloyed steel, interphase precipitates are formed along the moving alpha/gamma interphase boundary in parallel row arrangement [160]. Annealing of cold-rolled microalloyed steel within the ferrite phase temperature regime leads to general precipitation distributed along microstructural defects (such as dislocations, sub-grains and grain boundaries) within ferrite matrix [141]. In this PhD thesis, only general precipitation has been discussed and for interphase precipitation published articles [46,142,160] are recommended.

Microstructural defects such as dislocations and grain boundaries form the site for heterogeneous nucleation of precipitates [37,41,161–163]. Precipitation along grain boundaries or dislocations releases the strain energy introduced during hot- or cold-rolled deformation. A dense dislocation network is favourable for precipitation due to high strain field and large number of nucleation points. While, nucleation of precipitates in a dislocation free matrix is inhibited. Jones et al. [162] studied the influence of grain boundaries on NbC precipitation in austenite steel. During deformation dislocations are introduced within GB (also known as extrinsic dislocations) and favours precipitate nucleation during annealing. Moreover, GB with different orientations and topographical defects could also influence the precipitation behaviour [162]. Characterisation of precipitate size and amount in the region of high dislocation density is complex because of the interference of high strain fields with the electron beam in TEM.

There has been a discussion [164–170] about the precipitate morphology within ferrite matrix at different stages of annealing. Wang et al. [165] performed atomic scale investigation using APT and HR-TEM on the evolution of precipitate morphology during ageing of a Ti-Mo microalloyed ferritic steel. The early stages of precipitates are classified as embryo clusters (thickness of few atomic layers) coherent with ferrite matrix [165,166]. On further annealing, embryo cluster size increases to form clusters (multilayer of atoms) similar to Guinier – Preston (GP) zone in aluminium alloys [171,172]. GP clusters are also coherent with ferrite matrix but with higher lattice strain field. With further increase in cluster size on annealing, GP clusters grow and are transformed to NaCl structured precipitates with Baker-Nutting [173] relationship with BCC Fe-matrix, $[100]_{\text{BCC Fe-matrix}} // [100]_{\text{MC}}$ and $[010]_{\text{BCC Fe-matrix}} // [011]_{\text{MC}}$. The idea of GP clusters has been previously discussed for Nb [174–177] and V [178,179] microalloyed steels. While, Morales et al. [180], studied commercial V microalloyed steel under TEM and concluded carbonitride precipitates (even of smallest size ~ 2 nm) formed in ferrite phase during interphase precipitation are incoherent. Investigation of early stage of nanometre-sized (< 5 nm) precipitates in ferrite matrix is challenging because of ferromagnetic

nature of iron-ferrite matrix and embedment of fine precipitates limits the resolution and accuracy in information [159,165,181]. Early stage of precipitates in the form of clusters is still in academic discussion and has not been widely accepted for commercially microalloyed steels for industrial applications [164].

The effect of Mn solute atoms on precipitation kinetics in austenite phase has been studied previously [58,144,182–186]. Mn increases the solubility of NbC [182,183], VN [58,144,184] and TiC [185,186], decreases the diffusivity of C [185] and favours fine precipitation in the later stages of austenite to ferrite phase transformation. While, Ubhi and Baker [187] concluded that the effect of Mn was insignificant on precipitation kinetics of VC and had a pronounced effect on slowing down austenite to ferrite phase transformation and delaying onset of VC precipitation by ~ 10 min. The effect of Mn on precipitation kinetics of Nb or Ti or V in ferrite phase has not been investigated in as much detail as that in austenitic phase. Since dislocations and grain boundaries are favourable sites for nucleation of precipitates, segregation of Mn along microstructural defects could also affect the kinetics of precipitation in austenite and ferrite phases [182,188,189].

TEM specimen preparation to investigate morphology and statistical distribution of precipitates within the matrix is an important step in characterisation. There are several methods to prepare thin TEM foils in the literature [190]. Among them, carbon extraction replica, electropolishing and FIB-lift out are common for metallic samples [190–192]. Carbon extraction replica is useful to study precipitate crystallography, since the carbon film is usually thin (< 50 nm) and diffraction patterns from precipitates do not significantly interfere with replica and provide high signal to noise ratio. Unfortunately, there are limitations of carbon extraction replica such as [191,193]:

- Information about the matrix microstructure and the grain orientation are lost in carbon extraction replica sample. Only precipitates suspended in the carbon replica could be visible.
- During chemical analysis, there could be interference between chemical elements of precipitates and carbon replica film (such as carbon).
- Partial precipitate dissolution could introduce artificial reduction in the actual size of precipitates.
- Picking up only coarser precipitates.
- Agglomeration of fine particles and contamination from foreign chemical elements (such as oxides and silicon).

Another common method is electropolishing which has been used since the mid-1960's for metallic samples and involves electro-chemical reactions to thin down the sample [190]. The

classical electropolishing methods are useful for TEM specimen preparation but not preferred for the site specific study of nanometre-sized precipitates [194,195].

Combining FIB with SEM allows the selective lift out of material with high accuracy about ~ 10 nm [194,196] from a grain boundary or particular grain of interest. FIB-lift out TEM foil is of uniform thickness without wedge shaped formation [195]. One of the drawbacks of FIB-lift out is the introduction of artefacts from Ga ion damage and bending of sample [194,197–199]. Most of the artefacts could be eliminated by careful foil preparation following procedures [149,195,200]. Clark et al. [126] performed FIB-lift out TEM analysis on the interphase of austenite-ferrite during phase transformation from austenite to ferrite to investigate VC/VN interphase precipitate distribution and reported that the precipitates were distributed in irregularly spaced curvilinear patterns. Wang et al. [165] performed site specific FIB-lift out from [100] grain orientation of ferrite matrix to study the evolution of orientation relationship between precipitates and the matrix. FIB lift-out TEM analysis permits site specific investigation of chemical distribution of the solute atoms or precipitates, and to monitor their interaction with the grain boundary [126,201,202]. In this PhD work, the FIB-lift out method is extensively used to study precipitate distribution and size within ferrite matrix for different conditions.

Precipitation and recrystallization are complex and competing processes. During recrystallization, dislocation density decreases which leads to decrement in nucleation sites for precipitation. While fine precipitates pin along dislocation and grain boundaries and retard recrystallization kinetics. Moreover, precipitate forming microalloying elements could be present in solution and impede grain boundary motion by solute drag [203]. During annealing precipitates are formed and respective solute contents are decreased. A decrease in solute content of precipitate forming elements in matrix could favour grain boundary motion during annealing [112,204]. In general for higher annealing temperatures, recrystallization finishes before precipitation starts. For lower annealing temperatures, precipitation is likely to occur before recrystallization starts. For lower annealing temperatures, precipitates could significantly pin along dislocations and subgrain boundaries to impede recrystallization kinetics and influence final annealed recrystallized texture [96,109,205]. The effect of precipitation pinning and solute drag on recrystallization kinetics is discussed in the following section on recrystallization kinetics

2.10. Recrystallization kinetics

Johnson-Mehl-Avrami-Kolmogorov (JMAK) equation:

Stored energy acts as the driving force for recrystallization during annealing. Higher stored energy from deformation and lower impeding forces from precipitates and solute atoms

favours the recrystallization process. For an isotropic constant growth rate condition with random nucleation sites, recrystallization kinetics could be expressed using JMAK theoretical equation [206–211] given by:

$$X(t) = 1 - \exp(-kt^n) \quad (2.10-1)$$

Where, $X(t)$ is recrystallized volume fraction, n is JMAK exponent and k is constant dependent on grain nucleation rate, \dot{N} and grain growth rate, \dot{G} . JMAK equation is based on following assumptions:

1. Random nucleation sites
2. Constant \dot{N} and \dot{G}
3. Spherical grains

Value of n could vary from 4 to 1 depending upon distribution of recrystallized grain nucleation sites, grain growth rate etc. For grain growth in three dimensions with constant \dot{N} and \dot{G} , n value is 4. While, for site saturated nucleation and variable nucleation rate, n value is 3. For decreasing nucleation rate, n value is in between 3 to 4. Experimentally, n value is generally less than 2 and even less than 1 depending upon preferential distribution of nucleation sites within microstructure [96,211].

The value of the Avrami exponent, n , could be used as a benchmark value to compare recrystallization behaviour for different conditions. Conventionally the JMAK equation assumes uniform stored energy and random nucleation sites during annealing [212]. While in practical scenarios, recrystallization kinetics, for cold rolled and annealing, are dependent on annealing temperature, heating rate, cold-rolled deformation (%), distribution and size of microalloying precipitates, texture and grain size affecting stored energy and any inhomogeneity from industrial processing [96,108,109,120,136,156,213–217] and therefore complicated to predict using simplified mathematical equations.

For most practical cases, experimentally observed n values are lower than the theoretical n values [218]. Lower values of $n < 2$ [211] may reflect the effect of recovery on stored energy affecting recrystallization or spatial variation of net stored energy for recrystallized grain growth during annealing. Retardation of recrystallization due to precipitate pinning effect has also shown the decrement in n value [211]. Medina and Quispe [219] have observed the value of n in the range of 0.5 – 1 for V-microalloyed low-carbon steel during static recrystallization of hot-deformed austenite phase. Value of Avrami exponent, n is also shown to be varying for different initial grain size distribution [44,212,220]. Hutchinson et al. [44] studied the effect of different initial grain size distribution on the recrystallization kinetics of copper. For fine

grain microstructure (average grain size $\sim 15 \mu\text{m}$), n is ~ 2.7 and coarse grain microstructure (average grain size $\sim 50 \mu\text{m}$), n value is ~ 1.7 . Avrami exponents evaluated by Ji et al. [220] for Fe-30 wt. % Ni austenitic steel for fine grain size distribution (mode grain size $\sim 100 \mu\text{m}$) is 2.3 and coarse grain size distribution (mode grain size $\sim 160 \mu\text{m}$) is in the range of 1.2 – 1.4.

2.10.1. Driving force for recrystallization (stored energy of deformation)

Cold-rolling introduces thermo-mechanical energy to a deformed microstructure. Part of the thermo-mechanical energy is dissipated as heat and rest of the energy accumulates inside the material as dislocations [108,109,221–223]. Cold-rolling of steel leads to non-homogenous stored energy distribution within the microstructure. During annealing, stored energy acts as the driving force for recrystallization and favours the formation and growth of recrystallized nuclei [217]. Stored energy as a function of dislocation density is expressed by equation 2.10-1:

$$\Delta G_{SE} = 0.5 * \rho * \mu * b^2 * V_m \quad (2.10-1)$$

Where, ρ is dislocation density, μ is shear modulus, b is Burgers vector and V_m is molar volume.

Dillamore et al. [224] assumed stored energy from deformation is concentrated along the subgrain boundaries and established an empirical relationship as a function of subgrain size, d and misorientation angle, θ , which is give as:

$$E = \frac{K * V_m * \gamma_s}{d} \quad (2.10-2)$$

Subgrain boundary energy from Shockley-Read equation [225] is further expressed as:

$$\gamma_s = \gamma_m * \frac{\theta}{\theta_m} * \left(1 - \ln\left(\frac{\theta}{\theta_m}\right)\right) \quad (2.10-3)$$

Where, E is stored energy, K is constant dependent upon subgrain shape, V_m is molar volume, γ_s is subgrain boundary energy, γ_m is maximum grain boundary energy and θ_m is corresponding maximal misorientation. Betanda et al. [89] evaluated and compared stored energy for a cold-rolled Fe-48%Ni alloy using three approaches: Neutron diffraction based on diffraction peak broadening which considers both geometrically necessary dislocation (GND) and statistically stored dislocation (SSD) density [215,226], Dillamore et al. [224] approach which considers GND density associated with the subgrain boundary, and LAM approach which considers GND density of the microstructure including subgrains and subgrain boundaries. The Dillamore et al. approach underestimates stored energy, as it only includes GND density while LAM and Neutron diffraction methods are very similar which implies

SSD density contribution is negligible for stored energy evaluation. In this research work, GND density is evaluated from LAM-EBSD maps and used to further quantify stored energy and dislocation strengthening contribution to the mechanical properties.

2.10.2. Effect of grain size on recrystallization kinetics

For deformation at low strain (< 0.5 [96]), stored energy increases with a decrease in grain size. While for high strain levels, the effect of initial grain size prior to deformation on stored energy gradually decreases [96,227–229]. For low strain conditions, grain boundaries form the major obstacles to slip in both fine and coarse grains. During the initial stage of deformation, the rate of pile up of dislocations along the GB is higher in fine grains (slip distance \propto grain size [88]) and leads to higher stored energy than in coarse grains. With a further increase in strain, piling-up of dislocations along the GB is continued until the localised stress along the GB is high enough to release (or reduce) dislocations by cross slip [228] or for dislocation annihilation [229]. Oliferuk et al. [229] studied the amount of stored energy as a function of grain size and strain during tensile deformation of austenitic steel. For tensile strain < 0.1 , fine grains ($\sim 8 \mu\text{m}$) have higher stored energy as compared to coarse grains ($\sim 80 \mu\text{m}$). For tensile strain > 0.1 , the difference in grain size has a negligible effect on the amount of stored energy. While for deformed (strain 0.2 and 0.3) Fe-30 wt. % austenitic steel, fine grains (mode grain size $\sim 100 \mu\text{m}$) have higher stored energy as compared to coarser grains (mode grain size $\sim 160 \mu\text{m}$) [220].

The grain size also effects the number of nucleation sites for recrystallized grains. Presence of fine grain microstructure favours higher grain boundary nucleation sites during annealing [96]. While, coarse grain microstructure has lower grain boundary nucleation sites but can have a higher number of deformation bands [96,230,231] and shear bands [96,232,233] which act as nucleation sites [234–236] for recrystallized grains during annealing.

In the general case, a fine grain microstructure will have faster recrystallization kinetics than a coarse grain microstructure due to the higher number of statistically needed grain boundary nucleation sites per unit area for recrystallized grains and higher stored energy for further growth of recrystallized grains [96]. Ji et al. [220] have studied the recrystallization kinetics of cold-deformed (strain ~ 0.3) Fe-30 wt. % Ni austenitic steel for fine grain size (mode grain size $\sim 100 \mu\text{m}$) and coarse grain size (mode grain size $\sim 160 \mu\text{m}$) distributions. For low strain cold-deformed samples, the fine grain size distribution microstructure showed faster recrystallization kinetics due to higher number of nucleation sites and stored energy than coarse grain size distribution at annealing temperatures of $850 \text{ }^\circ\text{C}$ to $950 \text{ }^\circ\text{C}$. Fenghui et al. [237] demonstrated the effect of initial grain size difference on recrystallization kinetics of Fe-3 wt. % Si steel during hot-deformation in a Gleeble-2000 thermo-mechanical machine.

During hot-deformation of electrical steel at high strain ~ 0.9 , strain rate $\sim 30\text{s}^{-1}$ and target temperature of $1050\text{ }^\circ\text{C}$, recrystallization kinetics is in the order of microstructure_1 (average grain size $\sim 296\text{ }\mu\text{m}$) $>$ microstructure_2 (average grain size $\sim 520\text{ }\mu\text{m}$) $>$ microstructure_3 (average grain size $\sim 839\text{ }\mu\text{m}$).

2.10.3. Impeding force against recrystallization

2.10.3.1. Role of precipitates on recrystallization kinetics

Once nucleation is completed, recrystallized nuclei grow at the expense of stored energy. Developing fine recrystallized grains is dependent upon annealing cycle parameters, solute atoms and shape, size, inter-distance, and volume fraction of precipitates. Large particles enhance recrystallization nucleation while small particles inhibit the motion of interfaces during annealing by pinning at GB or dislocations which in return retards recrystallization. The role of large and small particles during annealing is mentioned below:

Large particles ($> 0.1\text{ }\mu\text{m}$ [96,122]) – Intensity of distortion and dislocation density is highest near large particles and decreases with increased distance from particle/matrix interface. Because of variation in dislocation density and orientation, finer recrystallized grains are formed near particles while coarse grains are formed away from it, therefore to avoid a heterogeneity of grain size distribution a high density of second phase particles are required. Particle stimulated nucleation (PSN) leads to the development of weak recrystallized texture; the region near the particle has various varieties of orientation and therefore multiple nuclei will have their own orientation which on a broader scale averages out and leads to a weak texture [96,108,122].

Small particles – Small particles pin GBs or dislocations and restrict their motion during annealing which hampers nucleation growth [238]. Zener pinning force for randomly distributed particles is given by [100,101,217,239]:

$$\Delta G_{pin} = \frac{3}{2} * \sigma * V_m * \frac{f}{r} \quad (2.10-4)$$

Where, f and r are the volume fraction and radius of particles respectively and σ is energy of grain boundaries. The mechanism of pinning is exactly the same as discussed in the case of precipitation strengthening, the only difference is that in this case GB/dislocation motion is inhibited. During annealing of cold-rolled microalloyed steel, recrystallization initiation temperature is increased due to inhibition of dislocation motion by fine precipitates [37], fine precipitates are also favourable for refinement of recrystallized grain size [240]. Choi et al. [37] investigated the difference in recrystallization behaviour of two cold-rolled ultra-low-carbon steel grades with different quantities of Ti (grade A containing $\sim 0.026\text{ wt. \%}$ of Ti and grade B containing $\sim 0.082\text{ wt. \%}$ of Ti). Since the wt. % of Ti is higher in case of grade B

than grade A, during annealing a higher volume fraction of fine TiC precipitates forms along dislocations in grade B. Fine precipitates interfere with dislocation movement and more effectively retard recovery and recrystallization kinetics in grade B as compared to the grade A. Belyakov et al. [41] observed the pinning of TiC precipitates along the grain boundaries of <001>//Compression-axis (CA) grains of Ti-microalloyed cold-worked steel in TEM, lower stored energy of <001> grains and precipitation pinning along grain boundaries resulted in slower recrystallization kinetics.

2.10.3.2. Role of solute drag on recrystallization kinetics

Solute atoms also have a retarding effect on GB movement during annealing. Solute atoms get adsorbed on GBs and change their energy and structure. Segregated solute atoms are dragged along with GBs and have a negative impact to its motion during annealing [108,153,247,203,239,241–246]. Migration of GB under solute drag is affected by solute concentration, diffusivity of solute atoms, interaction energy between solute atoms and GB [245]. Lücke and Detert [241] were the first researchers who theoretically found out the drag effect on GB movement by solute atoms. While Cahn [203], further developed solute drag theory and gave solute drag force for low and high GB velocity regimes, which is expressed as:

$$\Delta G_{sd} = \frac{C_o * \alpha * v}{1 + \beta^2 * v^2} \quad (2.10-5)$$

$$\alpha = \frac{N_v * (k * T)^2 * \delta}{E_o * X} * \left(\sinh\left(\frac{E_o}{k * T}\right) - \left(\frac{E_o}{k * T}\right) \right) \quad (2.10-6)$$

$$\beta^2 = \frac{\alpha * k * T * \delta}{2 * N_v * E_o^2 * X} \quad (2.10-7)$$

Where, C_o is concentration of solute atom, N_v is molar volume, k is Boltzmann constant, T is temperature, δ is grain boundary thickness, E_o is grain boundary interaction energy with atom, X is bulk diffusion constant and v is grain boundary velocity. Recent works [153,188,189,246] have shown that higher wt. % of Mn content in steel retards recovery/recrystallization rate via solute drag. Therefore, controlling the content of solute atoms is significant in recrystallized microstructure development.

2.10.3.3. Intrinsic boundary friction (IBF)

The solute drag equation as discussed above considers drag contribution from solute atoms/impurities against GB movement. In addition to that, there is also drag effect in pure metals with no contribution from impurity atoms. Cahn [203] gave the expression for intrinsic drag force as:

$$\Delta G_{IBF} = \frac{v}{M_i} \quad (2.10-8)$$

$$M_i = \frac{2.63}{T} * e^{\left(\frac{-20754}{T}\right)} \quad (2.10-9)$$

Where, M_i is intrinsic grain boundary mobility [182,203]. Therefore, net driving force for recrystallization could be summarised as:

$$\Delta G_{RX} = \Delta G_{SE} - \Delta G_{pin} - \Delta G_{sd} - \Delta G_{IBF} \quad (2.10-10)$$

$$\Delta G_{RX} = 0.5 * \rho * G * b^2 * V_m - \frac{3}{2} * \sigma * V_m * \frac{f}{r} - \frac{C_0 * \alpha * v}{1 + \beta^2 * v^2} - \frac{v}{M_i} \quad (2.10-11)$$

2.11. Recrystallization fraction evaluation

Recrystallization (%) is one of the most important parameters to compare the recrystallization kinetics among different steel grades. Depending upon annealing parameters (temperature, dwell time, heating rate etc.), steel chemistry and cold-rolled deformation (%), recrystallization fraction could vary from 0 to 1 as annealing proceeds [108]. Prasad et al. [29] investigated the effect of cold-rolled deformation (%) on recrystallization fraction of a HSLA grade steel during sub-critical annealing. With increased cold-rolled deformation (30 %, 45 % and 60 %) in HSLA grade steel, recrystallization (%) is increased for annealing temperature of 500 °C. With an increase in temperature to 600 °C, recrystallization (%) further increases with equiaxed recrystallized grain development [29].

Evaluation of recrystallization (%) by direct (optical microscopy, SEM) and indirect (calorimetry, neutron diffraction, XRD, EBSD and micro- and macro-hardness) methods have been investigated for different materials in the past [248–256]. Evaluation of recrystallization (%) via EBSD is fast and reliable when compared to other methods [250,251]. Along with recrystallization (%), other information about microstructure such as grain size, misorientation, aspect ratio, texture etc. could be acquired. For recrystallization (%) evaluation, various forms of post-processed EBSD data could be used. Jazaeri and Humphreys [250] post-processed EBSD data in an inbuilt software, VMAP [250,257] and evaluated high angle grain boundary (HAGB) fraction. Fractional change in HAGB (%) was calculated with respect to as-received and fully annealed microstructural conditions to evaluate recrystallization (%). Recrystallized (%) value measured by HAGB (%) method was similar to hardness and point counting method from optical image microscopy methods [250].

For an un-recrystallized matrix, local misorientation between measured points is higher than the recrystallized matrix. Local average misorientation of a centre point is evaluated from the neighbouring points [252]. Depending upon the user's choice, perimeter of the contributing neighbours (3x3, 5x5, 7x7, 9x9 and 11x11) could be varied to evaluate local average misorientation of the centre point. A tolerance value of LAM is set to distinguish recrystallized and un-recrystallized regions of a matrix. In general, a matrix with LAM value of less than 1°

is considered as recrystallized and greater than 1° is considered as un-recrystallized [35,96,251].

2.12. Texture development during annealing of cold-rolled steel

For cold-rolled steel, stored energy is different for different grain orientations. Dillamore et al. [224] reported stored energy in alpha fibre is in the order of $SE_{\{100\}\{011\}} < SE_{\{112\}\{011\}} < SE_{\{111\}\{011\}}$ based on the subgrain misorientation measurements. With an increase in rolling reduction, the intensity of both fibres is enhanced [62,87]. Wauthier-Monnin et al. [87] carried out dislocation density analyses for alpha and gamma fibres for different rolling strains (between 15% and 93%). Their study revealed a dislocation density $7.25E+15m^{-2}$ of the $\{111\}\{112\}$ grain orientation in the gamma fibre as compared to $4.28E+15m^{-2}$ of the $\{100\}\{110\}$ and $1.35E+15m^{-2}$ of the $\{112\}\{110\}$ grain orientations in the alpha fibre. Due to an increment in the intragranular misorientation in the grain orientation $\{111\}\{112\}$ of the gamma fibre at $\sim 76\%$ rolling strain, there is a significant increase in the dislocation density [87]. Since stored energy (SE) is linearly dependent on the dislocation density, the difference in the stored energy of the alpha and gamma fibres is reflected in the difference in the recrystallization rate of both fibres during annealing [125,156,214–216]. Since gamma fibres consist of grains of high stored energy, preferentially nucleation happens here first and grains grow by consuming grains of other orientation such as alpha fibres, because of this, strong gamma and weak alpha fibres are established [62,258]. Fig. 2.12-1 shows ODF maps of cold-rolled low-carbon annealed steel with recrystallization (%) of 0 %, 24 %, 66 % and 100 %. With an increase in recrystallization (%), bulk texture obtained from XRD reveals strong gamma fibre and weak alpha fibre. Further post-processing of EBSD data shows strong gamma texture in the recrystallized matrix and strong alpha in the un-recrystallized matrix, which explains preferential recrystallization of gamma fibre grains [259]. Sometimes the intensity of alpha fibre is increased and gamma fibre decreased because of Strain Induced Boundary Migration (SIBM), where grains of lower energy start growing by consuming higher stored energy matrix of gamma region [260]. Alternatively, recrystallization texture may also develop weakly due to PSN [61].

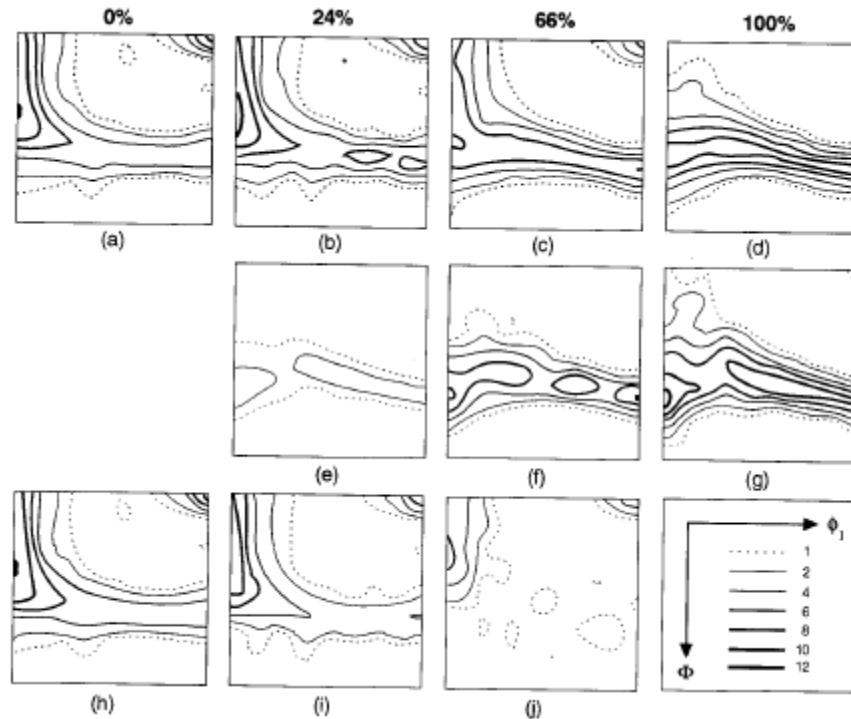


Fig. 2.12-1 ODF on the section $\phi_2=45^\circ$: bulk texture evaluated from XRD (a) - (d), recrystallized texture (e) - (g) and un-recrystallized texture (h) - (j) evaluated from EBSD of a steel for recrystallization (%) of 0%, 24%, 66% and 100% (taken from Hutchinson [259])

Recrystallization texture is also dependent on the precipitate distribution in microstructural regions corresponding with alpha or gamma fibres: if precipitates actively pin grain boundaries (GBs) of gamma fibres then during annealing it gives advantage to other grain orientations to preferably recrystallize, which results in weak gamma texture [156]. Investigating the preferential pinning of precipitates along different textural components is important to understand recrystallized texture development.

2.13. Mechanical properties of low-carbon steel

Strength and ductility are two basic mechanical properties of steel which are used in selecting particular steel grade for automotive body applications. In general, increases in strength lead to poor ductility [9,261,262]. Strength could be measured in terms of stress required to generate a certain amount of plastic deformation or maximum stress required to cause material failure. Ductility represents the capability of a material to deform to a particular shape before fracture. One of the conventional methods to evaluate both strength and ductility simultaneously is the uniaxial tensile test which gives estimated values of yield strength, ultimate tensile strength and elongation (%) for a particular steel grade [261]. Strength and elongation (%) properties for uniform elongation are independent of the sample geometry of American, European and Japanese testing standards as investigated by Hanlon et al. [262] for a commercial automotive grade, 22MnB5.

During continuous elongation of a dog-bone shaped uniaxial tensile steel sample, yielding does not take place uniformly. There is a drop in yield strength after achieving upper yield strength (UYS) to lower yield strength (LYS). Further elongation takes place for constant LYS by the formation and broadening of plastically deformed bands also known as Lüders bands [261,263–265]. After LYS point (marked as D in Fig. 2.13-1), uniform deformation takes place and the material work-hardens until failure takes place. In industrial practice, 0.2 % offset yield strength is defined as yield strength at 0.2 % of plastic strain [58]. Fig. 2.13-1 represents the diagrammatic sketch of engineering stress-strain curve for annealed mild steel taken from Sylwestrowicz and Hall [264]. UYS represents maximum stress generated by pileup of immobilized dislocations against point defects (such as C and N which creates Cottrell atmosphere around dislocation) [83,97,266,267] or precipitates [83,268]. Once the maximum level of yielding is reached, pileups of dislocations breaks away from surrounding point defects [97]. With an increase in volume fraction of fine precipitates, Lüders strain decreases because of increased work hardening rate [269,270]. Lüders band formation during local yielding throughout the gauge section of uniaxial tensile sample is common in low-carbon ferritic or mild steel than DP or TRIP steels [51,264,265,271]. In case of TRIP steels, retained austenite transforms to martensite upon deformation and provides higher work-hardening without localised deformation [271].

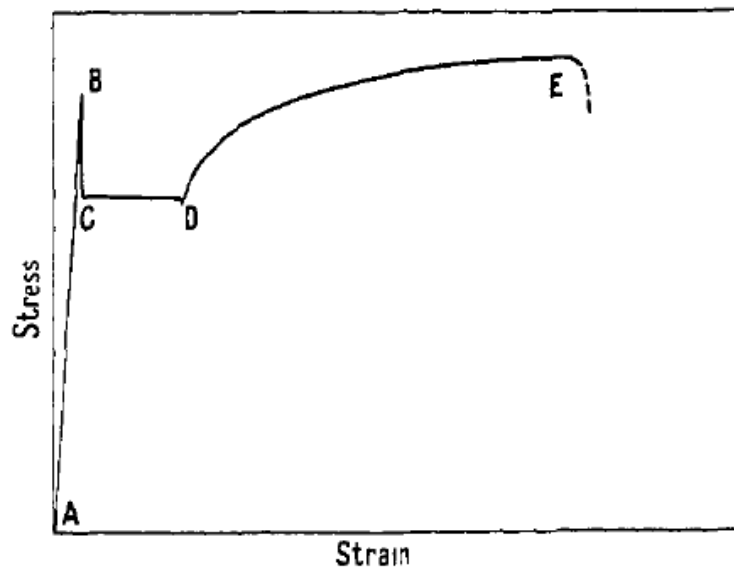


Fig. 2.13-1 Diagrammatic sketch of engineering stress versus engineering strain curve of mild steel. Notation 'A' represents starting of tensile test, 'B' represents upper yield stress, 'C' represents lower yield stress and starting of Lüder band formation, 'D' represents lower yield stress and completion of Lüders band spread across sample and 'E' represents failure of sample (taken from Sylwestrowicz and Hall [264])

Another way to study mechanical properties of steel is the hardness test which is a quick and efficient method and does not require a large sample size [272,273]. Hardness is defined as ratio of indentation load and either surface or projected area of indentation [83,274]. Moreover hardness testing is *quasi*-non-destructive and samples could be used for further tests such as EBSD; TEM study etc [251,272,273]. There are several well established hardness measurement methods (such as Brinell, Vickers, Berkovich, Knoop and Rockwell) [274–276] and most of them are extensively used to assess mechanical properties. Sometimes it is difficult to evaluate yield strength for a material by uniaxial tensile testing due to size or shape restrictions or material inhomogeneity [273]. Alternatively, yield stress can be estimated by Vickers hardness (HV) from widely known empirical equation [272–274]:

$$HV \sim 3 * \sigma_y \quad (2.13-1)$$

Equation (2.13-1) is valid for non-strain hardening materials. While for strain hardening materials, Tabor [277] suggested yield stress to be replaced as flow stress value for strain value range in between 8 % to 10 %.

Nanoindentation technique is well known to study mechanical properties in nanometre scale such as determining the dependence of hardness on grain orientation, matrix strength without GB contribution, hardness dependence on interparticle spacing etc [107,278,279]. During nanoindentation hardness measurement, contact area (between indenter and sample) is indirectly determined by measuring the depth of penetration of the indenter into the sample's surface. By knowing the depth of indentation and indenter geometry, contact area at full load can be calculated [280,281]. Nanoindentation technique also allows correlative study of material properties using other characterisation techniques such as EBSD and/or TEM [251,279,282]. Dziazyk et al. [251] applied nanoindentation hardness techniques to compare recrystallization behaviour with other EBSD analyses such as LAM. Nanoindentation was performed on cold-rolled, partially and fully recrystallized IF steel samples and subsequently EBSD maps were obtained of the matrix containing indents. Recrystallization fraction values evaluated using EBSD based LAM and grain average misorientation (GAM) methods were in correlation with local hardness of matrix measured by nanoindentation technique [251]. Correlative study using EBSD/TEM to understand microstructural properties and tensile/hardness experiments to evaluate strength and formability is significant for developing steel of required parameters for automotive applications.

3. Research questions, hypotheses and objectives

3.1. Research questions

Based on the above presented literature review following research questions are formulated.

1. It is well known that precipitates of carbo-nitrides of Ti and V nucleate along dislocations and grain boundaries and solute atoms of Mn segregate on these sites, which inhibit recrystallization kinetics during annealing. Moreover, Mn is commonly known to delay precipitation kinetics in austenite region which further affects recrystallization kinetics during inter-critical annealing. The effect of Ti, V or Mn on dynamic recrystallization of ferrite, interaction between interphase precipitates and austenite-ferrite interface during hot-rolling process is well known in the literature as well. The effect of Ti and Mn on the recrystallization kinetics and mechanical properties obtained after continuous sub-critical annealing of cold-rolled Ti-V and V-microalloyed single phase ferritic steel has not yet been discussed in detail. The main research questions related to the development of cold-rolled continuously-annealed microalloyed steels are:

- How much strength and elongation (%) will Ti microalloyed grade gain or lose compared to a base grade during sub-critical annealing?
- How will Ti(C/N) and V(C/N) co-exist in ferrite phase (as an individual or a complex precipitates); would they interfere with dislocations and grain boundaries to develop finer recrystallized grains during sub-critically annealing?
- What will be the effect of Mn solute atoms on Ti- and V- precipitation kinetics in ferrite phase during sub-critical annealing?
- How will the recrystallization process effect precipitation kinetics and vice versa during sub-critical annealing of a cold-rolled ferrite phase steel for three grades (base, Ti+ and Ti+Mn+)?

2. During cold-rolling of hot-rolled steel, grains elongate and two main texture components, alpha fibre and gamma fibre, are formed. It is well known that gamma fibre grains have higher stored energy than alpha fibre grains and therefore during sub-critical annealing of cold-rolled steel, gamma fibre grains recrystallize faster than alpha fibre grains. There have been qualitative investigation on recrystallized texture development in IF and ferritic steels performed by SEM/EBSD mapping on annealed samples. Quantitative investigation on difference in recrystallization behaviour of alpha and gamma fibres has not yet been discussed in detail:

- What will be the trend of change in average dislocation density in alpha and gamma fibres during sub-critical annealing of cold-rolled Ti-V microalloyed single phase ferritic steel?
- How to quantify recrystallization behaviour of alpha fibre grains during sub-critical annealing of cold-rolled Ti-V microalloyed single phase ferritic steel?
- What are the similarities and differences in evolution of recrystallized texture development observed on surface and within bulk material during sub-critical annealing of cold-rolled Ti-V microalloyed single phase ferritic steel?

3. Hot-rolled single ferritic phase with nanometre sized precipitate steel products have been investigated previously by JFE and Tata Steel, commercially known as NANOHITEN [283] and XPF [10] grades respectively. The steel has an excellent combination of strength and stretch-flange formability suitable for manufacturing of chassis and suspension parts for automotive applications. Taking the inspiration from hot-rolled XPF grades, three novel grades of cold-rolled low-carbon microalloyed steel (base grade containing V as microalloying element; Ti+ grade containing Ti as microalloying element in base grade; and Ti+Mn+ grade containing additional Mn in Ti+ grade) has been proposed for body-in-white (BIW) applications. In the current automotive market, cold-rolled multiphase steel grades (TS > ~ 600 MPa) are widely used for BIW parts, potentiality of a thin gauged cold-rolled and annealed single phase ferrite microstructure with nanometre sized random (non-interphase) precipitates and TS > ~ 600 MPa has not been explored in detail.

- How much precipitation strengthening from random precipitates will be obtained to compensate the loss of cold-rolled strength during sub-critical annealing of cold-rolled Ti-V microalloyed single phase ferritic steel?
- Will strength and elongation (%) properties of base, Ti+ and Ti+Mn+ grades after sub-critical annealing for suitable conditions be similar to DP and CP steel properties?
- Will random precipitation in base, Ti+ and Ti+Mn+ grades after sub-critical annealing be able to provide similar precipitation strength as that of interphase precipitation strengthening in hot-rolled steel grades of NANOHITEN and XPF, which annealing conditions will be required to achieve this?

3.2. Research hypotheses

3.2.1. Overall working hypothesis

The decrease of strength of as-cold rolled material will be to some extent offset by precipitation of fine V and Ti containing carbides within the ferrite matrix during annealing. These precipitates will provide both dispersion strengthening and grain boundary refinement via grain boundary pinning. The development of fine polygonal recrystallized grains during

annealing will simultaneously provide extended elongation and increase of formability as compared to the as-cold rolled textured microstructure prior to annealing.

3.2.2. Further hypotheses explored in this PhD research are as follows

1. The presence of V in base grade and additional Ti in Ti+ and Ti+Mn+ grades will combine with C and N to form fine V(C/N) and (Ti,V)(C/N) precipitates respectively and inhibit recrystallization kinetics by pinning along sub-grains and grain boundaries. Moreover the addition of extra solute Mn in Ti+Mn+ grade will further retard recrystallization kinetics by solute drag. It is hypothesized that recrystallization kinetics in base grade will be higher than the other two steel grades (Ti+ and Ti+Mn+) during sub-critical annealing.

2. Deformed gamma fibre grains have higher stored energy than deformed alpha fibre grains and therefore higher initial driving force for nucleation of recrystallization. It is hypothesized that by performing hot-stage *quasi* in-situ analysis of geometrically necessary dislocation (GND) density in alpha and gamma fibres, recrystallization behaviour and evolution of respective fibres can be quantified. During sub-critical annealing, recrystallization kinetics of gamma fibre grains will be higher than alpha fibre grains. Subsequently the drop in average geometrically necessary dislocation (GND) density will be significantly higher in the case of gamma fibre than alpha fibre.

3. It is hypothesized that the recrystallized microstructure in base, Ti+ and Ti+Mn+ grades of steel are dominated by gamma fibre grains due to higher potential for recrystallization as compared to alpha fibre grains.

3.3. Research objectives

3.3.1. Main objectives of this PhD project are as follows

1. To investigate recrystallization behaviour and recrystallization texture development in three cold-rolled microalloyed steel grades (base grade containing V as microalloying element; Ti+ grade containing Ti as microalloying element in base grade; and Ti+Mn+ grade containing additional Mn in Ti+ grade) during sub-critical annealing for different conditions: 700 °C for 0 s, 800 °C for 0 s; 800 °C for 2 min; 800 °C for 5 min; 800 °C for 15 min; 800 °C for 30 min; 800 °C for 1 hour and 800 °C for 2 hours.

2. To study the evolution of alpha and gamma fibres during static recrystallization in cold-rolled low-carbon Ti-V bearing microalloyed steel by performing hot stage *quasi* in-situ EBSD analysis of geometrically necessary dislocation (GND) density in respective fibres.

3. To study precipitate distribution within ferrite matrix and interaction with grain boundaries by analysing STEM-EDS chemical maps on samples of hot-rolled, cold-rolled and sub-critically annealed grades of steel prepared using FIB-lift out method.

4. To study mechanical properties including hardness, strength and formability using uniaxial tensile testing on as-received, partially and fully recrystallized samples for different heating parameters.
5. To develop correlative and *quasi* in-situ material characterisation techniques to study and understand recrystallization kinetics, recrystallized texture development, precipitation and recrystallization interaction in steel grades for the automotive body applications.

4. Methodology

4.1. Materials investigated

Three different new grades (base grade containing V as microalloying element; Ti+ grade containing Ti as microalloying element in base grade; and Ti+Mn+ grade containing additional Mn in Ti+ grade) of hot-rolled (500 mm x 110 mm x 3 mm) and cold-rolled (500 mm x 110 mm x 1mm) low-carbon microalloyed steel sheets were provided by Tata Steel Europe and investigated in this study. Chemical compositions of the three grades of steel, as determined by chemical analysis, are shown below in Table 4.1-1.

Table 4.1- 1: Chemical composition in weight (%) for the three grades of steel investigated in this study

Grades	C	Si	Mn	P	S	Al	V	Ti	N
Base	0.051	0.008	0.34	0.001	0.0009	0.033	0.15	-	0.0028
Ti+	0.051	0.007	0.34	0.001	0.0007	0.032	0.15	0.078	0.0022
Ti+Mn+	0.051	0.007	0.89	0.001	0.0009	0.030	0.15	0.075	0.0031

The purpose of adding Ti along with V in Ti+ and Ti+Mn+ grades is to study the effect of Ti precipitation on recrystallization kinetics and mechanical properties and compare with base grade containing only V as microalloying precipitating element. For Ti+Mn+ grade, additional Mn is added to study the effect of Mn solute on recrystallization behaviour and mechanical properties and compare with base and Ti+ grades. The reasons for choosing each particular element for the three grades are mentioned below:

- Si, Al and P: ferrite stabilisers [98,284]
- Ti and V: form carbides which provide precipitation strengthening and also act as ferrite stabilisers [98,284]
- Mn: for solid solution strengthening [98,99]
- S: as low as possible to avoid any detrimental effect such as brittle failure along grain boundaries [285]
- C: low carbon to maintain supersaturated ferrite matrix with fine nanometre sized precipitates [10,21,46]
- N: intentionally low to avoid coarse precipitates of TiN [10,21,46]

4.2. Details of laboratory processed hot-rolled and cold-rolled steel

Hot-rolling and cold-rolling processes were simulated in the laboratory at pilot scale at Tata Steel Europe R&D. Steel blocks of thickness ~ 30 mm were heated in a muffle furnace at $T \sim 1200^\circ\text{C}$. Manual descaling was employed to remove any oxide layer on heated slabs. Heated slabs were rolled in between a set of two rollers manually up to thickness of 3 mm. The final rolling temperature ~ 890°C was recorded by pyrometer. To simulate the industrial cooling process, strips were passed through a set of cooled rollers (run out table), where it was water cooled to temperature of ~ 580°C to avoid interphase precipitation and to ensure that all austenite grains were transformed to ferrite grains. Strips were then transferred to a cooling furnace for controlled slow cooling to room temperature in duration of 24 hours. Selected hot-rolled steel sheets (500 mm x 110 mm x 3 mm) were taken out from the processing route for microstructural investigations using SEM-EBSD and STEM, the rest of hot-rolled sheets were cold-rolled manually at room temperature to thickness of 1 mm with ~ 70 % reduction in thickness.

4.3. Experimental procedures to study microstructure properties of cold-rolled annealed samples

Typical industrial annealing cycles employed by Tata Steel Europe for annealing of cold rolled low-carbon microalloyed steel grades are shown in Fig. 4.3-1. Numbers 1 – 2 – 3 – 4 – 5 indicate cold-rolled steel heating and cooling steps throughout annealing process.

Step 1 – 2: Cold-rolled steel sheet is heated in Direct-fired furnace (DFF) in an open flame environment.

Step 2 – 3: Sheet is slowly heated and cooled inside Radiant-tube furnace (RTF) via radiation.

Step 3 – 4: Sheet is galvanized with Zn coating ($400^\circ\text{C} < T < 500^\circ\text{C}$).

Step 4 – 5: Galvanized sheet is slowly air cooled to room temperature.

In section 2.4 of the literature review “Process route for cold-rolled annealed steel”, the steps of a continuous annealing line cycle are explained in detail.

To avoid the possibility of coarsening of precipitates and promote fine recrystallized grain development, laboratory scale bulk size (6 mm x 6 mm x 1 mm) samples were annealed in a muffle furnace with fast heating rate (about $10^\circ\text{C}/\text{s}$ to $15^\circ\text{C}/\text{s}$) to simulate industrially designed annealing cycles A and B. Cycle C with lower heating rate promotes coarser precipitation and degrades precipitation strengthening [286] and was therefore not simulated during bulk muffle annealing experiments. Further longer dwell time of 0 s, 2 min, 5 min, 15 min, 30 min, 1 hr and 2 hrs annealing experiments were done at 800°C to study recrystallization behaviour of all three grades. EBSD and STEM analysis were carried out to

study microstructure and precipitate distribution for different annealing conditions. To understand the difference in softening behaviour in the three grades, nanoindentation analysis was carried out at different annealing conditions. Hot stage *quasi* in-situ EBSD was performed to study recrystallization kinetics of alpha and gamma fibres by analysing GND in respective fibres. Dilatometry experiments were done to evaluate starting and finishing temperature of phase transformation from ferrite to austenite in base, Ti+ and Ti+Mn+ steel grades. To study mechanical properties, hardness measurements were performed on bulk annealed samples in WMG and tensile experiments were performed on ISO/EM A50 size samples for uniaxial test in Tata Steel Europe. Further sub-sections discuss in detail about the experimental and software tools used to investigate recrystallization and precipitation behaviour.

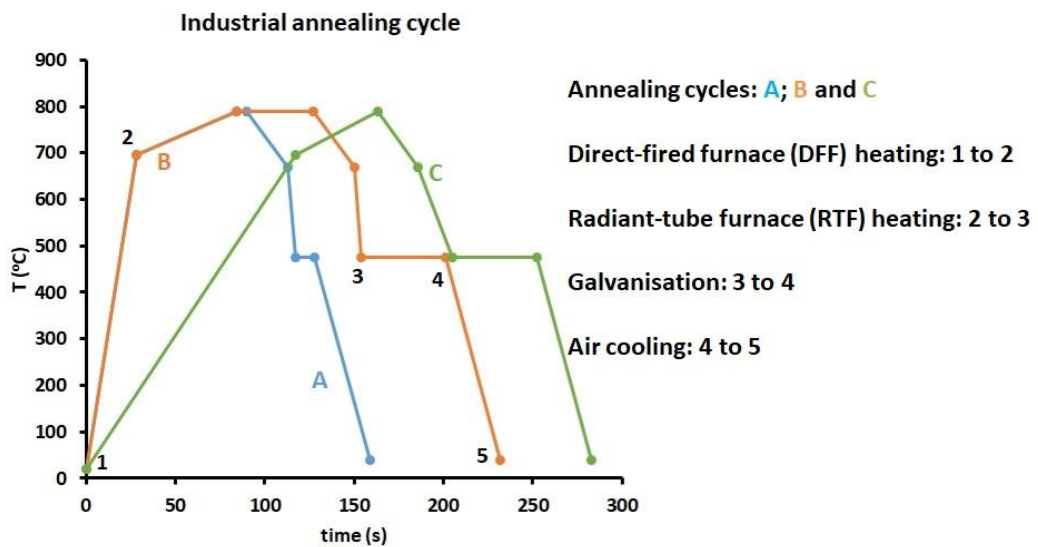


Fig. 4.3-1 Tata Steel industrial annealing cycles, A, B and C (permission from Tata Steel Europe)

4.3.1. Muffle furnace annealing and EBSD investigation of steel grades

Samples with dimensions of 6 mm × 6 mm × 1 mm were cut from the centre of the as-received sheet (Fig. 4.3-7) and annealed in a muffle furnace under following conditions: 700 °C 0 s, 800 °C 0 s; 800 °C 2 min; 800 °C 5 min; 800 °C 15 min; 800 °C 30 min; 800 °C 1 hour and 800 °C 2 hours. Heating rate was controlled to 10 – 15 °C /s. To simulate quick thermal response of the sample, a small metal block was kept inside the heated furnace for ~ 0.5 hours. A 'K type' thermocouple reader coupled with data logger was fitted inside the furnace which records the surface temperature of the metallic block as shown in Fig. 4.3-2. The temperature difference between the metallic block and muffle furnace (measured by inbuilt thermocouple) was recorded as 5 °C. As the target temperature was achieved, the muffle furnace was opened, the test sample was quickly put on the metallic block and the door was closed. Temperature was recorded throughout the annealing cycle. Once the required annealing temperature and

dwel time were achieved, the door was opened and the sample was taken out to be air cooled to room temperature. Fig. 4.3-3 shows the plot of the annealing temperature versus time of annealed samples for different annealing conditions: 700 °C 0 s, 800 °C 0 s, 800 °C 2 min and 800 °C 5 min measured by data logger along with industrial annealing cycles A, B and C. The cooling curves for all the annealing conditions were similar and are presented for 800 °C 5min annealing condition in Fig. 4.3-3.

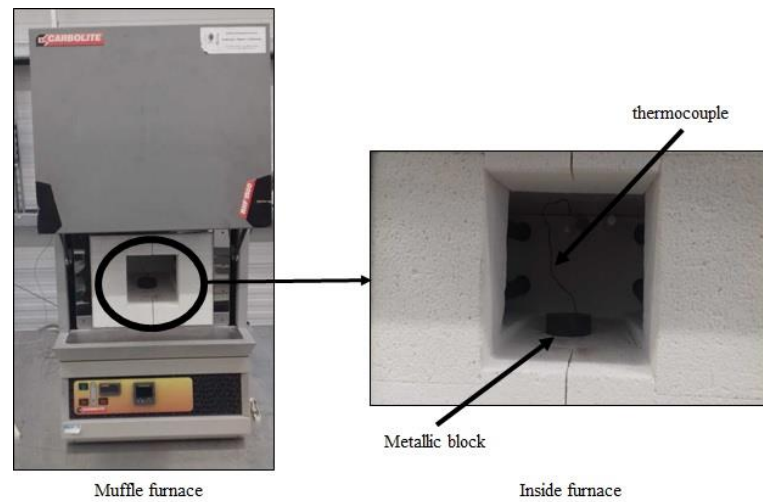


Fig. 4.3-2 Muffle furnace based in WMG. Thermocouple records surface temperature of metal block and feeds back to data logger equipment

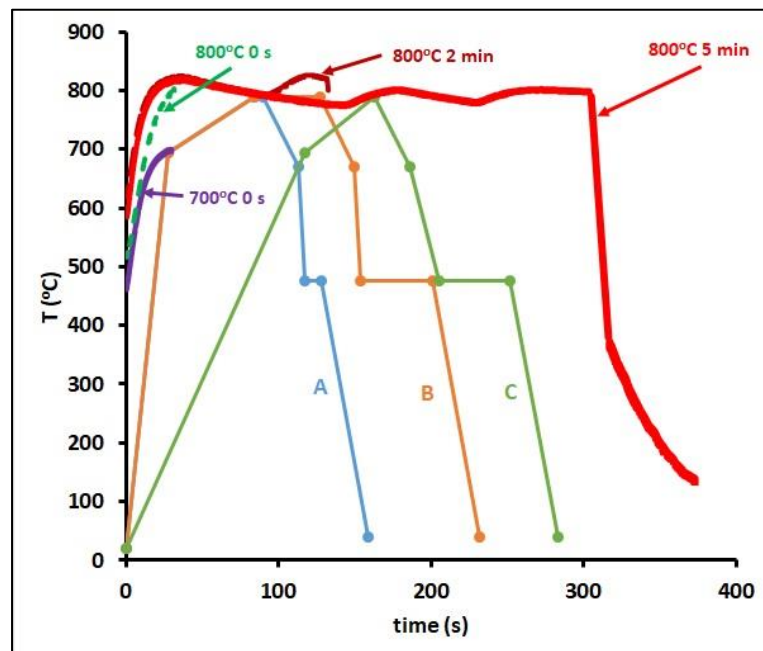


Fig. 4.3-3 Tata Steel industrial annealing cycles, A, B and C and temperature versus time plots recorded by data logger for annealing conditions of 700 °C 0 s, 800 °C 0 s, 800 °C 2 min and 800 °C 5 min. Tata Steel Industrial annealing cycles are shown after permission from Tata Steel Europe

For microstructural study, small samples (6 mm x 1 mm x 1mm) were cut in half parallel to the RD-ND plane from the bulk muffle furnace annealed sample (Fig. 4.3-7). Sectioned samples were mounted in Bakelite and polished using standard metallographic techniques for microstructural investigation in the transverse (TD) direction. Polished samples were placed on the stage inside SEM with the Rolling Direction (RD) parallel to X-axis, Transverse direction (TD) parallel to Z-axis and Normal direction (ND) parallel to Y axis of the stage coordinate axis system inside of the chamber of a FEG-SEM Carl Zeiss fitted with NordlysNano EBSD camera by Oxford Instruments [287].

For the EBSD data acquisition, an accelerating voltage of 20 kV, an aperture size of 240 μm with working distance of 22 mm and a step size of 0.15 μm to 0.3 μm was used depending upon the magnification used for image acquisition. MAD values obtained were less than 2°. Hough resolution (= 60) and pattern resolution (= 160 x 120 pixels) were set as constants during all analyses. For cold-rolled steel, indexing hit rate was > 80 % and cold-rolled annealed steel, indexing hit rate was > 95 %. No cleaning approach of the EBSD data set were utilised for GND and recrystallization (%) calculations. While, standard cleaning (Fig. 4.3-4) [288] of one iteration cycle and four neighbouring pixels was utilised for ND-IPF EBSD maps with a scratch as mechanical damage during polishing as presented in thesis.

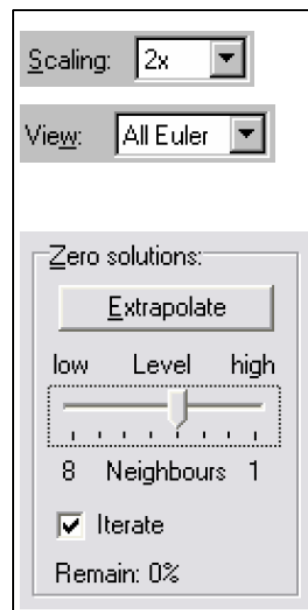


Fig. 4.3-4 Parameters for standard noise reduction function (taken from Channel 5 Oxford Instruments manual [288])

4.3.2. Texture study of bulk furnace annealed sample using EBSD

The muffle furnace-annealed bulk samples were also used to study the alpha and gamma fibre texture before and after annealing. In order to study texture in a statistically significant microstructural area, EBSD scans at low magnification of $\times 250$ were taken on the RD-ND

plane of as-received and annealed polished samples for different annealing conditions using the same EBSD data acquisition parameters as mentioned previously. To achieve representative texture analysis, at least 1000 recrystallized grains in partially recrystallized samples were analysed [289]. EBSD files were exported into HKL Channel 5 software of Oxford Instruments to evaluate Orientation Distribution Function (ODF) on the section $\phi_2=45^\circ$ plotted using Bunge notation [290] for Euler space representation. For partially recrystallized samples, ODF plots were obtained by selecting un-recrystallized and recrystallized microstructural matrices respectively [61]. For other cases such as cold-rolled state and annealed samples with negligible recrystallization fraction ($< 10\%$), ODF plots were obtained by selecting the complete microstructural matrix. Microstructural matrix with local average misorientation $< 1^\circ$ was characterised as recrystallized grains [35] during selection procedure.

4.3.3. Texture study using XRD

Bulk texture analysis of cold-rolled and muffle furnace annealed samples for 800 °C 2 hrs annealing condition were performed using X-ray diffraction technique [291] at Tata Steel Europe. Texture measurements were conducted at approximately mid-thickness layer of RD-TD plane. Pole figures, (110), (200) and (211) were acquired from Bruker D8 diffractometer fitted with an area sensitive detector (GADDS). Pole figure data from X-ray were exported into Van Houtte's MTM-FHM software package [292] to evaluate 2D ODF maps on the section $\phi_2=45^\circ$.

4.3.4. Hot stage *quasi in-situ* EBSD

The samples for hot stage *quasi in-situ* EBSD were cut parallel to the Rolling Direction (RD) - Normal Direction (ND) plane from the central part of the rolled sheet, machined to the size of 6 mm \times 1 mm \times 1 mm (Fig. 4.3-7) and mounted in Bakelite. The samples were polished using standard metallographic techniques. After polishing, the samples were extracted from Bakelite and placed onto a Gatan Murano 525 heating stage [293] shown in Fig. 4.3-5 with the Rolling Direction (RD) parallel to X-axis, Transverse direction (TD) parallel to Z-axis and Normal direction (ND) parallel to Y axis of the sample holder coordinate axis system inside of the chamber of a FEG-SEM Carl Zeiss fitted with NordlysNano EBSD camera by Oxford Instruments [287]. The samples were annealed at three different conditions: 700 °C 0 s, and 800 °C 0 s and 800 °C 2 min at the heating rate in between 10 °C/s to 15 °C/s (Fig. 4.3-6) and then cooled down to ambient temperature inside the SEM chamber. For the EBSD data acquisition, an accelerating voltage of 20 kV, an aperture size of 240 μ m with working distance of 22 mm and a step size of 0.15 μ m were used. Site specific EBSD scans at magnification of $\times 5k$ of the same locations of the material were taken prior and after heating the sample. Upon cooling, the sample temperature was stabilised at 200 °C to maintain thermal equilibrium and to minimise the thermal drift [125]. Fig. 4.3-6 shows the annealing

temperature versus time plot measured by thermocouple fitted inside the heating stage for different annealing conditions: 700 °C for 0 s, 800 °C for 0 s and 800 °C for 2 min along with industrial annealing cycles A, B and C.

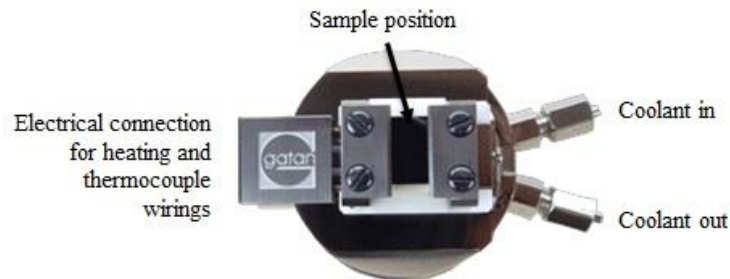


Fig. 4.3-5 Gatan Murano 525 heating stage for hot-stage In-situ EBSD experiment (taken from GATAN, Murano and Microtest In-situ Stages [293])

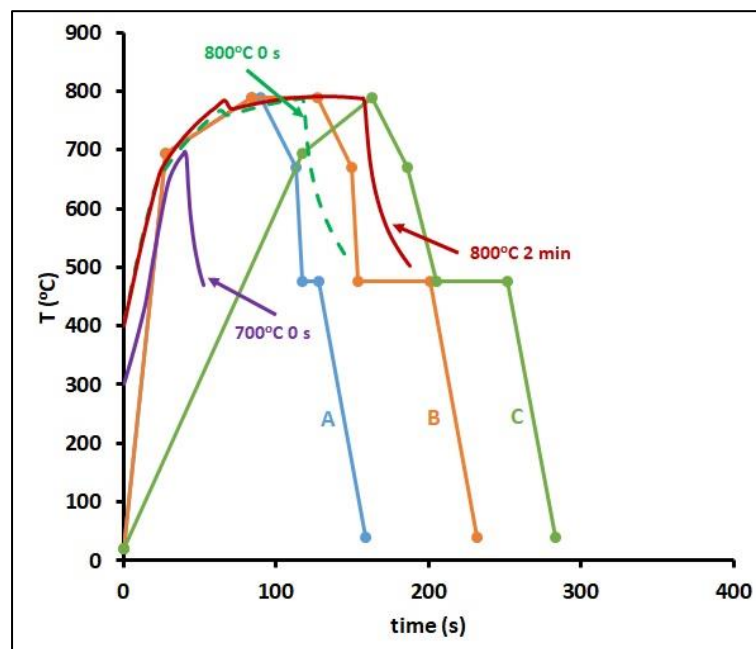


Fig. 4.3- 6 Tata Steel industrial annealing cycles, A, B and C and temperature versus time plots recorded by thermocouple in contact with the sample placed in hot-stage for annealing conditions of 700 °C 0 s, 800 °C 0 s, 800 °C 2 min and 800 °C 5 min. Tata Steel Industrial annealing cycles are shown after permission from Tata Steel Europe

4.3.5. Post processing of EBSD data

For post processing of the EBSD results, files were exported into HKL Channel 5 software of Oxford Instruments. Normal direction Inverse Pole Figure (ND-IPF) maps were obtained from Channel 5 software representing the crystal orientation alignment with respect to the normal direction, ND of the sample. Local average misorientation (LAM) maps with kernel size of 7×7 ($n=3$) were used to quantify fraction of recrystallized grains and GND density by

exporting .ctf files to MTEX texture analysis toolbox, MTEX-4.5.0 available in MATLAB R2016b (<http://mtex-toolbox.github.io/>) [294]. Further, grains with aspect ratio less than 2.6 were considered as recrystallized grains [295] and area of recrystallized grains was used to evaluate recrystallized fraction. Average GND density is calculated from local average misorientation to further evaluate stored energy (contribution from GND density only) implementing the same methodology of Wauthier-Monnin et al., Betanda et al. and Huang et al. [87,89,296] with aim to quantify the difference in rate of recrystallization of respective fibres during annealing at different conditions [125,156,214–216]. To evaluate a noise free GND density, the LAM value of all points were calculated and plotted based on a kernel size of 11×11 ($n=5$) to 3×3 ($n=1$) as described by Moussa et al. [297]. The LAM value for 0th neighbour ($n=0$) was evaluated after extrapolation and used as an average measurement for the noise. For a deformed matrix, the average measured noise is about 0.71° whereas for a recrystallized matrix this is about 0.25° [297,298]. The average measurement for the noise was used to eliminate noise from the average GND values [297]. The detailed information on noise and GND density calculations are mentioned in section 9.1 of the supplementary information chapter.

4.3.6. FIB-lift Out and TEM investigation of steel grades

Polished samples after normal and heated stage EBSD were further subjected to FIB lift-out TEM sample preparation after heating at conditions: 700°C 0 s, 800°C 0 s; 800°C 2 min; 800°C 5 min. Site-specific FIB lift-outs from recrystallized and un-recrystallized regions were carried out to prepare thin samples with dimension of $6\ \mu\text{m} \times 6\ \mu\text{m}$ and $0.1\ \mu\text{m}$ to $0.2\ \mu\text{m}$ thickness for precipitate investigation by TEM. A modified FIB-lift out method was implemented using initial ion milling at 30 kV by Gallium (Ga) ions followed by ion milling at 500 V at an angle of 12° on both sides of the FIB-lift out samples to minimise Ga ion damage and re-deposition inside the chamber of FEI Versa 3D Dual Beam [149,200]. Thinned samples were attached to a Copper grid and moved into the FEG-TEM FEI Talos F200X operating at 200 kV.

Complex precipitates of Titanium-Vanadium carbides (Ti,V)(C/N) were identified from high-resolution scanning transmission electron microscopy (STEM) imaging and chemical maps were obtained using four EDS Super-X Silicon Drift Detectors (SDD) fitted inside the TEM Talos at a collection angle of 0.9 srad [149]. For image analysis, STEM-EDS chemical maps were imported into ImageJ software [299] for quantitative analysis of precipitate dimensions and their distribution [300]. For this quantitative analysis, a minimum of 500 precipitates were analysed from 10 different STEM images taken from two different FIB-lift out samples for each annealing condition [149]. Precipitates were assumed to be circular (in 2D) for

quantitative analysis [58,301]. Fig. 4.3-7 represents the sample geometry for hot-stage *quasi* in-situ EBSD and furnace-annealing experiments.

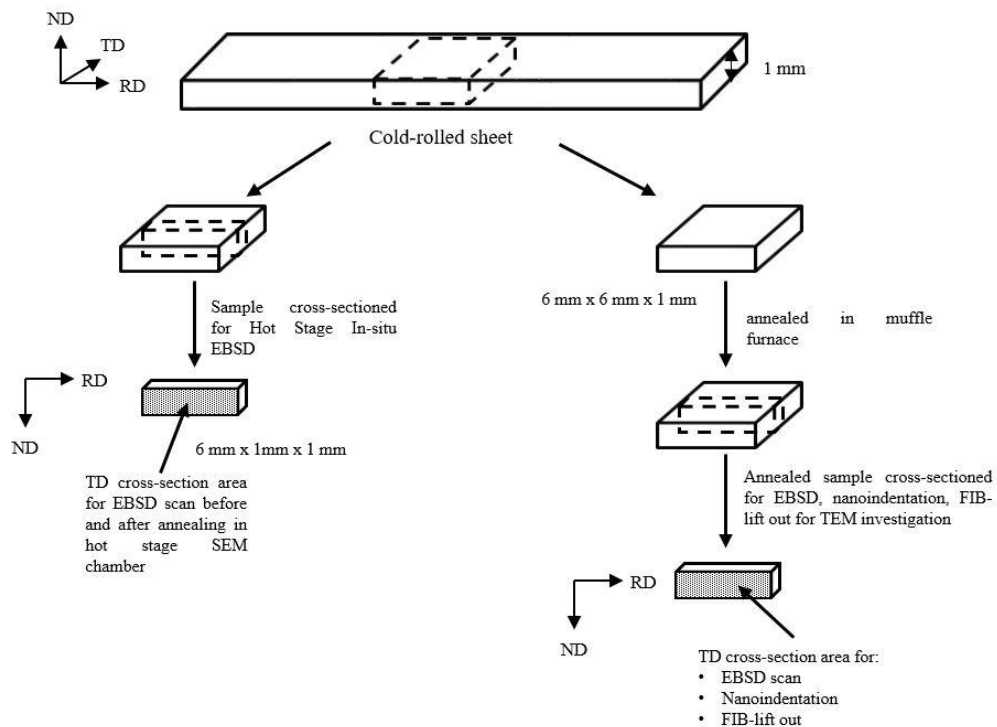


Fig. 4.3-7 Sample geometry for Hot Stage quasi In-situ EBSD (left) and EBSD, Nanoindentation and FIB-lift out TEM (right) investigation

4.3.7. Dilatometry

Samples of size 10 mm x 2 mm x 1 mm were cut from the centre of as-received sheet for dilatometry experiments. A Bähr-Thermoanalyse DIL 805A/D/T quenching dilatometer [302] was used to study phase transformation behaviour of three steel grades in a vacuum chamber environment. Samples were heated up to 1000 °C at a heating rate of 25 °C/s for a dwell time of 10 min. After heating, samples were quenched to room temperature by injecting He gas inside the chamber.

4.4. Mechanical testing

4.4.1. Nanoindentation experiment

Polished samples for EBSD were subsequently used for nanoindentation measurements of steel grades annealed at different conditions: 700 °C 0 s, 800 °C 0 s; 800 °C 2 min. A NanoTest Xtreme supplied by Micro Materials Ltd [303] was used to carry out nano-indent tests on steel grades at room temperature. Tests were carried out using a diamond Berkovich indenter with tip angle of 65.3° by applying maximum force of 10 mN for a dwell time of 10 s at maximum force. Around 50 to 90 indents were made on steel grades for different annealing conditions for statistically reliable values. Spacing between indents was 20 μm to avoid any

interference. Nanoindentation hardness for individual indents was evaluated from the force versus displacement curves using the Oliver-Pharr method [280]. Average hardness values of un-recrystallized ferrite matrix was calculated. The ferrite matrix is assumed to be un-recrystallized if its nanoindentation hardness is greater than average nanoindentation hardness for hot-rolled state [251]. For LAM-GND analysis, samples were taken for EBSD scans in Zeiss SEM. EBSD scan was performed on the area containing nanoindents. Average LAM value of un-recrystallized ferrite matrix is calculated for different annealing conditions [35].

4.4.2. Hardness measurement

The hardness value of a particular material is significant to understand the softening induced due to recrystallization. Moreover, empirically Vickers hardness value gives a good estimation of strength [274]. For hardness measurement, the muffle furnace annealed samples were cut in half and mounted in Bakelite for polishing. After polishing, Vickers hardness indentation tests were carried out at load of 1000 gf for a dwell time of 10 s in a Buehler Tukon 1102 [304]. For statistically reliable hardness result, 10 to 20 indents were made randomly over the surface of each tested sample.

4.4.3. Tensile testing

To evaluate strength and elongation properties, uniaxial tensile tests were performed on a 100 kN servo-hydraulic tensile testing machine for cold-rolled and annealed steel grades at Tata Steel Europe. The crosshead was operated using force control with a constant loading rate of 30 MPa/s. Dog-bone shaped tensile samples of ISO/EM A50 size [262] were sectioned from cold-rolled sheet for three grades of steel. To simulate annealing cold-rolled sheets of the three grades were annealed in a Continuous Annealing Simulator (CASim) for different conditions: to simulate laboratory annealing at 700 °C 0 s, 800 °C 0 s; 800 °C 2 min, 800 °C 5 min and to replicate industrial annealing cycles A, B and C. Dog bone shaped tensile samples of ISO/EM A50 size were sectioned from the annealed sheet for each grades for uniaxial tensile test. For each material condition, four tests were done for statistically reliable results. Fig. 4.4-1 represents schematic figure of tensile test sample.

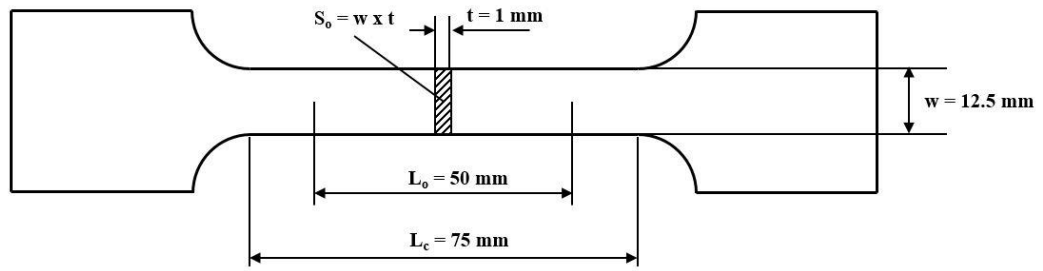


Fig. 4.4-1 Dog bone shaped tensile sample of ISO/EM A50 size. L_c , L_o , S_o , w and t are parallel length, original gauge length, original cross-sectional area of the parallel length, original width of the parallel length of test sample, original thickness of test sample respectively

5. Results

5.1. As-received hot-rolled state

Fig. 5.1-1 shows a low magnification Normal Direction Inverse Pole Figure (ND-IPF) map of hot-rolled base grade. Average grain size of hot-rolled base, Ti+ and Ti+Mn+ grades is 10 μm , 7 μm and 5 μm respectively. In order to investigate the initial precipitation state difference in the three grades, FIB-lift out sample is prepared from hot-rolled steel grades and investigated in STEM. Fine (precipitate size, $d < 5 \text{ nm}$) V(C/N) precipitates in hot-rolled base grade and titanium rich (Ti,V)(C/N) precipitates in hot-rolled Ti+ and Ti+Mn+ grades are sparsely distributed along subgrain and grain boundaries as shown in Fig. 5.1-2.

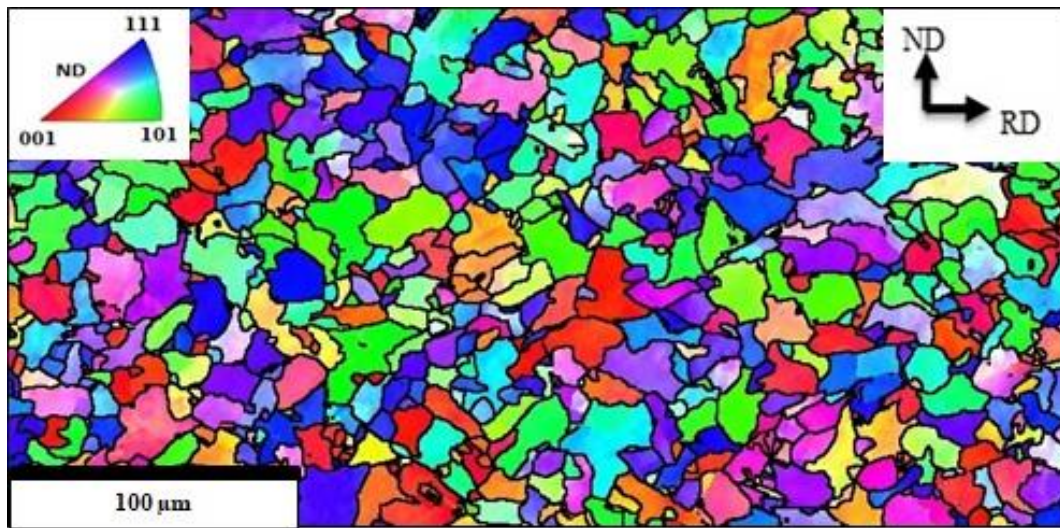


Fig. 5.1-1 Normal Direction Inverse Pole Figure (ND-IPF) map of hot-rolled low-carbon microalloyed steel (as-received) for the TD section of the base grade sample

Ti+ and Ti+Mn+ grades contain Ti as an additional precipitating element along with V and Ti+Mn+ grade contains higher wt. % of Mn solute atoms than other two grades. During the hot-rolling process, fine precipitates of (Ti,V)(C/N) and Mn solute atoms are effective in controlling ferrite grain size development by precipitate pinning and solute drag effect respectively along grain boundaries in Ti+ and Ti+Mn+ grades of steel [58]. Moreover addition of Mn lowers the austenite-ferrite transformation temperature (A_{c3}) and leads to refinement of final hot-rolled Ti+Mn+ grade microstructure [182,246].

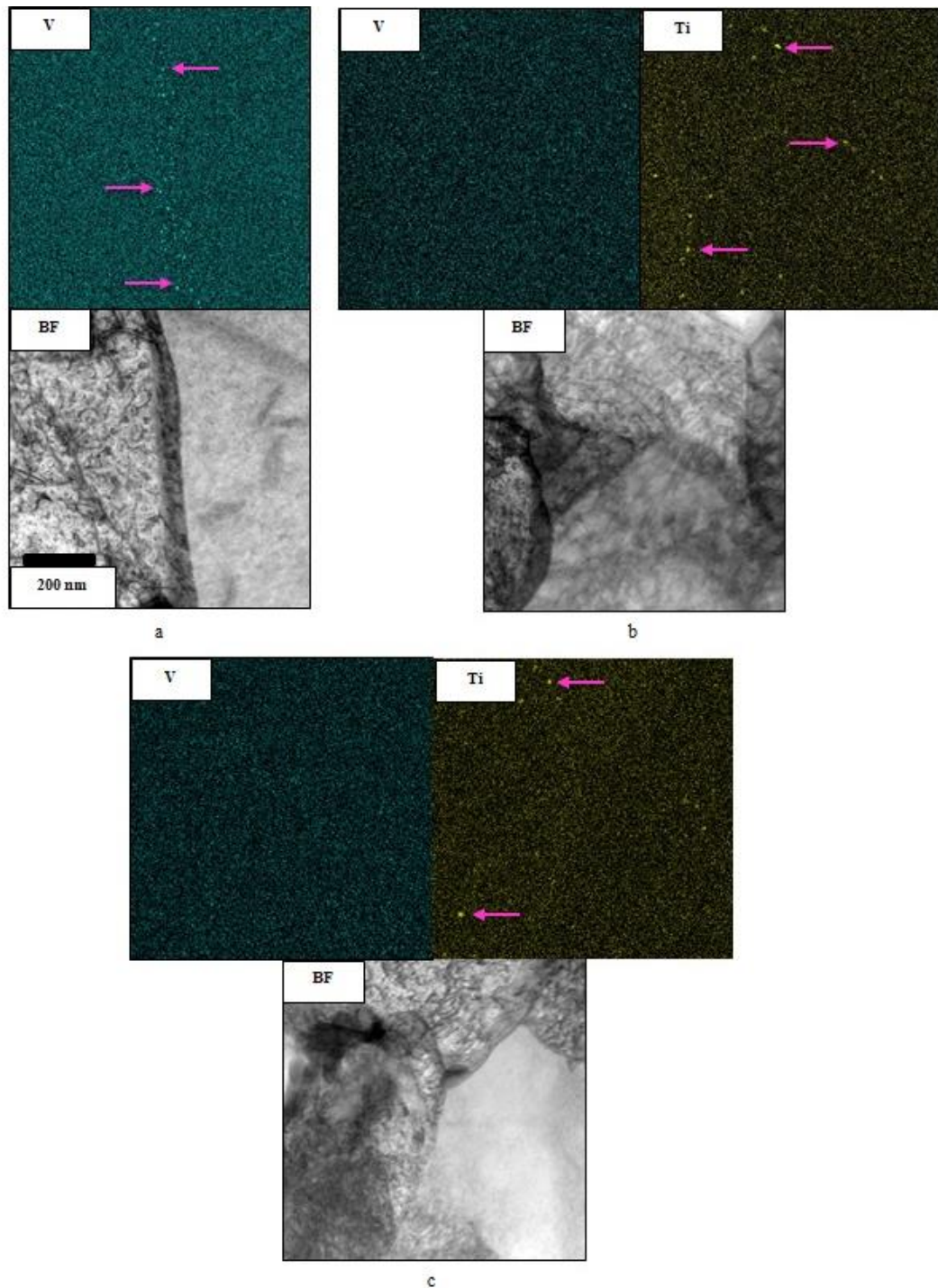


Fig. 5.1-2 STEM bright field (BF) image and EDS chemical maps of carbo-nitrides of Vanadium V(C/N) decorated along grain boundary and carbo-nitrides of Titanium and Vanadium (Ti,V)(C/N) present in ferrite matrix of hot-rolled condition of low-carbon microalloyed steel (as-received) of three different grades, base (a), Ti+ (b) and Ti+Mn+ (c). Arrows mark the precipitates present in ferrite matrix of hot-rolled base, Ti+ and Ti+Mn+ grades

5.2. As-received cold-rolled state

Fig. 5.2-1 shows a Normal Direction Inverse Pole Figure (ND-IPF) map of the cold-rolled (as-received) state of Ti+ microalloyed steel grade. Due to heavy deformation of 70 % with a reduction in thickness to 1 mm, two distinct fibres, alpha ($\langle 110 \rangle // RD$) and gamma ($\langle 111 \rangle // ND$) are formed. Apart from the alpha and gamma fibres, there is also a third type of deformed microstructure, which is neither alpha nor gamma fibre signified by randomly orientated subgrains divided by high angle grain boundaries. ND-IPF and 2D ODF maps (Fig. 5.2-1) represent strong alpha and gamma fibres in cold-rolled Ti+ grade. As-received cold-rolled microstructure and texture is very similar for base, Ti+ and Ti+Mn+ grades. The amount of stored energy is assumed to be similar in all three grades of steel because of similar cold-rolled deformation (%) ~ 70 % [215]. Before annealing, the average GND density and average Stored Energy (SE) of the alpha and gamma fibres were evaluated to understand the difference in kinetics of recrystallization in both fibres during subsequent annealing. In the cold-rolled condition of Ti+ grade, the average GND density and average Stored Energy (SE) values for the gamma fibre are $1.17E+15m^{-2}$ and 18.43 J/mol respectively which is higher than that of the alpha fibre with values of $7.57E+14m^{-2}$ and 11.88 J/mol, respectively. Therefore, during annealing it is expected that the kinetics of recrystallization will be higher for the gamma fibre due to higher driving force as discussed further [125,156,214–216,224]. In Fig. 5.2-1, alpha fibre grains are not only represented as red colour for grain orientation spread around $\{001\}\langle 110 \rangle$ but also purple (combination of red and blue) colour for grain orientation spread around $\{112\}\langle 110 \rangle$ and blue colour for grain orientation spread around $\{111\}\langle 110 \rangle$ which belongs to both alpha and gamma fibres. Detailed information on GND density calculation is mentioned in section 9.1 of the supplementary information chapter.

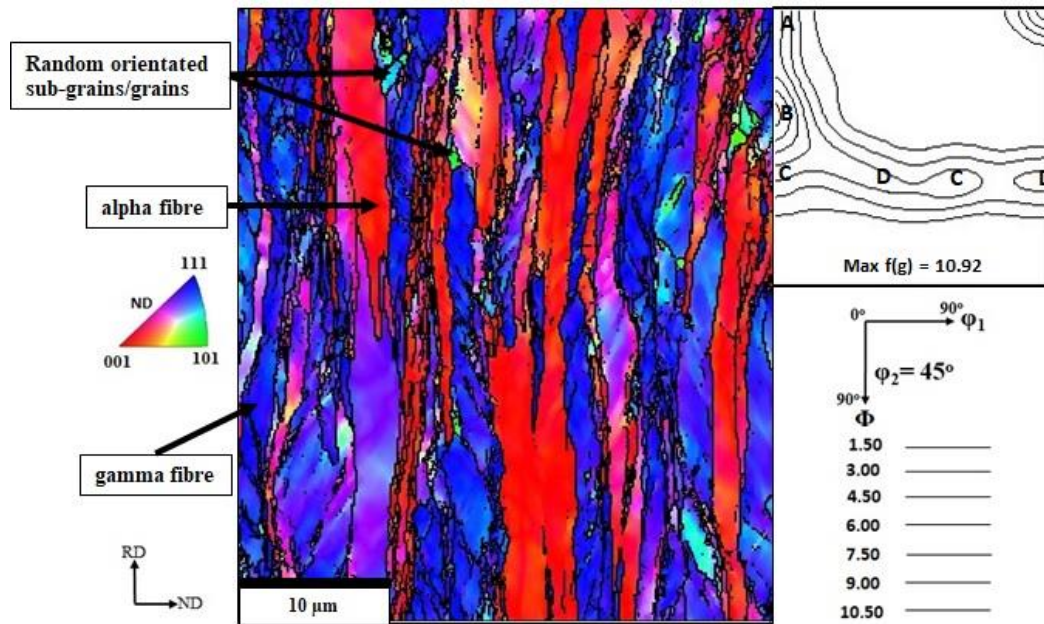


Fig. 5.2-1 Normal Direction Inverse Pole Figure (ND-IPF) and ODF on the section $\phi_2=45^\circ$ maps of cold-rolled low-carbon microalloyed steel (as-received) for the TD cross-section of the Ti+ grade sample. Arrows mark the alpha and gamma fibres and random oriented sub-grains/grains in the cold-rolled state. A = $\{001\}\langle 110\rangle$; B = $\{121\}\langle 110\rangle$; C = $\{111\}\langle 110\rangle$ and D = $\{111\}\langle 121\rangle$ grain orientation

5.3. Identification of ferrite to austenite phase transformation temperature

In order to perform sub-critical annealing within the ferrite phase regime, ferrite to austenite starting and finishing temperature is determined by dilatometry experiment and also compared with equilibrium values evaluated from Thermo-Calc software using TCFE9 database. Samples are annealed for annealing condition of 1000 °C 10 min at heating rate ~ 25 °C/s. Ferrite to austenite starting temperature (T_s) is in the order of base < Ti+Mn+ < Ti+ as shown in Fig. 5.3-1 and Fig. 5.3-2. Numerical values of starting temperature, T_s (by dilatometry experiment T_s of base, Ti+ and Ti+Mn+ grades are 834 °C, 859 °C and 851 °C respectively and by Thermo-Calc software T_s of base, Ti+ and Ti+Mn+ grades are 740 °C, 798 °C and 760 °C respectively) and finishing temperature, T_f (by dilatometry experiment T_f of base, Ti+ and Ti+Mn+ grades are 976 °C, 971 °C and 943 °C respectively and by Thermo-Calc software T_f of base, Ti+ and Ti+Mn+ grades are 890 °C, 898 °C and 874 °C respectively) of ferrite to austenite phase are mentioned in Table 5.3-1. V and Ti are ferrite stabilisers and Mn favours austenite formation during austenite to ferrite phase transformation [182,246]. Presence of Ti along with V and low wt. % of Mn (~ 0.35 %) in Ti+ grade facilitates highest starting temperature of ferrite to austenite among three grades of steel.

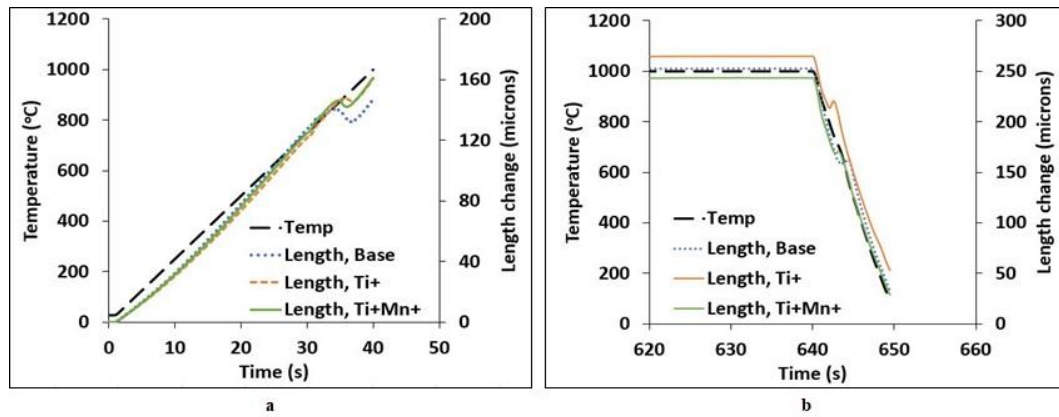


Fig. 5.3-1 Dilatometry trace with respect to temperature and time of 0 s to 50 s (a) and 620 s to 660 s (b) of the ferrite to austenite phase transformation for base, Ti+ and Ti+Mn+ grades of steel. Maximum heating temperature of 1000 °C at 25 °C/s for a dwell time of 10 min and air cooled to room temperature. Sample temperature is maintained at 1000 °C for time of 40 s to 640 s and therefore dilatometry trace plot for time, 50 s to 620 s is not shown

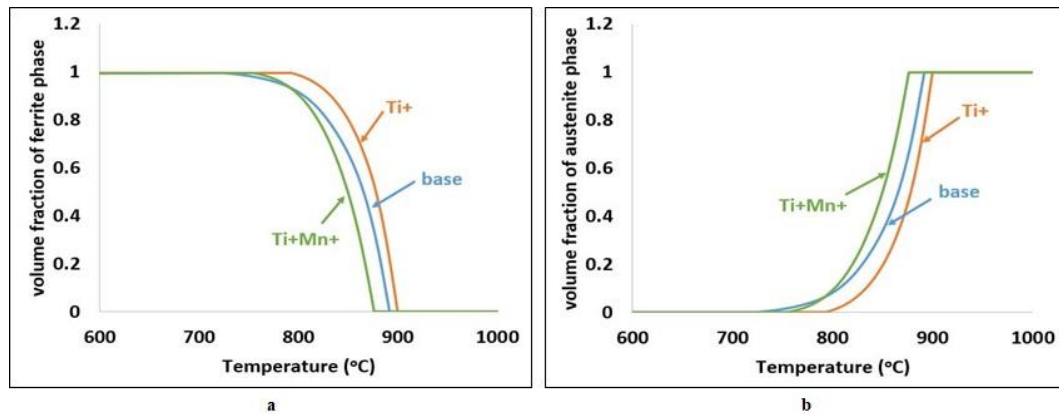


Fig. 5.3-2 Variation of volume fraction of ferrite phase (a) and austenite phase (b) with increase in temperature from 600 °C to 1000 °C for base, Ti+ and Ti+Mn+ grades of steel in equilibrium condition evaluated from ThermoCalc using TCFE9 database

Table 5.3-1 Ferrite to austenite phase transformation starting (T_s) and finishing (T_f) temperatures evaluated using Dilatometry (heating rate ~ 25 °C/s) and Thermo-Calc using TCFE9 database (equilibrium state) for base, Ti+ and Ti+Mn+ grades of steel

Grades	Dilatometry		Thermo-Calc	
	T_s (°C)	T_f (°C)	T_s (°C)	T_f (°C)
Base	834	976	740	890
Ti+	859	971	798	898
Ti+Mn+	851	943	760	874

Phase transformation temperatures evaluated from dilatometry and Thermo-Calc are different because Thermo-Calc considers equilibrium condition without any effect of heating rate and cold-rolled deformation (%) on phase transformation behaviour. Further sub-sections include results of recrystallization and precipitation behaviour among three grades upon muffle annealing of bulk sized samples.

5.4. EBSD study of muffle furnace annealed samples

Samples sized 6 mm x 6 mm x 1 mm of cold-rolled condition are annealed in a muffle furnace for different annealing conditions: 700 °C 0 s; 800 °C 0 s; 800 °C 2 min; 800 °C 5 min; 800 °C 15 min; 800 °C 30 min; 800 °C 1 hr and 800 °C 2 hrs at heating rate ~ 10 °C/s to study recrystallization behaviour among base, Ti+ and Ti+Mn+ steel grades. EBSD scans are performed on the section cut in half, parallel to RD-ND plane of the sample. For annealing temperature of 700 °C with no dwell, nucleation has been initiated within samples of base, Ti+ and Ti+Mn+ grades but with insignificant change in microstructure as shown in Fig. 5.4-1a, 5.4-2a and 5.4-3a respectively. For annealing condition of 800 °C 0 s, base grade is almost fully recrystallized with the development of quasi-polygonal recrystallized grains. For annealing condition of 800 °C 5 min, recrystallization process is completed in base grade (Fig. 5.4-1d). Grain growth starts at annealing temperature of 800 °C for dwell of 15 min and continues with massive competitive grain growth for dwell time of 2 hrs in base grade (Fig. 5.4-1h).

For annealing conditions: 800 °C 0 s; 800 °C 2 min; 800 °C 5 min; 800 °C 15 min; 800 °C 30 min; 800 °C 1 hr, recrystallization kinetics is slower in Ti+ and Ti+Mn+ grades than in the base grade, with un-recrystallized ferrite matrix dominated by alpha fibre grains. {001}<110> grains of alpha fibre (shown as red coloured texture in ND-IPF EBSD maps of Fig. 5.4-2 and Fig. 5.4-3) have the lowest stored energy. Therefore during annealing at temperature of 800 °C for longer dwell time of 2 min to 1 hr, {001}<110> grains have not fully recrystallized [41,305–307]. Moreover, additional pinning effect of Ti precipitates along GBs could possibly retard recrystallization of {001}<110> grain in Ti+ and Ti+Mn+ grades.

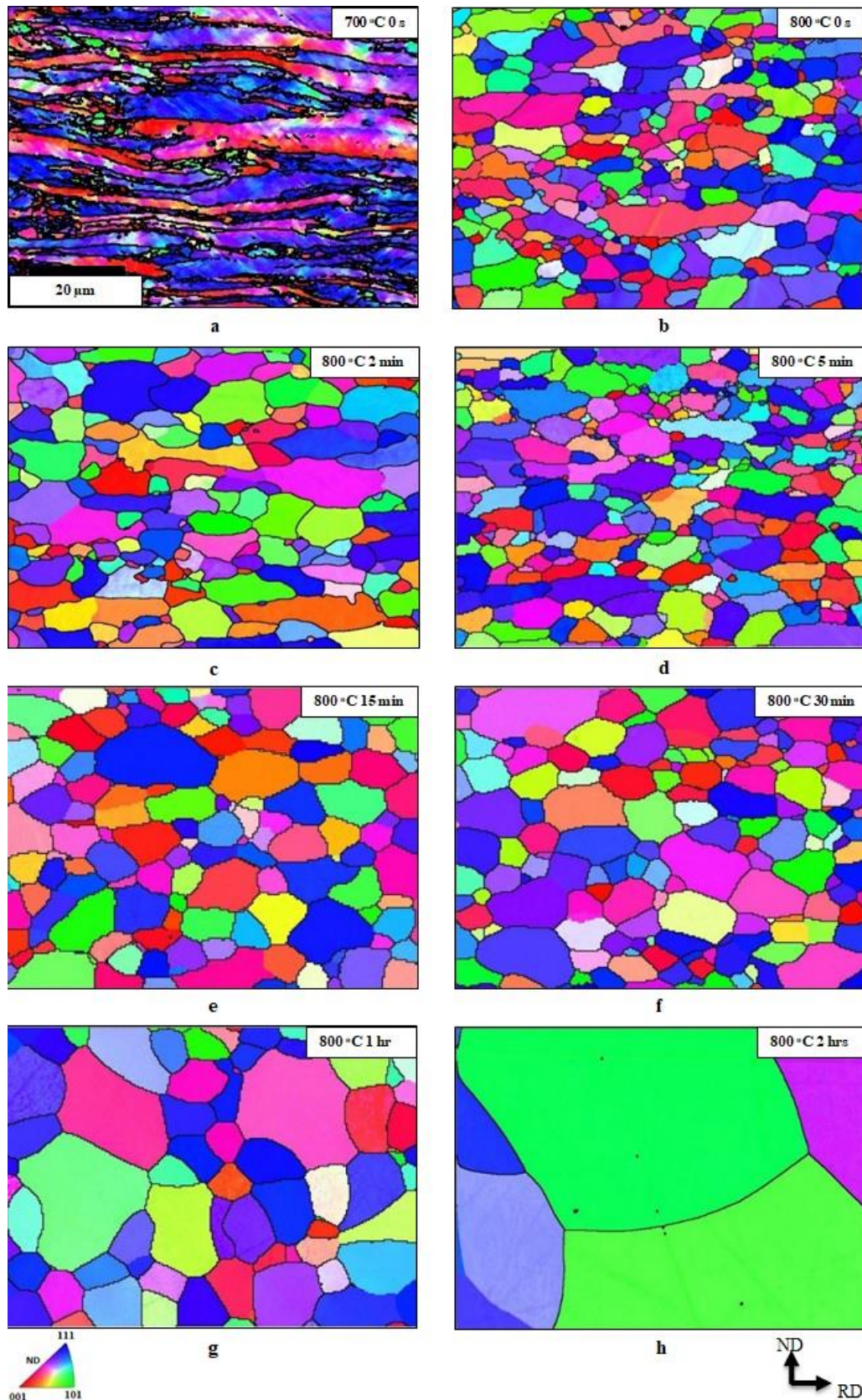


Fig. 5.4-1 Normal Direction Inverse Pole Figure (ND-IPF) maps of low-carbon microalloyed steel of base grade after annealing at 700 °C 0 s (a), 800 °C 0 s (b), 800 °C 2 min (c), 800 °C 5 min (d), 800 °C 15 min (e), 800 °C 30 min (f), 800 °C 1 hr (g) and 800 °C 2 hrs (h)

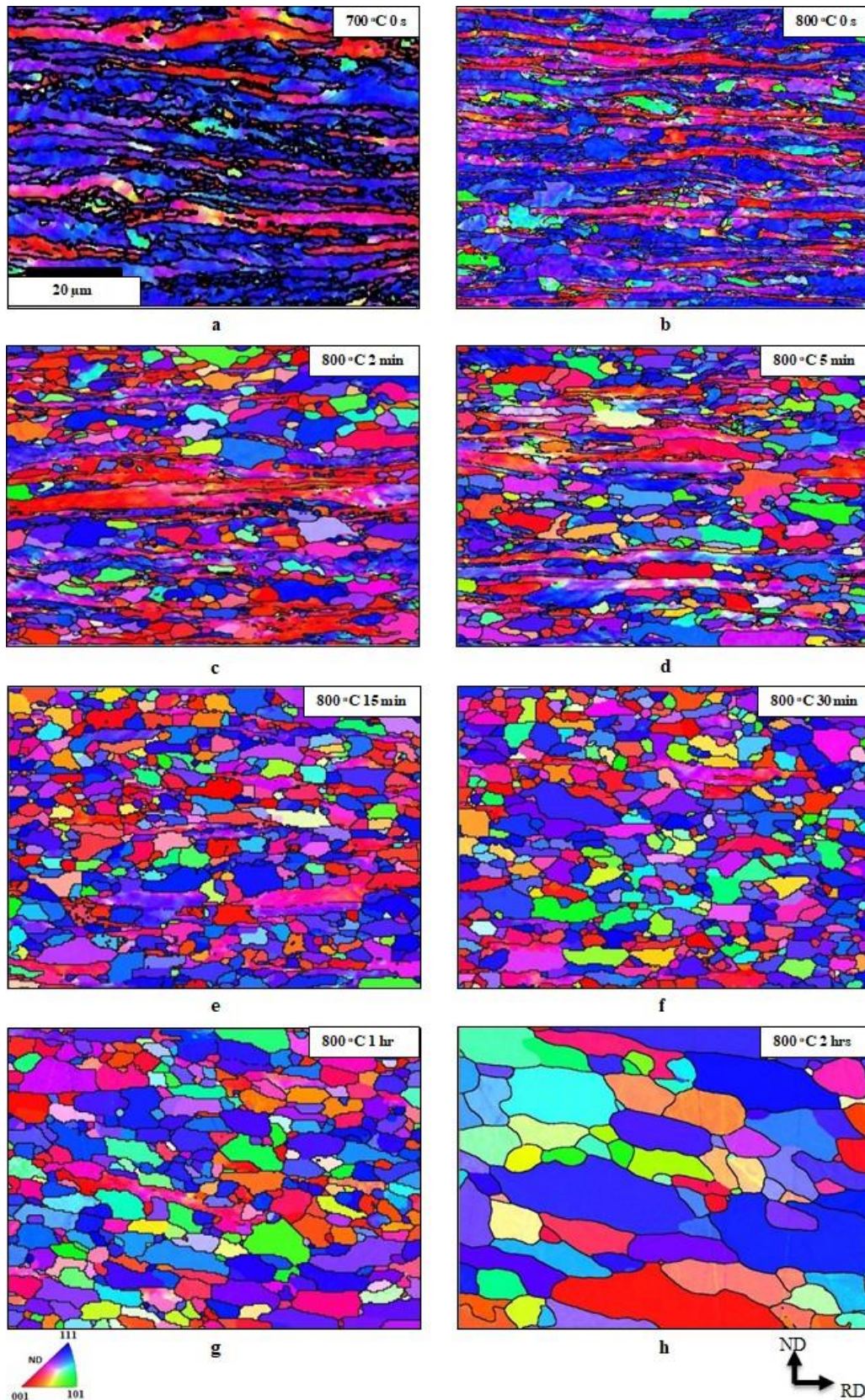


Fig. 5.4-2 Normal Direction Inverse Pole Figure (ND-IPF) maps of low-carbon microalloyed steel of Ti+ grade after annealing at 700 °C 0 s (a), 800 °C 0 s (b), 800 °C 2 min (c), 800 °C 5 min (d), 800 °C 15 min (e), 800 °C 30 min (f), 800 °C 1 hr (g) and 800 °C 2 hrs (h)

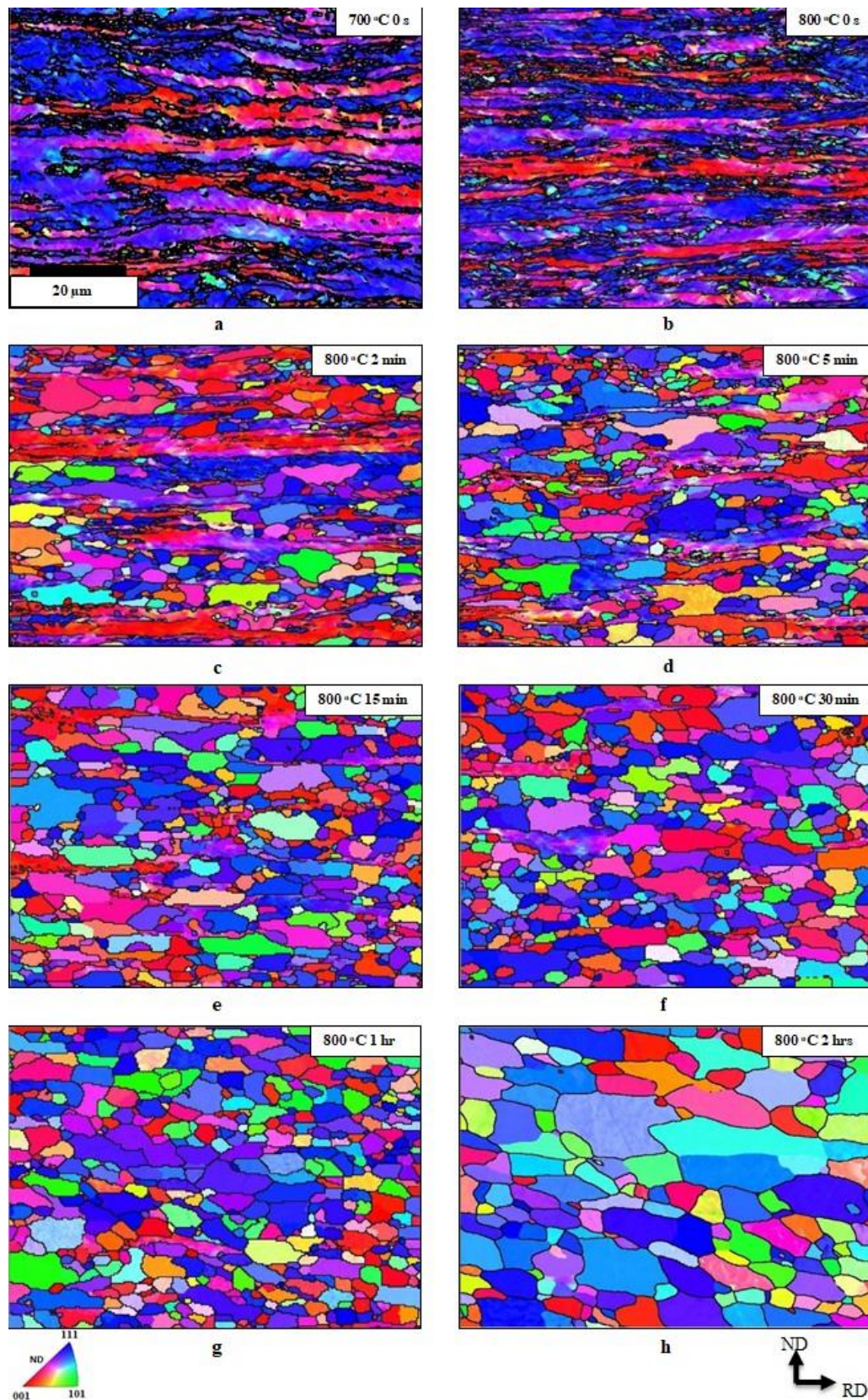


Fig. 5.4-3 Normal Direction Inverse Pole Figure (ND-IPF) maps of low-carbon microalloyed steel of Ti+Mn+ grade after annealing at 700 °C 0 s (a), 800 °C 0 s (b), 800 °C 2 min (c), 800 °C 5 min (d), 800 °C 15 min (e), 800 °C 30 min (f), 800 °C 1 hr (g) and 800 °C 2 hrs (h)

For annealing condition of 800 °C 0 s, microstructure of Ti+Mn+ grade is similar to that for annealing condition of 700 °C 0 s with nucleation of recrystallization occurring along higher angle grain boundaries. Fig. 5.4-4 shows recrystallized grain nucleus along HAGB between alpha and gamma fibres (arrow marked as A) and between alpha and other random grain orientations (arrow marked as B) of Ti+Mn+ grade treated at 800 °C 0 s annealing condition. Areas of higher local misorientation form potential sites for nucleation of recrystallization such as deformation bands and HAGB between alpha/gamma texture [108,308].

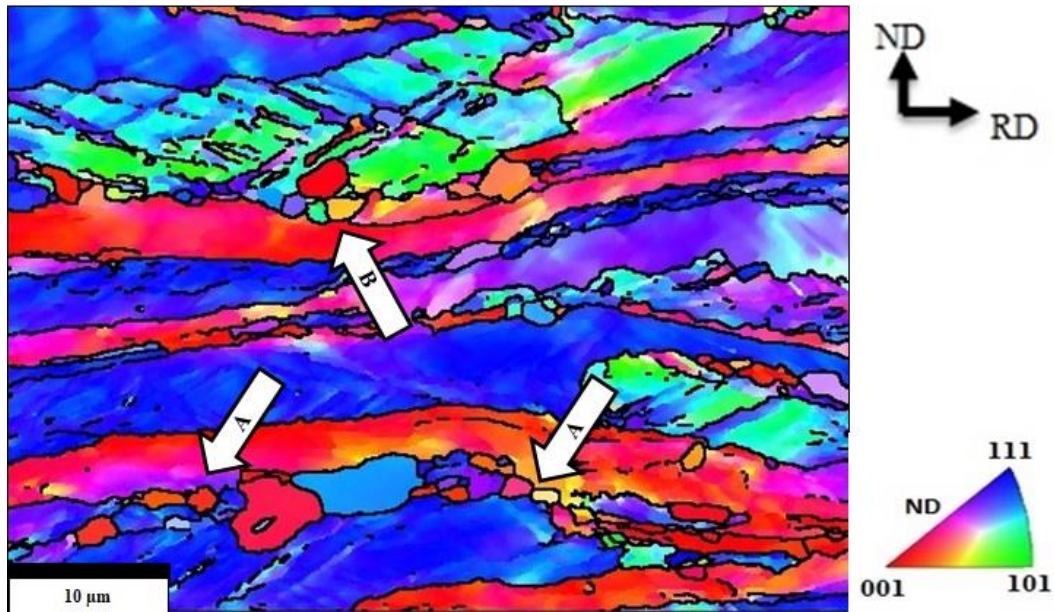
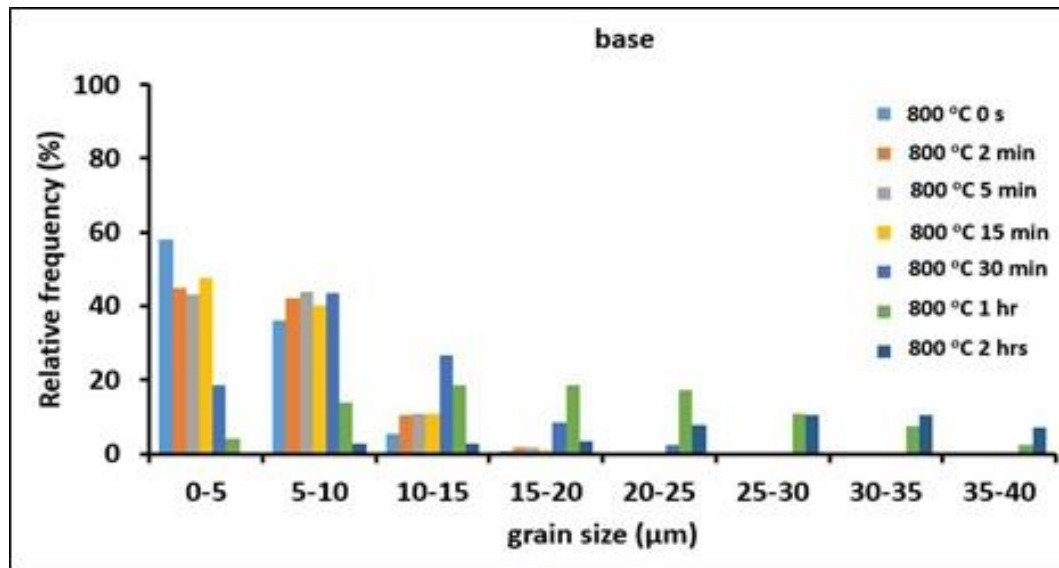
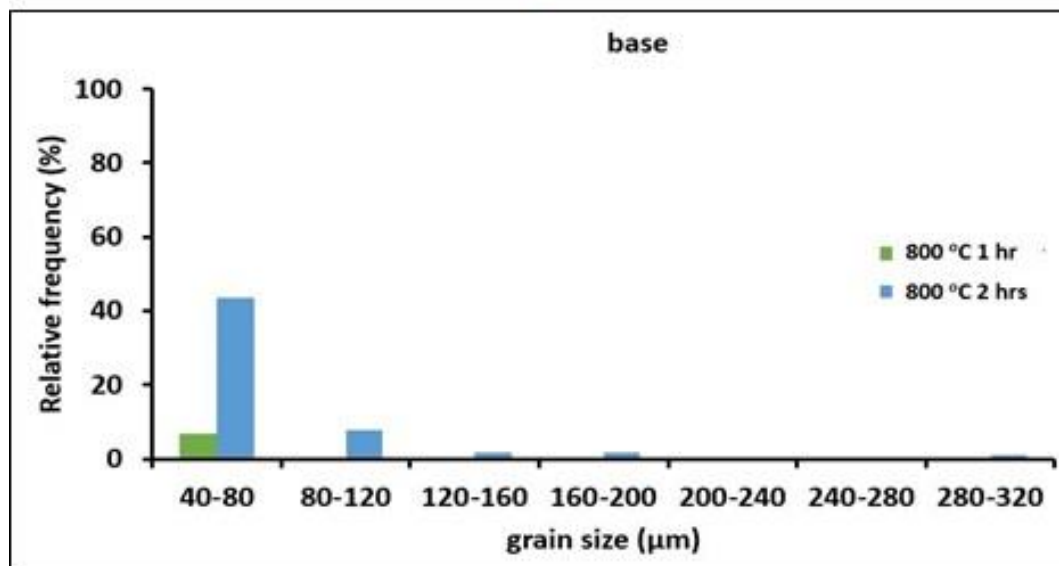


Fig. 5.4-4 Normal Direction Inverse Pole Figure (ND-IPF) map of low-carbon microalloyed steel of Ti+Mn+ grade after annealing at 800 °C 0 s at high magnification of x5k. Arrows 'A' and 'B' indicate nucleation of recrystallized grains along HAGB of alpha/gamma fibre and higher misorientation region between alpha fibre and random grain orientations respectively

For quantitative analysis, EBSD data is post-processed to evaluate recrystallized grain size relative frequency (%) and average recrystallized grain size of three grades for different annealing conditions. Grains with an aspect ratio less than 2.6 are considered recrystallized [295] and quantified for relative frequency (%) and average grain size evaluation as shown in Fig. 5.4-5, 5.4-6 and 5.4-7. Minimum of 1000 recrystallized grains are analysed to provide statistically significant data. Relative frequency (%) of fine (< 10 μm) recrystallized grains in Ti+ and Ti+Mn+ grades is higher than base grade as shown in Fig. 5.4-5 and 5.4-6. Maximum recrystallized grain size of Ti+ and Ti+Mn+ grade is between 20 μm to 25 μm. While for base grade, relative frequency (%) of recrystallized grain (size > 30 μm) is greater than 10 %. For annealing condition of 800 °C 2 hrs, average grain size of base grade (~ 50 μm) is higher than Ti+ and Ti+Mn+ grades (~ 6 μm) as shown in Fig. 5.4-7.



a



b

Fig. 5.4-5 Relative frequency (%) of grain size with aspect ratio greater than 2.6 of base grade for different annealing conditions: 800 °C 0 s; 800 °C 2 min; 800 °C 5 min; 800 °C 15 min; 800 °C 30 min; 800 °C 1 hr and 800 °C 2 hrs

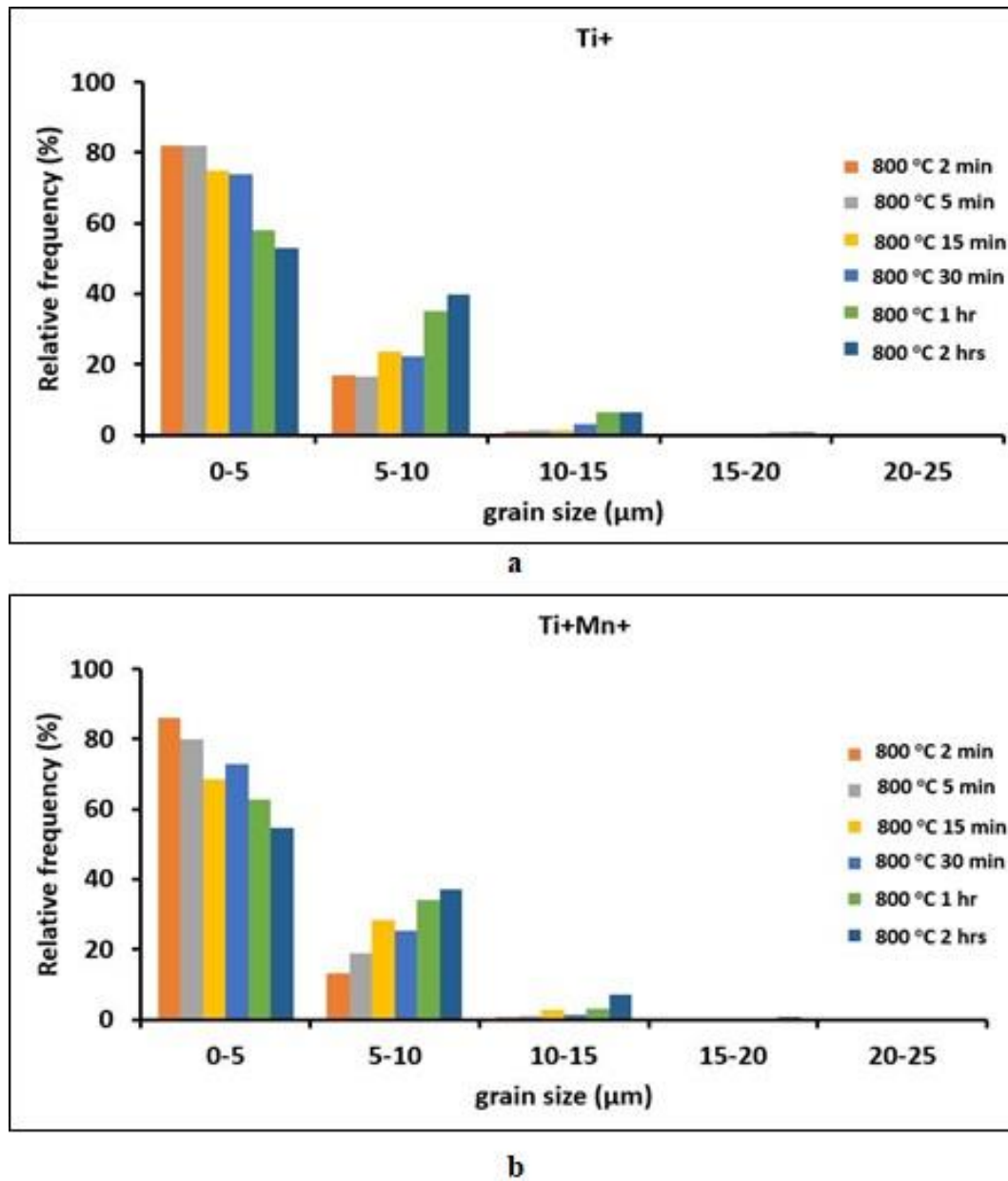
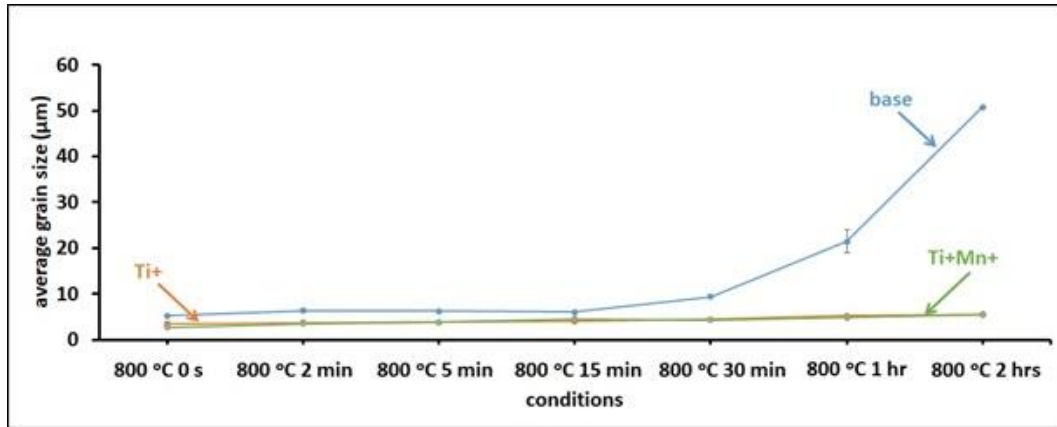
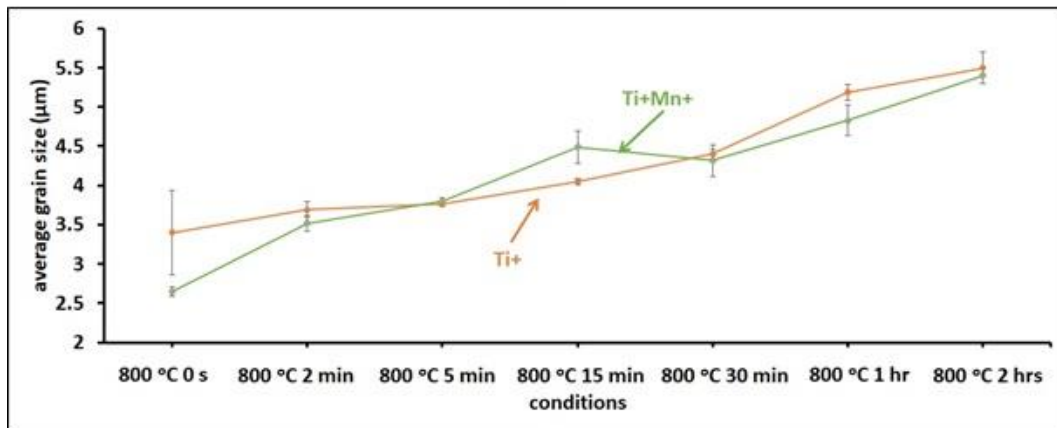


Fig. 5.4-6 Relative frequency (%) of grain size with aspect ratio greater than 2.6 of Ti+ (a) and Ti+Mn+ (b) grades for different annealing conditions: 800 °C 2 min; 800 °C 5 min; 800 °C 15 min; 800 °C 30 min; 800 °C 1 hr and 800 °C 2 hrs



a



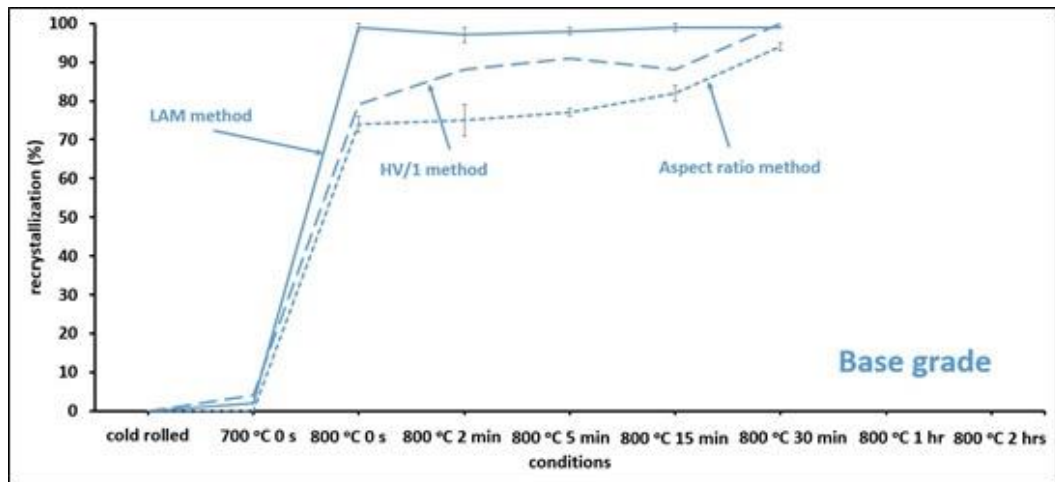
b

Fig. 5.4-7 Average grain size with aspect ratio greater than 2.6 of base, Ti+ and Ti+Mn+ grades (a) and Ti+ and Ti+Mn+ grades (b) for different annealing conditions: 800 °C 0 s; 800 °C 2 min; 800 °C 5 min; 800 °C 15 min; 800 °C 30 min; 800 °C 1 hr and 800 °C 2 hrs

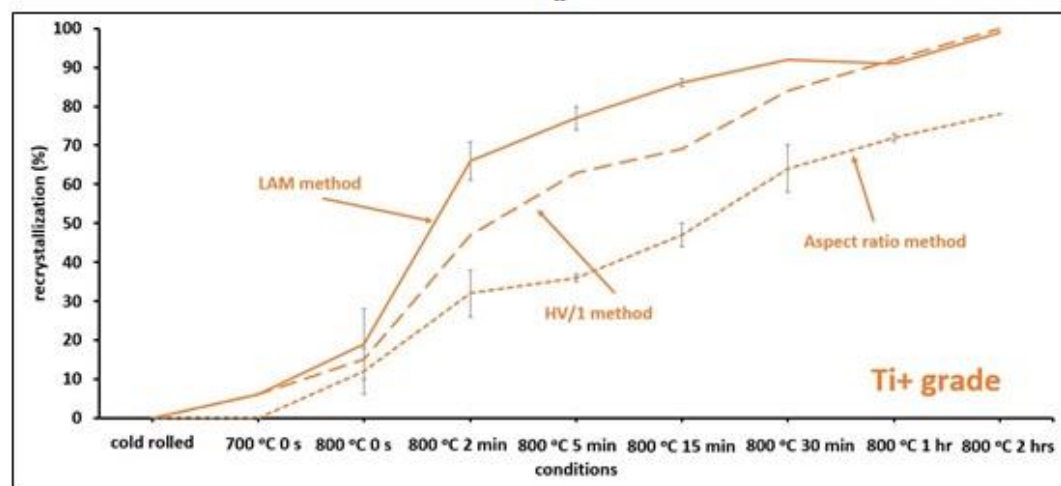
5.5. Recrystallization (%) and JMAK equation

Recrystallization (%) is evaluated by three methods as described in the section 4.3.5 of methodology: LAM, aspect ratio and hardness (HV/1) to quantitatively understand recrystallization behaviour among three grades as shown in Fig. 5.5-1. Vickers hardness (HV/1) values of base, Ti+ and Ti+Mn+ grades for different conditions are presented in Table 5.5-1 and later discussed in detail within the section 5.8.2 of mechanical properties. Fig. 5.5-2 shows an example of evaluation of recrystallization (%) using LAM map. Corresponding ND-IPF EBSD map of partially recrystallized sample is shown in Fig. 5.6-2c in the section 5.6 of hot-stage *quasi* in-situ EBSD of this chapter. With increased annealing temperature and dwell time, recrystallization (%) is increased as shown in Fig. 5.5-1. For annealing condition of 800 °C 0 s: base grade is almost fully recrystallized and average recrystallization (%) of Ti+ grade (LAM method ~ 19 %) is slightly higher than Ti+Mn+ grade (LAM method ~ 8 %). With increase in dwell time (≥ 2 min) at 800 °C, average recrystallization (%) of Ti+ and Ti+Mn+ are very similar (for annealing condition of 800 °C 2 min, 800 °C 5 min, 800 °C 15

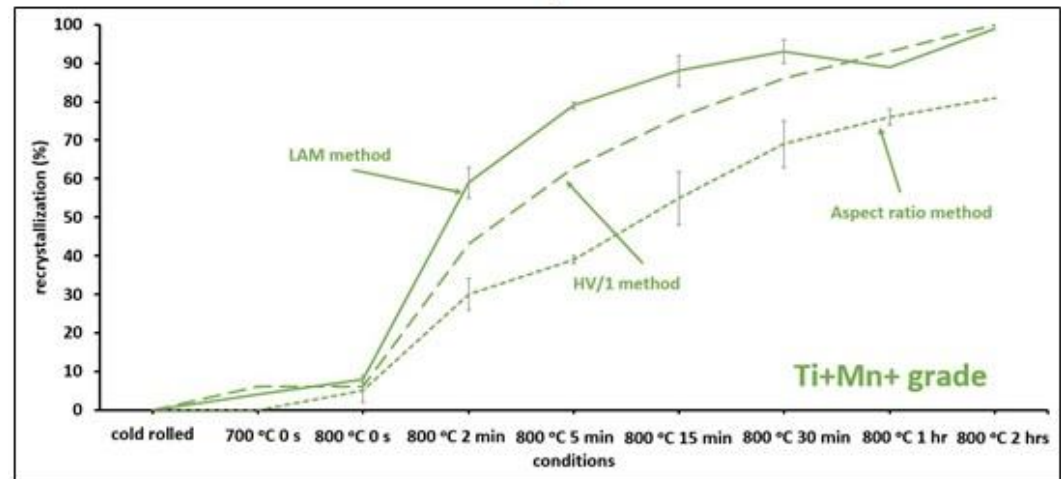
min, 800 °C 30 min, 800 °C 1 hr and 800 °C 2 hrs, average recrystallization (%) evaluated by LAM method of Ti+ grade are 66 %, 77 %, 86 %, 92 %, 91 % and 99 % respectively and of Ti+Mn+ grade are 59 %, 79 %, 88 %, 93 %, 89 % and 99 % respectively) as shown in Fig. 5.5-1b and 5.5-1c.



a



b



c

Fig. 5.5-1 Recrystallization (%) measurements using three different methods: local average misorientation (LAM), aspect ratio (AR) and Vickers hardness (HV/1) of base (a), Ti+ (b) and Ti+Mn+ (c) grades of steel for different conditions: cold-rolled; 700 °C 0 s; 800 °C 0 s; 800 °C 2 min; 800 °C 5 min; 800 °C 15 min; 800 °C 30 min; 800 °C 1 hr and 800 °C 2 hrs

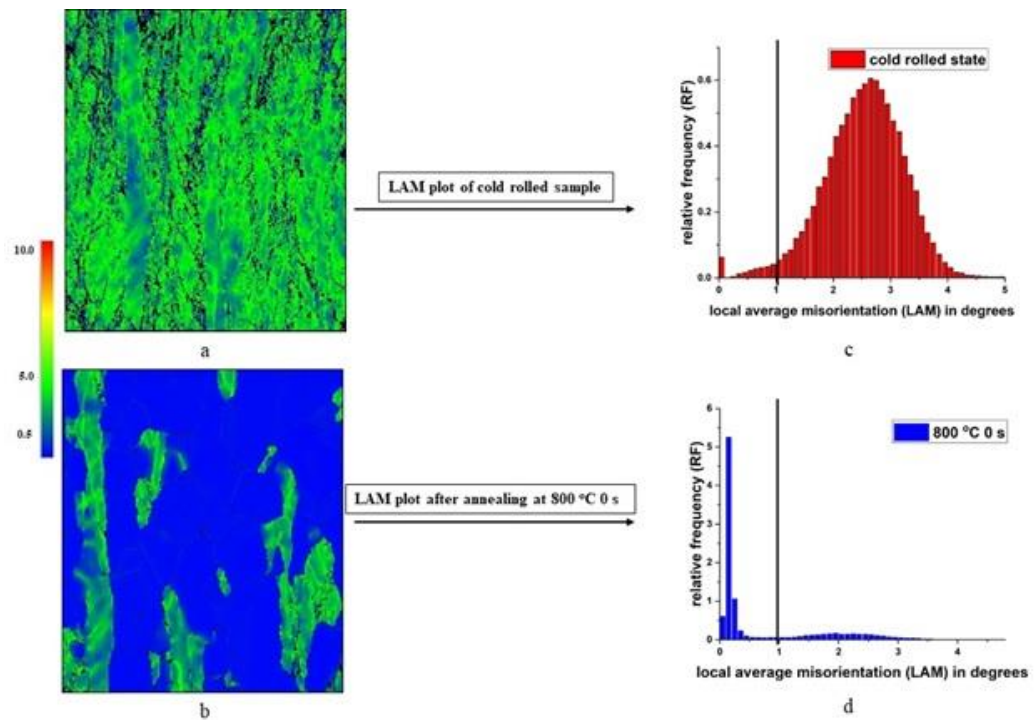


Fig. 5.5-2 Local average misorientation (LAM) map (a) and (b) and plots (c) and (d) before and after annealing of low-carbon microalloyed steel at 800 °C 0 s

Table 5.5-1 Vickers hardness (HV/1) measurements of base, Ti+ and Ti+Mn+ grades of steel for different conditions

Conditions	Base	Ti+	Ti+Mn+
Cold-rolled	220 ± 5	280 ± 7	290 ± 3
700 °C 0 s	225 ± 3	270 ± 3	330 ± 5
800 °C 0 s	124 ± 4	254 ± 20	300 ± 4
800 °C 2 min	113 ± 2	196 ± 8	213 ± 7
800 °C 5 min	110 ± 2	168 ± 8	176 ± 5
800 °C 15 min	114 ± 2	156 ± 2	154 ± 2
800 °C 30 min	99 ± 2	130 ± 2	136 ± 3
800 °C 1 hr	73 ± 3	116 ± 2	123 ± 2
800 °C 2 hrs	66 ± 3	101 ± 2	110 ± 2

Recrystallization kinetics are expressed using Johnson-Mehl-Avrami-Kolmogorov (JMAK) equation for annealing conditions: 800 °C 0 s, 800 °C 2 min, 800 °C 5 min, 800 °C 15 min, 800 °C 30 min, 800 °C 1 hr and 800 °C 2 hrs. Since base grade is fully recrystallized at 800 °C 0 s, therefore recrystallization (%) values of Ti+ and Ti+Mn+ grades are used in JMAK equations to evaluate constants. JMAK equation is expressed in logarithmic form (equation 5.5-1) and un-known constants, n and k are determined by line fitting method as shown in Fig. 5.5-3.

$$\ln(-\ln(1 - X(t))) = n * \ln(t) + \ln(k) \quad (5.5-1)$$

Value of Avrami constant, n is less than 1 for both Ti+ and Ti+Mn+ grades at annealing temperature of 800 °C. A lower value of n could be because of non-homogenous stored energy distribution within ferrite matrix, non-homogenous grain size distribution and sluggish recrystallization behaviour during annealing [40,96,218,309–311].

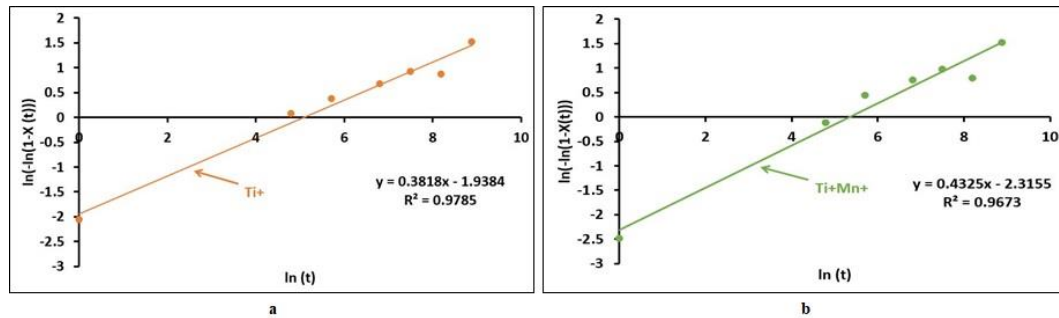


Fig. 5.5-3 Logarithmic plot of recrystallization fraction and time of Ti+ and Ti+Mn+ grades of steel for annealing temperature of 800 °C

5.6. *Quasi in-situ* analysis of geometrically necessary dislocation density in α - fibre and γ -fibre after annealing at 700 °C 0 s; 800 °C 0 s and 800 °C 2 min

Previous results are focussed on the recrystallization behaviour of base, Ti+ and Ti+Mn+ steel grades. From the ND-IPF EBSD maps it was observed that alpha fibre grains take longer dwell time to recrystallize during annealing of Ti+ and Ti+Mn+ grades. Hot stage *quasi in-situ* EBSD is performed to study onset of nucleation and alpha and gamma recrystallized texture development on the surface of Ti+ grade sample during sub-critical annealing. Difference between surface and bulk microstructural observation for hot *quasi in-situ* EBSD is discussed in detail in sub-section 6.3.2 of discussion chapter.

Initiation of nucleation of recrystallization has started in locations as indicated by arrows A, B and C in IPF map of Fig. 5.6-1b for annealing condition of 700 °C 0 s. The arrow marked A has grain orientation $\{112\}\langle 110 \rangle$ of the alpha fibre texture and nucleation occurred from a deformed matrix with similar orientation. The arrow marked B has grain orientation $\{111\}\langle 110 \rangle$ of the gamma fibre texture and nucleation is expected to be linked with the gamma

fibre orientation due to its higher initial stored energy. Apart from nucleation of grains with alpha and gamma fibre orientations, some other grains with different orientations such as grain orientation $\{313\}\langle 031\rangle$ marked as C have also nucleated from the deformed region surrounded by high angle grain boundaries. The above grain nucleation characteristics are consistent with the results of Thomas et al. [120] obtained after annealing of IF steel.

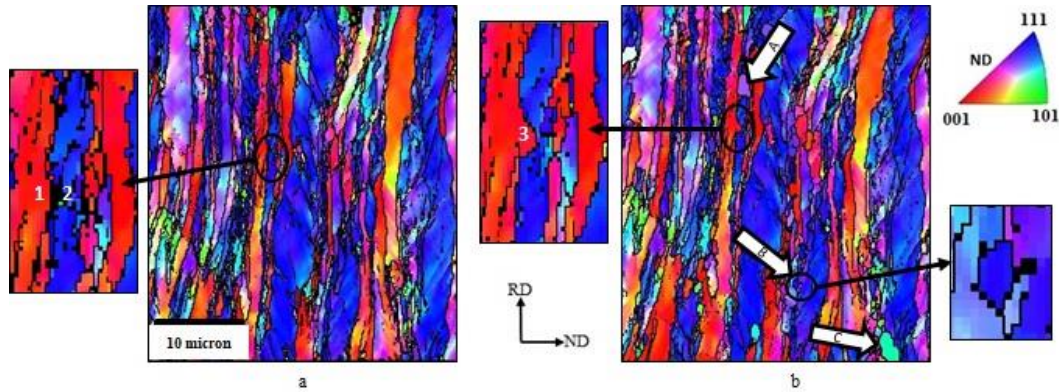


Fig. 5.6-1 Normal Direction Inverse Pole Figure (ND-IPF) maps of low-carbon microalloyed steel before annealing (a) and after annealing at 700 °C 0 s (b). In Fig. 5.6-1a, the alpha fibre region is marked as **1** and the gamma fibre region is marked as **2** for the cold-rolled state. In Fig. 5.6-1b, a bulged portion of the alpha fibre region is marked as **3** for the annealed sample. Arrows marked as A, B and C in Fig. 5.6-1b are recrystallized nucleus after annealing

At a higher magnification, the bulging of alpha fibre texture grain boundaries to the deformed matrix of gamma fibre texture is observed. The average GND density has been calculated for the regions **1**, **2** and **3** in Fig. 5.6-1 by capturing the average misorientation value from about 50 pixels. It was found that the average GND density value of region **1** is less than that of region **2** and that the difference in average GND density value between both the regions is about $1.4\text{E}+14\text{m}^{-2}$. Because of the difference in average GND density and stored energy, high angle grain boundaries from low average GND regions of the deformed alpha fibre have migrated to the high average GND density regions of deformed gamma fibre, decreasing the average GND density value from $1.4\text{E}+15\text{m}^{-2}$ to $1.1\text{E}+15\text{m}^{-2}$ in region **3**. In a previous study on carbon steels by H. Réglé, bulging of subgrain boundaries into gamma grain boundaries has been observed and related to differences in recovery rate and subgrain size [312,313]. In the magnified ND-IPF images of regions **1**, **2** and **3** in Fig. 5.6-1 black dots are non-indexed points due to the noise which results from the heavy cold-rolling deformation (about 70 % thickness reduction) and possibly the minor damage of the sample during preparation. The black lines correspond with high-angle grain boundaries ($> 10^\circ$) separating the alpha and gamma fibres.

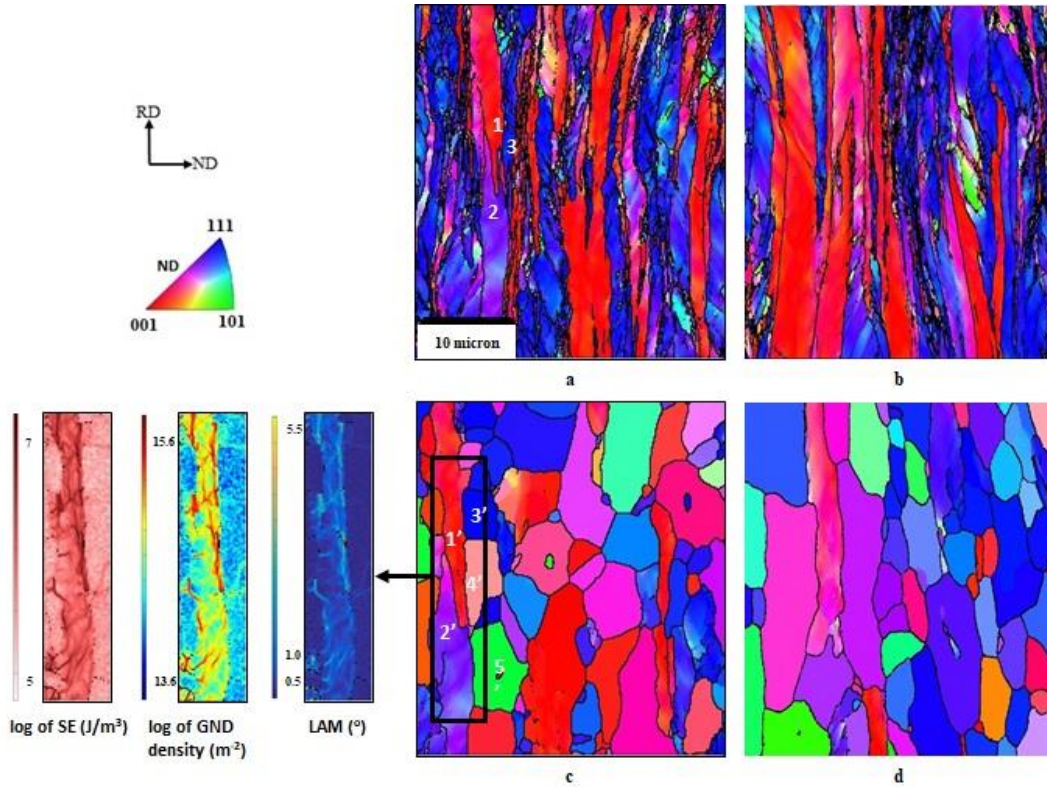


Fig. 5.6-2 Normal Direction Inverse Pole Figure (ND-IPF) maps for two annealing conditions: before (a) and after (c) annealing at 800 °C 0 s, and before (b) and after (d) annealing at 800 °C 2 min. For 800 °C 0 s annealing condition, site specific local average misorientation (LAM), log of geometrically necessary dislocation (GND) density and log of stored energy (SE) map is shown for the un-recrystallized and recrystallized matrix of annealed sample

With an increase in temperature and dwell time to 800 °C 0 s and 800 °C 2 min, the recrystallization process is initiated and the recrystallization fraction is increased as shown qualitatively by the ND-IPF maps in Fig. 5.6-2. Since the gamma fibre has a higher initial stored energy (driving force for recrystallization) as compared to alpha fibre in cold rolled state, therefore during annealing it could be observed from ND-IPF maps in Figs. 5.6-2c and d that the alpha fibre is still in recovery stage while grains belonging to the gamma fibre are fully recrystallized and the stored energy is released lowering the GND density. Site specific local average misorientation, GND density and Stored Energy (SE) maps are shown from the matrix of alpha, gamma, and other orientations. After annealing at 800 °C 0 s, average GND density values in region 1' (grain orientation spread around $\{001\}\langle 110 \rangle$) and 2' (grain orientation spread around $\{112\}\langle 110 \rangle$) of the un-recrystallized alpha fibre are $6.1\text{E}+14\text{m}^{-2}$ and $2.0\text{E}+14\text{m}^{-2}$ respectively, which decreased as compared to the as-received average GND values in region 1 and 2 of $6.2\text{E}+14\text{m}^{-2}$ and $2.3\text{E}+14\text{m}^{-2}$, as shown in Figs. 5.6-2a and c respectively. While in the case of recrystallized grain 3' (grain orientation $\{111\}\langle 110 \rangle$) of gamma fibre texture), recrystallized grain 4' (grain orientation $\{123\}\langle 121 \rangle$) and recrystallized

grain 5' (grain orientation $\{313\}\langle 031\rangle$) the average GND density values are $2.3E+13m^{-2}$, $3.2E+13m^{-2}$ and $4.0E+13m^{-2}$ respectively. Qualitatively and from the average GND values, a drop in the stored energy has not taken place much in the un-recrystallized alpha fibre matrix and therefore un-recrystallized grains belonging to the alpha fibre have potential for further recrystallization during increment of dwell time by 2 min for 800 °C.

5.7. Texture analysis of muffle annealed samples

Cold-rolled texture of base, Ti+ and Ti+Mn+ steel grades consists of strong alpha and gamma texture as shown in Fig. 5.7-1a, 5.7-1b and 5.7-1c respectively. Alpha fibre of base and Ti+ steel grades has maximum orientation density peak at $\{112\}\langle 110\rangle$ grain [314]. In the case of Ti+Mn+ grade, maximum orientation density peak is around $\{001\}\langle 110\rangle$ grain [315] as shown in Fig. 5.7-1c. Gamma fibre texture has the maximum orientation density peak at $\{111\}\langle 110\rangle$ grain rather than $\{111\}\langle 112\rangle$ grain, which is shown as the characteristics of low-carbon steel deformed between 70 % and 80 % by Hölscher et al. using their “pancake” mathematical modelling [316]. As has been shown in Fig. 5.4-1a, 5.4-2a and 5.4-3a complete recrystallization has not taken place in the samples annealed at 700 °C 0 s and only limited nucleation occurred with the presence of about ~ 95% of as-deformed matrix, therefore texture of the complete matrix (un-recrystallized and recrystallized) of annealed steel is evaluated and it is found to be similar to the cold-rolled (as-received) steel texture as shown in Fig. 5.7-1a, 5.7-1b and 5.7-1c.

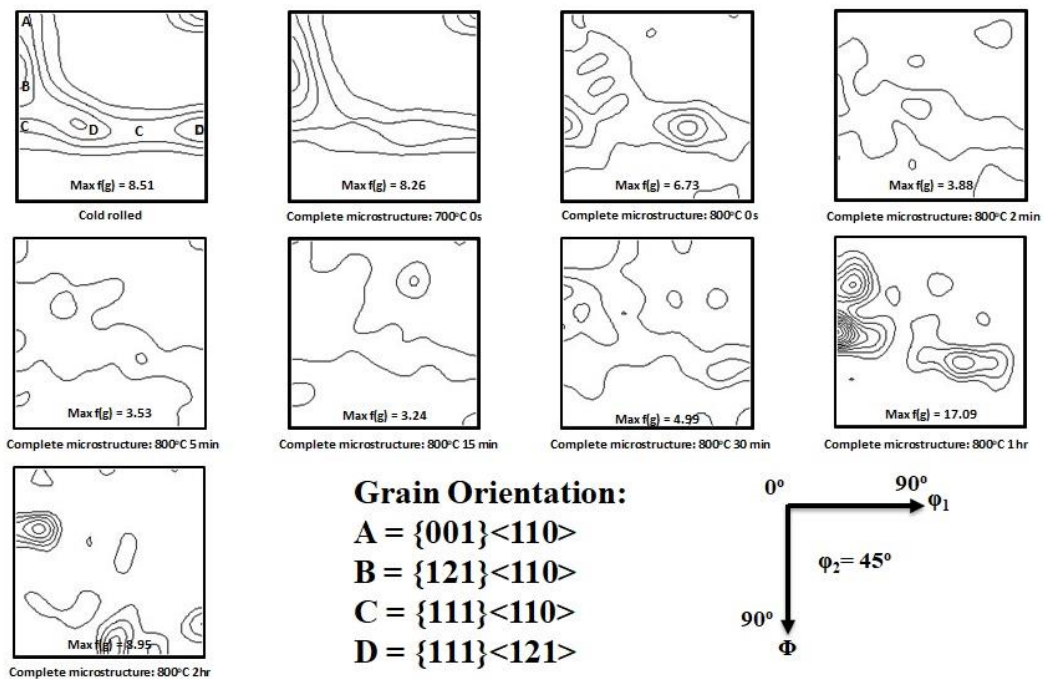


Fig. 5.7-1a ODF on the section $\phi_2=45^\circ$ texture maps of base grade steel

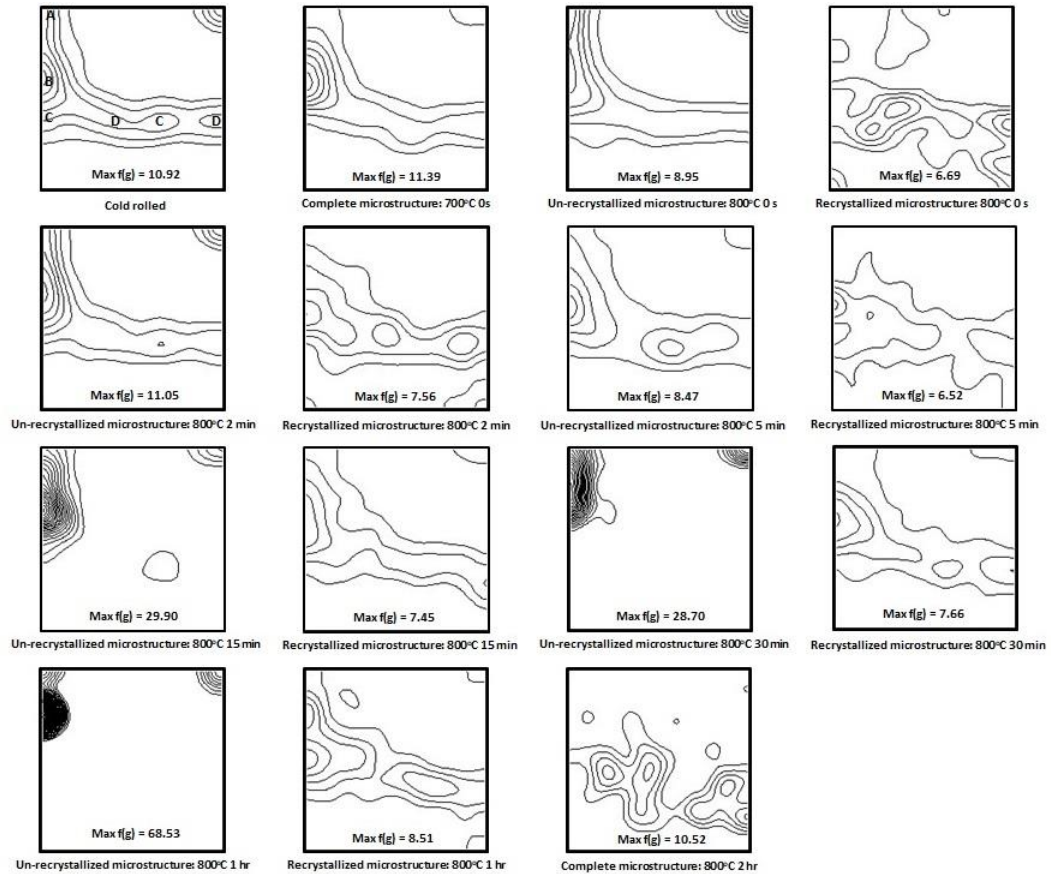


Fig. 5.7-1b ODF on the section $\varphi_2=45^\circ$ texture maps of Ti+ grade steel

Texture of the complete recrystallized microstructure of base grade annealed at different conditions of 800 °C 0 s, 800 °C 2 min, 800 °C 5 min, 800 °C 15 min and 800 °C 30 min, resembles gamma texture. During the grain growth stage (when average grain size grows above 30 μm) of the base grade for annealing condition of 800 °C 1 hr and 800 °C 2 hrs, complete textural information could not be obtained using the EBSD method since fewer grains than 1000 at magnifications x200 to x500 are acquired and show only strong peaks (> 8) around grain orientations, $\{121\}\langle 110\rangle$ and $\{111\}\langle 110\rangle$. In the case of recrystallized matrix for Ti+ grade, for annealing conditions of 800 °C 0 s, 800 °C 2 min, 800 °C 5 min, 800 °C 15 min, 800 °C 30 min, 800 °C 1 hr and 800 °C 2 hrs, maximum orientation density peak is at around $\{111\}\langle 110\rangle$ grain in alpha fibre as compared to the peak at $\{112\}\langle 110\rangle$ grain in cold-rolled condition. Recrystallized texture is dominated with strong gamma fibre texture. Un-recrystallized texture is mainly composed of lower stored energy alpha grains as shown in Fig. 5.7-1b. Complete microstructural texture of Ti+Mn+ grade annealed at 800 °C 0 s is similar to the cold-rolled texture as there is insignificant change in microstructure during annealing. Texture results of Ti+Mn+ grade are similar to Ti+ grade with gamma fibre grains dominant in the recrystallized microstructure which are preferentially formed during annealing due to higher stored energy [224,306], and alpha fibre grains dominant in the un-

recrystallized microstructure for dwell time of 2 min and longer at 800 °C as shown in Fig. 5.7-1c. Texture of complete microstructure of Ti+Mn+ grade shows relatively weaker gamma texture than that of Ti+ grade for annealing condition of 800 °C 2 hrs as shown in Fig. 5.7-1c.

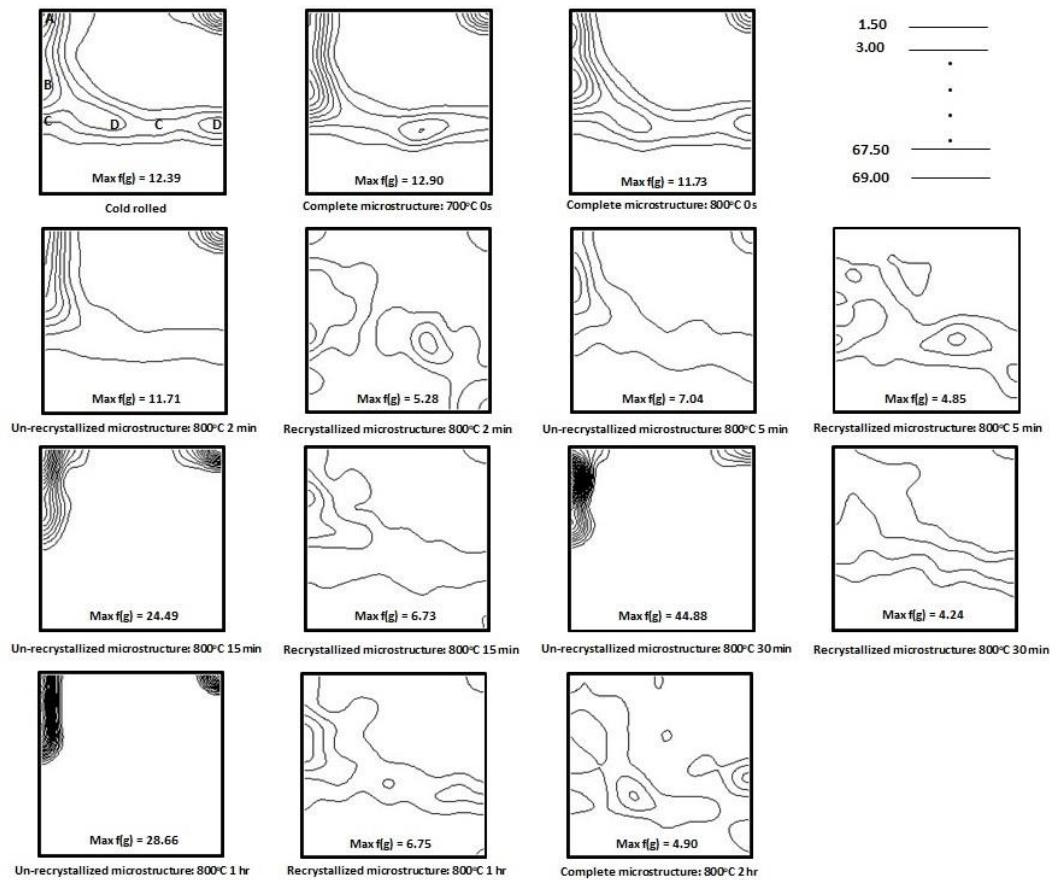


Fig. 5.7-1c ODF on the section $\varphi_2=45^\circ$ texture maps of Ti+Mn+ grade steel

X-ray diffraction (XRD) measurements are carried out and 2D ODF maps are plotted to study bulk texture of three grades for cold-rolled and 800 °C 2 hrs conditions as shown in Fig. 5.7-2. Cold-rolled bulk texture of base, Ti+ and Ti+Mn+ grades obtained from XRD consist of strong alpha and gamma fibres as shown in Fig. 5.7-2. Bulk texture of base, Ti+ and Ti+Mn+ grades annealed at 800 °C 2 hrs condition is dominated with stronger gamma fibre than alpha fibre as shown in Fig. 5.7-2. Texture intensity of gamma fibre of base grade is weaker than Ti+ and Ti+Mn+ grades for annealing condition of 800 °C 2 hrs. Texture data of Ti+ and Ti+Mn+ grades obtained from XRD are similar to each other containing strong gamma fibre and weak alpha fibre and is in contrast to the earlier EBSD data observations (Fig. 5.7-1b and 5.7-1c). Also texture results of base grade obtained from EBSD data (Fig. 5.7-1a) and XRD data (Fig. 5.7-2) for annealing condition of 800 °C 2 hrs are different. The above difference in texture results of complete microstructure obtained from EBSD and XRD data for annealing condition of 800 °C 2hrs is discussed in detail in section 6.1.6 of the discussions chapter. In

further sub-sections, STEM-EDS maps are presented for three grades at different conditions to understand precipitates' interaction with recrystallization process.

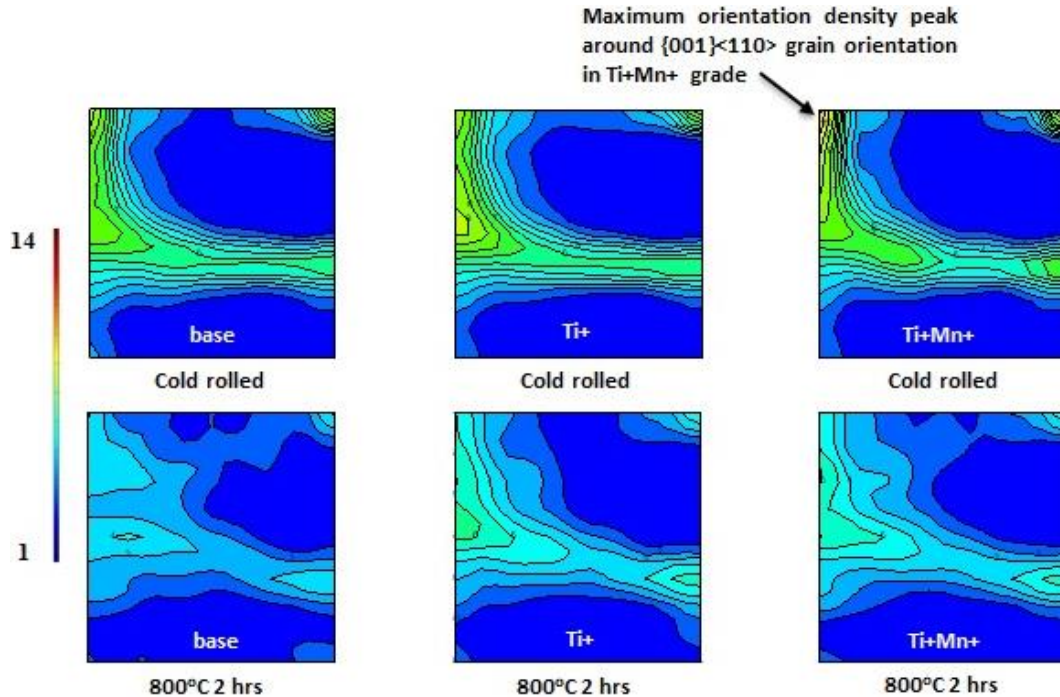


Fig. 5.7-2 ODF on the section $\phi_2=45^\circ$ texture maps of base, Ti+ and Ti+Mn+ grades of steel for cold-rolled state and 800 °C 2 hrs annealing condition respectively

5.8. Precipitate study of muffle furnace annealed samples

For temperature of 700 °C with no dwell, fine ($d < 15$ nm) precipitates of V(C/N) in base grade and (Ti,V)(C/N) in Ti+ and Ti+Mn+ grades are found to form in the un-recrystallized deformed bands and on recovered sub-grain boundaries as shown in STEM-EDS chemical maps of Ti+ and Ti+Mn+ grades of Fig. 5.8-1 and Fig. 5.8-2 respectively. Fine precipitates decorated along defects provide resistance to boundary motion by Zener pinning during annealing [101]. Carbo-nitrides of Ti and V exist as complex precipitates due to their mutual solubility with each other in both Ti+ and Ti+Mn+ grades [142,154]. With increase in temperature to 800 °C and dwell time to 0 s, 2 min and 5 min, relative frequency (%) of coarse precipitates ($d > 15$ nm) is increased as shown in the Fig. 5.8-6. Because of the increased temperature, dwell time, and the fact that precipitates are coarser, grain boundaries are able to move [101] and the deformed grains and bands are recrystallized into a fully grown strain free grains. For annealing conditions of 800 °C 2 min and 800 °C 5 min, fine ($d < 15$ nm) and coarse ($d > 15$ nm) precipitates are located inside recrystallized grains as shown in Fig. 5.8-4a, 5.8-4b and 5.8-5 and fine precipitates are decorated along un-recrystallized grain boundary as shown in Fig. 5.8-4c. STEM-EDS mapping is also performed on carbon replica samples of Ti+ grade annealed at 800 °C 5 min. High magnification ($\times 180k$) V and Ti chemical maps and

selected area diffraction (SAED) pattern of the one of the (Ti,V)(C/N) precipitates (marked with an arrow) with zone axis parallel to $[\bar{1}12]$ direction are shown in Fig. 5.8-3.

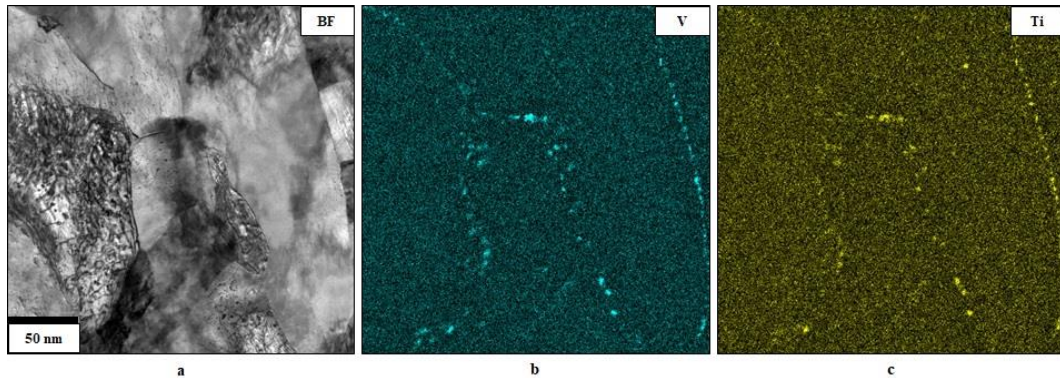


Fig. 5.8-1 STEM bright field (BF) image (a) and EDS chemical maps (b) and (c) of carbonitrides of Titanium and Vanadium (Ti,V)C precipitates pinned to a sub-grain boundary at 700 °C 0 s for Ti+ grade steel at two different FIB-lift out samples after bulk-furnace annealing

The data in Fig. 5.8-6 shows that relative frequency (%) of finer precipitates ($d < 15$ nm) are higher for 700 °C 0 s and 800 °C 0 s and relative frequency (%) of coarser precipitates ($d > 15$ nm) are higher for 800 °C 2 min and 5 min for three grades. There is no significant difference in precipitation characteristics between Ti+ and Ti+Mn+ grades. For annealing conditions of 700 °C 0 s and 800 °C 0 s, relative frequency (%) of finer precipitates (< 10 nm) evaluated is ~ 10 % higher in Ti+Mn+ than Ti+ grade as shown in Fig. 5.8-6b and 5.8-6c. The statistical evaluation of precipitate size for annealing conditions of 700 °C 0 s and 800 °C 0 s may not be accurate due to nature of precipitates. For no dwell conditions, precipitates are very fine and closely spaced along microstructural defects which make post-processing of STEM-EDS maps in ImageJ software difficult. Detailed steps of precipitate size and volume fraction calculations are mentioned in section 9.3 of the supplementary information chapter. For annealing conditions of 700 °C 0 s, 800 °C 0 s, 800 °C 2 min and 800 °C 5 min, average diameter of precipitates of base grade are 12.4 nm, 13.1 nm, 20.4 nm and 21.4 nm respectively, of Ti+ grade are 11.9 nm, 14.1 nm, 13.8 nm and 16 nm respectively and of Ti+Mn+ grade are 10.7 nm, 13.6 nm, 11.5 nm and 14.3 nm respectively (Fig. 5.8-7). Average precipitate size is increased with increases in annealing temperature and dwell time for all three grades. For base grade, average precipitate size is coarser than Ti+ and Ti+Mn+ grades with increase in dwell time to 2 min and 5 min for annealing temperature of 800 °C.

The precipitate number density in the hot-rolled state is considerably lower ($< 10^{20} \text{ m}^{-3}$) than cold-rolled annealed conditions as shown in Fig. 5.8-8. During annealing, fine new precipitates nucleate along sub-grain and grain boundaries (Fig. 5.8-1 and 5.8-2) and possibly impairs grain boundary migration. In the case of the base grade for longer dwell time (> 0 s) at an annealing temperature of 800 °C, precipitates start coarsening and average precipitate

number density decreases to $\sim 3.7E+20 \text{ m}^{-3}$. While for Ti+ and Ti+Mn+ grades, precipitate number density decreases for dwell time $> 2 \text{ min}$ at annealing temperature of $800 \text{ }^\circ\text{C}$.

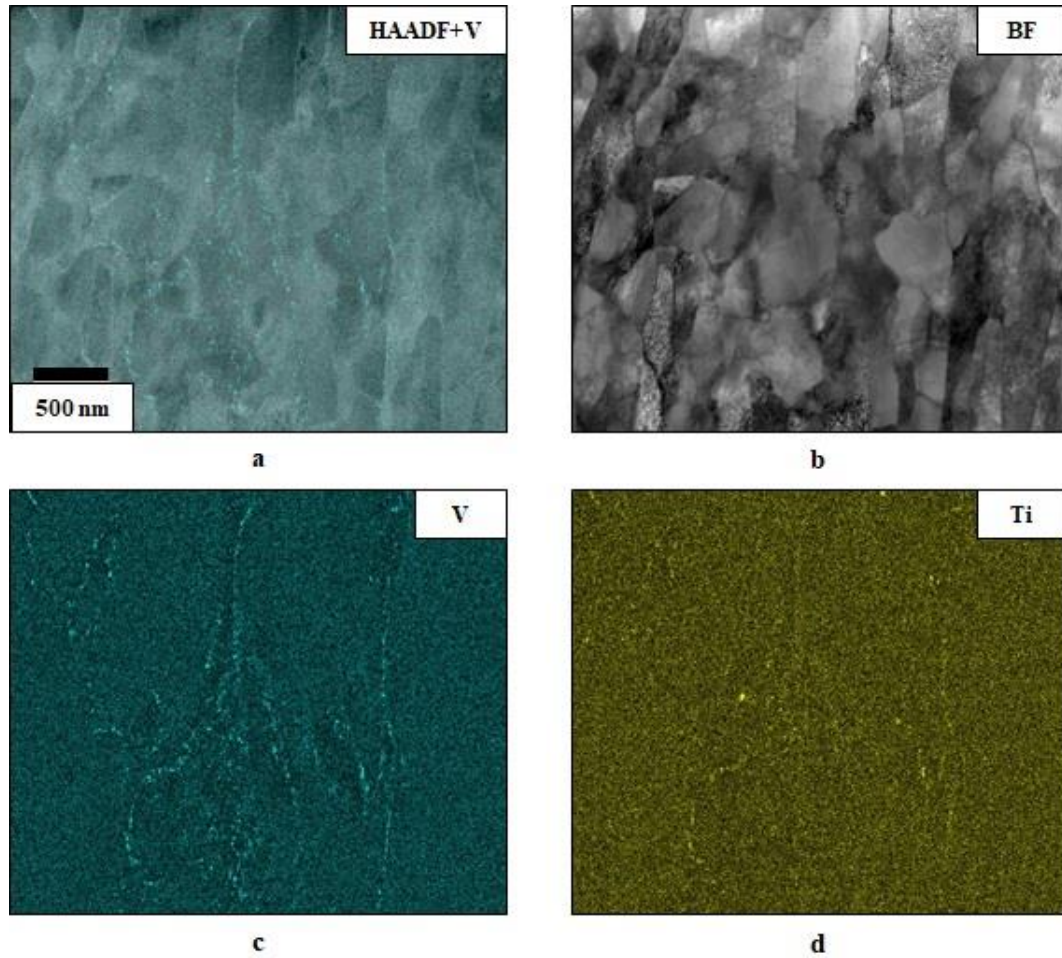


Fig. 5.8-2 STEM high-angle annular dark-field (HAADF) image superimposed with Vanadium EDS chemical map (a), bright field (BF) image (b) and EDS chemical maps of carbo-nitrides of Titanium and Vanadium (Ti,V)C precipitates (c) and (d) pinned to a sub-grain boundary at $700 \text{ }^\circ\text{C}$ 0 s for Ti+Mn+ grade steel at two different FIB-lift out samples after bulk-furnace annealing

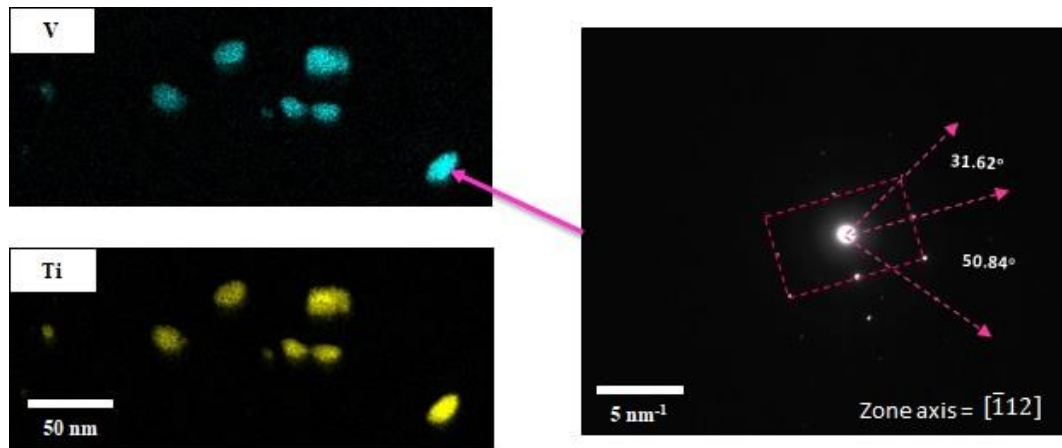


Fig. 5.8-3 EDS chemical maps (left) and diffraction pattern (right) of one of the (Ti,V)(C/N) precipitates suspended in carbon replica film (shown with a pink arrow) of Ti+ grade sample treated at 800 °C 5 min annealing condition

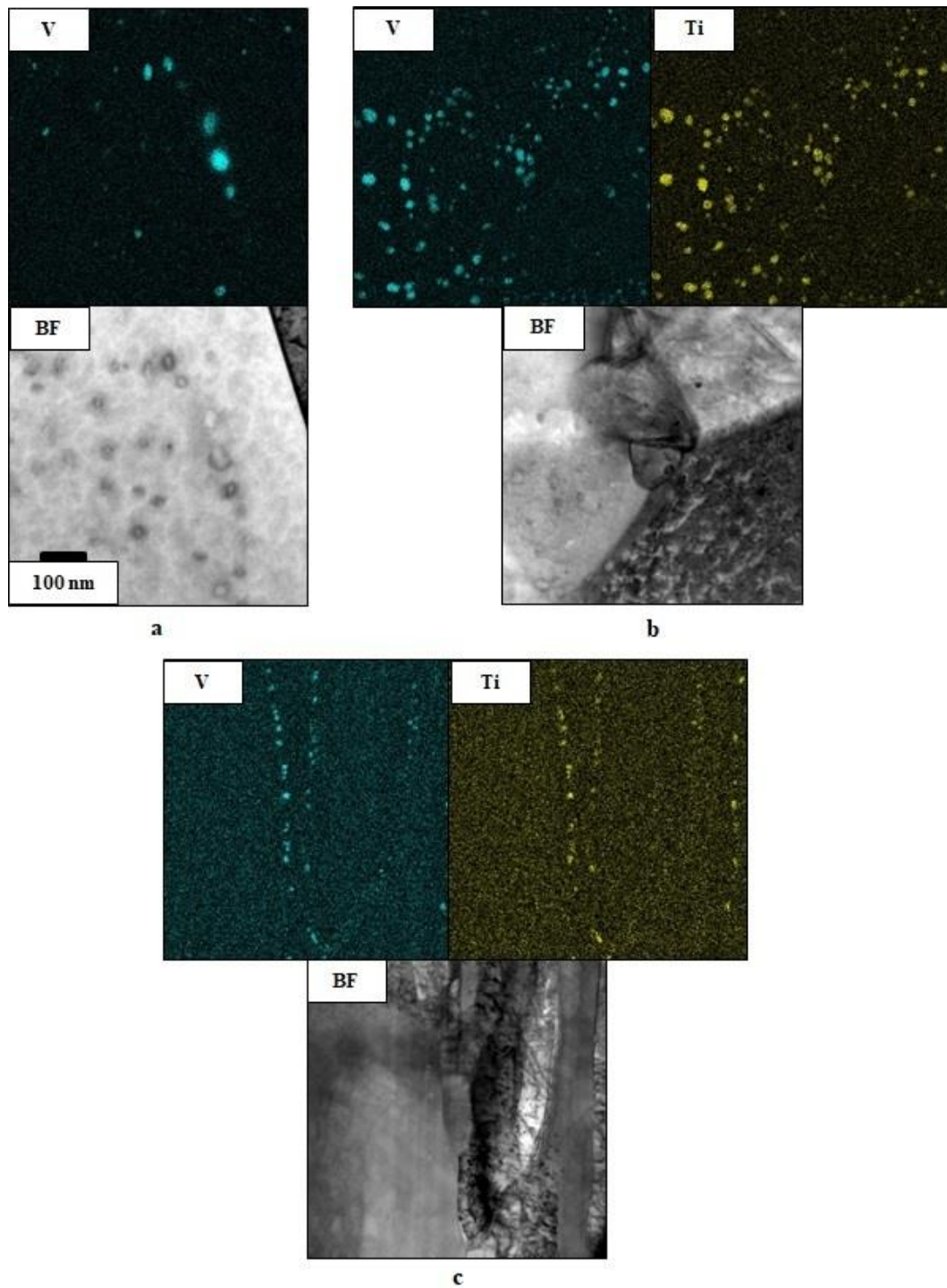


Fig. 5.8-4 STEM bright field (BF) image and EDS chemical maps of carbo-nitrides of Vanadium V(C/N) precipitates for base (a) and carbo-nitrides of Titanium and Vanadium (Ti,V)C precipitates for Ti+ (b) and Ti+Mn+ (c) grades of steel annealed at 800 °C 2 min condition at two different FIB-lift out samples for each grade after bulk-furnace annealing

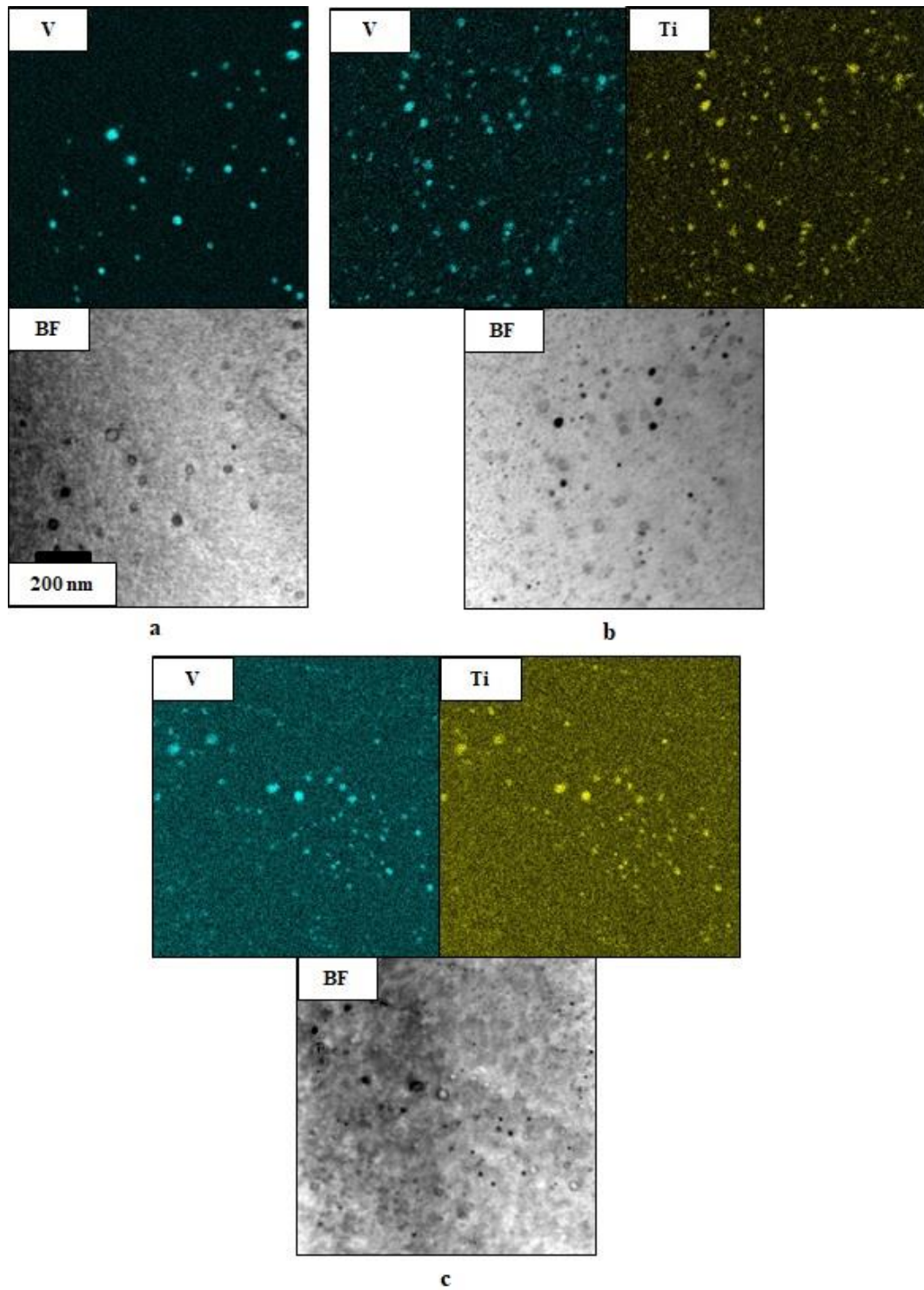
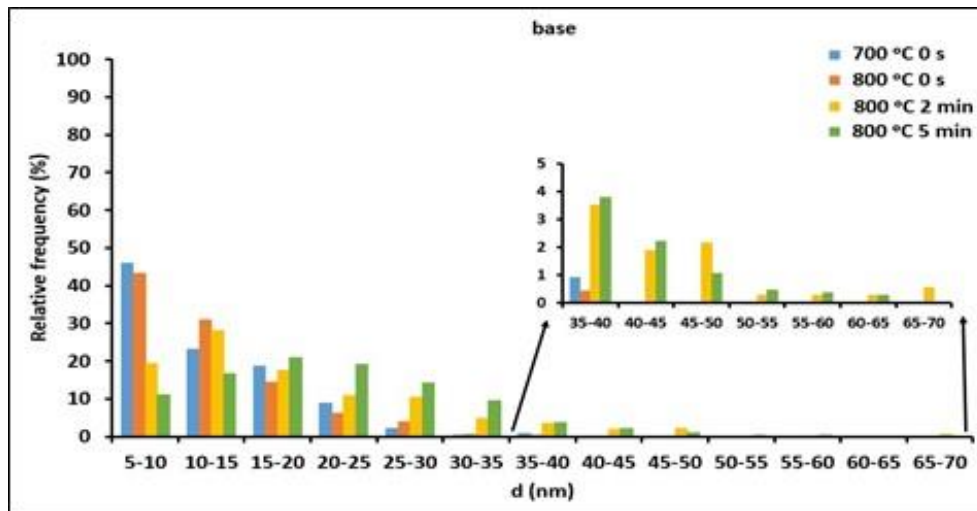
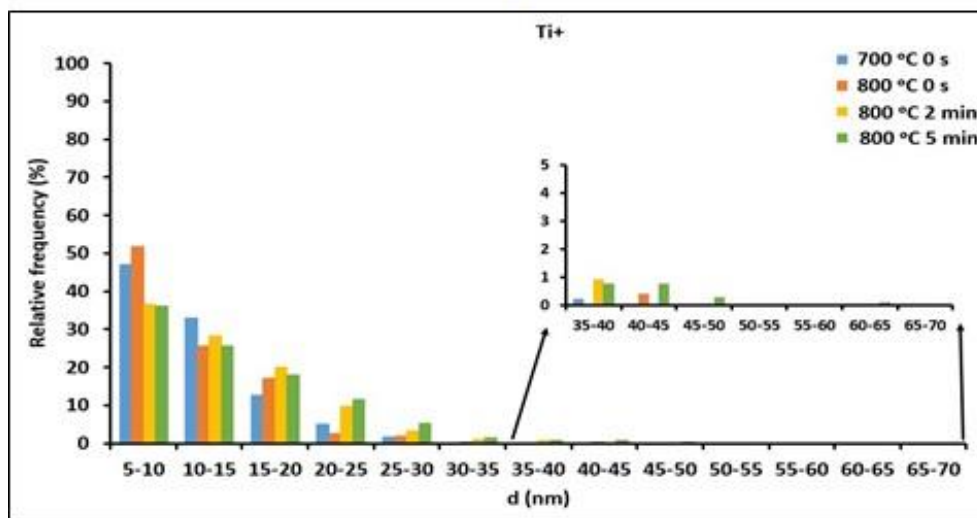


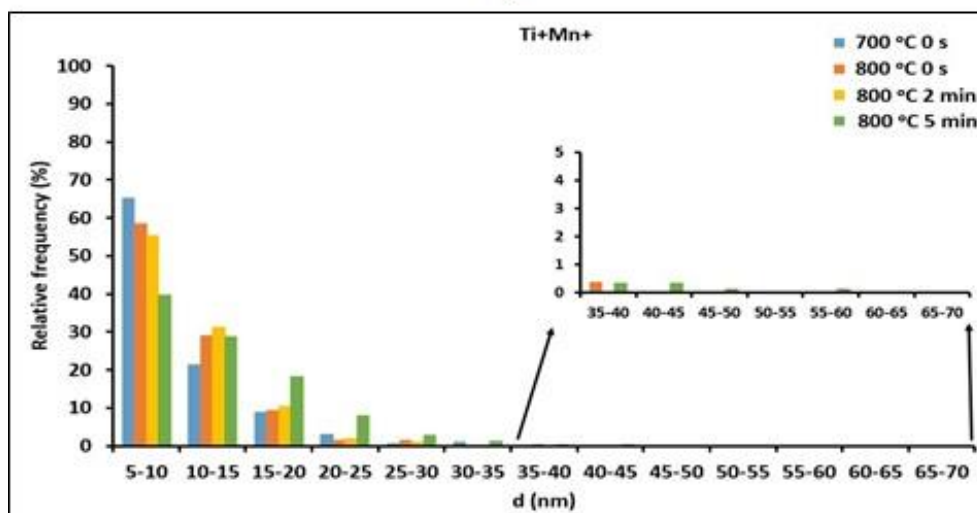
Fig. 5.8-5 STEM bright field (BF) image and EDS chemical maps of carbo-nitrides of Vanadium V(C/N) precipitates for base (a) and carbo-nitrides of Titanium and Vanadium (Ti,V)C precipitates for Ti+ (b) and Ti+Mn+ (c) grades of steel annealed at 800 °C 5 min condition at two different FIB-lift out samples for each grade after bulk-furnace annealing



a



b



c

Fig. 5.8-6 Relative frequency (%) of precipitate size of base (a), Ti+ (b) and Ti+Mn+ (c) grades of steel for different annealing conditions: 700 °C 0 s; 800 °C 0 s; 800 °C 2 min and 800 °C 5 min

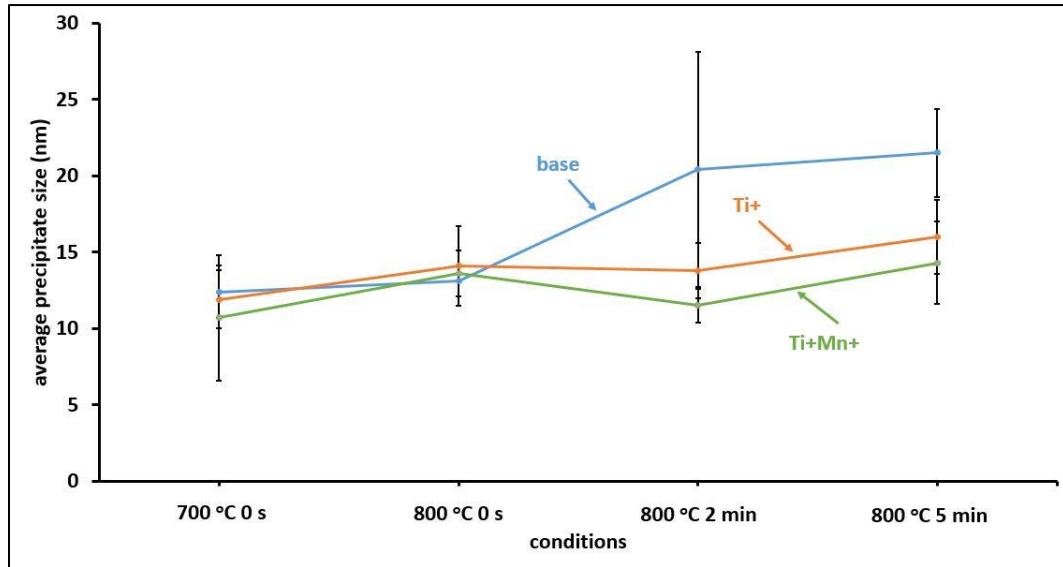


Fig. 5.8-7 Average precipitate size of base (a), Ti+ (b) and Ti+Mn+ (c) grades of steel for different annealing conditions: 700 °C 0 s; 800 °C 0 s; 800 °C 2 min and 800 °C 5 min

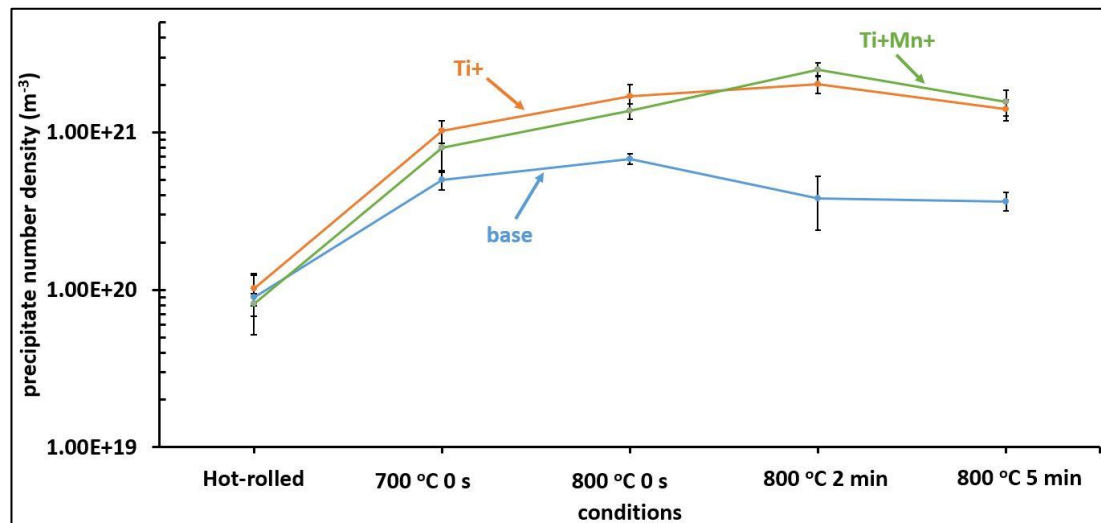


Fig. 5.8-8 Precipitate number density of base, Ti+ and Ti+Mn+ grades of steel for different conditions: hot-rolled; 700 °C 0 s; 800 °C 0 s; 800 °C 2 min and 800 °C 5 min

5.9. Mechanical properties

5.9.1. Nanoindentation analysis of muffle furnace annealed samples

Nanoindentation measurements are carried out on the polished samples after EBSD analysis in as cold-rolled and annealed at 700 °C 0 s, 800 °C 0 s and 800 °C 2 min to understand the difference in softening behaviour among base, Ti+ and Ti+Mn+ steel grades. Fig. 5.9-1 represents band contrast (BC) map of 90 (10 x 9) indents across annealed microstructure of Ti+ grade treated for 800 °C 2 min condition. The BC map is divided into four different regions, 1, 2, 3 and 4 and their corresponding ND-IPF and GND density maps are presented sideways as shown in Fig. 5.9-1. Distribution of GND density of un-recrystallized ferrite matrix (order

of 10^{14} m^{-2} to 10^{15} m^{-2}) is higher than recrystallized ferrite matrix (order of 10^{13} m^{-2}) as shown in GND maps in Fig. 5.9-1. Also, GND density (order of 10^{14} m^{-2}) near the indent is higher than recrystallized ferrite matrix (order of 10^{13} m^{-2}) because of the dislocation pile up introduced during the nanoindentation experiment.

Average GND density of the un-recrystallized ferrite matrix of base, Ti+ and Ti+Mn+ grades for each conditions is evaluated (Fig. 5.9-2) to understand the difference in softening behaviour among different steel grades. Due to static recovery and recrystallization, drop in average GND density within the un-recrystallized ferrite matrix of base grade ($1.0\text{E}+15 \text{ m}^{-2}$) is highest as compared to Ti+ ($3.8\text{E}+14 \text{ m}^{-2}$) and Ti+Mn+ ($1.9\text{E}+14 \text{ m}^{-2}$) for annealing condition of $800 \text{ }^\circ\text{C}$ 0 s. A smaller drop in average GND density for Ti+Mn+ grade ($1.9\text{E}+14 \text{ m}^{-2}$) than Ti+ grade ($3.8\text{E}+14 \text{ m}^{-2}$) indicates negligible static recovery within un-recrystallized ferrite matrix for annealing condition of $800 \text{ }^\circ\text{C}$ 0 s. While, for $800 \text{ }^\circ\text{C}$ 2 min annealing condition drop in average GND density for Ti+ grade ($7.2\text{E}+14 \text{ m}^{-2}$) and Ti+Mn+ grade ($6.9\text{E}+14 \text{ m}^{-2}$) are very similar as shown in Fig. 5.9-2.

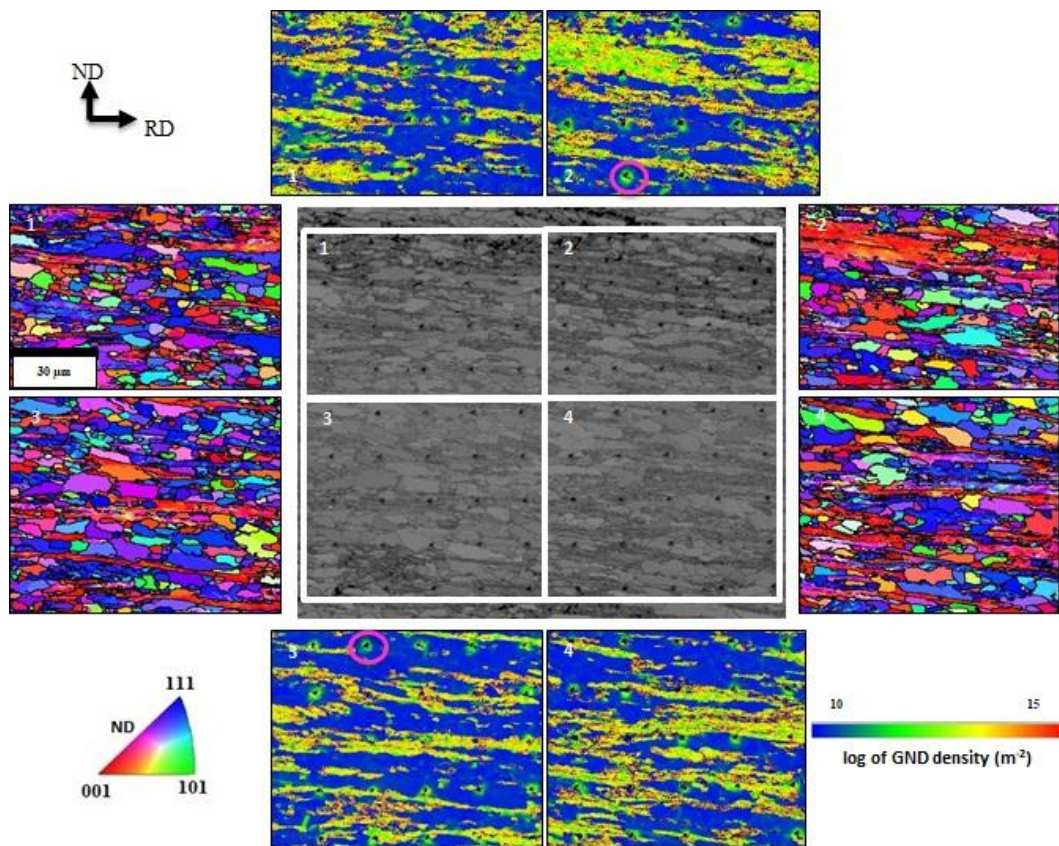


Fig. 5.9-1 Band contrast (BC) map (centre) of Ti+ grade steel with 90 nanoindents after bulk furnace annealing at $800 \text{ }^\circ\text{C}$ 2 min condition. Normal direction inverse pole figure (ND-IPF) maps (left and right) and geometrically necessary dislocation (GND) density maps (top and bottom) of corresponding regions, numbered as 1, 2, 3 and 4 in white colour. Circles mark the dislocation pile up near the indents introduced during nanoindentation

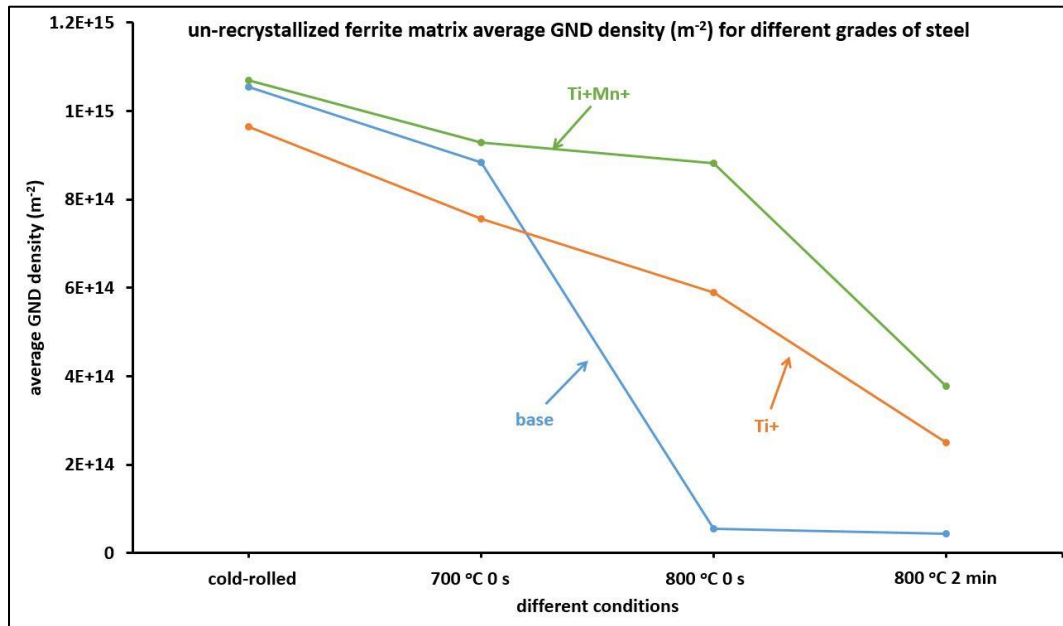


Fig. 5.9-2 Average geometrically necessary dislocation (GND) density of base, Ti+ and Ti+Mn+ grades of steel for different conditions: cold-rolled; 700 °C; 800 °C 0 s and 800 °C 2 min

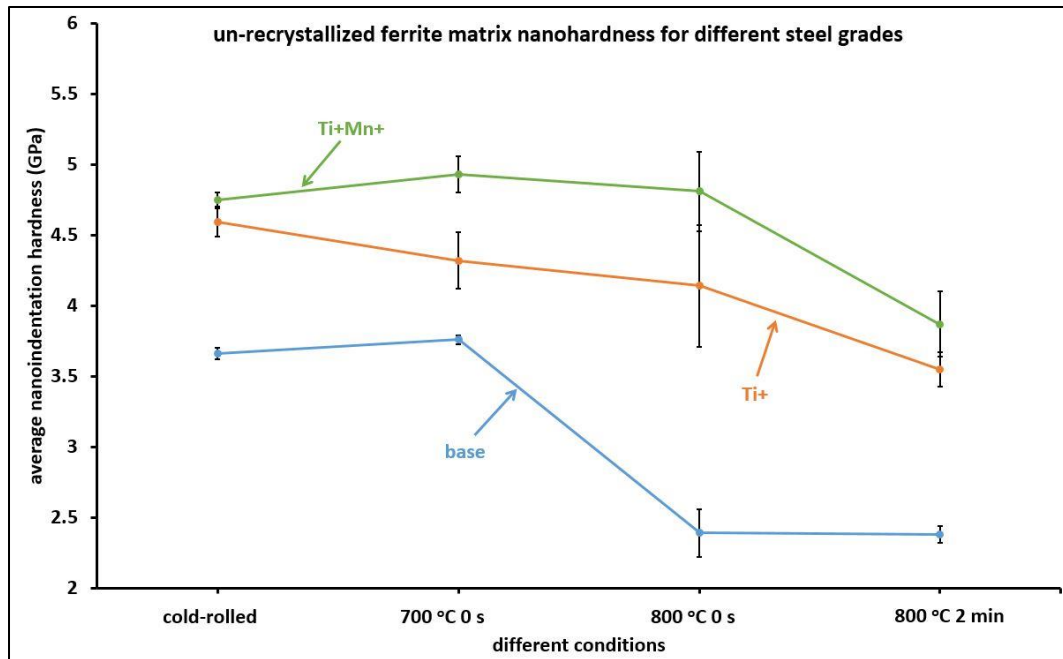


Fig. 5.9-3 Average nanoindentation hardness of base, Ti+ and Ti+Mn+ grades of steel for different conditions: cold-rolled; 700 °C; 800 °C 0 s and 800 °C 2 min

Average nanoindentation hardness is evaluated from the un-recrystallized ferrite matrix of base, Ti+ and Ti+Mn+ grades for each conditions as shown in Fig. 5.9-3. The trend in change in hardness values for different conditions of three grades is very similar to the trend in change in average GND density of the un-recrystallized ferrite matrix. The highest drop in average

nanindentation hardness takes place in base grade (1.27 GPa) for annealing condition 800 °C 0 s. The drop in average nanindentation hardness in Ti+ grade (0.45 GPa) is higher than Ti+Mn+ grade (~ 0 GPa) for annealing condition of 800 °C 0 s. For annealing condition of 800 °C 2 min, the drop in average nanindentation hardness for Ti+ grade (~ 1 GPa) and Ti+Mn+ grade (~ 0.9 GPa) is very similar.

For the nanindentation hardness results presented above (Fig. 5.9-3), ferrite matrix is assumed to be un-recrystallized if its nanindentation hardness is greater than average nanindentation hardness for hot-rolled state [251]. Nanindentation hardness of hot-rolled base, Ti+ and Ti+Mn+ grades are 2.11 ± 0.06 GPa, 3.31 ± 0.19 GPa and 3.24 ± 0.08 GPa respectively.

5.9.2. Microhardness and Uniaxial tensile measurements

Hardness measurements are carried out on samples sized 6 mm x 6 mm x 1 mm of base, Ti+ and Ti+Mn+ grades treated for different conditions of as cold-rolled, annealed 700 °C 0 s, 800 °C 0 s, 800 °C 2 min, 800 °C 5 min, 800 °C 15 min, 800 °C 30 min, 800 °C 1 hr and 800 °C 2 hrs. For cold-rolled state, average hardness of Ti+ (280 ± 7 HV/1) and Ti+Mn+ (290 ± 3 HV/1) grades are similar and higher than base grade (220 ± 5 HV/1). The rate of softening is highest in the base grade with a decrease in hardness (96 HV/1) for annealing condition of 800 °C 0 s. Average hardness of base grade (~ 115 HV/1) is almost similar from dwell time of 0 s to 15 min at annealing temperature of 800 °C. With an increase in dwell time to 15 min and longer, average hardness of base grade further decreases to ~ 66 HV/1 for 800 °C 2 hrs. With an increase in dwell time to 2 min and longer for annealing temperature of 800 °C, average hardness of Ti+ and Ti+Mn+ grades are similar as shown in Fig. 5.9-4.

Room temperature uniaxial tensile tests are performed to measure strength and elongation (%) properties of base, Ti+ and Ti+Mn+ grades treated for different conditions of as cold-rolled, and annealed at 700 °C 0 s, 800 °C 0 s, 800 °C 2 min and 800 °C 5 min. Proof strength (yield strength at 0.2 % strain), $R_{0.2}$ is evaluated from the tensile curve and compared with empirical yield strength (YS) obtained from Vickers hardness using the relation (equation 5.9-1) as shown below:

$$HV \sim 3 * \sigma_y \quad (5.9-1)$$

There is insignificant difference between the empirical yield strength and $R_{0.2}$ values of three grades for different conditions as shown in Fig. 5.9-5. In cold-rolled state, average $R_{0.2}$ and tensile strength (TS) of Ti+ ($R_{0.2} = 946 \pm 47$ MPa and TS = 949 ± 44 MPa) and Ti+Mn+ ($R_{0.2} = 1003 \pm 2$ MPa and TS = 1018 ± 8 MPa) grades are higher than base grade ($R_{0.2} = 702 \pm 8$

MPa and $TS = 719 \pm 6$ MPa). For annealing condition of $700\text{ }^{\circ}\text{C}$ 0 s, strength values are similar to that of cold-rolled state with poor elongation (%) ($EL < 3\%$). For annealing temperature of $800\text{ }^{\circ}\text{C}$, $R_{0.2}$ of base grade significantly decreases to 350 - 390 MPa as shown in Fig. 5.9-5, because of dislocation softening, recrystallization of deformed texture [61] and precipitate coarsening in recrystallized ferrite matrix. The elongation (%) of base grade is increased up to 33 % for annealing condition of $800\text{ }^{\circ}\text{C}$ 5 min as shown in Fig. 5.9-7.

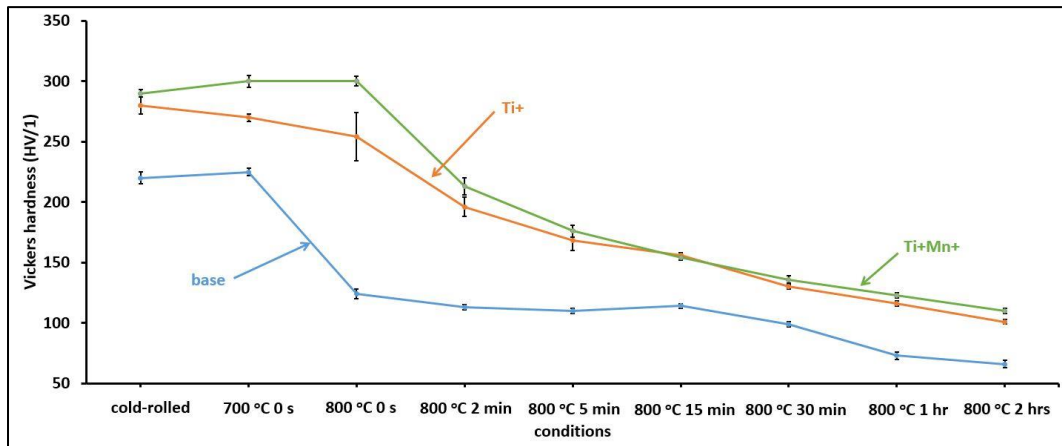


Fig. 5.9-4 Average Vickers hardness of base, Ti+ and Ti+Mn+ grades of steel for different conditions: $700\text{ }^{\circ}\text{C}$ 0 s; $800\text{ }^{\circ}\text{C}$ 0 s; $800\text{ }^{\circ}\text{C}$ 2 min; $800\text{ }^{\circ}\text{C}$ 5 min; $800\text{ }^{\circ}\text{C}$ 15 min; $800\text{ }^{\circ}\text{C}$ 30 min; $800\text{ }^{\circ}\text{C}$ 1 hr and $800\text{ }^{\circ}\text{C}$ 2 hrs

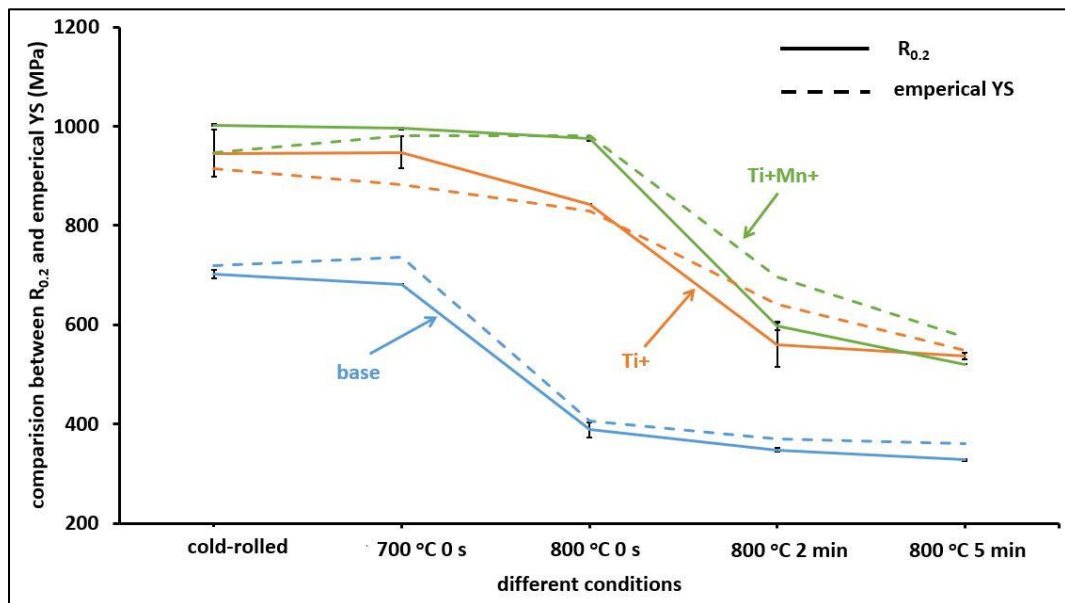


Fig. 5.9-5 Comparison of Yield strength at 0.2 % strain ($R_{0.2}$) and empirical yield strength (YS) of base, Ti+ and Ti+Mn+ grades of steel for different conditions: cold-rolled; $700\text{ }^{\circ}\text{C}$ 0 s; $800\text{ }^{\circ}\text{C}$ 0 s; $800\text{ }^{\circ}\text{C}$ 2 min; $800\text{ }^{\circ}\text{C}$ 5 min

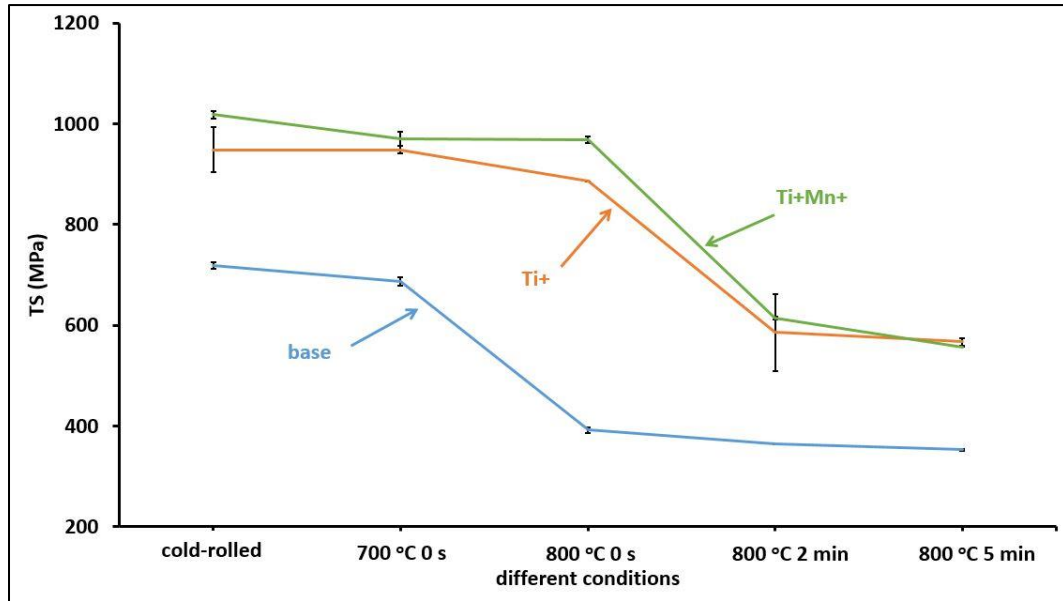


Fig. 5.9-6 Tensile strength (TS) of base, Ti+ and Ti+Mn+ grades of steel for different conditions: cold-rolled; 700 °C 0 s; 800 °C 0 s; 800 °C 2 min; 800 °C 5 min

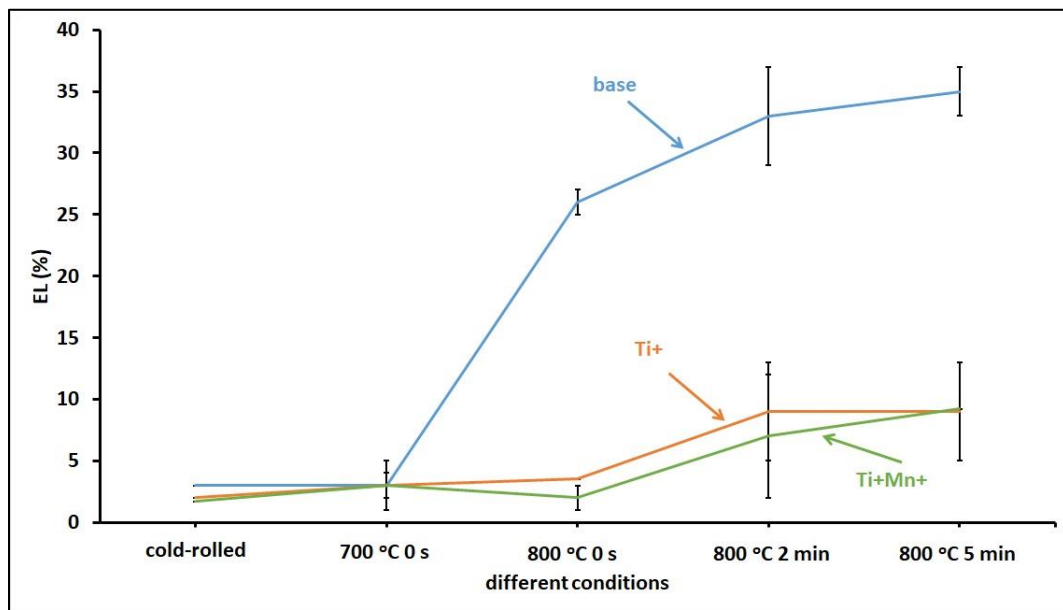


Fig. 5.9-7 Elongation, EL (%) of base, Ti+ and Ti+Mn+ grades of steel for different conditions: cold-rolled; 700 °C 0 s; 800 °C 0 s; 800 °C 2 min; 800 °C 5 min

For annealing condition of 800 °C 0 s, $R_{0.2}$ of Ti+ grade is decreased by approximately 100 MPa, which is more than Ti+Mn+ grade at about 20 MPa. With an increase in dwell time to 2 min for annealing temperature of 800 °C, $R_{0.2}$ of Ti+ and Ti+Mn+ grades have decreased to ~ 560 MPa and ~ 600 MPa respectively. Elongation (%) of Ti+ and Ti+Mn+ grades is low at around ~ 9 % as shown in Fig. 5.9-7.

6. Discussion

Based upon previous results, three main sections are discussed in this chapter: results of EBSD and STEM on the as-received and muffle furnace annealed steel grades, mechanical properties of each annealed condition, and hot-stage *quasi* in-situ EBSD testing. The first section includes discussion about the effect of carbo-nitrides of titanium and vanadium precipitates and Mn solute atoms on the recrystallization behaviour of base, Ti+ and Ti+Mn+ steel grades, cold-rolled and annealed texture development in the three steel grades and recrystallization (%) evaluation by three methods: LAM, aspect ratio and hardness (HV/1). The second section includes discussion about strengthening contribution from different elements (such as grain size, dislocation density, solid solution, inherent matrix and precipitation strengthening) and comparison of strength and elongation (%) properties of the base, Ti+ and Ti+Mn+ grades with multiphase steel grades. The third section includes discussion about reliability of surface microstructural observation of hot stage *quasi* in-situ EBSD and the role of alpha and gamma fibres on recrystallization mechanism during annealing.

6.1. EBSD and STEM analysis of the as-received and muffle furnace annealed steel grades

6.1.1. Initial precipitate state in the hot-rolled steel grades

STEM-EDS experiment shows microstructure with negligible amount of precipitates in the hot-rolled steel grades. For a virtually pure iron-carbon alloy, maximum solubility of carbon in ferrite matrix is ~ 0.022 wt. % at 727 °C [79]. For the three steel grades studied in this thesis, the carbon content in base, Ti+ and Ti+Mn+ is ~ 0.05 wt. % which is higher than the above maximum solubility in ferrite phase. Therefore, the excessive carbon content about 0.028 wt. % (0.05 %– 0.022 %) is present in the form of iron-carbide and/or complex carbides of Ti and V in hot-rolled state, depending on the coiling temperature and cooling rate after coiling. Fig. 6.1-1 shows iron-carbide along grain boundary of ferrite matrix in hot-rolled Ti+ grade. Lower coiling temperature ($T \sim 580$ °C) during hot-rolling process favours precipitating elements (Ti and V) to be in solution state and promotes the formation of microstructure with a lower volume fraction of fine precipitates [146–149]. During annealing of cold-rolled steel grade, iron-carbide dissolves to release carbon back into ferrite matrix, as the alloy carbides are thermodynamically more stable than iron carbides [84]. Upon further annealing, free C in ferrite phase combines with Ti and V to form precipitates in the cold-rolled annealed steel grades.

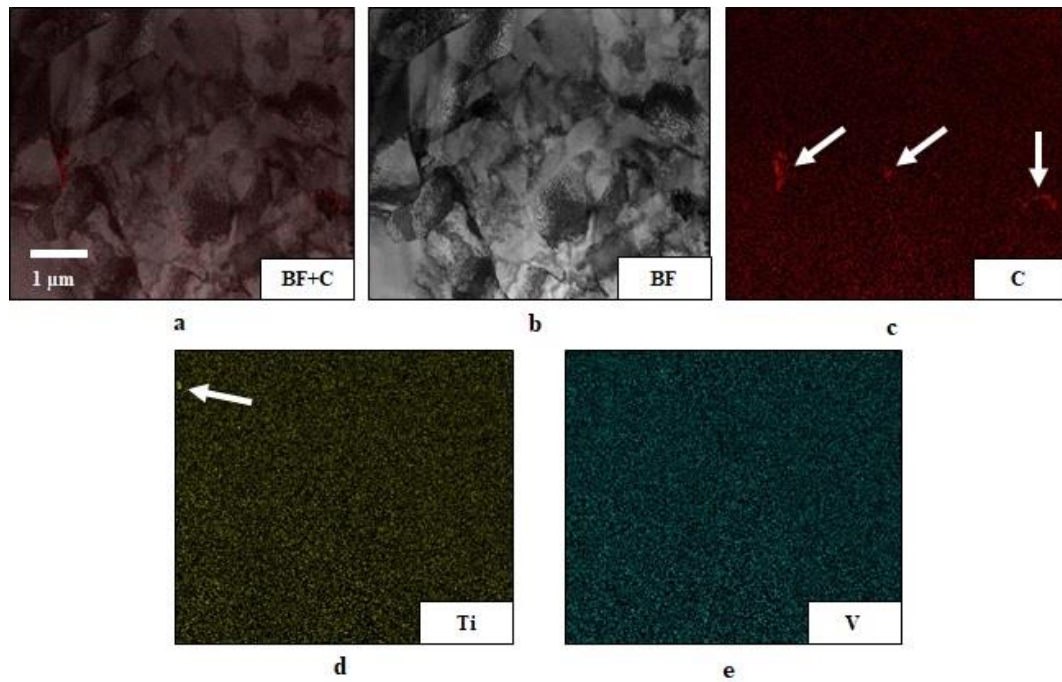


Fig. 6.1-1 STEM bright-field (BF) image superimposed with Carbon EDS chemical map (a) bright field (BF) image (b) and EDS chemical map of C (c), Ti (d) and V (e). Iron-carbide along sub-grain boundary in the hot-rolled Ti+ grade. Arrows mark the iron-carbide in C chemical map and carbo-nitride of titanium in Ti chemical map

6.1.2. Difference in grain size in hot-rolled steel grades

The average grain size of the hot-rolled steel grades is in the order of base (10 μm) > Ti+ (7 μm) and Ti+Mn+ (5 μm). The hot rolling parameters used for all three steels was nominally the same. The difference in initial average grain size among the three grades could be due to differences in non-recrystallization temperature (T_{nr}). T_{nr} is defined as the temperature below which static recrystallization is no longer completed between two successive rolling passes [317–319]. Approximate value of T_{nr} is evaluated for base ($T_{nr} \sim 940$ °C), Ti+ ($T_{nr} \sim 1011$ °C) and Ti+Mn+ ($T_{nr} \sim 1011$ °C) grades using empirical relationship proposed by Boratto et al. [320]

$$T_{nr} = 887 + 464C + (6445Nb - 644\sqrt{Nb}) + (732V - 230\sqrt{V}) + 890Ti + 363Al - 357Si \quad (6.1-1)$$

Where, C, Nb, V, Ti, Al and Si are wt. % of carbon, niobium, vanadium, titanium, aluminium and silicon.

Since, finish hot-rolling temperature (~ 890 °C) is similar for the three grades and is lower than T_{nr} , therefore deformation of the steel sheet within the austenitic region leads to formation of mixture of recrystallized austenite grains, elongated (pancaked) austenite grains and deformation bands [321]. Ti+ and Ti+Mn+ grades would have higher fraction of pancaked austenite microstructure i.e. un-recrystallized austenite matrix than base grade due to higher

value of T_{nr} . During phase transformation from austenite to ferrite, recrystallized austenite grain boundaries, grain boundaries surrounding pancaked austenite microstructure, deformation bands within grains etc. will form the nucleation sites for ferrite grains [318,319,321]. Higher fraction of elongated austenite grain microstructure (higher ratio of grain boundary surface area to grain volume) in Ti+ and Ti+Mn+ grades would lead to a finer ferrite grain microstructure as compared to the base grade because of the higher number of ferrite nucleation sites [318,321]. Ti+Mn+ grade contains higher Mn (~ 0.89 wt. %) than Ti+ grade (~ 0.35 wt. %) in solid solution. Higher Mn solute drag effect in Ti+Mn+ grade could lead to higher fraction of un-recrystallized pancaked austenite microstructure than Ti+ grade [318]. Higher fraction of un-recrystallized pancaked austenite microstructure in Ti+Mn+ grade would result in finer (average grain size ~ 5 μm) ferrite grain microstructure as compared to Ti+ grade (average grain size ~ 7 μm).

6.1.3. Recrystallization and precipitation behaviour of the muffle furnace annealed base, Ti+ and Ti+Mn+ steel grades

Recrystallization kinetics of the base grade is higher than the Ti+ and Ti+Mn+ grades during sub-critical annealing. For the 800 °C 0 s annealing condition, base, Ti+ and Ti+Mn+ grades have shown significant difference in recrystallization behaviour. Base is almost fully recrystallized with average recrystallization (%) measured by LAM method being ~ 99 %. While, recrystallization (%) of the Ti+Mn+ (recrystallization (%) by LAM method ~ 8 %) is less than the Ti+ grade (recrystallization (%) by LAM method ~ 19 %) with only limited nucleation around HAGB. With an increase in dwell time to 2 min and longer for annealing temperature of 800 °C, recrystallization behaviour of the Ti+ and Ti+Mn+ grades is similar. Therefore, it is important to discuss in detail similarities and differences in recrystallization and precipitation behaviour of base and Ti+ grades, and also additional Mn effect on recrystallization and precipitation behaviour of the Ti+Mn+ grade for different annealing conditions.

6.1.3.1 Recrystallization and precipitation behaviour of the base and Ti+ grades

Recrystallization and precipitation take place simultaneously and interact with each other in a complex form during annealing of microalloyed steel. On the other hand, precipitates interfere with dislocation and grain boundary movement and affect recovery and recrystallization kinetics. On the other hand, dislocations present in cold-rolled deformed and annealed ferrite microstructure affect precipitation process [204]. Radius and volume fraction of precipitates are experimentally (from STEM-EDS maps) and numerically (from MatCalc simulation) determined and compared with each other for the base and Ti+ grades as shown in Fig. 6.1-2. Parameters used for simulation of precipitation size and volume fraction are shown in Table 6.1-1. For simulation, a start temperature of 600 °C is set and is gradually increased to 800 °C

with increase over time (heating rate ~ 10 °C/s). Experimentally defined annealing conditions of 700 °C 0 s, 800 °C 0 s, 800 °C 2 min and 800 °C 5 min are equivalent to simulation time of 13 s, 25 s, 145 s and 325 s respectively.

Table 6.1-1 Parameters for MatCalc simulation of precipitate size and volume fraction

Type of precipitates	Diffusivity in ferrite (m^2s^{-1})	Interfacial energy	Dislocation density in ferrite (m^{-2})	Critical energy for nucleation on dislocations
VC	$D_V^\alpha = 3.05 \times 10^{-4} \exp\left(-\frac{239000}{RT}\right)$ [322]	0.445 [323]	1.05×10^{15}	0.01 [324]
TiC	$D_{Ti}^\alpha = 3.15 \times 10^{-4} \exp\left(-\frac{248000}{RT}\right)$ [325]	0.425 [323]	0.97×10^{15}	0.01 [324]

Experimental and numerical results of precipitate size and volume fraction are similar to each other for the annealing conditions of 800 °C 0 s, 800 °C 2 min and 800 °C 5 min as shown in Fig. 6.1-2a and 6.1-2b. For the annealing condition of 700 °C 0 s, experimental precipitate volume is higher than numerical predictions. For 700 °C 0 s, precipitates are very fine and closely spaced between each other along subgrain and grain boundaries. Quantification of precipitate size and volume fraction using ImageJ software may not be accurate and could result in different experimental and numerical observations.

MatCalc simulation estimates critical radius of nucleation of precipitates in the Ti+ grade approximately 0.22 nm smaller than 4.2 nm in the base grade. Driving force for the formation of TiC particle is much higher than for VC because of the lower solubility of Ti in ferrite matrix than that of V [58]. The higher driving force for nucleation promotes finer critical radius of nucleation of precipitates [324,326,327]. Driven by the above higher force, the simulated precipitation kinetics is much faster in the Ti+ grade than in the base grade. For example, the precipitated volume fraction after 30 s annealing of Ti+ grade is about 0.15 %, which is much higher than the value (nearly zero or negligible) for the base grade. The faster precipitation kinetics in the Ti+ grade than in the base grade has a dramatic effect on the recrystallization kinetics in these two grades, as will be discussed next.

With increase in dwell time above 2 min at annealing temperature of 800 °C, precipitate coarsening occurs in the simulated radius curve of VC (base grade) due to diffusion of solute

atoms from the ferrite matrix [326]. Precipitate coarsening involves growth of larger precipitates at the expense of smaller precipitates. However, the coarsening of TiVC (Ti+ grade) occurs at much later stage of annealing, i.e., after 1000 s (~ 15 min) annealing. Therefore, precipitate coarsening is easier to occur in the base than in the Ti+ grade during annealing at 800 °C as shown in Fig. 6.1-2. The above difference in the coarsening behaviour is mainly due to the different composition of precipitates in these two grades. For the base grade, the precipitates are pure vanadium carbide (VC), but they are complex titanium vanadium carbide in the form of $Ti_yV_{1-y}C$ (average composition: $y \approx 0.4$) for the Ti+ grade. The above different coarsening behaviour also has a significant effect on recrystallization kinetics in these two grades [326].

Precipitate size and volume fraction are used in equation 6.1-2 to evaluate Zener pinning force for different annealing conditions:

$$\Delta G_{pin} = \frac{3}{2} * \sigma * V_m * \frac{f}{r} \quad (6.1-2)$$

Where, f and r are numerical values of precipitate volume fraction and radius, and σ is interfacial energy of precipitates-ferrite matrix, and V_m is molar volume. Fig. 6.1-3 shows numerical values of precipitate pinning force as a function of annealing time and corresponding ND-IPF EBSD maps of the base and Ti+ grades for the annealing condition of 800 °C 0 s, 800 °C 5 min, 800 °C 15 min and 800 °C 1 hr.

For 800 °C 0 s, precipitation pinning force in the Ti+ grade of approximately 1 J/mol is higher than in the base grade which is 0.06 J/mol as shown in Fig. 6.1-3. At this annealing time, the measured recrystallized fraction is about 100 % and 19 % in the base and Ti+ (Fig 5.5-2) respectively. Comparing the above precipitation and recrystallization behaviour in these two grades, it's shown that the precipitation is faster than the recrystallization in the Ti+ grade, whilst the opposite situation happened in the base grade, i.e., the precipitation is much slower than the recrystallization. Once a lot of fine precipitates form in the Ti+ grade, the precipitation pinning force is effective in retarding recrystallization process in the Ti+ grade for the annealing condition of 800 °C 0 s. In the case of the base grade, not much precipitates form under this annealing condition and recrystallization almost completes. Therefore, precipitation has negligible effect in retarding the recrystallization process in base grade. With an increase of dwell time to 2 min and to 5 min at 800 °C, recrystallization and precipitation occur concurrently in the Ti+ grade. The precipitation pinning force (about 1.75 Jmol^{-1}) can certainly be higher than the driving force for at least some grains belonging to alpha fibre. This means that the recrystallization of those alpha grains is prevented temporally by the precipitates. Thus the presence of lower stored energy alpha fibre grains lead to a sluggish recrystallization process in the Ti+ grade.

With an increase in dwell time to 15 min and longer at 800 °C, precipitate pinning force decreases (Fig. 6.1-3) in both base and Ti+ grades because of precipitate coarsening. When the pinning force decreases lower than the driving force for recrystallization in the Ti+ grade, the recrystallization of those alpha grains with low stored energy can resume. For the base grade, because recrystallization almost completes when the annealing temperature reaches 800 °C, the grain growth behaviour is affected by the precipitation coarsening in this grade. Some grains with much larger size than others can be observed for 1 and 2 hours annealing at 800 °C, as shown in Fig 5.4-1g and h.

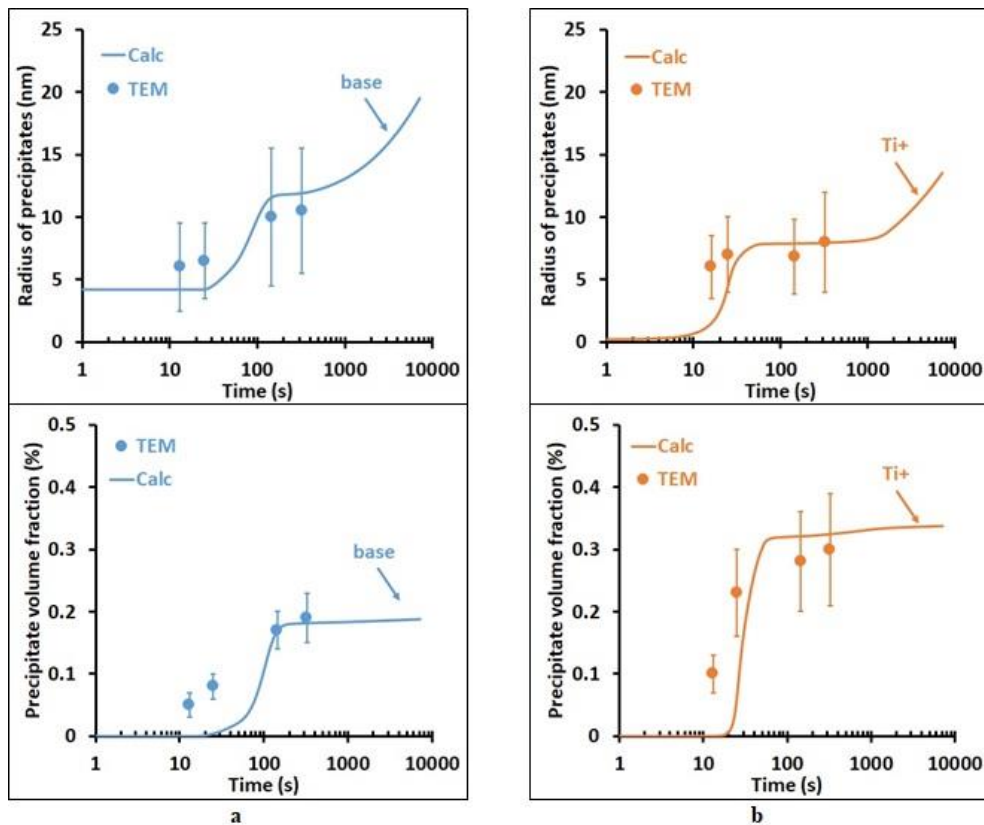


Fig. 6.1-2 Variation of experimentally evaluated (solid dot) and numerically evaluated, radius of precipitate (top) and precipitate volume fraction (%) (bottom) with increase in annealing time of the base (a) and the Ti+ (b) grades of steel. Annealing conditions: 700 °C 0 s, 800 °C 0 s, 800 °C 2 min and 800 °C 5 min correspond numerically to time: 13 s, 25 s, 145 s and 325 s respectively

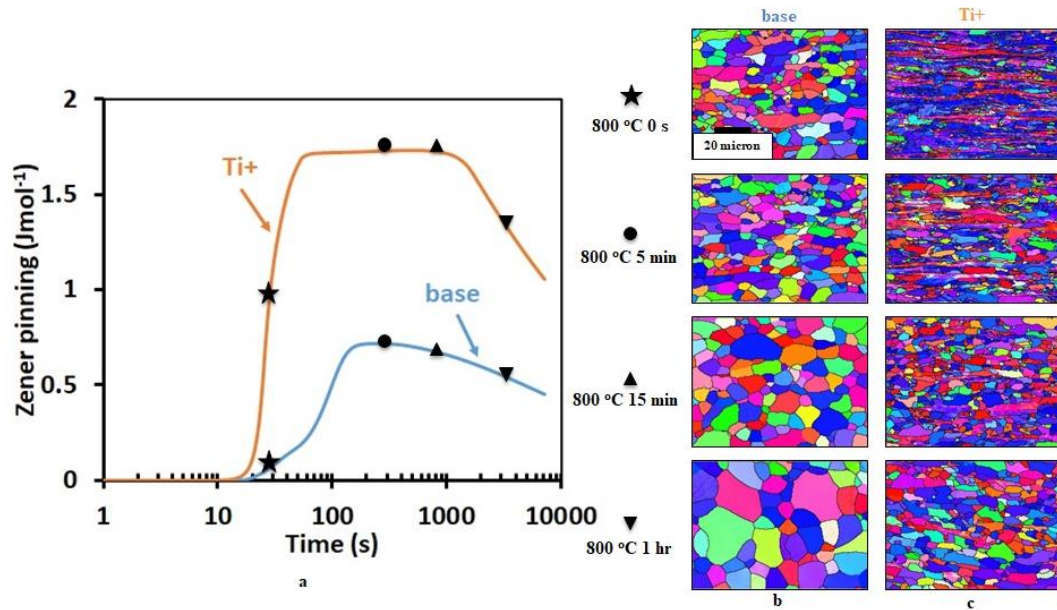


Fig. 6.1-3 Variation of numerically evaluated Zener pinning force with increase in annealing time of the base and Ti+ grades of steel (a), ND-IPF maps of base (b) and Ti+ (c) grades for annealing condition of 800 °C 0 s, 800 °C 5 min, 800 °C 15 min and 800 °C 1 hr . Annealing conditions: 800 °C 0 s, 800 °C 5 min, 800 °C 15 min and 800 °C 1 hr correspond numerically to time: 25 s, 325 s, 925 s and 3625 s respectively

The experimental value of Zener pinning force is evaluated for the base and Ti+ grades annealed at 800 °C 0 s condition for three different cases as explained below. For all the three cases, the experimental value of precipitate size and volume fraction are calculated after post-processing of STEM-EDS maps in ImageJ software. The pinning force is calculated for precipitate size range of 5 nm to 25 nm for a bin width of 5 nm.

First case: Average volume fraction (f) for each bin width is calculated to evaluate corresponding Zener pinning force (Fig. 6.1-4a).

Second case: Zener pinning force evaluated in first case is presented in a cumulative form (Fig. 6.1-4b).

Third case: To estimate maximum pinning force for each bin width, average volume fraction of precipitates of each bin width is assumed equal to average volume fraction of precipitates of complete precipitate data set. For each bin width, maximum precipitate pinning force is calculated and plotted in Fig. 6.1-4c. In the same plot, the pinning force is calculated for precipitate size range of 5 nm to 25 nm for constant precipitate volume fraction equal to equilibrium value. ThermoCalc and TCFE7 database predicts equilibrium precipitate volume fraction of 0.0019 and 0.0033 in the base and Ti+ grades respectively. The third case of maximum precipitate pinning force calculation can be correlated to a practical scenario of a cluster of high volume fraction of fine precipitates pinned along a dislocation or GB.

For each different case, the Zener pinning force in the Ti+ grade is higher than in the base grade. The Ti+ grade contains Ti and V as precipitating elements, while the base grade contains only V as a precipitating element. Moreover, solubility of Ti is lower than V in ferrite matrix. During annealing at 800 °C 0 s, a higher amount of (Ti,V)(C/N) precipitates out which results in higher precipitation pinning force in the Ti+ grade than in the base grade. From ND-IPF EBSD and STEM-EDS chemical maps it is observed that recrystallization and precipitation occur simultaneously in the base and Ti+ grades. For the base grade, precipitation is not significant enough to slow down recrystallization at 800 °C. While for the Ti+ grade, precipitation is significant enough to interfere with the grain boundary motion and result in sluggish recrystallization kinetics [96,109,205].

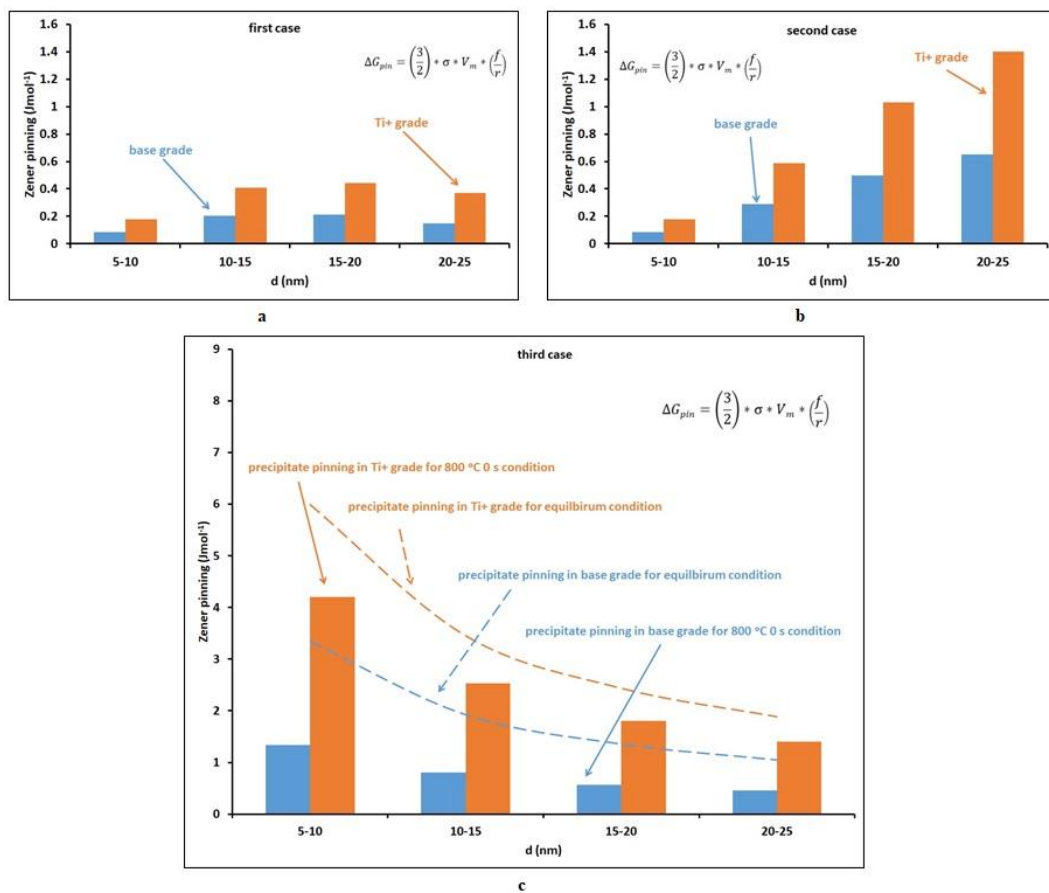


Fig. 6.1-4 Experimental value of Zener pinning force in the base and Ti+ grades for three different cases. Three different cases are explained in the above paragraph

6.1.3.2. Recrystallization and precipitation behaviour of the Ti+Mn+ grade

Ti+Mn+ grade has lower recrystallization (%) than the Ti+ grade at the annealing condition of 800 °C 0 s. For longer dwell times (> 0 s) at the annealing temperature of 800 °C, recrystallization behaviour of the Ti+ and Ti+Mn+ grades are similar. There is a difference in concentration of Mn solute atoms in the Ti+ grade (0.35 wt %) and the Ti+Mn+ grade (0.89 wt %). The cold-rolled texture contains strong alpha and gamma fibres with maximum

orientation density peak around $\{001\}\langle 110\rangle$ alpha fibre grain in the Ti+Mn+ grade and around $\{112\}\langle 110\rangle$ alpha fibre grain in the Ti+ grade (refer Fig. 5.7-1b, 5.7-1c and 5.7-2 in results chapter). It is well known that Mn solute atoms retard recrystallization kinetics by solute drag mechanism during annealing, when Mn solute atoms segregate along GB and exert solute drag force against its motion during annealing [153,188,189,243–246]. Higher amount of Mn solute atoms causes higher solute drag effect against dislocation and GB motion and could result in delay in nucleation for recrystallization in Ti+Mn+ grade for the annealing condition of 800 °C 0 s as compared to Ti+ grade. Fig. 6.1-5 shows a FIB-lift out STEM-EDS map of Mn segregation along microstructural defect in the Ti+Mn+ grade treated under the annealing condition of 800 °C 0 s.

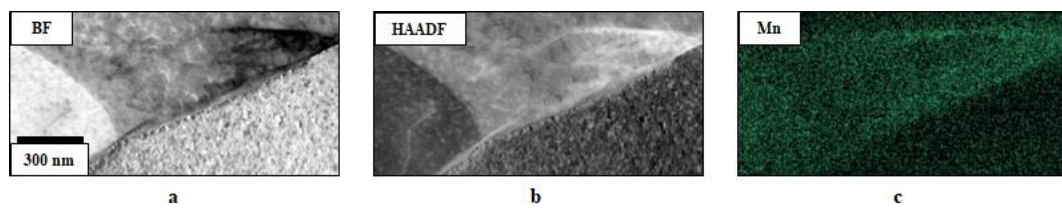


Fig. 6.1-5 STEM bright field (BF) (a), high-angle annular dark-field (HAADF) (b) images and EDS chemical map of Mn (c) of the Ti+Mn+ grade of steel annealed under the 800 °C 0 s condition

Ushioda et al. [188] have studied the role of Mn in delaying recovery during annealing, where dissolved C from cementite combines with Mn to form Mn-C complex. Mn-C complex or Mn-C dipole is formed by interaction (attractive) between Mn substitutional atoms and C interstitial atoms [328–331]. Interaction between the Mn substitutional atom and C interstitial atom is originated from the elastic-strain field around Mn substitutional atom in BCC Fe lattice [331,332]. Mn-C complex interferes with dislocation movement during recovery and leads to a delay in incubation time for recrystallization, i.e. nucleation of recrystallization is delayed. Moreover from the literature [120,305] it is known that $\{001\}\langle 110\rangle$ grains of alpha fibre have lower stored energy than $\{112\}\langle 110\rangle$ grains of alpha fibre. Therefore, the difference in maximum peak of texture intensity in cold-rolled state could also result in slower recrystallization kinetics of the Ti+Mn+ grade than the Ti+ grade for the annealing condition of 800 °C 0 s.

To understand in detail the significance of the solute drag, solute drag (SD) of Mn and intrinsic boundary friction (IBF) [182] are plotted against the boundary velocity of the Ti+ and Ti+Mn+ grades as shown in Fig. 6.1-6. Solute drag force (ΔG_{sd}) and intrinsic boundary friction force (ΔG_{IBF}) are calculated using equations as shown below:

$$\Delta G_{sd} = \frac{C_o * \alpha * v}{1 + \beta^2 * v^2} \quad (6.1-3)$$

$$\alpha = \frac{N_v * (k*T)^2 * \delta}{E_o * X} * \left(\sinh\left(\frac{E_o}{k*T}\right) - \left(\frac{E_o}{k*T}\right) \right) \quad (6.1-4)$$

$$\beta^2 = \frac{\alpha * k * T * \delta}{2 * N_v * E_o^2 * X} \quad (6.1-5)$$

$$\Delta G_{IBF} = \frac{v}{M_i} \quad (6.1-6)$$

$$M_i = \frac{2.63}{T} * e^{\left(\frac{-20754}{T}\right)} \quad (6.1-7)$$

Where, C_o is concentration of Mn solute atoms (0.0015 for the Ti+ grade and 0.0039 for the Ti+Mn+ grade), N_v is molar volume (value of $7 \times 10^{-6} \text{ m}^3/\text{mol}$), k is Boltzmann constant (value of $1.38 \times 10^{-23} \text{ m}^2 \text{ kgs}^{-2} \text{ K}^{-1}$), T is temperature (value of 1073 K), δ is grain boundary thickness (value of $5 \times 10^{-10} \text{ m}$, assumed two times of Burgers vector of Fe lattice), E_o is grain boundary interaction energy with atoms (value of $1.7608 \times 10^{-20} \text{ J/atoms}$), X is bulk diffusion constant (value of $0.000076 * \exp(-224400/R*T) \text{ m}^2/\text{s}$), v is grain boundary velocity, and M_i is intrinsic grain boundary mobility [46,58,112,182,203,325,333]. Detailed calculations of solute drag and intrinsic boundary friction can be found in the section 9.2 of supplementary information chapter.

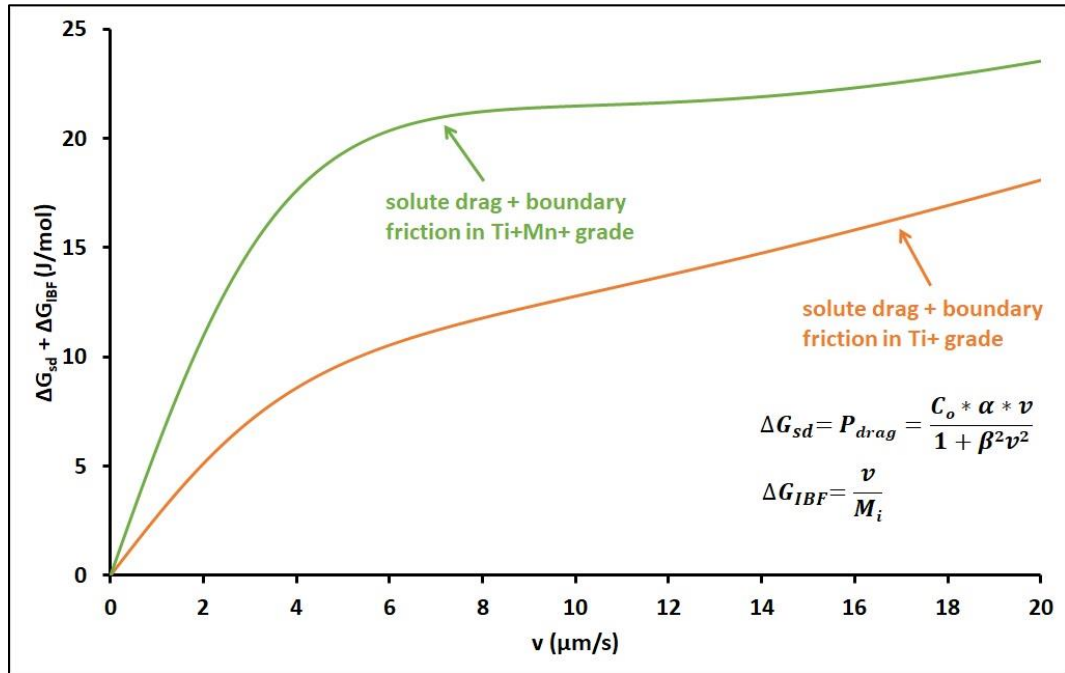


Fig. 6.1-6 Variation of effective drag i.e. combined solute drag (SD) and intrinsic boundary friction (IBF) with increase in grain boundary velocity during annealing for the Ti+ and Ti+Mn+ grades of steel

Effective drag ($\Delta G_{sd} + \Delta G_{IBF}$) by Mn solute atoms is higher in the Ti+Mn+ grade than the Ti+ grade due to higher amount of Mn solutes. The recrystallization behaviour of both grades is

sluggish, therefore the velocity of grain boundary is considerably low ($< 0.5 \mu\text{m/s}$, see below for this estimation of growth speed). For the annealing condition of 800°C 0 s , velocity of grain boundary is estimated using first order approximation as explained below [96].

Nucleation for recrystallization starts at 700°C 0 s in the Ti+ and Ti+Mn+ grades. The time to achieve the annealing temperature of 800°C is $\sim 15 \text{ s}$ (recorded by data logger during bulk annealing experiment). Average grain size at 800°C 0 s of the Ti+ and Ti+Mn+ grades is $3.4 \mu\text{m}$ and $2.65 \mu\text{m}$ respectively. From first order approximation value of average grain boundary velocity (average grain size/time) of the Ti+ and Ti+Mn+ grades is $\sim 0.23 \mu\text{m/s}$ and $\sim 0.18 \mu\text{m/s}$ respectively. For longer dwell time ($> 0 \text{ s}$), average grain boundary velocity would be lower than the previous value. From Mn solute drag versus boundary velocity plot in Fig. 6.1-6 it could be observed that drag effect of Mn solute on boundary mobility for longer dwell time ($> 0 \text{ s}$) is not significant in Ti+ and Ti+Mn+ grades and explains similar recrystallization behaviour for both grades.

Mn also affects precipitation kinetics in the austenite phase. It's proposed that higher amount of Mn solutes increases the solubility of TiC precipitate in austenite phase [185,186] and delays precipitation kinetics. The effect of Mn solute content on precipitation kinetics in austenite phase is well known [58,144,182–186], however there is not significant data published on Mn solute content effect on the precipitate solubility in the ferrite phase. The equilibrium precipitate volume fraction is plotted for the three grades for equilibrium state as shown in Fig. 6.1-7. There is negligible effect of Mn solute content on precipitation thermodynamics in ferrite phase of the Ti+ and Ti+Mn+ steel grades, when temperature is lower than 750°C . Mn can indirectly influence precipitation kinetics by segregating along dislocations and interfere with precipitation process in ferrite [182,188]. The role of Mn on precipitation kinetics in ferrite and interaction with C to form Mn-C complex requires better high-resolution experimental study utilising for example site specific APT investigations of Mn and C segregation in ferrite matrix and interaction of Mn solute atoms and precipitates along dislocations and grain boundaries.

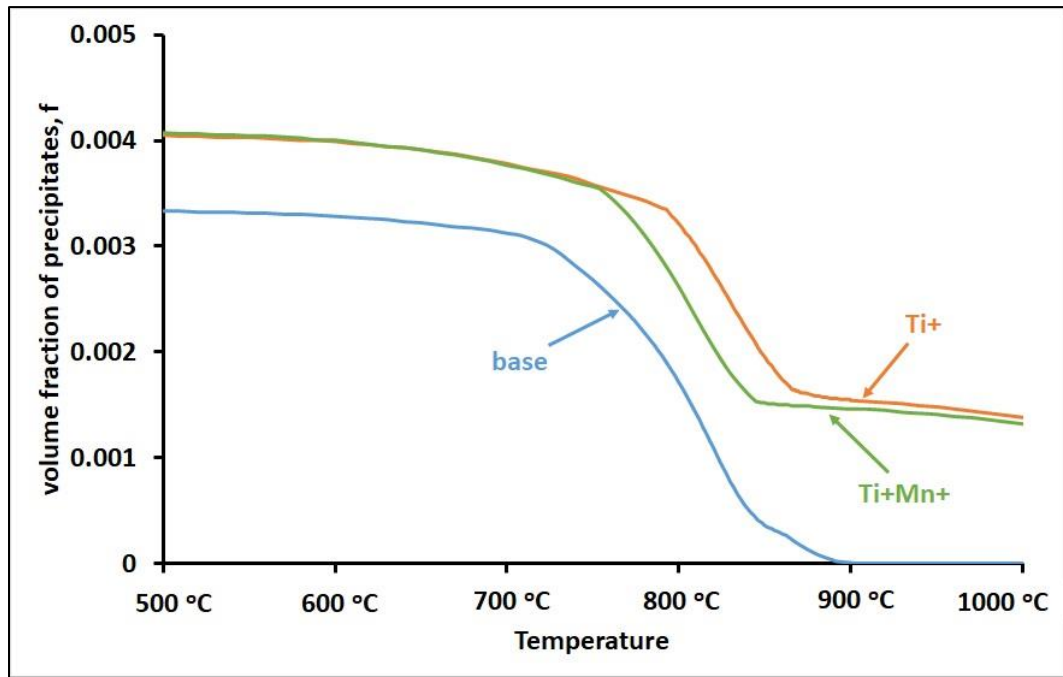


Fig. 6.1-7 Variation of volume fraction of precipitates with increase in temperature 500 °C to 1000 °C for the base, Ti+ and Ti+Mn+ grades of steel in equilibrium condition evaluated from ThermoCalc using TCFE9 database

6.1.4. Effect of different hot-rolled grain sizes on the recrystallization kinetics

Fine grain microstructures are expected to have higher recrystallization kinetics than coarse grain microstructures due to the higher number of statistically needed grain boundary nucleation sites per unit area for recrystallized grains and higher stored energy for further growth of recrystallized grains during annealing of cold-deformed samples [96]. In the hot-rolled state, the average grain size of steel grades is in the order of base (10 μm) > Ti+ (7 μm) > Ti+Mn+ (5 μm). Therefore, recrystallization kinetics should be highest in Ti+Mn+ grade and least in base grade in the absence of Ti-V precipitate pinning and Mn solute drag effect. From the results presented in this thesis, it could be observed that initiation and completion of recrystallization takes place earlier in the base grade as compared to Ti+ and Ti+Mn+ grades for annealing temperature of 800 °C. Effect of difference in initial grain size on the rate of progress of recrystallization is negligible. Average grain size difference between base and Ti+ grades (~ 3 μm) and Ti+ and Ti+Mn+ grades (~ 2 μm) are not significant as compared to available literature [44,220,229,237], where large difference in grain sizes (for example difference in average grain size of 35 μm [44], 72 μm [229] and greater than 200 μm [237]) have significant influence in the difference in recrystallization kinetics among different samples.

Sub-grain and grain boundaries not only form the favourable site for nucleation of recrystallized grains but also for precipitates to nucleate and grow [58]. Smaller average grain

size in hot-rolled Ti+ grade than hot-rolled base grade favours higher volume fraction of fine precipitates than base grade (Fig. 6.1-2) to nucleate along sub-grain and grain boundaries and resist their motion during annealing of cold-rolled steel samples. Combination of higher number of nucleation sites per unit area for precipitates and presence of Ti along with V microalloying precipitate elements in Ti+ and Ti+Mn+ grades lead to sluggish recrystallization kinetics.

Ti+ and Ti+Mn+ hot-rolled steel grades have similar average grain size $\sim 7 \mu\text{m}$ and $\sim 5 \mu\text{m}$ respectively. Additional Mn in Ti+Mn+ grade (0.89 wt. %) could lead to higher fraction of un-recrystallized pancaked austenite microstructure via solute drag than Ti+ grade and result in relatively finer ferrite grain size microstructure in hot-rolled state. During sub-critical annealing, recrystallization behaviour of Ti+ and Ti+Mn+ grades are very similar as discussed in sub-section 6.1.3.2 and therefore leads to similar average recrystallized ferrite grain size (Fig. 5.4-7) [219].

6.1.5. Evaluation of recrystallization fraction

Recrystallization fraction is evaluated using three different methods: LAM, aspect ratio and HV/1; all three methods show similar trends of increase for each grade. Values of recrystallized fraction obtained by the three methods for different annealing conditions are more or less in the order of LAM method > HV/1 > Aspect ratio. Matrix with LAM value of less than 1° is considered as recrystallized and greater than 1° is considered as un-recrystallized [35,96,251]. The LAM method does not take into account grain shape or size. Hardness of material depends upon dislocation density, therefore fractional change in hardness values is utilised to evaluate recrystallization fraction [249]. On the other hand, the aspect ratio method depends on the grain shape, where the aspect ratio of a deformed elongated grain present in partially recrystallized sample is usually greater than 3, while the aspect ratio of a spherical shaped grain formed during grain growth stage is ~ 1 . Therefore, the aspect ratio of a recrystallized grain is in between 1 to 3. For this study a tolerance value of the aspect ratio of 2.6 is set to distinguish recrystallized and un-recrystallized grains [295]. For recrystallization fraction evaluation, grains with aspect ratio lower than 2.6 are selected to designate the area fraction of recrystallized ferrite matrix. LAM, HV/1 and aspect ratio methods show similar trends in increment of recrystallization (%) of the base, Ti+ and Ti+Mn+ grades and quantitatively explains the highest recrystallization kinetics of the base grade during annealing.

6.1.6. Development of texture of furnace annealed samples

During cold-rolling, grains in polycrystals undergo rotation from less stable orientations towards more stable orientations to form texture [334,335]. The cold rolling texture of the investigated chemical compositions of the base and Ti+ grades mainly consists of alpha and

gamma fibres with the ODF density peaks at around $\{112\}\langle110\rangle$ and $\{111\}\langle110\rangle$. This texture is very similar to the typical cold rolling texture observed in body centred cubic metals. However, for the Ti+Mn+ grade, maximum peak of alpha fibre is found to be around $\{001\}\langle110\rangle$ grain orientation as shown in Fig. 6.1-8.

In Toroghinezhad et al. [315], dynamic strain aging and strain rate sensitivity were mentioned to explain Mn effect on warm rolling texture formation in low-carbon steel. It was mentioned that Mn, C and Cr form complex immobile atoms and retard the slip behaviour of dislocations on slip systems, causing the deformation to be more heterogeneous and increasing amount of shear bands. But Toroghinezhad et al. [315] observed that with increase in Mn, shear band intensity was reduced which is contrary to C, Cr and B and orientation density around $\{001\}\langle110\rangle$ grains was dominant in the deformed microstructure. The effect of Mn solute content on strength of orientation density around $\{001\}\langle110\rangle$ grain for room temperature cold-rolled deformation of steel has not been understood in detail.

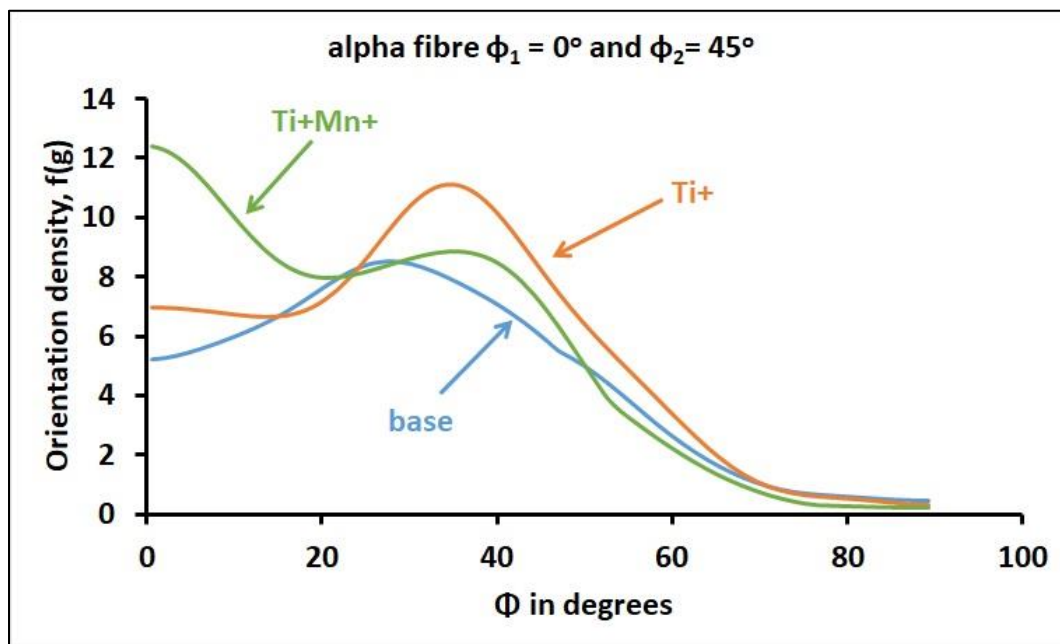


Fig. 6.1-8 Variation in orientation density of alpha fibre grains with increase in Φ from 0° to 90° for constant $\phi_2 = 45^\circ$ for the cold-rolled low-carbon microalloyed steel of base, Ti+ and Ti+Mn+ grades

For the annealing temperature of 800°C and dwell time of 0 s and longer, preferential nucleation of high stored energy gamma fibre grains is the favoured subgrain growth mechanism [224], which could be the possible reason for the strengthening of gamma fibre in recrystallized region of the Ti+ and Ti+Mn+ grades as shown in Fig. 5.7-1b and 5.7-1c respectively. Similarly, in the case of alpha fibre grains, preferential nucleation takes place first in higher stored energy grains, $\{111\}\langle110\rangle$ [216] and thus allows further growth in the

competitive process of annealing [216,336]. Another reason for the slower recrystallization kinetics of alpha fibre grains is related to the lattice curvature. Regions of sharp lattice curvature facilitates nucleation for recrystallization due to higher misorientations ($> 15^\circ$). In cold-rolled low-carbon steel, alpha fibre grains lack the sharp lattice curvature as compared to gamma fibre grains and therefore form much less potential sites for nucleation during annealing [337,338]. The above competition between different alpha fibre grains results in a drop in area fraction of $\{112\}\langle 110\rangle$ and $\{001\}\langle 110\rangle$ grains from $\sim 27\%$ and $\sim 11.8\%$ in the cold-rolled state to $\sim 7.5\%$ and $\sim 1.4\%$ in the annealed state for 800°C 0 s and to $\sim 10\%$ and $\sim 3.9\%$ in the annealed state for 800°C 2 min in the Ti+ grade respectively. Another possible reason for the decrease of the area fraction of $\{001\}\langle 110\rangle$ grains in the recrystallized matrix for annealing at 800°C could be the formation of $\{111\}\langle 121\rangle$ grains from one of the slip systems, $\{121\}\langle 111\rangle$ of $\{001\}\langle 110\rangle$ grains as was explained by Lee in his edge dislocation alignment model during annealing [339].

2D ODF map is plotted for Ti+Mn+ grade annealed at 800°C 2 hrs as shown in Fig. 6.1-9. 2D ODF map represents strong gamma fibre with negligible alpha fibre intensity which is in contrast to 2D ODF map (Fig. 5.7-1c) shown previously in section 5.7 of results chapter. Texture information obtained from XRD and EBSD are also different for the base grade annealed at 800°C 2 hrs. Due to significant grain growth, a lower amount of grains than required at least 1000 is present in the EBSD scans at low magnification of x200 to x500 of base grade annealed at 800°C 2 hrs, which unfortunately does not provide statistically significant texture information. However, cold-rolled texture results obtained from EBSD and XRD are similar to each other for the base, Ti+ and Ti+Mn+ steel grades.

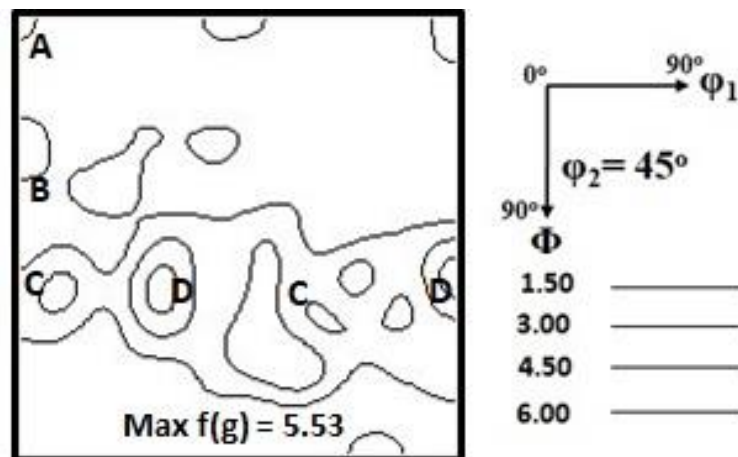


Fig. 6.1-9 ODF on the section $\phi_2=45^\circ$ texture map of the Ti+ grade steel annealed at the 800°C 2 hrs condition

Texture results obtained from EBSD map for cold-rolled condition and intermediate stages of recrystallization are reliable and close to bulk texture information obtained from XRD. For

grain growth stage (annealing condition of 800 °C 2 hrs), texture information obtained from XRD is more reliable than EBSD method. XRD method process higher volume fraction of grains to evaluate average texture information of the sample [340].

Development of gamma texture is stronger in the Ti+ and Ti+Mn+ grades than in the base grade during annealing. Ti and V microalloying elements decrease the content of interstitial elements (C and N) in solid solution state and minimises the chance of weak gamma texture in annealed steel [216]. Mn also affects recrystallized texture development in steels. Hu and Goodman [189] investigated the effect of Mn content on {111} texture development during annealing. With an increase in wt. % of Mn from 0.05 % to 0.56 % in low carbon steel, intensity of {111} texture decreases. Mn in solid solution state could delay recrystallization process of gamma fibre grains by solute drag [189] and give preferential advantage to lower stored energy grains of alpha fibre to nucleate and grow to recrystallized grains [216]. In this study, the intensity of gamma fibre is similar for fully recrystallized samples of the Ti+ and Ti+Mn+ grades for the annealing condition of 800 °C 2 hrs. Additional Mn content in the Ti+Mn+ grade does not have detrimental effect on gamma fibre development because of negligible solute drag effect on recrystallization as explained above in the sub-section 6.1.3.2.

6.2 Mechanical properties

6.2.1. Correlation between variation of nanoindentation hardness and GND density of muffle furnace annealed samples

Progress in recrystallization is accompanied with decrease in dislocation density [108]. In general, hardness is the contribution from solid solution strengthening of ferrite matrix, precipitation strengthening, dislocation strengthening and grain size strengthening. Change in hardness and dislocation density of the un-recrystallized ferrite matrix can be used to understand softening behaviour or recrystallization kinetics [35,250] among base, Ti+ and Ti+Mn+ grades during sub-critical annealing. From the average GND density and average nanoindentation hardness plots (Fig. 5.9-2 and 5.9-3), it could be observed that variation in nanoindentation hardness and average GND density values are in correlation with each other and explain the softening behaviour among different grades of steel for cold-rolled and annealed conditions of 700 °C 0 s, 800 °C 0 s and 800 °C 2 min. The drop in average GND density and average nanoindentation hardness of un-recrystallized ferrite matrix is highest in the base grade for different annealing conditions. Therefore, the trend in change in average nanoindentation hardness and average GND density confirms fastest softening rate of base grade as compared to other two grades, Ti+ and Ti+Mn+ for different conditions.

6.2.2. Combined strength evaluation for the base, Ti+ and Ti+Mn+ grades for the annealing condition of 800 °C 2 min

Strength and elongation properties of partially recrystallized steel is in between low strength - high elongation of fully recrystallized steel and high strength - low elongation cold-rolled steel [341]. Since the industrial annealing cycle is designed with the aim to reduce the cost of heating to its minimum, therefore the dwell time of the annealing cycle is generally preferred from 0 s to 2 min at the target temperature of ~ 800 °C. For the studied annealing condition of 800 °C 0 s, average elongation (%) of the Ti+ (3.5 %) and Ti+Mn+ (2 %) grades is low and is similar to the cold-rolled condition. For a longer dwell time of 2 min at 800 °C, average yield strength ($R_{0.2}$) and elongation (%) of the Ti+ grade are 560 MPa and 9 % respectively and of the Ti+Mn+ grade are 598 MPa and 7 % respectively.

In this context, strengthening contribution from dislocation density, grain size, inherent ferrite matrix, precipitate and solid solution of the base, Ti+ and Ti+Mn+ grades is evaluated for the annealing condition of 800 °C 2 min. The empirical relation to evaluate combined strength comprising of solid solution strength, inherent strength of matrix and grain refinement strength of ferritic microalloyed steel is given by Pickering et al. [342,343] (Equation 6.2-1):

$$\sigma_y(\text{MPa}) = 15.4(3.5 + 2.1[\%Mn] + 5.4[\%Si] + 23[\%N] + 1.13d^{-0.5}) \quad (6.2-1)$$

Where [%Mn], [%Si] and [%N] are the weight (%) of manganese, silicon and nitrogen in ferrite solution respectively and d is the average ferrite grain size in mm. For this study, free carbon and nitrogen are assumed to be negligible in the solid solution and are taken in combination with titanium and vanadium as carbides and nitrides for the annealing condition of 800 °C 2 min.

Average GND density is used in the equation 6.2-2 to evaluate dislocation density strength [89,102]:

$$\sigma_d = \alpha M \mu b \rho^{0.5} \quad (6.2-2)$$

Where α is a constant, M is average Taylor factor, μ is shear modulus, b is magnitude of the Burger's vector and ρ is dislocation density. Typical values for Fe ($\alpha \sim 0.3$, $M \sim 3$, $\mu \sim 75$ GPa and $b \sim 0.25$ nm) are used in equation 6.2-2. Average GND density of the base, Ti+ and Ti+Mn+ grades are $\sim 1.00E+13$ m⁻², $1.05E+14$ m⁻² and $1.15E+14$ m⁻² respectively. The detailed information on noise and GND density calculations are mentioned in section 9.1 of the supplementary information chapter.

Precipitation strengthening is evaluated using Ashby-Orowan equation [58]:

$$\sigma_p = 10.8 \frac{\sqrt{f}}{d} \ln \frac{d}{6.125 \times 10^{-4}} \quad (6.2-3)$$

Where f and d are average volume fraction and size of precipitate. Average precipitate size used in equation 6.2-3 is given in section 5.8 of results chapter. Average volume fraction of precipitates of the base, Ti+ and Ti+Mn+ grades for the annealing condition of 800 °C 2 min are ~ 0.002, ~ 0.003 and ~ 0.002 respectively. Solid solution strength, inherent strength of matrix, grain refinement strength, dislocation density strength and precipitation strength are added together to evaluate effective yield strength and compared with yield strength ($R_{0.2}$) from the tensile test of different grades as shown in Fig. 6.2-1.

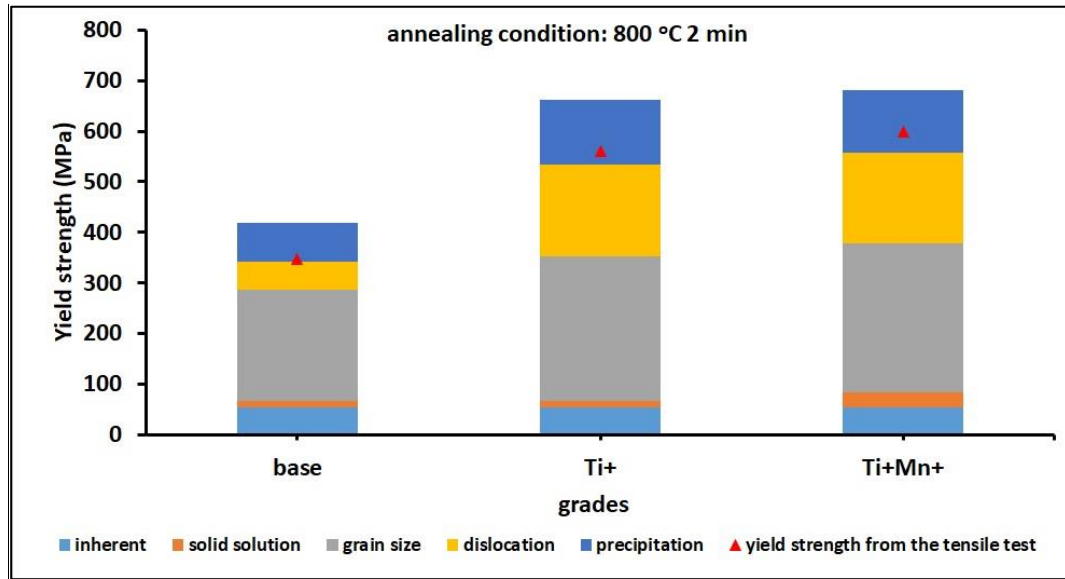


Fig. 6.2-1 Effective yield strength (combination of inherent, solid solution, grain size, dislocation, precipitation strength) and yield strength from the tensile test for the base, Ti+ and Ti+Mn+ grades of steel for the annealing condition of 800 °C 2 min

Grain size strengthening is dominant for the base, Ti+ and Ti+Mn+ grades of steel. High dislocation density ($\sim 10^{14} \text{ m}^{-2}$) in un-recrystallized ferrite matrix and fine precipitates lead to higher yield strength (200 MPa to 250 MPa) of the Ti+ and Ti+Mn+ grades than the base grade. Effective yield strength is about 16 % to 20 % higher than yield strength from the tensile test as shown in Fig. 6.2-1. For the grain size strengthening calculation, average recrystallized grain size is used in equation 6.2-1. Partially recrystallized matrix is a mixture of un-recrystallized elongated grains and quasi-polygonal recrystallized grains. It is assumed that average grain size of the partially recrystallized sample is equal to average recrystallized grain size [344] and could result in overestimation of grain size strengthening contribution. Higher contribution from grain size strengthening could further result in higher effective yield strength value than yield strength from the tensile test.

Precipitation strength in the base grade is lower than the other two grades for the annealing condition of 800 °C 2 min. Coarser average precipitate size and lower average volume fraction of V(C/N) in the base grade ($\sim 20 \text{ nm}$ and 0.002) than (Ti/V)(C/N) in the Ti+ grade ($\sim 14 \text{ nm}$

and 0.003) lead to lower precipitation strengthening in the base grade (Fig. 6.2-2). Similarly, a high volume fraction of very fine precipitates (~ 3 nm) in the hot-rolled commercial steel products of Tata Steel Europe, XPF 800 and XPF 1000 [10] and JFE Steel Corporations, NANOHITEN [283] lead to high precipitation strength of 400 MPa to 500 MPa. During phase transformation from austenite to ferrite, precipitates nucleate along dislocations, subgrain/grain boundaries and at the austenite to ferrite moving interphase [46]. By controlling the coiling temperature and sample chemistry, very fine (~ 5 nm) rows of interphase precipitates are developed to provide high precipitation strengthening [10,21]. During sub-critical annealing of cold-rolled low-carbon microalloyed steel, precipitates nucleate along dislocations and subgrain/grain boundaries. Controlling the dwell time of sub-critical annealing cycle to simultaneously obtain fine recrystallized grain and fine precipitates is challenging. Annealing time required to achieve fine fully recrystallized grains distribution in cold-rolled annealed steel can lead to precipitate coarsening and dislocation annihilation [31]. Coarse precipitates and low dislocation density in ferrite matrix result in low strength of steel.

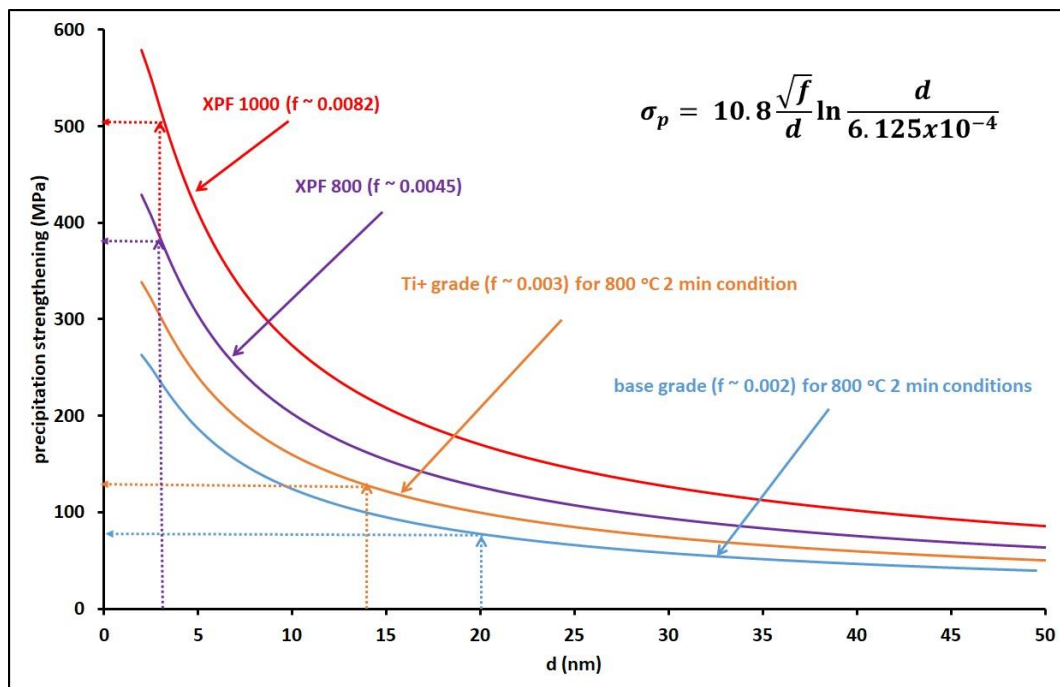


Fig. 6.2-2 Variation of precipitation strengthening with increase in precipitate size from 0 nm to 50 nm for cold-rolled annealed at 800 °C 2 min products, base and Ti+ grades of steel and Tata Steel's commercial hot-rolled products, XPF 800 and XPF 1000 grades of steel [10]. Notation 'f' stands for volume fraction of precipitates

6.2.3. Strength and ductility of the bulk annealed samples for different Tata Steel industrial designed cycles: A, B and C

Strength and ductility of the base, Ti+ and Ti+Mn+ grades are compared with DP and CP steel grades. Larger sized samples of the base, Ti+ and Ti+Mn+ grades are annealed for industrial

defined cycles A, B and C (Fig. 6.2-3) in a Continuous Annealing Simulator (CASim) and tensile strength and elongation (%) properties are plotted in a diagram as shown in Fig. 6.2-4. Strength and elongation (%) of the Ti+ and Ti+Mn+ grades are similar to each other for the three different annealing cycles: A, B and C. The longer dwell time of 2 min for annealing cycle B leads to a decrease in tensile strength (in the range of 740 MPa to 780 MPa) and increase in elongation (in the range of 7 % to 10 %) of the Ti+ and Ti+Mn+ grades as shown in Fig. 6.2-4. Due to incomplete recrystallization and coarse precipitation in the Ti+ and Ti+Mn+ grades, ductility (< 10 %) is poor and could not achieve level of strength (> 900 MPa) and ductility (> 10 %) as that of DP and martensitic steel grades.

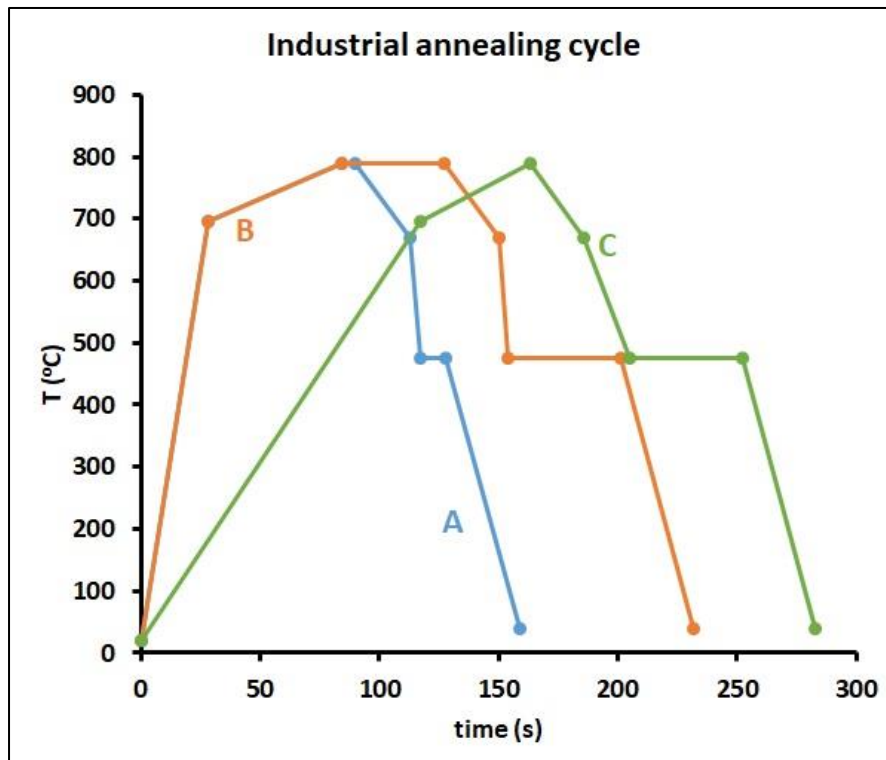


Fig. 6.2-3 Tata Steel industrial annealing cycles, A, B and C (permission from Tata Steel Europe)

Tensile strength and ductility of fully recrystallized cold-rolled continuously-annealed low-carbon microalloyed steel for automotive BIW applications is in the range of 300 - 600 MPa and 15 - 30 % respectively [13,24,341,345]. In Japanese automobile sector [346], high strength steel sheets of tensile strength value of 220 - 500 MPa and elongation (%) value of 30 - 50 % are used for outer panels, inner panels and other structural automotive body parts. High strength steel (TS > 600 MPa) sheet for automotive body applications such as for bumper reinforcement and door impact beam require moderate amount of ductility less than 20 % and 10 % respectively [341,346].

In general DP or martensitic [13] [347], or TWIP [348] or UHSS [349] steel grades are used for light-weighting automotive structures such as bumper or door impact beams which require high strength and moderate ductility properties. Recovered/partially recrystallized cold-rolled annealed steel with higher level of tensile strength (with slight decrease in cold-rolled strength) and moderate ductility properties are also used for automotive body parts which require high strength and small amount of formability [50,348–351]. Cold-rolled recovered annealed low-carbon microalloyed steel SAE J2340 series, commonly known as 120XF (TS = 883 MPa and EL (%) = 12 %), 135XF (TS = 985 MPa and EL (%) = 7 %) and 140XF (TS = 1028 MPa and EL (%) = 5.6 %) are used for light-weighting BIW applications (example bumper brackets, supports and reinforcing beams) [350,351]. Cold-rolled continuously-annealed thin gauge (~ 1 mm) Ti+ and Ti+Mn+ grades of high tensile strength (750 – 880 MPa) and moderate ductility (2 – 10 %) properties have the potential to be used in light-weighting automotive BIW applications where high strength and moderate ductility properties are required.

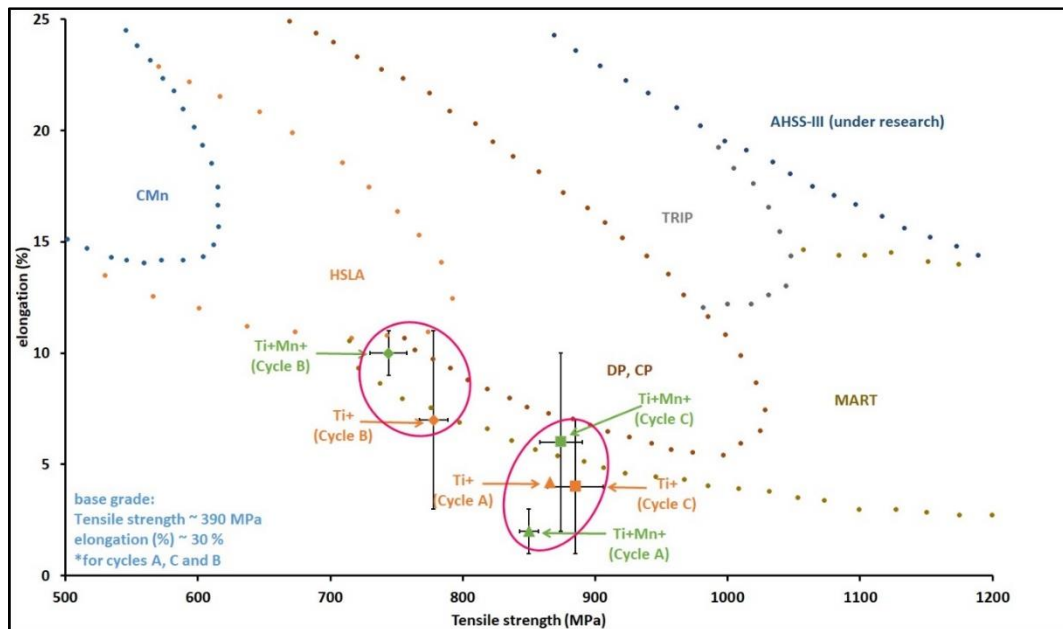


Fig. 6.2-4 Plot of elongation (%) and tensile strength properties of the base, Ti+ and Ti+Mn+ steel grades annealed for industrially simulated cycles, A, B and C in Continuous Annealing Simulator (CASim) on a AHSS elongation (%) versus tensile strength diagram. AHSS elongation (%) versus tensile strength diagram is reproduced after Hall [49])

6.3. Hot stage *quasi in-situ* EBSD study of the Ti+ grade steel

6.3.1. Role of alpha and gamma fibres during annealing

Average stored energy of gamma fibre (18.43 J/mol) is higher than alpha fibre (11.88 J/mol) in cold-rolled Ti+ grade. LAM approach is used to evaluate stored energy as a function of GND density [89] [96].

$$\Delta G_{SE} = 0.5 * \rho * \mu * b^2 * V_m \quad (6.3-1)$$

Where, ρ is dislocation density, μ is shear modulus, b is Burgers vector and V_m is molar volume. Average GND density is used in equation 6.3-1 for stored energy calculation. For cold-rolled Ti+ grade, average GND density of gamma and alpha fibres are $1.17E+15m^{-2}$ and $7.57E+14 m^{-2}$ respectively. Calculation of GND density is mentioned in section 9.1 of supplementary chapter. Typical values for Fe ($\mu \sim 75$ GPa, $b \sim 0.25$ nm and $V_m \sim 7.1E-6$ m³/mol) are used in equation 6.3-1.

Stored energy of alpha fibre grain orientations of cold-rolled (70 % reduction) low-carbon steel are calculated by Dillamore et al. [224] using TEM experiments and by Every and Hatherly [352] using X-ray Fourier analysis. Average stored energy of alpha fibre of cold-rolled low-carbon steel is estimated from stored energy versus alpha fibre grain orientation plots (refer Fig. 5 [63]) after Dillamore et al. [224] and Every and Hatherly [352] presented in Hutchinson's [63] research publication. Estimated average stored energy of alpha fibre of cold-rolled low-carbon steel is ~ 8.97 J/mol after Dillamore et al. [224] and ~ 8.55 J/mol after Every and Hatherly [352]. Average stored energy of alpha fibre evaluated by LAM approach as a function of GND density in this thesis is greater by 2 to 3 J/mol than estimated values after Dillamore et al. [224] and Every and Hatherly [352]. Stored energy evaluation by Dillamore et al. [224] approach considers only GNDs in subgrain boundaries and disregard stored energy contribution from dislocations present inside subgrains [89]. Stored energy evaluation by X-ray Fourier analysis performed by Every and Hatherly [352] consider only SSDs in their measurements [87]. Also, Betanda et al. [89] have shown that contribution of SSDs in stored energy evaluation of cold-rolled Fe-48% Ni steel is only ~ 8 % of total stored energy value. Since stored energy evaluation by LAM approach considers GNDs within subgrains and subgrain boundaries [89], therefore calculated average stored energy of alpha fibre of cold-rolled Ti+ grade by LAM approach is higher than estimated average stored energy values measured after Dillamore et al. [224] and Every and Hatherly [352].

Wauthier-Monnin et al. [87] have studied dislocation density evolution in different alpha and gamma fibre grain orientations with increase in cold-rolling strain (%) of low-carbon steel by XRD approach. Average dislocation density of alpha ($4.42E+15 m^{-2}$) and gamma ($5.31E+15 m^{-2}$) fibres of cold-rolled (70 % deformed) low-carbon steel (Table 6.3-1) are estimated from the plot of dislocation density versus rolling strain (%) (refer Fig. 9 [87]) presented in Wauthier-Monnin et al. [87] research publication. Dislocation density measurements by XRD approach performed by Wauthier-Monnin et al. [87] consider both GND and SSD. Therefore, estimated average dislocation density of alpha ($4.42E+15 m^{-2}$) and gamma ($5.31E+15 m^{-2}$) fibres of cold-rolled low-carbon steel after Wauthier-Monnin et al. [87] is higher than

dislocation density of alpha ($7.57\text{E}+14\text{ m}^{-2}$) and gamma ($1.17\text{E}+15\text{m}^{-2}$) fibres of cold-rolled Ti+ grade measured by LAM approach [89].

In order to further understand the difference in evolution of average GND density in un-recrystallized and recrystallized portions of alpha and gamma fibres and its role on the recrystallization mechanism under different annealing conditions, average GND density and recrystallization (%) are calculated and plotted for respective fibres [35]. Numerical values of average GND density of alpha and gamma fibres of Ti+ grade for cold-rolled and annealed conditions of $700\text{ }^{\circ}\text{C}$ 0 s, $800\text{ }^{\circ}\text{C}$ 0 s and $800\text{ }^{\circ}\text{C}$ 2 min are also presented in Table 6.3-1. In Fig. 6.3-1a it can be observed that the average GND density is higher in the un-recrystallized portion as compared to recrystallized region. For the annealing condition of $700\text{ }^{\circ}\text{C}$ 0 s, the decrease in average GND density is higher in un-recrystallized gamma fibre texture ($3.0\text{E}+14\text{m}^{-2}$) compared to un-recrystallized alpha fibre texture ($1.1\text{E}+14\text{m}^{-2}$). With a further increase in temperature to $800\text{ }^{\circ}\text{C}$ and dwell time from 0 s to 2 min, average GND density decreases due to static recovery. The drop in average GND density is higher for un-recrystallized gamma fibre grains ($6.2\text{E} +14\text{m}^{-2}$ for $800\text{ }^{\circ}\text{C}$ 0 s and $9.8\text{E}+14\text{m}^{-2}$ for $800\text{ }^{\circ}\text{C}$ 2 min) than for un-recrystallized alpha fibre grains ($1.4\text{E}+14\text{m}^{-2}$ for $800\text{ }^{\circ}\text{C}$ 0 s and $4.5\text{E}+14\text{m}^{-2}$ for $800\text{ }^{\circ}\text{C}$ 2 min). The smaller drop in the mean GND density of un-recrystallized alpha fibre from the cold-rolled state to annealed state at $700\text{ }^{\circ}\text{C}$ 0 s, $800\text{ }^{\circ}\text{C}$ 0 s and $800\text{ }^{\circ}\text{C}$ 2 min in Fig. 6.3-1a indicates that the extent of static recovery is negligible in this fibre. But the results of larger drop in mean GND density for un-recrystallized gamma fibre imply that static recovery is much faster and readily occurred even at annealing state $700\text{ }^{\circ}\text{C}$ 0 s. For recrystallized grains of alpha and gamma fibre orientation, average GND density value is about $4.5\text{E}+13\text{m}^{-2}$, which is as expected considerably lower than for the un-recrystallized matrix.

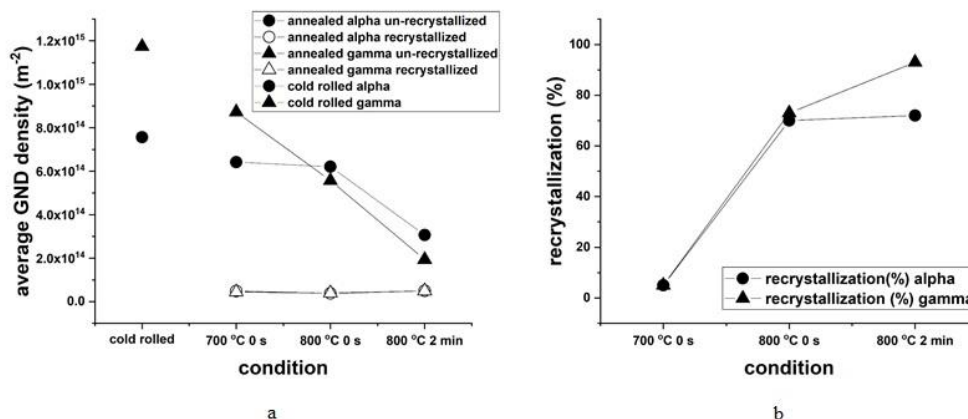


Fig. 6.3-1 Average GND density plot for cold-rolled alpha and gamma fibres and recrystallized and un-recrystallized matrix (grains) of alpha and gamma fibres at different annealing conditions (a). Fig. 6.3-1b shows recrystallization (%) of alpha and gamma matrix (grains) at different annealing conditions for low-carbon microalloyed steel of Ti+ grade

Table 6.3-1 Average GND density of cold-rolled alpha and gamma fibres and un-recrystallized and recrystallized matrix of alpha and gamma fibres at different annealing conditions

Conditions	Average GND density (m^{-2})			
	Un-recrystallized matrix		Recrystallized matrix	
	Alpha fibre	Gamma fibre	Alpha fibre	Gamma fibre
Cold-rolled	7.57E+14 m^{-2} *4.42E+15 m^{-2} [87]	1.17E+15 m^{-2} *5.31E+15 m^{-2} [87]	-	-
700 °C 0 s	6.42E+14 m^{-2}	8.72E+14 m^{-2}	4.84E+13 m^{-2}	4.42E+13 m^{-2}
800 °C 0 s	6.21E+14 m^{-2}	5.57E+14 m^{-2}	3.80E+13 m^{-2}	3.92E+13 m^{-2}
800 °C 2 min	3.07E+14 m^{-2}	1.94E+14 m^{-2}	4.98E+13 m^{-2}	4.95E+13 m^{-2}

*dislocation density (GND + SSD) [87]

Similarly with an increase in the heat input from 700 °C 0 s to 800 °C 2 min, recrystallization (%) for both fibres have increased. From qualitative ND-IPF maps in Fig. 5.6-2 and quantitative average GND (m^{-2}) density and recrystallization (%) results shown in Fig. 6.3-1a and 6.3-1b respectively, it could be observed that due to the higher initial stored energy in the cold-rolled gamma fibre, as compared to the cold-rolled alpha fibre, drop in the average GND density and increase in the recrystallization fraction (%) is higher in the case of gamma fibre grains. Annealing at 800 °C with an increase in dwell time from 0 s to 2 min results in negligible increment in recrystallization (%) (from 70% to 72%) for alpha fibre grains, while for gamma fibre grains increment in recrystallization (%) is significant (from 73% to 93%). The above measured recrystallized fractions in alpha and gamma fibres imply that fine precipitates of (Ti,V)(C/N) probably pinned recrystallized alpha grains from 0 s to 2 min at 800 °C, while they cannot stop the recrystallization of gamma fibre grains. Sinclair et al. [313] investigated recrystallized texture development in Ti-microalloyed cold-rolled ferritic stainless steel during subcritical annealing. Fine (10 – 50 nm) Ti(C/N) precipitates are preferentially located along the alpha fibre grain boundaries parallel to ND (region of larger orientation gradient). Fine precipitates pinned along alpha-alpha and alpha-gamma inhibit the growth of nucleated recrystallized grains during annealing. The experimental and simulation work on the precipitation of complex $\text{Ti}_y\text{V}_{1-y}\text{C}$ in this thesis also shows that before recrystallization can readily start (800 °C 0 s), a lot of precipitates (about 15 % to 30 % with

10 nm diameter) already form on the dislocations in the deformed microstructure. These fine precipitates probably pin the recrystallization behaviour of those alpha grains with low stored energy. The combination of lower stored energy and preferential pinning of alpha fibre resulted in sluggish recrystallization kinetics of alpha fibre grains, as observed in Fig 6.3-1b.

6.3.2. Reliability of hot stage *quasi in-situ* EBSD

Since the surrounding boundary conditions of a free surface microstructure are different from the interior bulk microstructure, such as that the surface microstructure is exposed to a gas (of pressure, $P \sim 5 \times 10^{-6}$ mbar) inside the SEM chamber [140], it is important to discuss the differences or similarities in recrystallized microstructure development on the surface and in the interior of the sample for the same annealing conditions. To investigate the above case, hot stage *quasi in-situ* EBSD samples were polished down to $\sim 300 \mu\text{m}$ along transverse direction (TD) and high magnification ($\times 5\text{k}$) EBSD scans were performed on annealed samples. The microstructure on the surface and in the interior of the hot stage *quasi in-situ* EBSD sample is very similar qualitatively to each other after annealing for three different conditions, 700°C 0 s, 800°C 0 s and 800°C 2 min as shown in the results chapter in Figs. 5.6-1b, 5.6-2c and 5.6-2d (surface) and discussion chapter in Figs. 6.3-2a, 6.3-2b and 6.3-2c (interior) respectively. Recrystallized grains are quasi-polygonal for both surface and interior of annealed samples. For annealing condition of 700°C 0 s, negligible nucleation could be observed even inside the sample as shown in Fig. 6.3-1a, which further confirms that an annealing temperature of 700°C with no dwell is not sufficient for complete recrystallization. Presence of un-recrystallized alpha fibre grains for the annealing conditions of 800°C 0 s and 800°C 2 min in Fig. 6.3-2b and 6.3-2c respectively confirms that the slower recrystallization kinetics of the alpha fibre grains is not only observed on the surface but also inside the bulk.

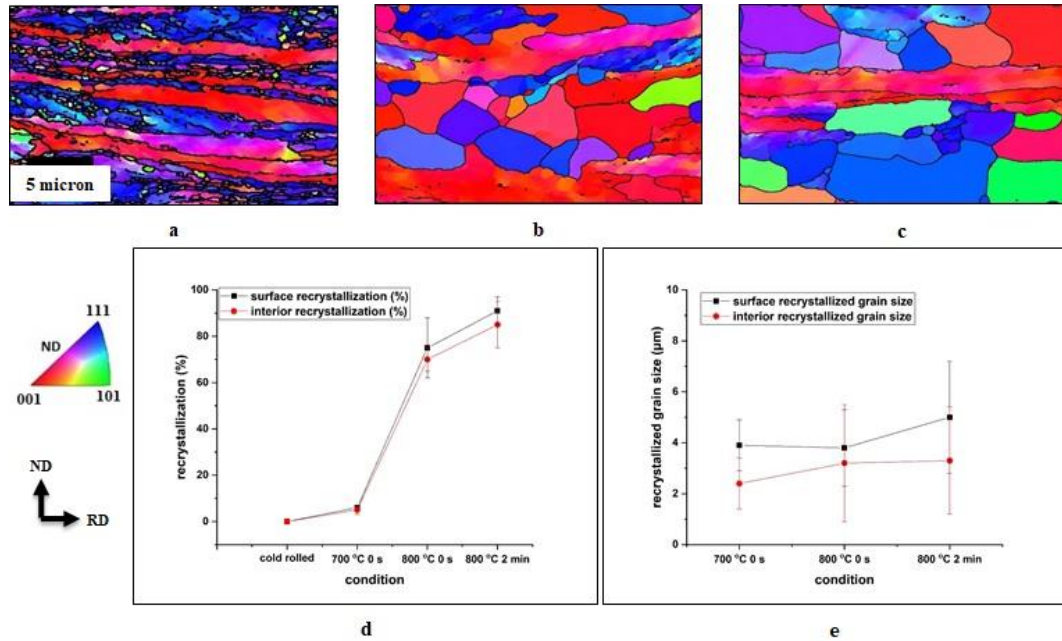


Fig. 6.3-2 Normal Direction Inverse Pole Figure (ND-IPF) maps of interior microstructure of hot stage quasi in-situ samples of Ti+ grade steel for three annealing conditions: 700 °C 0 s (a), 800 °C 0 s (b) and 800 °C 2 min (c). Fraction recrystallized (%) (d) and recrystallized grain size (μm) (e) quantified on surface and interior microstructure of hot stage quasi in-situ samples for cold-rolled state and annealed states obtained at different annealing conditions

Since qualitatively there is not any significant effect of the free surface on the recrystallized microstructural development, to further understand quantitatively the difference in recrystallized microstructure on the surface and in the interior, recrystallization (%) and average recrystallized grain size are plotted as shown in Fig. 6.3-2d and 6.3-2e respectively. Average recrystallized grain size on the surface is about 1.2 to 1.6 times coarser compared to the interior of the sample for the same annealing conditions. Average recrystallization (%) is higher by 5 % for the surface compared to the interior of the sample for the annealing condition of 800 °C 0 s and 800 °C 2 min. From the above quantified results, it could be seen that the values for recrystallization (%) and grain size are within the standard deviation for the surface and the interior but with a slight increase in average values for the surface, possibly due to the following factors: easier shape deformation on the free surface as compared to the bulk [294,353], temperature gradient from surface to interior, the free surface energy [125,140], or absence of recrystallized grains which would nucleate above the free surface [128,133,354,355]. Mullins had previously discussed the effect of free surface on grain growth, and it was mentioned that as the surface microstructures are exposed to the gas, there are various free surface energies associated with grain boundary movement. Grains of higher surface free energy could be consumed by grains of lower free surface energy and lead to grain coarsening [140]. Moreover, during annealing using hot stage EBSD most of the recrystallized

nuclei are formed below the surface and then grow to reach the free surface [128,133,354,355]. Therefore, by the end of the annealing process, the number of recrystallized grains on the surface would be statistically half as many as in the interior. Hence, average recrystallized grain area on the surface would be almost double compared to the interior, and the average recrystallized grain size about 1.4 times larger than the recrystallized grain size in the interior, which also agrees with the results shown in Fig. 6.3-2e. Overall, from both qualitative and quantitative results no significant deviation in recrystallized microstructural development on the surface and in the interior of the annealed sample was evident, which is consistent with the observations from other researchers [125] [133].

7. Further work

Based on the research investigations carried out in this PhD, certain areas that could be explored in future are mentioned below.

7.1. Academic insight

1. In this PhD work, it is shown both qualitatively and quantitatively that the recrystallization behaviour of alpha fibre grains is sluggish both on the surface and inside the material during sub-critical annealing of the cold-rolled low-carbon microalloyed steel of the Ti+ grade. It is important to understand preferential nucleation sites of precipitates along different textural orientations, i.e. whether precipitates are preferentially nucleating along alpha/alpha or alpha/gamma or gamma/other orientations or alpha/other orientation boundary. To understand preferential nucleation sites of precipitates, correlative study [356,357] using EBSD and STEM would be required.

2. Ti+Mn+ grade containing 0.89 wt. % of Mn has maximum texture intensity peak around $\{001\}\langle 110\rangle$ alpha fibre grains in the cold-rolled condition. While the other two grades, base and Ti+ containing less wt. % of Mn ~ 0.35 % show maximum texture intensity peak around $\{112\}\langle 110\rangle$ alpha fibre grains in the cold-rolled state. The difference in initial cold-rolled texture influences recovery and recrystallization behaviour during annealing. Therefore, it is important to understand the effect of Mn wt. % on cold-rolled texture development. To carry out the investigation, series of fixed number of cold-rolled samples need to be prepared with similar chemistry as that of Ti+ grade but with varying wt. % of Mn (0 %, 0.5 %, 1 %, 1.5 % and 2 %) for low (30 %) and high (70 %) cold-rolled deformation (%) states. Either XRD or EBSD experiment could be performed to study bulk texture of the sample for different conditions: cold-rolled, 700 °C 0 s, 800 °C 0 s and 800 °C 2 min to understand the influence of Mn on the development of cold-rolled and recrystallized texture.

3. The early stage of precipitation for annealing condition of 700 °C 0 s is very fine and closely spaced to each other which makes the morphological study of precipitates difficult in STEM. Combination of HR-TEM and APT is efficient in performing site specific qualitative studies of the nature of precipitates i.e. either cluster of atoms or coherent precipitate with a definite crystal lattice [166]. Sample could be further analysed in SANS for acquiring bulk-scale quantitative information of precipitates [149].

7.2. Industrial perspective

1. The idea of cold-rolled supersaturated ferrite phase matrix originated from Tata Steel Europe successful commercial hot-rolled product, XPF. Precipitation strengthening of the base, Ti+ and Ti+Mn+ grades for the annealing condition of 800 °C 2 min is less than the hot-rolled steel products because of coarse precipitation. Moreover, mechanical properties of the

Ti+ and Ti+Mn+ grades are not comparable to DP and CP grades due to partially recrystallized ferrite matrix and coarse precipitation. Two possible metallurgical routes to develop annealed material with similar mechanical properties to that of DP and CP steel grades are suggested and mentioned below.

- Perform inter-critical annealing of the cold-rolled microalloyed steel grades to transform low volume fraction of ferrite phase (5 % to 10 %) to austenite phase and then cool down to form final microstructure comprising of low volume fraction (5 % to 10 %) of martensite phase and higher volume fraction of very fine random precipitates in recrystallized ferrite matrix.
- Perform inter-critical annealing of the cold-rolled microalloyed steel grades to completely transform ferrite phase to austenite phase and then cool down to room temperature to have very fine interphase and random precipitates in ferrite matrix formed during coiling.

Both metallurgical routes require set of trials with various defined heating and cooling parameters and subsequent microstructure and mechanical investigations.

8. Conclusions

Three cold-rolled low-carbon microalloyed steel grades, base, Ti+ and Ti+Mn+ were investigated in this study. Difference in recrystallization behaviour, recrystallized texture development, recrystallization-precipitation interaction and mechanical properties were studied during sub-critical annealing. Hot-stage *quasi* in-situ analysis of the evolution of GND density in alpha and gamma fibres was carried out to quantify the difference in recrystallization kinetics of alpha and gamma fibres during sub-critical annealing. Based on the results and discussions, conclusions are summarised below:

8.1. Recrystallization and textural behaviour

1. Recrystallization kinetics is fastest in the base grade as compared to the Ti+ and Ti+Mn+ grades. Presence of additional Ti-microalloying element along with V in Ti+ and Ti+Mn+ grades is effective in retarding the recrystallization process during sub-critical annealing.
2. Higher intensity of {001}<110> grain orientation and additional Mn solute atoms in the Ti+Mn+ grade leads to a slower recovery rate as compared to the base and Ti+ grades under the annealing condition of 800 °C 0 s.
3. There is insignificant difference observed in recrystallization kinetics between the Ti+ and Ti+Mn+ grades for longer dwell time (> 0 s) at the annealing temperature of 800 °C. The solute drag effect by additional Mn solute atoms on recrystallization kinetics of the Ti+Mn+ grade is negligible due to sluggish subgrain/grain boundary movement.
4. For fully recrystallized ferrite matrix, intensity of gamma texture is weaker in the base grade than the Ti+ and Ti+Mn+ grades. Additional Ti-microalloying element along with V in Ti+ and Ti+Mn+ grades favours stronger gamma texture.

8.2. Hot-stage *quasi* in-situ EBSD

1. Evaluating average GND density from the same region indicates a slower recovery rate in alpha fibre than in gamma fibre for the annealing conditions of 700 °C 0 s, 800 °C 0 s and 800 °C 2 min.
2. At the lower annealing temperature of 700 °C with no dwell, nucleation of recrystallization has initiated both on surface and in the interior of hot stage *quasi* in-situ annealed samples but the temperature and dwell time are not sufficient for full recovery and recrystallization. With longer dwell time above 2 min at 800 °C recrystallization has progressed with higher recrystallization fraction in gamma fibre grains as compared to alpha fibre grains of the Ti+ grade. The minor increase in the recrystallized fraction of alpha fibre from 0 s to 2 min at 800 °C implies that fine precipitates probably pinned recrystallized grains. The pinning force however did not stop the recrystallization behaviour of gamma fibre grains. Additionally, due

to lower stored energy and lack of sharp lattice curvature in alpha fibre, recovery and recrystallization time is longer for alpha fibre than for gamma fibre.

3. In this study, there is no significant difference in the microstructure on the surface and the interior of hot stage *quasi* in-situ EBSD annealed samples, only minor difference is that the average recrystallized fraction is slightly higher on the sample surface than in the sample interiors.

8.3. Industrial implications

1. Coarsening of precipitates during sub-critical annealing of the base, Ti+ and Ti+Mn+ grades leads to lower precipitation strengthening as compared to the hot-rolled steel grades of XPF 800, XPF 1000 and NANOHTEN, where higher precipitation strengthening is achieved by very fine (~ 3 nm) interphase precipitation.

2. Precipitation pinning potential is higher for the Ti+ grade than for base grade due to the presence of additional Ti-microalloying element along with V in the Ti+ grade.

3. Ti+ and Ti+Mn+ grades after annealing under industrial cycles A, B and C are lower on strength and ductility balance comparable to multiphase steel such as DP and CP grades due to partially recrystallized ferrite matrix and coarse precipitates.

4. Cold-rolled annealed partially recrystallized steel grades, Ti+ and Ti+Mn+ of high strength (750 – 880 MPa) with moderate ductility (2 – 10 %) have the potentiality to be used in BIW parts for high strength and moderate ductility applications.

5. Although Ti+ and Ti+Mn+ steel grades are lower on strength and ductility balance compared to DP and CP steels, it is an interesting industrial alloy with cost benefits as compared to multiphase steel grades but needs further development via intercritical annealing.

8.4. Development of the Methodology

1. LAM, HV/1 and aspect ratio methods show similar trends in increment in recrystallization (%) of the base, Ti+ and Ti+Mn+ grades.

2. Bulk texture analysis using EBSD post-processed data is largely dependent upon the number of grains taken into consideration. EBSD gives reliable texture information for the cold-rolled and intermediate stages of the recrystallization process. For advanced grain growth conditions i.e. for the annealing condition of 800 °C 2 hrs, bulk texture analysis using XRD gives accurate information.

3. Correlative and quasi in-situ material characterisation techniques such as room temperature EBSD, nanoindentation-EBSD, STEM, hot-stage *quasi* in-situ EBSD and mechanical testing allow to quantify recrystallization behaviour, texture development and precipitation-

recrystallization interactions in novel steel grades to optimise their response for advanced applications.

9. Supplementary information

9.1. Calculation of geometrically necessary dislocation (GND) density

EBSD data is obtained from Channel 5 software of Oxford Instruments in the form of .ctf file. File is exported to MTEX texture analysis toolbox, MTEX-4.5.0 available in MATLAB R2016b (<http://mtex-toolbox.github.io/>) for GND density post-processing. Misorientation value is extracted from alpha and gamma fibre grains and fed back to equation 9.1-1 to evaluate corresponding GND density:

$$\rho_{GND} = \frac{2\theta}{ub} \quad (9.1-1)$$

Where, θ is misorientation angle, ρ_{GND} is GND density, b is scalar value of Burgers vector and u is the unit length.

To evaluate the average GND density of a respective grain orientation, a rectangular box is drawn inside the grain of interest. Multiple boxes (typically in the range from 1 to 10) are constructed inside the grain to include sufficient amount of LAM data associated with each pixel. Rectangular boxes are constructed both at the centre and in regions close to the grain boundary, but excluding the grain boundary, to consider the dislocation density of a respective grain orientation. The rectangular box is not drawn across grain boundaries because the dislocation density information associated with the grain boundary would not reflect average GND density of a particular grain orientation. HAGB is an interface which is reflected as a jump in LAM value across one grain to another and therefore construction of rectangular box across it is omitted in this study [358]. The equation used in MATLAB code to draw a rectangle is mentioned below:

$$\text{region} = [x_0 \ y_0 \ L \ W]*1; \quad (9.1-2)$$

Where, x_0 and y_0 are co-ordinates and L and W are dimensions of the rectangle. Fig. 9.1-1 shows an example of the rectangle drawn over alpha fibre (grain orientation spread around $\{112\}\langle 110\rangle$). Misorientation value is extracted from each pixel within the rectangular area to evaluate average GND density.

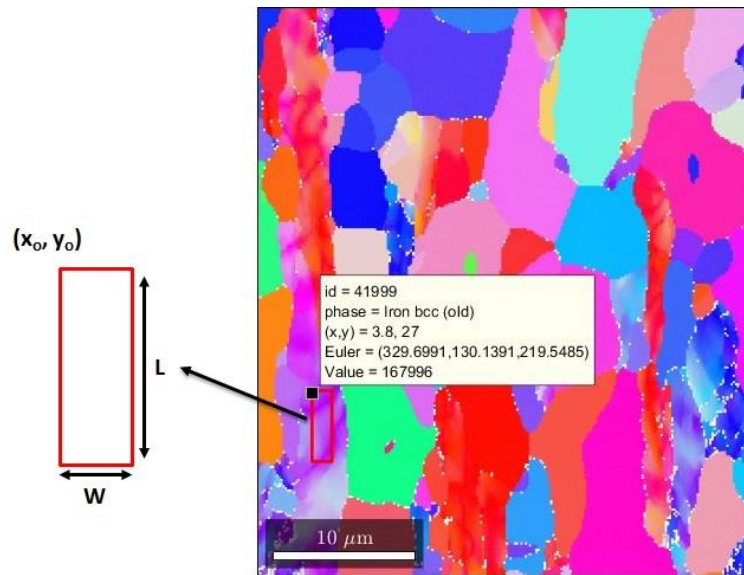


Fig. 9.1-1 Normal Direction Inverse Pole Figure (ND-IPF) map of annealed sample of Ti+ grade for 800 °C 0 s condition obtained from MTEX toolbox available in MATLAB R2016b (<http://mtex-toolbox.github.io/>). Red rectangle diagram is drawn to extract misorientation data from the area of interest in the EBSD image

Before calculating GND density, noise is removed from the misorientation value for each pixel. Noise is calculated based on the method used by previous researchers [297,359]. Average misorientation values are obtained for a same EBSD scanned map for five different filter types (3 x 3; 5 x 5; 7 x 7; 9 x 9 and 11 x 11). Corresponding average LAM values are plotted against different filter sizes and extrapolated to estimate average LAM value at the origin. In ideal case, misorientation value at origin should be zero. In the case of noise there is a non-zero value at origin. Fig. 9.1-2 represents different filter types 3 x 3 (first neighbour, $n = 1$) to 11 x 11 (fifth neighbour, $n = 5$). For step size (u) of 0.15 μm , value of 'x' for first neighbour is 0.15 μm .

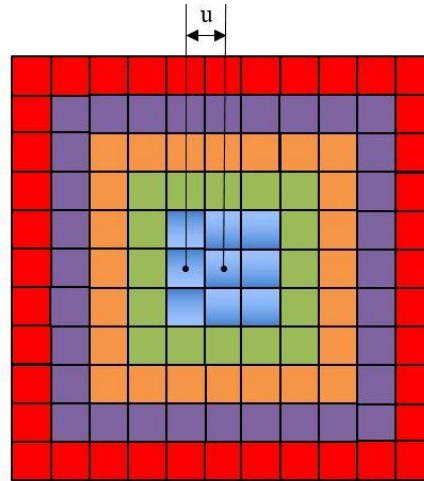


Fig. 9.1-2 Pixels of different square filter type. Blue colour for 3 x 3 filter type, green colour for 5 x 5 filter type, orange colour for 7 x 7 filter type, violet colour for 9 x 9 filter type and red colour for 11 x 11 filter type. Notation 'u' indicates step size used for EBSD scan

The average LAM value is evaluated (Fig. 9.1-3) for different filter types (3 x 3; 5 x 5; 7 x 7; 9 x 9 and 11 x 11) for three different sites (1, 2 and 3) from deformed ferrite matrix of annealed sample of Ti+ grade for 800 °C 0 s condition. Average LAM values at the origin for three different sites, 1, 2 and 3 are 0.41°, 0.85° and 0.87° respectively. Therefore average LAM value of a deformed matrix is ~ 0.71°.

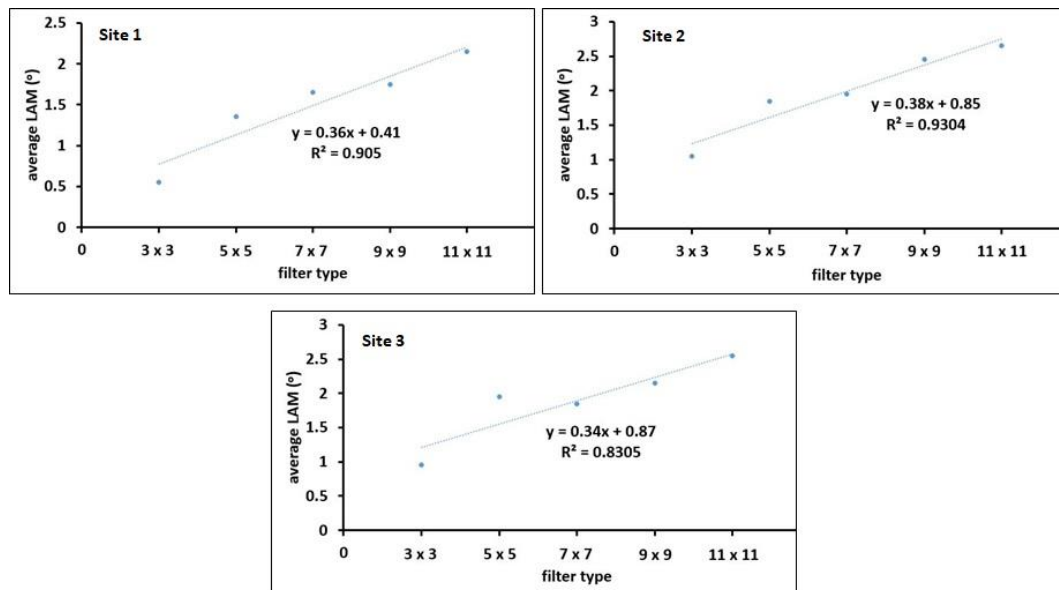


Fig. 9.1-3 Average local average misorientation (LAM) versus different filter types (3 x 3, 5 x 5, 7 x 7, 9 x 9 and 11 x 11) for three different sites (1, 2 and 3) of deformed ferrite matrix of Ti+ grade sample for annealing condition of 800 °C 0 s

Full MATLAB code is shown below:

```
clear all; close all; clc;
%% Import Script for EBSD Data
%
```

```

% This script was automatically created by the import wizard. You
should
% run the whole script or parts of it in order to import your data.
There
% is no problem in making any changes to this script.

%% Specify Crystal and Specimen Symmetries

% crystal symmetry
CS = {...
    'notIndexed',...
    crystalSymmetry('m-3m', [3.66 3.66 3.66], 'mineral', 'Iron fcc',
'color', 'light blue'),...
    crystalSymmetry('m-3m', [2.866 2.866 2.866], 'mineral', 'Iron bcc
(old)', 'color', 'light green')};

% plotting convention
setMTEXpref('xAxisDirection','east');
setMTEXpref('zAxisDirection','intoPlane');

%% Specify File Names

% path to files
pname = 'C:\Users\KAPOOR2_I\Documents\MATLAB\mtex\In-situ\800C
0s\ti\an';

% which files to be imported
fname = [pname '\Project 1vj CRA Ti plus 795 fast 790 fast Map Data
268.ctf'];

%% Import the Data

% create an EBSD variable containing the data
ebsd = loadEBSD(fname,CS,'interface','ctf',...
    'convertEuler2SpatialReferenceFrame');
%F = splineFilter;
%ebsd = smooth(ebsd('indexed'),F,'fill');

figure()
plot(ebsd)

oM = ipdfHSVOrientationMapping(ebsd('Iron bcc (old)'));
oM.inversePoleFigureDirection = xvector;

% compute the colors
color = oM.orientation2color(ebsd('Iron bcc (old)').orientations);
region = [x_0 y_0 L W]*1;
figure()
plot(ebsd('Iron bcc (old)'),color)
rectangle('position',region,'edgecolor','r','linewidth',2)
condition = inpolygon(ebsd,region);
ebsd = ebsd(condition)
% ignore grain boundary misorientations
grains = calcGrains(ebsd,'angle',1*degree);

figure()

```

```

plot(ebsd,ebsd.KAM./degree);
c = ebsd.KAM./degree; % LAM value in degrees!!
d = noise value % degrees!!
d1 = d*0.0174533
c1 = ebsd.KAM - d1; % LAM value in radians!!
hold on
plot(ebsd('notIndexed'),'FaceColor','black')
hold off
1/degree
u = 2*abs(ebsd.unitCell(1,1))*1e-6;
b = 0.243e-9;
%GDiss = log10(c1.*(2/(u*b)));

GND = c1.*(2/(u*b));
sm = 75e+9;
SE = GND.*(sm*b*b/2);
%LSE = log10(SE);

%figure()
%plot(ebsd,GDiss);
%colorbar;
%colormap jet
%hold on
%plot(ebsd('notIndexed'),'FaceColor','black')
%hold off

%figure()
%plot(ebsd,LSE);
%colorbar;
%colormap Parula
%hold on
%plot(ebsd('notIndexed'),'FaceColor','black')
%hold off

```

For example:

Input values: d (noise value) = 0.71° and region = [3.8 27 1.4 5]*1;

Output value: Average GND density values (after noise removal) = 1.98E+14 m⁻²

9.2. Solute drag parameter calculation

Calculation of solute drag and intrinsic boundary friction for Ti+Mn+ grades is explained below. For the current situation, calculation of intrinsic boundary friction is only shown for velocity = 0.23 µm/s.

$$\Delta G_{sd} = \frac{C_o * \alpha * v}{1 + \beta^2 * v^2} \quad (9.2-1)$$

$$\alpha = \frac{N_v * (k * T)^2 * \delta}{E_o * X} * \left(\sinh\left(\frac{E_o}{k * T}\right) - \left(\frac{E_o}{k * T}\right) \right) \quad (9.2-2)$$

$$\beta^2 = \frac{\alpha * k * T * \delta}{2 * N_v * E_o^2 * X} \quad (9.2-3)$$

$$\Delta G_{IBF} = \frac{v}{M_i} \quad (9.2-4)$$

$$M_i = \frac{2.63}{T} * e^{\left(\frac{-20754}{T}\right)} \quad (9.2-5)$$

Table 9.2- 1 Parameters for solute drag force calculation after Clark [46], Gladman [58], Zurob et al. [112,182], Cahn [203] Xu [325] and Wicaksono and Militzer [333]

Parameters	Value
C_o (atomic concentration for Ti+Mn+ grade)	0.0039
a (lattice parameter of Fe-BCC)	2.8×10^{-10} m
N_v (molar volume)	$2/a^3$
k (Boltzmann constant)	$1.38 \times 10^{-23} \text{ m}^2 \text{ kgs}^{-2} \text{ K}^{-1}$
T (temperature)	1073 K
δ (grain boundary thickness) ~ two times of burgers vector of Fe (assumption)	5×10^{-10} m
E_o (grain boundary interaction energy with atom)	1.7608×10^{-20} J/atoms
X (bulk diffusion constant)	$0.000076 * \exp(-224400/R*T)$ m^2/s
v (grain boundary velocity)	Variable

Based on above parameters, values of α , β^2 , ΔG_{sd} , ΔG_{IBF} and M_i are as follows:

$$\alpha = 1.88 \times 10^{14} \text{ kgm}^{-2} \text{ s}^{-1}$$

$$\beta^2 = 2.73 \times 10^{10} \text{ m}^{-2} \text{ s}^{-2}$$

$$M_i = 9.77 \times 10^{-12} \text{ m}^4/\text{Js}$$

For $v = 0.23 \text{ } \mu\text{m/s}$, $\Delta G_{sd} = 1.21 \text{ J/mol}$ and $\Delta G_{IBF} = 0.17 \text{ J/mol}$

9.3 Selection of areas for STEM-EDS analysis

During annealing of cold-rolled steel, sub-grain and grain boundaries form the major sites for precipitate nucleation. In order to obtain precipitate size, volume fraction and number density information along grain boundaries and within grains, FIB-lift out was performed from the un-recrystallized and recrystallized ferrite matrix in a sample of interest. During initial stage of STEM-EDS analysis, low magnification scan of the FIB-lift out lamella is performed as shown in Fig. 9.3-1a. Microstructural defects are decorated by precipitates. Once the general layout of precipitates across the FIB-lift out sample is identified, high magnification STEM-EDS scans are performed at different sites containing precipitates. Sites with no precipitate visibility in the low magnification map (Fig. 9.3-1a) are also studied at high magnification to identify any fine precipitate distribution within that region.

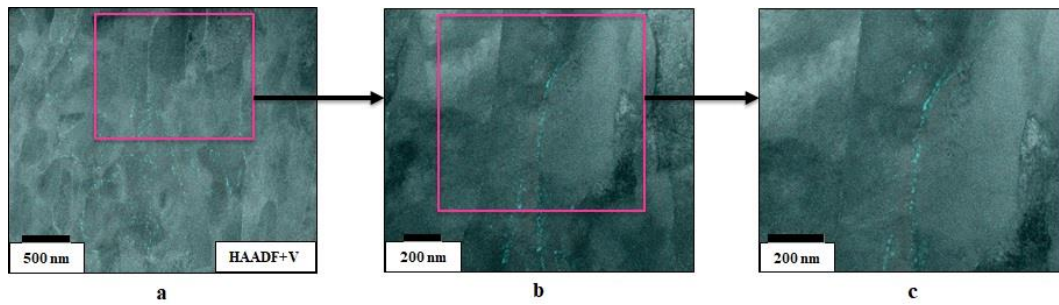


Fig. 9.3-1 STEM high-angle annular dark-field (HAADF) image superimposed with Vanadium EDS chemical map. Pink coloured rectangular box in Fig. 9.3-1a and 9.3-1b represents the site of interest at higher magnification.

An example is demonstrated to identify one of the sites of interest (Fig. 9.3-1):

The pink coloured rectangular box in Fig. 9.3-1a shows an area of interest. Magnification is increased to identify that particular area as shown in Fig. 9.3-1b. To collect statistical information of fine and coarse precipitates, magnification is further increased to obtain updated STEM-EDS map as shown in Fig. 9.3-1c. High magnification STEM-EDS scanned area (Fig. 9.3-1c) is then post-processed in Image J software as explained in section 9.4.

Similar method is applied for at least 10 different sites from two different FIB-lift out samples for each annealing condition. Although several areas have been selected to analyse precipitation the measurement may not be the ‘true’ value. This is a long-standing issue for FIB-lift out TEM precipitate investigation. Previous researchers [149,360] have used Small Angle Neutron Scattering (SANS) to characterise precipitates over a much larger volume. Even though precipitate number density, size or volume fraction may not be same as true value but by selection (using FIB-lift out technique) of the potential precipitate nucleation sites such as sub-grain and grain boundaries and within grains, statistically representative information of precipitates in cold-rolled annealed steel grades can be obtained.

9.4. ImageJ post-processing of STEM images

Quantification of precipitate size, counts (%) and volume fraction are done by post-processing of STEM-EDS chemical map in ImageJ software. For the initial stages of precipitation, precipitates are very fine and closely spaced along grain boundary. Quantification of individual fine precipitates is a complex procedure. While quantification of coarse precipitates is relatively easier. To explain the above points, two examples (Fig. 9.4-1 and Fig. 9.4-2) of the Ti+ grade for the annealing condition of 700 °C 0 s and 800 °C 2 min are presented. STEM-EDS map is post-processed in ImageJ software to obtain bandpass filter (BPF) and threshold (THD) images. The area of selected precipitates are obtained from threshold image. Precipitate size (2 x radius) and volume are evaluated from precipitate area. For analysis, precipitates are assumed to be spherical.

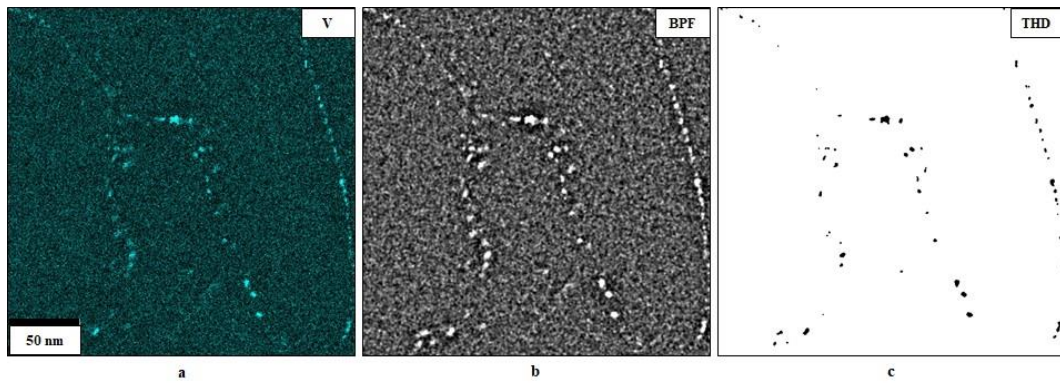


Fig. 9.4-2 STEM -EDS chemical map of carbo-nitrides of Vanadium precipitates pinned to a sub-grain boundary at 700 °C 0 s for the Ti+ grade steel at two different FIB-lift out samples after bulk-furnace annealing (a), post-processed images from ImageJ software, bandpass filter (BPF) and threshold (THD) (b) and (c) respectively

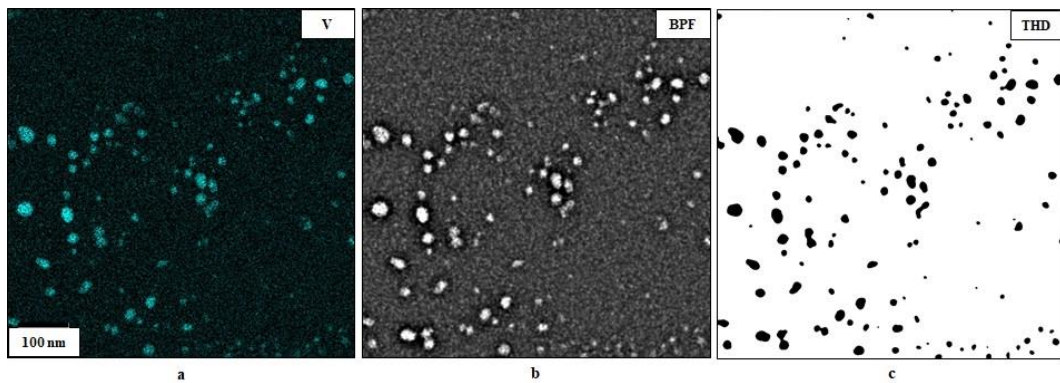


Fig. 9.4-3 STEM-EDS chemical map of carbo-nitrides of Vanadium precipitates at 800 °C 2 min for the Ti+ grade steel at two different FIB-lift out samples after bulk-furnace annealing (a), post-processed images from ImageJ software, bandpass filter (BPF) and threshold (THD) (b) and (c) respectively

Output for annealing condition of 700 °C 0 s: Output for annealing condition of 800 °C 2 min:

Area(nm ²)	d(nm)	Volume(nm ³)	Area(nm ²)	d(nm)	Volume(nm ³)
22.72	5.4	81.439	19.75	5	66.041
26.12	5.8	100.43	24.69	5.6	92.294
27.26	5.9	107.05	33.47	6.5	145.67
27.26	5.9	107.05	33.47	6.5	145.67
27.26	5.9	107.05	35.12	6.7	156.55
30.67	6.2	127.74	37.86	6.9	175.24
31.8	6.4	134.9	40.6	7.2	194.63
31.8	6.4	134.9	40.6	7.2	194.63
32.94	6.5	142.2	48.29	7.8	252.4
34.07	6.6	149.62	49.38	7.9	261.05
35.21	6.7	157.15	51.58	8.1	278.65
35.21	6.7	157.15	55.42	8.4	310.34

39.75	7.1	188.54	56.52	8.5	319.61
43.16	7.4	213.29	58.16	8.6	333.67
44.3	7.5	221.77	59.26	8.7	343.16
45.43	7.6	230.34	59.81	8.7	347.94
46.57	7.7	239.04	66.39	9.2	406.95
49.97	8	265.75	66.39	9.2	406.95
51.11	8.1	274.86	66.94	9.2	412
59.06	8.7	341.42	68.04	9.3	422.17
61.33	8.8	361.31	68.59	9.3	427.29
68.15	9.3	423.17	69.14	9.4	432.43
71.55	9.5	455.31	72.98	9.6	468.97
72.69	9.6	466.18	75.72	9.8	495.66
76.1	9.8	499.35	81.76	10	556.09
78.37	10	521.87	87.79	11	618.78
82.91	10	567.9	91.08	11	653.92
84.05	10	579.61	94.38	11	689.69
85.18	10	591.41	94.38	11	689.69
86.32	10	603.28	95.47	11	701.75
89.73	11	639.34	96.02	11	707.82
90.86	11	651.52	97.67	11	726.09
97.68	11	726.17	97.67	11	726.09
97.68	11	726.17	98.77	11	738.36
97.68	11	726.17	98.77	11	738.36
113.6	12	910.53	99.86	11	750.71
118.1	12	965.7	104.8	12	807.07
123.8	13	1036.2	106.4	12	826.16
136.3	13	1196.9	108.6	12	851.84
140.8	13	1257.3	110.8	12	877.79
143.1	13	1287.8	110.8	12	877.79
143.1	13	1287.8	112.5	12	897.42
144.2	14	1303.2	112.5	12	897.42
145.4	14	1318.6	114.7	12	923.81
176	15	1757.1	118	12	963.88
206.7	16	2235.6	122.9	13	1025
218.1	17	2422.4	130	13	1115.5
235.1	17	2711.7	131.7	13	1136.8
260.1	18	3155.3	131.7	13	1136.8
263.5	18	3217.5	133.3	13	1158.2
268	18	3301.1	133.9	13	1165.3
271.4	19	3364.3	136.1	13	1194.1
544	26	9545.4	138.3	13	1223.1
			139.9	13	1245
			141.6	13	1267
			144.9	14	1311.5
			144.9	14	1311.5
			149.2	14	1371.6

153.1	14	1424.8
160.8	14	1533.4
163.5	14	1572.9
170.1	15	1668.8
171.7	15	1693.1
175.6	15	1750.2
179.4	15	1807.9
185.5	15	1899.9
186.6	15	1916.8
187.1	15	1925.3
203.6	16	2184.9
206.3	16	2229.2
216.7	17	2400.3
218.4	17	2427.7
218.9	17	2436.8
225.5	17	2547.6
230.5	17	2631.7
239.8	17	2793.1
240.3	17	2802.7
244.7	18	2879.8
245.3	18	2889.5
251.9	18	3006.6
257.3	18	3105.4
261.2	18	3175.2
262.3	18	3195.2
262.3	18	3195.2
262.8	18	3205.3
270.5	19	3346.8
281.5	19	3552.5
295.2	19	3815.4
297.4	19	3858
302.3	20	3954.5
303.4	20	3976
306.7	20	4040.9
308.9	20	4084.4
316	20	4226.6
317.1	20	4248.7
317.7	20	4259.7
319.3	20	4292.9
321	20	4326.1
325.4	20	4415.1
350.6	21	4938.7
380.8	22	5589.9
383.5	22	5650.4
384.6	22	5674.6
401.6	23	6055.2

411	23	6267.4
416.5	23	6393.3
425.8	23	6609.3
436.2	24	6853.5
441.7	24	6983.2
454.3	24	7284.6
463.1	24	7496.8
485.6	25	8049.7
488.9	25	8131.7
507.5	25	8601.5
580.5	27	10522
651.9	29	12520
691.4	30	13675
718.8	30	14497
746.2	31	15335
820.3	32	17674

From the above two sets of data, average precipitate size, counts (%), volume fraction etc. could be easily calculated. Volume fraction of precipitate is calculated by dividing total volume precipitates by volume of the image processed. Volume of image is calculated by multiplying area of image to thickness of sample. Since thickness of sample is varying between 100 nm to 200 nm, therefore volume fraction of precipitate is calculated for four different sample thickness of 100 nm, 125 nm, 150 nm and 200 nm. Average volume fraction of precipitate is then calculated from four different values as shown in Table 9.4-1. For statistical evaluation of precipitate size and volume fraction, at least 500 precipitates are required.

Table 9.4-1 Precipitate size and volume fraction information obtained from Fig. 9.4-1 and Fig. 9.4-2

Annealing condition	Average precipitate size, d (nm)	Total volume of precipitates (nm ³)	Area of image (nm ²)	Volume fraction of precipitates (assuming thickness 200 nm)	Volume fraction of precipitates (assuming thickness 150 nm)	Volume fraction of precipitates (assuming thickness 125 nm)	Volume fraction of precipitates (assuming thickness 100 nm)	Average volume fraction of precipitates
700 °C 0 s	11	54294.92	119195.5	0.000228	0.000304	0.000364	0.000456	0.000338
800 °C 2 min	15	344469.7	575365.2	0.002993	0.003991	0.00479	0.005987	0.00444

9.5. Verification of MatCalc model

In this section the MatCalc simulation used for precipitate size and volume calculation in base and Ti+ grades for different annealing conditions is validated. Yamasaki and Bhadeshia [322] work of tempering of Fe-C-V martensitic steel is modelled in MatCalc. Precipitate size and volume fraction are obtained from MatCalc simulation for 600 °C and compared with experimental results of V₄C₃ precipitate size and volume fraction as shown in Fig. 9.5-1. Parameters used for simulation of precipitation size and volume fraction are shown in Table 9.5-1. Experimental and MatCalc simulation results of precipitate size and volume fraction are similar to each other. Precipitate nucleation ends in between 50 hours to 100 hours for tempering temperature of 600 °C. For longer tempering time (> 100 hours), precipitates are coarsened for constant volume fraction as shown in Fig. 9.5-1b. Dislocation density of 10¹⁵ m⁻² is used in MatCalc simulation for precipitate size and volume fraction calculation.

Table 9.5-1 Parameters for MatCalc simulation of precipitate size and volume fraction

Type of precipitate	Diffusivity in ferrite (m^2s^{-1})	Interfacial energy	Dislocation density in ferrite (m^{-2})
VC	$D_V^\alpha = 3.05 \times 10^{-4} \exp\left(-\frac{239000}{RT}\right)$ [322]	0.445 [323]	1.00×10^{15}

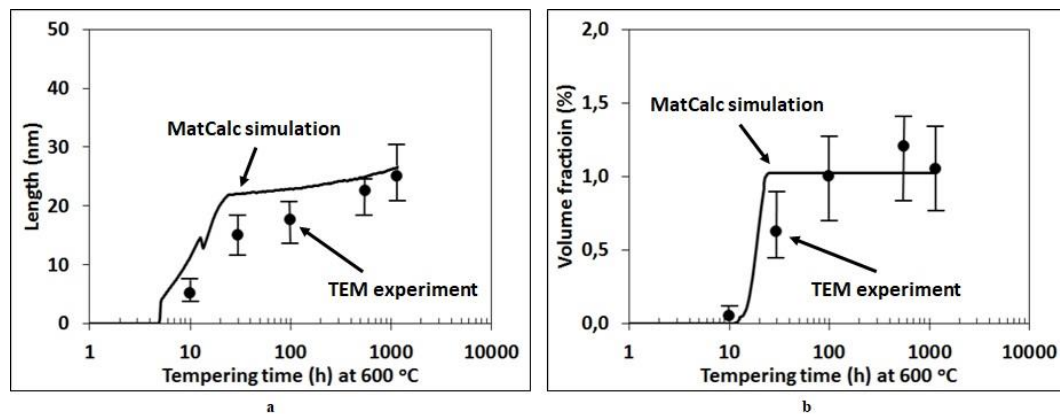


Fig. 9.5-1 Comparison of TEM experimental and MatCalc simulation results of V_4C_3 precipitate size (a) and volume fraction (b) in Fe-V-C martensitic steel tempered at 600 °C. Experimental results are taken from Yamasaki and Bhadeshia paper [322]

9.6 Sensitivity of GND analysis to certain EBSD parameters

- Increased deformation (%) of cold-rolled steel makes diffraction patterns more diffuse and possibly increases MAD values (i.e. higher angular misfit between detected and simulated Kikuchi bands) [361]. Higher MAD value leads to overestimation of GND value (GND + noise [362] [363]). While, performing noise reduction analysis [297] could minimise the effect of high MAD values on GND evaluation.
- Jiang et al. [364], have studied the variation of GND value for different binning parameters for Cu crystal and it was shown that the average GND value is relatively constant with an increase in binning parameter from 1 x 1 to 8 x 8.
- From the user's experience point of view, multiple cycles of cleaning of the acquired EBSD data set (of indexing hit rate < 80 %) in Channel 5 software may lead to inaccuracy in estimation of grain orientation and pixel to pixel misorientation values.
- For a Si crystal it has been shown that with an increase in HR from 30 to 100, peak value of the LAM distribution shifts towards lower value < 0.2° (Fig. 9.6-1) [365].

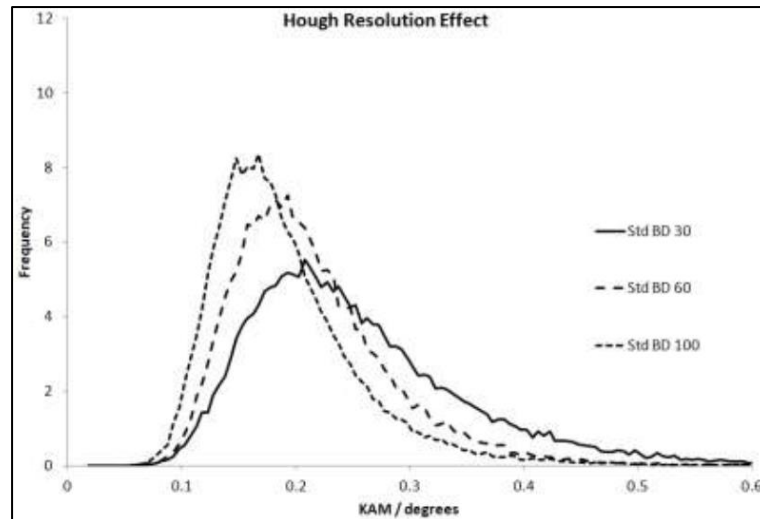


Fig. 9.6-1 Distribution of local average misorientation for Hough Resolution of 30, 60 and 100 of a Si single crystal (taken from Aztec European EBSD user meeting in Frankfurt 2019) [365]

For the evaluation of GND density results as presented in this thesis, parameters such as binning (= 4 x 4) and Hough resolution (= 60) are constant for different cases and no cleaning approach of the EBSD data set were utilised before GND evaluation. The distribution of different MAD values ($< 2^\circ$) could introduce noise and result in an overestimation of the average GND density value. Therefore for this study, noise reduction is crucial [297] and performed to minimise the effect of variation of MAD values and of external damage from sample polishing on the estimation of the average GND density of alpha and gamma fibres.

References

- [1] J.M. Allwood, J.M. Cullen, M.A. Carruth, *Sustainable Materials with Both Eyes Open*, UIT Cambridge Limited, 2012.
- [2] F. Field-III, J. Clark, *A Practical Road to Lightweight Cars*, MIT Technol. Rev. (n.d.).
- [3] N. Baluch, Z.M. Udin, C.S. Abdullah, *Advanced high strength steel in auto industry: an overview*, Eng. Technol. Appl. Sci. Res. 4 (2014) 686–689.
- [4] A. Arankalle, *Advances in Light Weight Materials for Body-in-White (BIW)*, in: *Innov. Des. Dev. Pract. Aerosp. Automot. Eng.*, Springer, 2017: pp. 517–525.
- [5] R. Rana, S.B. Singh, *Automotive Steels: Design, Metallurgy, Processing and Applications*, Elsevier Science, 2016.
- [6] 2017 UK greenhouse gas emissions: provisional figures - statistical release, 2018.
- [7] Business Energy and Industrial Strategy Committee, *Electric vehicles: driving the transition*, House of Commons. (2018) 6. <https://publications.parliament.uk/pa/cm201719/cmselect/cmbeis/383/383.pdf>.
- [8] R. Grimes, R. Dashwood, H. Flower, *Processing of high superplastic strain rate aluminium alloys*, Alum. Int. Today. 15 (2003) 64.
- [9] I. Kapoor, R.G. Narayanan, S. Taylor, V. Janik, R. Dashwood, *Predicting the Warm Forming Behavior of WE43 and AA5086 Alloys*, in: *Procedia Eng.*, 2017: pp. 897–904. <https://doi.org/10.1016/j.proeng.2016.12.136>.
- [10] R.A. Rijkenberg, A. Blowey, P. Bellina, C. Wooffindin, *Advanced High Stretch-Flange Formability Steels for Chassis & Suspension Applications 3 . Product concept : tensile properties and microstructure*, in: *4th Int. Conf. Steels Cars Truck*. June 15-19, Braunschweig, Ger., 2014: pp. 426–433.
- [11] H. Adam, *Carbon fibre in automotive applications*, Mater. Des. 18 (1997) 349–355. [https://doi.org/10.1016/S0261-3069\(97\)00076-9](https://doi.org/10.1016/S0261-3069(97)00076-9).
- [12] T. Sakayama, G. Murayma, Y. Naito, K. Saita, Y. Miyazakki, H. Oikawa, T. Nose, *similar metal joining technologies for steel sheet and aluminum alloy sheet in auto body*, 2012. <https://doi.org/10.1016/j.proeng.2016.12.136>.
- [13] P.K. Mallick, *Materials, Design and Manufacturing for Lightweight Vehicles*, CRC press, Boca Raton, 2010. <https://doi.org/10.1533/9781845697822.2.309>.

- [14] A.T. Mayyas, A. Qattawi, A.R. Mayyas, M.A. Omar, Life cycle assessment-based selection for a sustainable lightweight body-in-white design, *Energy*. 39 (2012) 412–425. <https://doi.org/10.1016/j.energy.2011.12.033>.
- [15] R. KUZIAK, R. KAWALLA, S. WAENGLER, Advanced high strength steels for automotive industry, *Arch. Civ. Mech. Eng.* 8 (2008) 103–117. [https://doi.org/https://doi.org/10.1016/S1644-9665\(12\)60197-6](https://doi.org/https://doi.org/10.1016/S1644-9665(12)60197-6).
- [16] N. Gope, D.K. Rout, S. Mukherjee, G. Jha, A.N. Bhagat, A.K. Verma, D. Bhattarjee, High strength steels for automotive applications: Recent trends and experience at tata steel, *SAE Trans.* 26 (2005) 333–344.
- [17] T. Nanda, V. Singh, V. Singh, Third generation of advanced high-strength steels : Processing routes and properties, in: *Proc. Inst. Mech. Eng. Part L J. Mater. Des. Appl.*, 2016: pp. 1–30. <https://doi.org/10.1177/1464420716664198>.
- [18] K. Takashima, K. Hasegawa, Y. Toji, Y. Funakawa, Void generation in cold-rolled dual-phase steel sheet having excellent stretch flange formability, *ISIJ Int.* 57 (2017) 1289–1294. <https://doi.org/10.2355/isijinternational.ISIJINT-2017-086>.
- [19] K. Hasegawa, K. Kawamura, T. Urabe, Y. Hosoya, Effects of microstructure on stretch-flange-formability of 980 MPa grade cold-rolled ultra high strength steel sheets, *ISIJ Int.* 44 (2004) 603–609. <https://doi.org/10.2355/isijinternational.44.603>.
- [20] P.B. Lake, J.J. Grenawalt, Partially Annealed High Strength Cold Rolled Steels, *SAE Trans.* (1977). <https://doi.org/10.4271/770163>.
- [21] Y. Funakawa, T. Shiozaki, K. Tomita, T. Yamamoto, E. Maeda, Development of High Strength Hot-rolled Sheet Steel Consisting of Ferrite and Nanometer-sized Carbides, *ISIJ Int.* 44 (2004) 1945–1951. <https://doi.org/10.2355/isijinternational.44.1945>.
- [22] T. Inoue, S. Kinoshita, Initiation of ductile fracture voids in a spheroidized steel, *J. JSTP.* 14 (1973) 291.
- [23] H. Hofmann, D. Mattissen, T.W. Schaumann, Advanced Cold Rolled Steels for Automotive Applications, *Steel Res. Int.* 80 (2009) 22–28. <https://doi.org/10.2374/SRI08SP113>.
- [24] Tata, Strip products and services catalogue 2018, (2018).
- [25] K. Yoshida, Present and Future Status of High Strength Steel Sheets for Japanese Autobodyes., *Trans. Iron Steel Inst. Japan.* 21 (1981) 761–766. <https://doi.org/10.2355/isijinternational1966.21.761>.

- [26] Z. Liu, R.O. Olivares, Y. Lei, C.I. Garcia, G. Wang, Microstructural characterization and recrystallization kinetics modeling of annealing cold-rolled vanadium microalloyed HSLA steels, *J. Alloys Compd.* 679 (2016) 293–301. <https://doi.org/10.1016/j.jallcom.2016.04.057>.
- [27] M. JANOŠEC, I. SCHINDLER, V. VODÁREK, J. PALÁT, S. RUSZ, P. SUCHÁNEK, M. RŮŽIČKA, E. MÍSTECKÝ, Microstructure and mechanical properties of cold rolled, annealed HSLA strip steels, *Arch. Civ. Mech. Eng.* 7 (2007) 29–38. [https://doi.org/10.1016/S1644-9665\(12\)60208-8](https://doi.org/10.1016/S1644-9665(12)60208-8).
- [28] W. Bleck, Cold-rolled, high-strength sheet steels for auto applications, *Jom.* 48 (1996) 26–30. <https://doi.org/10.1007/BF03222991>.
- [29] N. Prasad, S. Kumar, P. Kumar, S.N. Ojha, Mechanical properties of a cold-rolled annealed HSLA steel, *J. Mater. Sci.* 26 (1991) 5158–5162. <https://doi.org/10.1007/BF01143207>.
- [30] T. Matsuoka, K. Yamamori, Metallurgical aspects in cold rolled high strength steel sheets, *Metall. Trans. A.* 6 (1975) 1613–1622. <https://doi.org/10.1007/BF02641975>.
- [31] J. Raines, D. Matlock, J.G. Speer, R. Glodowski, Influence of V(C,N)precipitation potential on recovery annealing response of microalloyed sheet steel, *Iron Steel Technol.* 8 (2011) 109–116.
- [32] V. Shah, Effect of alloying elements and heating rates on ferrite recrystallization in dual phase steels, DELFT UNIVERSITY OF TECHNOLOGY, 2017.
- [33] G.E. Dieter, D.J. Bacon, Mechanical metallurgy, McGraw-hill New York, 1986.
- [34] A. Karmakar, M. Ghosh, D. Chakrabarti, Cold-rolling and inter-critical annealing of low-carbon steel: Effect of initial microstructure and heating-rate, *Mater. Sci. Eng. A.* 564 (2013) 389–399. <https://doi.org/10.1016/j.msea.2012.11.109>.
- [35] T. Ogawa, N. Maruyama, N. Sugiura, N. Yoshinaga, Incomplete recrystallization and subsequent microstructural evolution during intercritical annealing in cold-rolled low carbon steels, *ISIJ Int.* 50 (2010) 469–475. <https://doi.org/10.2355/isijinternational.50.469>.
- [36] C. Ji, L. Wang, M. yong Zhu, Effect of Subcritical Annealing Temperature on Microstructure and Mechanical Properties of SCM435 Steel, *J. Iron Steel Res. Int.* 22 (2015) 1031–1036. [https://doi.org/10.1016/S1006-706X\(15\)30108-4](https://doi.org/10.1016/S1006-706X(15)30108-4).
- [37] J.-Y. Choi, B.-S. Seong, S.C. Baik, H.-C. Lee, Precipitation and Recrystallization

- Behavior in Extra Low Carbon Steels, *ISIJ Int.* 42 (2002) 889–893. <https://doi.org/10.2355/isijinternational.42.889>.
- [38] S. Satoh, T. Obara, K. Tsunoyama, Effect of Precipitate Dispersion of Recrystallization Texture of Niobium-added Extra-low Carbon Cold-rolled Steel Sheet, *Trans. Iron Steel Inst. Japan.* 26 (1986) 737–744.
- [39] A. Martínez-de-Guerenu, F. Arizti, M. Díaz-Fuentes, I. Gutiérrez, Recovery during annealing in a cold rolled low carbon steel. Part I: Kinetics and microstructural characterization, *Acta Mater.* 52 (2004) 3657–3664. <https://doi.org/https://doi.org/10.1016/j.actamat.2004.04.019>.
- [40] M. Oyarzábal, A. Martínez-de-Guerenu, I. Gutiérrez, Effect of stored energy and recovery on the overall recrystallization kinetics of a cold rolled low carbon steel, *Mater. Sci. Eng. A.* 485 (2008) 200–209. <https://doi.org/https://doi.org/10.1016/j.msea.2007.07.077>.
- [41] A. Belyakov, F.G. Wei, K. Tsuzaki, Y. Kimura, Y. Mishima, Incomplete recrystallization in cold worked steel containing TiC, *Mater. Sci. Eng. A.* 471 (2007) 50–56. <https://doi.org/10.1016/j.msea.2007.04.022>.
- [42] P.A. Beck, Annealing of cold worked metals, *Adv. Phys.* 3 (1954) 245–324. <https://doi.org/10.1080/00018735400101203>.
- [43] D.G. Rodrigues, C.M. de Alcântara, D.B. Santos, T.R. de Oliveira, B.M. Gonzalez, Effects of Annealing Conditions on Recrystallization, Texture, and Average Normal Anisotropy Coefficient of a Niobium-Stabilized Ferritic Stainless Steel, *Steel Res. Int.* 88 (2017) 1–12. <https://doi.org/10.1002/srin.201700214>.
- [44] B. Hutchinson, S. Jonsson, L. Ryde, On the kinetics of recrystallisation in cold worked metals, *Scr. Metall.* 23 (1989) 671–676. [https://doi.org/https://doi.org/10.1016/0036-9748\(89\)90510-3](https://doi.org/https://doi.org/10.1016/0036-9748(89)90510-3).
- [45] H. long YI, L. xiu DU, G. dong WANG, X. hua LIU, Strengthening Mechanism of a New 700 MPa Hot Rolled High Strength Steel, *J. Iron Steel Res. Int.* 15 (2008) 76–80. [https://doi.org/10.1016/S1006-706X\(08\)60036-9](https://doi.org/10.1016/S1006-706X(08)60036-9).
- [46] S. Clark, Nano-Structuring of Micro-Alloyed Steels via Nano-Precipitate Formation, University of Warwick, 2019.
- [47] Ö.N. Cora, M. Koç, Promises and Problems of Ultra / Advanced High Strength Steel (U / AHSS) Utilization in Auto Industry PROMISES AND PROBLEMS OF ULTRA

- / ADVANCED HIGH STRENGTH, in: Solmaz E, Kaya N Oztu Rk F 7th Otomotiv Teknol. Kongresi, Bursa, Turkey, 2014: pp. 26–27. <https://doi.org/10.13140/2.1.4725.0883>.
- [48] M.Y. Demeri, Chapter 1 - Introduction, in: Adv. High-Strength Steels—Science, Technol. Appl., ASM International, 2013: pp. 1–22.
- [49] J.N. Hall, Evolution of Advanced High Strength Steels in Automotive Applications, in: Present. Jt. Policy Coun. Auto/Steel Partnersh., autosteel.org, 2011.
- [50] C.D. Horvath, Advanced steels for lightweight automotive structures, Woodhead Publishing Limited, 2010. <https://doi.org/10.1533/9781845697822.1.35>.
- [51] C.C. Tasan, M. Diehl, D. Yan, M. Bechtold, F. Roters, L. Schemmann, C. Zheng, N. Peranio, D. Ponge, M. Koyama, K. Tsuzaki, D. Raabe, An Overview of Dual-Phase Steels: Advances in Microstructure-Oriented Processing and Micromechanically Guided Design, *Annu. Rev. Mater. Res.* 45 (2015) 391–431. <https://doi.org/10.1146/annurev-matsci-070214-021103>.
- [52] J.N. Hall, J.R. Fekete, 2 - Steels for auto bodies: A general overview, in: R. Rana, S.B. Singh (Eds.), *Automot. Steels*, Woodhead Publishing, 2017: pp. 19–45. <https://doi.org/https://doi.org/10.1016/B978-0-08-100638-2.00002-X>.
- [53] J. Reed, Advanced High-Strength Steel Technologies in the 2015 Ford Edge, *Gt. Des. Steel*, Livonia MI. (2015).
- [54] D. Matlock, J. Speer, E. De Moor, P. Gibbs, Recent developments in advanced high strength sheet steels for automotive applications: an overview, *Jestech.* 15 (2012) 1–12.
- [55] F.C. Campbell, Chapter 19 - Plain Carbon Steels, in: *Elem. Metall. Eng. Alloy.*, ASM International, Ohio, 2008: pp. 349–370.
- [56] C.W.J. Hol, J. de Roo, L. Kampmeijer, T. Dirkson, G. Schipper, M. La Maire, J. van der Lugt, Model predictive controller for strip-tracking during tail-out of the finishing mill, *IFAC Proc. Vol.* 46 (2013) 397–402.
- [57] N.R. Wigley, Property prediction of continuous annealed steels, DISS, Cardiff University, 2012.
- [58] T. Gladman, *The physical metallurgy of microalloyed steels*, Institute of Materials, London, 1997.
- [59] D. Llewellyn, R. Hudd, *Steels: metallurgy and applications*, Elsevier, 1998.

- [60] J.M. Rodriguez-Ibabe, ed., *Thin Slab Direct Rolling of Microalloyed Steel*, 1st ed., Trans Tech Publishers, Switzerland, 2007.
- [61] M. Almojil, *Deformation and Recrystallisation in Low Carbon Steels*, 2010.
- [62] O. Engler, V. Randle, *Introduction to texture analysis: macrotexture, microtexture and orientation mapping*, CRC press, 2014.
- [63] B. Hutchinson, Deformation microstructures and textures in steels, *Philos. Trans. R. Soc. London. Ser. A Math. Phys. Eng. Sci.* 357 (1999) 1471–1485. <https://doi.org/10.1098/rsta.1999.0385>.
- [64] R.K. Ray, J.J. Jonas, R.E. Hook, Cold rolling and annealing textures in low carbon and extra low carbon steels, 1994. <https://doi.org/10.1179/095066094790326112>.
- [65] M. Butrón-Guillén, J. Jonas, R.K. Ray, Effect of austenite pancaking on texture formation in a plain carbon and A Nb microalloyed steel, *Acta Metall. Mater.* 42 (1994) 3615–3627.
- [66] D. Schläfer, H.J. Bunge, The Development of the Rolling Texture of Iron Determined by Neutron-Diffraction, *Texture, Stress. Microstruct.* 1 (1974) 157–171.
- [67] S.G. Chowdhury, E. V. Pereloma, D.B. Santos, Evolution of texture at the initial stages of continuous annealing of cold rolled dual-phase steel: Effect of heating rate, *Mater. Sci. Eng. A.* 480 (2008) 540–548. <https://doi.org/10.1016/j.msea.2007.07.060>.
- [68] T. Obara, K. Sakata, T. Irie, Metallurgy of Continuous-Annealed Steel, in: Eds BI Bramfitt PL Magonan, TMS, Warrendale, USA, n.d.: pp. 83–84.
- [69] P.R. Mould, An Overview of Continuous-Annealing Technology for Steel Sheet Products, *JOM J. Miner. Met. Mater. Soc.* 34 (1982) 18–28. <https://doi.org/10.1007/BF03339145>.
- [70] R. Pradhan, Continuously Annealed Cold Rolled Microalloyed Steels With Different Microstructures, *HSLA Steels, Technol. Appl.* (1983) 193–201.
- [71] M. Fein, M. Böck-schnepps, S. Strommer, M. Niederer, A. Steinboeck, A. Kugi, Model-based control and optimization of continuous strip annealing furnaces, *Heat Process.* 14 (2016) 57–63.
- [72] I.O. Davies, Method of galvanising a steel strip in a continuous hot dip galvanising line, EP 2 458 022 A1, 2010.
- [73] C.B. Smith, K.E. Parmenter, *Management of Process Energy*, 2016.

<https://doi.org/10.1016/b978-0-12-802506-2.00011-2>.

- [74] D.O. Marlow, Modelling direct-fired annealing furnaces for transient operations, *Appl. Math. Model.* 20 (1996) 34–40. [https://doi.org/10.1016/0307-904X\(95\)00103-Q](https://doi.org/10.1016/0307-904X(95)00103-Q).
- [75] M. Flamme, A. Milani, J. Wüning, W. Blasiak, W. Yang, D. Szewczyk, J. Sudo, S. Mochida, Radiant Tube Burners, in: *Ind. Combust. Test.*, Taylor & Francis Group, 2010: pp. 487–504.
- [76] R. Speets, H. Wu, P. Pronk, Improving the performance of continuous annealing lines by model predictive control, in: *INFUB10, Porto (Portugal)*, INFUB10, Porto (Portugal), 2015: pp. 1–9.
- [77] H. Wu, B. Van Benschop, O. Ben Driss, F. Frinking, R. Speets, Furnace combustion and control renovation to improve the productivity of a continuous annealing line, *Energy Procedia.* 120 (2017) 454–461. <https://doi.org/10.1016/j.egypro.2017.07.219>.
- [78] V. Kuklík, J. Kudláček, 2 - Hot-dip galvanizing, in: V. Kuklík, J. Kudláček (Eds.), *Hot-Dip Galvaniz. Steel Struct.*, Butterworth-Heinemann, Boston, 2016: pp. 7–16. <https://doi.org/https://doi.org/10.1016/B978-0-08-100753-2.00002-1>.
- [79] W. Callister, D. Rethwisch, *Materials science and engineering: an introduction*, John Wiley & Sons, United States of America, 2007. [https://doi.org/10.1016/0025-5416\(87\)90343-0](https://doi.org/10.1016/0025-5416(87)90343-0).
- [80] F.L.G. Oliveira, M.S. Andrade, A.B. Cota, Kinetics of austenite formation during continuous heating in a low carbon steel, *Mater. Charact.* 58 (2007) 256–261. <https://doi.org/10.1016/j.matchar.2006.04.027>.
- [81] Y. Liu, W. Sun, Effects of Heating Rate on the Phase Transformation Temperature of Austenite in M Steel Sheet, in: F. Marquis (Ed.), *Proc. 8th Pacific Rim Int. Congr. Adv. Mater. Process.*, Springer International Publishing, 2016: pp. 835–838.
- [82] J. PROHÁSZKA, PHASE TRANSFORMATIONS IN STEEL DURING RAPID HEAT TREATMENT, *Period. Polytech. Mech. Eng.* 32 (2019). <https://doi.org/https://doi.org/N/A>.
- [83] E.J. Mittemeijer, *Fundamentals of Materials Science, The Microstructure–Property Relationship Using Metals as Model Systems*, Springer-Verlag Berlin Heidelberg, 2010. <https://doi.org/10.1007/978-3-642-10500-5>.
- [84] H. Bhadeshia, R. Honeycombe, *Steels: Microstructure and Properties*, Butterworth-Heinemann, Great Britain, 2011.

- [85] L. Yumen, Z. Jingen, Deformation dislocation structure and fracture in a low carbon steel, *Mater. Sci. Eng.* 84 (1986) 137–145. [https://doi.org/10.1016/0025-5416\(86\)90231-4](https://doi.org/10.1016/0025-5416(86)90231-4).
- [86] A. Č, J. Vilys, V. Č, V. Kvedaras, Investigation of dislocation structure of low carbon steel during static loading, 60 (2006) 59–66.
- [87] A. Wauthier-Monnin, T. Chauveau, O. Castelnau, H. Réglé, B. Bacroix, The evolution with strain of the stored energy in different texture components of cold-rolled if steel revealed by high resolution X-ray diffraction, *Mater. Charact.* 104 (2015) 31–41. <https://doi.org/10.1016/j.matchar.2015.04.005>.
- [88] M.F. Ashby, The deformation of plastically non-homogeneous materials, *Philos. Mag.* 21 (1970) 399–424. <https://doi.org/10.1080/14786437008238426>.
- [89] Y. Ateba Betanda, A.L. Helbert, F. Brisset, M.H. Mathon, T. Waeckerlé, T. Baudin, Measurement of stored energy in Fe-48%Ni alloys strongly cold-rolled using three approaches: Neutron diffraction, Dillamore and KAM approaches, *Mater. Sci. Eng. A.* 614 (2014) 193–198. <https://doi.org/10.1016/j.msea.2014.07.037>.
- [90] S. Wright, M. Nowell, D. Field, A Review of Strain Analysis Using Electron Backscatter Diffraction, *Microsc. Microanal.* 17 (2011) 316–329. <https://doi.org/10.1017/S1431927611000055>.
- [91] J. Jiang, T.B. Britton, A.J. Wilkinson, Evolution of dislocation density distributions in copper during tensile deformation, *Acta Mater.* 61 (2013) 7227–7239. <https://doi.org/10.1016/j.actamat.2013.08.027>.
- [92] M. Calcagnotto, D. Ponge, E. Demir, D. Raabe, Orientation gradients and geometrically necessary dislocations in ultrafine grained dual-phase steels studied by 2D and 3D EBSD, *Mater. Sci. Eng. A.* 527 (2010) 2738–2746. <https://doi.org/10.1016/j.msea.2010.01.004>.
- [93] N. Hansen, X. Huang, G. Winther, Grain orientation, deformation microstructure and flow stress, *Mater. Sci. Eng. A.* 494 (2008) 61–67. <https://doi.org/10.1016/j.msea.2007.10.086>.
- [94] L.P. Kubin, A. Mortensen, Geometrically necessary dislocations and strain-gradient plasticity: A few critical issues, *Scr. Mater.* 48 (2003) 119–125. [https://doi.org/10.1016/S1359-6462\(02\)00335-4](https://doi.org/10.1016/S1359-6462(02)00335-4).
- [95] H. Gao, Y. Huang, W.D. Nix, J.W. Hutchinson, Mechanism-based strain gradient

- plasticity— I. Theory, *J. Mech. Phys. Solids.* 47 (1999) 1239–1263.
[https://doi.org/10.1016/S0022-5096\(98\)00103-3](https://doi.org/10.1016/S0022-5096(98)00103-3).
- [96] F.J. Humphreys, M. Hatherly, *Recrystallization and Related Annealing Phenomena*, Elsevier, The Netherlands, 2004. <https://doi.org/10.1016/B978-008044164-1/50020-7>.
- [97] A. Cottrell, This week's citation classic, *Curr. Contents.* (1990) 28–28.
<http://garfield.library.upenn.edu/classics1990/A1990EH31000001.pdf>.
- [98] M. Maalekian, Christian Doppler Laboratory for Early Stages of Precipitation The Effects of Alloying Elements on Steels (I), *Eff. Alloy. Elem. Steels.* 1 (2007) 36.
[https://doi.org/10.1016/S0026-2714\(98\)00110-3](https://doi.org/10.1016/S0026-2714(98)00110-3).
- [99] K.E. Thelning, *Steel and Its Heat Treatment*, Elsevier Science, 2013.
- [100] T. Gladman, D. Dulleu, Grain-Size Control in Steels, *Met. Sci.* 8 (1974) 167–176.
<https://doi.org/10.1179/msc.1974.8.1.167>.
- [101] T. Gladman, On the Theory of the Effect of Precipitate Particles on Grain Growth in Metals, *Proc. R. Soc. London. Ser. A. Math. Phys. Sci.* 294 (1966) 298–309.
<http://rspa.royalsocietypublishing.org/content/294/1438/298.abstract>.
- [102] R.D.K. Misra, H. Nathani, J.E. Hartmann, F. Siciliano, Microstructural evolution in a new 770MPa hot rolled Nb–Ti microalloyed steel, *Mater. Sci. Eng. A.* 394 (2005) 339–352. <https://doi.org/https://doi.org/10.1016/j.msea.2004.11.041>.
- [103] Y. Li, D.N. Crowther, P.S. Mitchell, T.N. Baker, The Evolution of Microstructure during Thin Slab Direct Rolling Processing in Vanadium Microalloyed Steels, *ISIJ Int.* 42 (2002) 636–644. <https://doi.org/10.2355/isijinternational.42.636>.
- [104] G. Xu, X. Gan, G. Ma, F. Luo, H. Zou, The development of Ti-alloyed high strength microalloy steel, *Mater. Des.* 31 (2010) 2891–2896.
<https://doi.org/10.1016/j.matdes.2009.12.032>.
- [105] X. Mao, X. Huo, X. Sun, Y. Chai, Strengthening mechanisms of a new 700 MPa hot rolled Ti-microalloyed steel produced by compact strip production, *J. Mater. Process. Technol.* 210 (2010) 1660–1666. <https://doi.org/10.1016/j.jmatprotec.2010.05.018>.
- [106] Y.F. Shen, C.M. Wang, X. Sun, A micro-alloyed ferritic steel strengthened by nanoscale precipitates, *Mater. Sci. Eng. A.* 528 (2011) 8150–8156.
<https://doi.org/10.1016/j.msea.2011.07.065>.
- [107] J. Moon, S. Kim, J. il Jang, J. Lee, C. Lee, Orowan strengthening effect on the nanoindentation hardness of the ferrite matrix in microalloyed steels, *Mater. Sci. Eng.*

- A. 487 (2008) 552–557. <https://doi.org/10.1016/j.msea.2007.10.046>.
- [108] R. Dierk, Recovery and Recrystallization: Phenomena, Physics, Models, Simulation, in: D.E. Laughlin, K. Hono (Eds.), Phys. Metall., Elsevier B.V., UK, 2014: pp. 2291–2397.
- [109] R.D. Doherty, D.A. Hughes, F.J. Humphreys, J.J. Jonas, D.J. Jensen, M.E. Kassner, W.E. King, T.R. Mcnelley, H.J. Mcqueen, A.D. Rollett, Current issues in recrystallization : a review, Mater. Sci. Eng. A. 238 (1997) 219–274.
- [110] P.H. Pumphrey, H. Gleiter, The annealing of dislocations in high-angle grain boundaries, Philos. Mag. A J. Theor. Exp. Appl. Phys. 30 (1974) 593–602. <https://doi.org/10.1080/14786439808206584>.
- [111] D. Raabe, K. Lücke, Annealing textures of BCC metals, Scr. Metall. Mater. 27 (1992) 1533–1538. [https://doi.org/http://dx.doi.org/10.1016/0956-716X\(92\)90140-A](https://doi.org/http://dx.doi.org/10.1016/0956-716X(92)90140-A).
- [112] H.S. Zurob, C.R. Hutchinson, Y. Brechet, G.R. Purdy, Rationalization of the softening and recrystallization behaviour of microalloyed austenite using mechanism maps, Mater. Sci. Eng. A. 382 (2004) 64–81. <https://doi.org/10.1016/j.msea.2004.04.024>.
- [113] P.R. Rios, F. Siciliano Jr, H.R.Z. Sandim, R.L. Plaut, A.F. Padilha, Nucleation and growth during recrystallization, Mater. Res. 8 (2005) 225–238. http://www.scielo.br/scielo.php?script=sci_arttext&pid=S1516-14392005000300002&nrm=iso.
- [114] P.A. Beck, P.R. Sperry, Strain Induced Grain Boundary Migration in High Purity Aluminum, J. Appl. Phys. 21 (1950) 150–152.
- [115] P.A. Beck, The Formation of Recrystallization Nuclei, J. Appl. Phys. 20 (1949).
- [116] R.W. Cahn, A New Theory of Recrystallization Nuclei, Proc. Phys. Soc. Sect. A. 63 (1950) 323. <http://stacks.iop.org/0370-1298/63/i=4/a=302>.
- [117] A. Cottrell, Theory of dislocations, Prog. Met. Phys. 1 (1949) 77–126.
- [118] A. Belyakov, Y. Kimura, K. Tsuzaki, Recovery and recrystallization in ferritic stainless steel after large strain deformation, Mater. Sci. Eng. A. 403 (2005) 249–259. <https://doi.org/https://doi.org/10.1016/j.msea.2005.05.057>.
- [119] B. Soleimani Amiri, G.H. Akbari, Recrystallization Behavior of Deep Drawing Low Carbon Steel Sheets Produced by Mobarakeh Steel Plant, Int. J. Iron Steel Soc. Iran. 2 (2005) 36–42. http://journal.issiran.com/article_4791.html.

- [120] I. Thomas, S. Zaefferer, F. Friedel, D. Raabe, High-Resolution EBSD Investigation of Deformed and Partially Recrystallized IF Steel, *Adv. Eng. Mater.* 5 (2003) 566–570. <https://doi.org/10.1002/adem.200300373>.
- [121] F.J. Humphreys, The nucleation of recrystallization at second phase particles in deformed aluminium, *Acta Metall.* 25 (1977) 1323–1344. [https://doi.org/http://dx.doi.org/10.1016/0001-6160\(77\)90109-2](https://doi.org/http://dx.doi.org/10.1016/0001-6160(77)90109-2).
- [122] R.P. de Siqueira, H.R.Z. Sandim, D. Raabe, Particle Stimulated Nucleation in Coarse-Grained Ferritic Stainless Steel, *Metall. Mater. Trans. A.* 44 (2013) 469–478. <https://doi.org/10.1007/s11661-012-1408-x>.
- [123] H.S. Ubhi, J. Parsons, N. Othen, S. Campbell, R. Poole, A. Gholinia, In-situ EBSD phase transformation and recrystallisation, *J. Phys. Conf. Ser.* 522 (2014). <https://doi.org/10.1088/1742-6596/522/1/012011>.
- [124] S. Tokita, H. Kokawa, Y.S. Sato, H.T. Fujii, In situ EBSD observation of grain boundary character distribution evolution during thermomechanical process used for grain boundary engineering of 304 austenitic stainless steel, *Mater. Charact.* 131 (2017) 31–38. <https://doi.org/10.1016/j.matchar.2017.06.032>.
- [125] H. NAKAMICHI, F.J. HUMPHREYS, I. BROUGH, Recrystallization phenomena in an IF steel observed by in situ EBSD experiments, *J. Microsc.* 230 (2008) 464–471. <https://doi.org/10.1111/j.1365-2818.2008.02006.x>.
- [126] V. Janik, S. Clark, P. Srirangam, A. Rijkenberg, S. Seetharaman, Application of In-Situ Material Characterization Methods to Describe Role of Mo During Processing of V-Bearing Micro-Alloyed Steels, in: *HSLA Steels 2015, Microalloying 2015 {&} Offshore Eng. Steels 2015*, Springer International Publishing, Cham, 2016: pp. 289–295. https://doi.org/10.1007/978-3-319-48767-0_31.
- [127] Y. Zhang, A. Godfrey, D. Juul Jensen, In-situ investigation of local boundary migration during recrystallization, *Metall. Mater. Trans. A Phys. Metall. Mater. Sci.* 45 (2014) 2899–2905. <https://doi.org/10.1007/s11661-014-2222-4>.
- [128] F. Brisset, A. Helbert, T. Baudin, In Situ Electron Backscatter Diffraction Investigation of Recrystallization in a Copper Wire, *Microsc. Microanal.* 19 (2013) 969–977. <https://doi.org/10.1017/S1431927613000299>.
- [129] D.P. Field, L.T. Bradford, M.M. Nowell, T.M. Lillo, The role of annealing twins during recrystallization of Cu, *Acta Mater.* 55 (2007) 4233–4241. <https://doi.org/10.1016/j.actamat.2007.03.021>.

- [130] N. Bozzolo, S. Jacomet, R.E. Logé, Fast in-situ annealing stage coupled with EBSD: A suitable tool to observe quick recrystallization mechanisms, *Mater. Charact.* 70 (2012) 28–32. <https://doi.org/10.1016/j.matchar.2012.04.020>.
- [131] G.G.E. Seward, D.J. Prior, J. Wheeler, S. Celotto, D.J.M. Halliday, R.S. Paden, M.R. Tye, High-temperature electron backscatter diffraction and scanning electron microscopy imaging techniques: In-situ investigations of dynamic processes, *Scanning*. 24 (2002) 232–240. <https://doi.org/10.1002/sca.4950240503>.
- [132] S. Takajo, C.C. Merriman, S.C. Vogel, D.P. Field, In-situ EBSD study on the cube texture evolution in 3 wt% Si steel complemented by ex-situ EBSD experiment — From nucleation to grain growth, *Acta Mater.* 166 (2019) 100–112. <https://doi.org/10.1016/j.actamat.2018.11.054>.
- [133] C. KERISIT, R.E. LOGÉ, S. JACOMET, V. LLORCA, N. BOZZOLO, EBSD coupled to SEM in situ annealing for assessing recrystallization and grain growth mechanisms in pure tantalum, *J. Microsc.* 250 (2013) 189–199. <https://doi.org/10.1111/jmi.12034>.
- [134] D. Guan, W.M. Rainforth, L. Ma, B. Wynne, J. Gao, Twin recrystallization mechanisms and exceptional contribution to texture evolution during annealing in a magnesium alloy, *Acta Mater.* 126 (2017) 132–144. <https://doi.org/10.1016/j.actamat.2016.12.058>.
- [135] D. Guan, W.M. Rainforth, J. Gao, L. Ma, B. Wynne, Individual effect of recrystallisation nucleation sites on texture weakening in a magnesium alloy: Part 2- shear bands, *Acta Mater.* 145 (2018) 399–412. <https://doi.org/10.1016/j.actamat.2017.12.019>.
- [136] P.J. Hurley, F.J. Humphreys, A study of recrystallization in single-phase aluminium using in-situ annealing in the scanning electron microscope, *J. Microsc.* 213 (2004) 225–234. <https://doi.org/10.1111/j.0022-2720.2004.01300.x>.
- [137] M. Hillert, On the theory of normal and abnormal grain growth, *Acta Metall.* 13 (1965) 227–238. [https://doi.org/https://doi.org/10.1016/0001-6160\(65\)90200-2](https://doi.org/https://doi.org/10.1016/0001-6160(65)90200-2).
- [138] W. Mao, M. Zhang, P. Yang, Behaviors of Normal Grain Growth in Polycrystalline Fe–3%Si Alloys, *Steel Res. Int.* 85 (2014) 1215–1219. <https://doi.org/10.1002/srin.201300350>.
- [139] A.T. Motta, D.R. Olander, B. Wirth, Chapter 8 Grains and Grain boundaries, in: *Light Water React. Mater.*, American Nuclear Society, 2017: pp. 1–27.

- [140] W.W. Mullins, The effect of thermal grooving on grain boundary motion, *Acta Metall.* 6 (1958) 414–427.
- [141] T.-P. Wang, F.-H. Kao, S.-H. Wang, J.-R. Yang, C.-Y. Huang, H.-R. Chen, Isothermal treatment influence on nanometer-size carbide precipitation of titanium-bearing low carbon steel, *Mater. Lett.* 65 (2011) 396–399. <https://doi.org/10.1016/j.matlet.2010.10.022>.
- [142] R. Lagneborg, T. Siwecki, S. Zajac, B. Hutchinson, Role of vanadium in microalloyed steels, *Scand. J. Metall.* 28 (1999) 186–241.
- [143] J.G. Speer, S. Mehta, S.S. Hansen, Composition of vanadium carbonitride precipitates in microalloyed austenite, *Scr. Metall.* 18 (1984) 1241–1244. [https://doi.org/10.1016/0036-9748\(84\)90114-5](https://doi.org/10.1016/0036-9748(84)90114-5).
- [144] P.L. Mangonon, The Heat Treatment of Vanadium-Modified Alloy Steels, *JOM.* 33 (1981) 18–24. <https://doi.org/10.1007/BF03339420>.
- [145] T.N. Baker, Microalloyed steels, *Ironmak. Steelmak.* 43 (2016) 264–307. <https://doi.org/10.1179/1743281215Y.0000000063>.
- [146] V.S.A. Challa, W.H. Zhou, R.D.K. Misra, R. O'Malley, S.G. Jansto, The effect of coiling temperature on the microstructure and mechanical properties of a niobium–titanium microalloyed steel processed via thin slab casting, *Mater. Sci. Eng. A.* 595 (2014) 143–153. <https://doi.org/10.1016/j.msea.2013.12.002>.
- [147] R. Riva, C. Mapelli, R. Venturini, Effect of coiling temperature on formability and mechanical properties of mild low carbon and HSLA steels processed by thin slab casting and direct rolling, *ISIJ Int.* 47 (2007) 1204–1213. <https://doi.org/10.2355/isijinternational.47.1204>.
- [148] R. Song, N. Fonstein, H.J. Jun, N. Pottore, D. Bhattacharya, S. Jansto, Effects of Nb on Microstructural Evolution and Mechanical Properties of Low-Carbon Cold-Rolled Dual-Phase Steels, *Metallogr. Microstruct. Anal.* 3 (2014) 174–184. <https://doi.org/10.1007/s13632-014-0133-9>.
- [149] Y.Q. Wang, S.J. Clark, V. Janik, R.K. Heenan, D.A. Venero, K. Yan, D.G. McCartney, S. Sridhar, P.D. Lee, Investigating nano-precipitation in a V-containing HSLA steel using small angle neutron scattering, *Acta Mater.* 145 (2018) 84–96. <https://doi.org/10.1016/j.actamat.2017.11.032>.
- [150] X. Mao, X. Huo, X. Sun, Y. Chai, Strengthening mechanisms of a new 700MPa hot

- rolled Ti-microalloyed steel produced by compact strip production, *J. Mater. Process. Technol.* 210 (2010) 1660–1666. <https://doi.org/https://doi.org/10.1016/j.jmatprotec.2010.05.018>.
- [151] S. Yannacopoulos, M.C. Chaturvedi, Thermomechanical Treatment of a Titanium bearing HSLA steel, *Can. Metall. Q.* 27 (1988) 163–168. <https://doi.org/10.1179/cmq.1988.27.2.163>.
- [152] K.A. Taylor, Solubility products for titanium-, vanadium-, and niobium-carbide in ferrite, *Scr. Metall. Mater.* 32 (1995) 7–12.
- [153] D.A. Porter, K.E. Easterling, *Phase Transformations in Metals and Alloys*, Third Edition (Revised Reprint), Taylor & Francis, 1992.
- [154] H. Adrian, Thermodynamic model for precipitation of carbonitrides in high strength low alloy steels containing up to three microalloying elements with or without additions of aluminium, *Mater. Sci. Technol. (United Kingdom)*. 8 (1992) 406–420. <https://doi.org/10.1179/mst.1992.8.5.406>.
- [155] S. Shanmugam, M. Tanniru, R.D.K. Misra, D. Panda, S. Jansto, Microalloyed V-Nb-Ti and V steels Part 2 - Precipitation behaviour during processing of structural beams, *Mater. Sci. Technol.* 21 (2005) 165–177. <https://doi.org/10.1179/174328405X18656>.
- [156] S.W. Ooi, G. Fourlaris, A comparative study of precipitation effects in Ti only and Ti-V Ultra Low Carbon (ULC) strip steels, *Mater. Charact.* 56 (2006) 214–226. <https://doi.org/10.1016/j.matchar.2005.11.010>.
- [157] L.A. Dobrzański, M. Ligarski, Role of Ti in the W-Mo-V high-speed steels, *J. Mater. Process. Technol.* 64 (1997) 101–116. [https://doi.org/https://doi.org/10.1016/S0924-0136\(96\)02558-7](https://doi.org/https://doi.org/10.1016/S0924-0136(96)02558-7).
- [158] J. Bobynko, A.J. Craven, D. McGrouther, I. MacLaren, G. Paul, Nanocharacterisation of precipitates in austenite high manganese steels with advanced techniques: {HRSTEM} and {DualEELS} mapping, *J. Phys. Conf. Ser.* 522 (2014) 12031. <https://doi.org/10.1088/1742-6596/522/1/012031>.
- [159] M. Gouné, P. Maugis, F. Danoix, Nucleation and growth of carbo-nitride nanoparticles in α -Fe-based alloys and associated interfacial process, *Nanotechnol. Rev.* 4 (2015) 517–532. <https://doi.org/10.1515/ntrev-2015-0032>.
- [160] R.W.K. Honeycombe, R.F. Mehl, Transformation from austenite in alloy steels, *Metall. Trans. A.* 7 (1976) 915–936. <https://doi.org/10.1007/BF02644057>.

- [161] W. Kesternich, Dislocation-controlled precipitation of TiC particles and their resistance to coarsening, *Philos. Mag. A Phys. Condens. Matter, Struct. Defects Mech. Prop.* 52 (1985) 533–548. <https://doi.org/10.1080/01418618508237645>.
- [162] A.R. Jones, P.R. Howell, B. Ralph, The precipitation of niobium carbide at grain boundaries in an austenitic stainless steel, *J. Mater. Sci.* 11 (1976) 1593–1599. <https://doi.org/10.1007/BF00737514>.
- [163] Y. Han, J. Shi, L. Xu, W.Q. Cao, H. Dong, TiC precipitation induced effect on microstructure and mechanical properties in low carbon medium manganese steel, *Mater. Sci. Eng. A.* 530 (2011) 643–651. <https://doi.org/https://doi.org/10.1016/j.msea.2011.10.037>.
- [164] T.N. Baker, Processes, microstructure and properties of vanadium microalloyed steels, *Mater. Sci. Technol.* 25 (2009) 1083–1107. <https://doi.org/10.1179/174328409X453253>.
- [165] J. Wang, M. Weyland, I. Bikmukhametov, M.K. Miller, P.D. Hodgson, I. Timokhina, Transformation from cluster to nano-precipitate in microalloyed ferritic steel, *Scr. Mater.* 160 (2019) 53–57. <https://doi.org/10.1016/j.scriptamat.2018.09.039>.
- [166] S. Mukherjee, I.B. Timokhina, C. Zhu, S.P. Ringer, P.D. Hodgson, Three-dimensional atom probe microscopy study of interphase precipitation and nanoclusters in thermomechanically treated titanium–molybdenum steels, *Acta Mater.* 61 (2013) 2521–2530. <https://doi.org/https://doi.org/10.1016/j.actamat.2013.01.028>.
- [167] S. Mukherjee, I. Timokhina, C. Zhu, S.P. Ringer, P.D. Hodgson, Clustering and precipitation processes in a ferritic titanium-molybdenum microalloyed steel, *J. Alloys Compd.* 690 (2017) 621–632. <https://doi.org/https://doi.org/10.1016/j.jallcom.2016.08.146>.
- [168] I. Timokhina, M.K. Miller, J. Wang, H. Beladi, P. Cizek, P.D. Hodgson, On the Ti-Mo-Fe-C atomic clustering during interphase precipitation in the Ti-Mo steel studied by advanced microscopic techniques, *Mater. Des.* 111 (2016) 222–229. <https://doi.org/10.1016/j.matdes.2016.08.086>.
- [169] Y. Lv, P.D. Hodgson, L. Kong, W. Gao, Molecular Dynamics Modelling of Diffusional Formation of Titanium Carbide Clusters in Iron Matrix, in: *TMS 2014 143rd Annu. Meet. {&} Exhib.*, Springer International Publishing, Cham, 2016: pp. 503–509.
- [170] E. V. Pereloma, S.S. Hazra, C. Zhu, S.P. Ringer, A.A. Gazder, Atom probe analysis of

- clusters and precipitates in severely deformed and annealed interstitial free steel, *Mater. Sci. Technol.* 27 (2011) 735–738. <https://doi.org/10.1179/1743284710Y.0000000012>.
- [171] A. GUINIER, Structure of Age-Hardened Aluminium-Copper Alloys, *Nature*. 142 (1938) 569–570. <https://doi.org/10.1038/142569b0>.
- [172] G.D. PRESTON, Structure of Age-Hardened Aluminium-Copper Alloys, *Nature*. 142 (1938) 570. <https://doi.org/10.1038/142570a0>.
- [173] R.G. Baker, Precipitation processes in steels, *ISI Spec. Rep.* 64 (1959) 1.
- [174] F. Danoix, T. Epicier, F. Vurpillot, D. Blavette, Atomic-scale imaging and analysis of single layer GP zones in a model steel, *J. Mater. Sci.* 47 (2012) 1567–1571. <https://doi.org/10.1007/s10853-011-6008-4>.
- [175] A.J. Breen, K.Y. Xie, M.P. Moody, B. Gault, H.W. Yen, C.C. Wong, J.M. Cairney, S.P. Ringer, Resolving the morphology of niobium carbonitride nano-precipitates in steel using atom probe tomography, *Microsc. Microanal.* 20 (2014) 1100–1110. <https://doi.org/10.1017/S1431927614012872>.
- [176] K.Y. Xie, T. Zheng, J.M. Cairney, H. Kaul, J.G. Williams, F.J. Barbaro, C.R. Killmore, S.P. Ringer, Strengthening from Nb-rich clusters in a Nb-microalloyed steel, *Scr. Mater.* 66 (2012) 710–713. <https://doi.org/https://doi.org/10.1016/j.scriptamat.2012.01.029>.
- [177] M. Perez, E. Courtois, D. Acevedo, T. Epicier, P. Maugis, Precipitation of niobium carbonitrides in ferrite: Chemical composition measurements and thermodynamic modelling, *Philos. Mag. Lett.* 87 (2007) 645–656. <https://doi.org/10.1080/09500830701427003>.
- [178] A.K. Seal, R.W.K. Honeycombe, The effect of tantalum and niobium on the tempering of certain vanadium and molybdenum steels, *J. Iron Steel Inst.* 188 (1958) 343–350.
- [179] E. Smith, J. Nutting, The Tempering of Low-Alloy Creep-Resistant Steels Containing Chromium, Molybdenum, and Vanadium, *J. Iron. Steel Int.* 192 (1957) 314–329.
- [180] E. V. Morales, J. Gallego, H.J. Kestenbach, On coherent carbonitride precipitation in commercial microalloyed steels, *Philos. Mag. Lett.* 83 (2003) 79–87. <https://doi.org/10.1080/0950083021000056632>.
- [181] M.C. Brandes, L. Kovarik, M.K. Miller, M.J. Mills, Morphology, structure, and chemistry of nanoclusters in a mechanically alloyed nanostructured ferritic steel, *J. Mater. Sci.* 47 (2012) 3913–3923. <https://doi.org/10.1007/s10853-012-6249-x>.

- [182] H.S. ZUROB, G. ZHU, S. V SUBRAMANIAN, G.R. PURDY, C.R. HUTCHINSON, Y. BRECHET, Analysis of the Effect of Mn on the Recrystallization Kinetics of High Nb Steel: An Example of Physically-based Alloy Design, *ISIJ Int.* 45 (2005) 713–722. <https://doi.org/10.2355/isijinternational.45.713>.
- [183] M.G. Akben, I. Weiss, J.J. Jonas, Dynamic precipitation and solute hardening in A V microalloyed steel and two Nb steels containing high levels of Mn, *Acta Metall.* 29 (1981) 111–121. [https://doi.org/https://doi.org/10.1016/0001-6160\(81\)90092-4](https://doi.org/https://doi.org/10.1016/0001-6160(81)90092-4).
- [184] J.H. Woodhead, *Vanadium in High Strength Steels*, Vanitec Publ. (1979).
- [185] M.G. Akben, T. Chandra, P. Plassiard, J.J. Jonas, Dynamic precipitation and solute hardening in a titanium microalloyed steel containing three levels of manganese, *Acta Metall.* 32 (1984) 591–601. [https://doi.org/https://doi.org/10.1016/0001-6160\(84\)90070-1](https://doi.org/https://doi.org/10.1016/0001-6160(84)90070-1).
- [186] Z. Wang, X. Sun, Z. Yang, Q. Yong, C. Zhang, Z. Li, Y. Weng, Effect of Mn concentration on the kinetics of strain induced precipitation in Ti microalloyed steels, *Mater. Sci. Eng. A.* 561 (2013) 212–219. <https://doi.org/10.1016/j.msea.2012.10.085>.
- [187] H.S. Ubhi, T.N. Baker, The influence of manganese and silicon on the precipitation of vanadium carbide in steel, *Mater. Sci. Eng. A.* 111 (1989) 189–199. [https://doi.org/10.1016/0921-5093\(89\)90212-8](https://doi.org/10.1016/0921-5093(89)90212-8).
- [188] K. Ushioda, N. Yoshinaga, O. Akisue, Influences of Mn on Recrystallization Behavior and Annealing Texture Formation in Ultralow-carbon and Low-carbon Steels, *ISIJ Int.* 34 (1994) 85–91. <https://doi.org/10.2355/isijinternational.34.85>.
- [189] H. Hu, S.R. Goodman, Effect of manganese on the annealing texture and strain ratio of low-carbon steels, *Metall. Trans.* 1 (1970) 3057–3064. <https://doi.org/10.1007/BF03038419>.
- [190] P.E. Fischione, *Materials specimen preparation for transmission electron microscopy*, EA Fischione Instruments, Inc. Export. PA, USA. (1992).
- [191] W.E. Stumpf, C.M. Sellars, Measurement of particle density and volume fraction from extraction replicas, *Metallography.* 1 (1968) 25–34. [https://doi.org/https://doi.org/10.1016/0026-0800\(68\)90015-3](https://doi.org/https://doi.org/10.1016/0026-0800(68)90015-3).
- [192] J. Li, T. Malis, S. Dionne, Recent advances in FIB–TEM specimen preparation techniques, *Mater. Charact.* 57 (2006) 64–70. <https://doi.org/https://doi.org/10.1016/j.matchar.2005.12.007>.

- [193] E.A. Kenik, P.J. Maziasz, Application of extraction replicas and analytical electron microscopy to precipitate phase studies, Oak Ridge National Lab., 1984.
- [194] M. Jublot, M. Texier, Sample preparation by focused ion beam micromachining for transmission electron microscopy imaging in front-view, *Micron*. 56 (2014) 63–67. <https://doi.org/10.1016/j.micron.2013.10.007>.
- [195] S. Bals, W. Tirry, R. Geurts, Y. Zhiqing, D. Schryvers, High-quality sample preparation by low kV FIB thinning for analytical TEM measurements, *Microsc. Microanal.* 13 (2007) 80–86. <https://doi.org/10.1017/S1431927607070018>.
- [196] J.F. Walker, J.C. Reiner, C. Solenthaler, Focused ion beam sample preparation for TEM, *Microsc. Semicond. Mater.* 146 (1995) 629–634.
- [197] L.A. Giannuzzi, F.A. Stevie, A review of focused ion beam milling techniques for TEM specimen preparation, *Micron*. 30 (1999) 197–204. [https://doi.org/10.1016/S0968-4328\(99\)00005-0](https://doi.org/10.1016/S0968-4328(99)00005-0).
- [198] R. Wirth, Focused Ion Beam (FIB): A novel technology for advanced application of micro- and nanoanalysis in geosciences and applied mineralogy, *Eur. J. Mineral.* 16 (2004) 863–876. <https://doi.org/10.1127/0935-1221/2004/0016-0863>.
- [199] J. Mayer, L. a Giannuzzi, T. Kamino, J. Michael, TEM Sample Preparation and FIB-Induced Damage, *MRS Bull.* 32 (2007) 400–407. <https://doi.org/10.1557/mrs2007.63>.
- [200] J. Scott, F.T. Docherty, M. MacKenzie, W. Smith, B. Miller, C.L. Collins, A.J. Craven, Sample preparation for nanoanalytical electron microscopy using the FIB lift-out method and low energy ion milling, *J. Phys. Conf. Ser.* 26 (2006) 223–226. <https://doi.org/10.1088/1742-6596/26/1/053>.
- [201] L. Wang, S. Parker, A. Rose, G. West, R. Thomson, Effects of Solute Nb Atoms and Nb Precipitates on Isothermal Transformation Kinetics from Austenite to Ferrite, *Metall. Mater. Trans. A Phys. Metall. Mater. Sci.* 47 (2016) 3387–3396. <https://doi.org/10.1007/s11661-016-3548-x>.
- [202] S.D. Catteau, H.P. Van Landeghem, J. Teixeira, J. Dulcy, M. Dehmas, S. Denis, A. Redjaïmia, M. Courteaux, Carbon and nitrogen effects on microstructure and kinetics associated with bainitic transformation in a low-alloyed steel, *J. Alloys Compd.* 658 (2016) 832–838. <https://doi.org/10.1016/j.jallcom.2015.11.007>.
- [203] J.W. Cahn, The impurity-drag effect in grain boundary motion, *Acta Metall.* 10 (1962) 789–798. [https://doi.org/https://doi.org/10.1016/0001-6160\(62\)90092-5](https://doi.org/https://doi.org/10.1016/0001-6160(62)90092-5).

- [204] H.S. Zurob, Y. Brechet, G. Purdy, A model for the competition of precipitation and recrystallization in deformed austenite, *Acta Mater.* 49 (2001) 4183–4190. [https://doi.org/https://doi.org/10.1016/S1359-6454\(01\)00315-9](https://doi.org/https://doi.org/10.1016/S1359-6454(01)00315-9).
- [205] E. Hornbogen, Recrystallization of metallic materials, *Metall.* 27 (1973) 780–787.
- [206] B. Johnson, R.F. Mehl, Trans, in: AIME, 1939: p. 416.
- [207] M. Avrami, Kinetics of phase change. I General theory, *J. Chem. Phys.* 7 (1939) 1103–1112.
- [208] M. Avrami, Kinetics of Phase Change. II Transformation-Time Relations for Random Distribution of Nuclei, *J. Chem. Phys.* 8 (1940) 212–224. <https://doi.org/10.1063/1.1750631>.
- [209] M. Avrami, Granulation, phase change, and microstructure kinetics of phase change. III, *J. Chem. Phys.* 9 (1941) 177–184. <https://doi.org/10.1063/1.1750872>.
- [210] A.N. Kolmogorov, Statistical theory of nucleation processes., *Izu. Akad. Nauk SSSR.* 3 (1937) 355–366.
- [211] T. Furu, K. Marthinsen, E. Nes, Modelling recrystallisation, *Mater. Sci. Technol.* (United Kingdom). 6 (1990) 1093–1102. <https://doi.org/10.1179/mst.1990.6.11.1093>.
- [212] A.D. Rollett, D.J. Srolovitz, R.D. Doherty, M.P. Anderson, Computer simulation of recrystallization in non-uniformly deformed metals, *Acta Metall.* 37 (1989) 627–639. [https://doi.org/10.1016/0001-6160\(89\)90247-2](https://doi.org/10.1016/0001-6160(89)90247-2).
- [213] S.-H. Hong, D.N. Lee, Grain coarsening in IF steel during strain annealing, *Mater. Sci. Eng. A.* 357 (2003) 75–85. [https://doi.org/10.1016/S0921-5093\(03\)00257-0](https://doi.org/10.1016/S0921-5093(03)00257-0).
- [214] G. Bhargava, L. Patra, S. Pai, D. Mishra, A Study on Microstructure, Texture and Precipitation Evolution at Different Stages of Steel Processing in Interstitial Free High Strength Steels, *Trans. Indian Inst. Met.* 70 (2017) 631–637. <https://doi.org/10.1007/s12666-017-1089-7>.
- [215] C. Fang, Annealing and Precipitation Behavior During Batch Annealing of HSLA Steels, University of Science and Technology Beijing, 2000.
- [216] W.B. Hutchinson, Development and control of annealing textures in low-carbon steels, *Int. Met. Rev.* 29 (1984) 25–40. <https://doi.org/10.1179/imtr.1984.29.1.25>.
- [217] T. Suzuki, Y. Ishii, A. Itami, K. Ushioda, N. Yoshinaga, H. Tezuka, Influence of Precipitates on Behavior of Recrystallization and Grain Growth in Extra Low Carbon

- Ti-Bearing Cold-Rolled Steel Sheets, *Mater. Sci. Forum.* 204–206 (1996) 673–678.
<https://doi.org/10.4028/www.scientific.net/msf.204-206.673>.
- [218] H. Luo, J. Sietsma, S. Van Der Zwaag, Effect of inhomogeneous deformation on the recrystallization kinetics of deformed metals, *ISIJ Int.* 44 (2004) 1931–1936.
<https://doi.org/10.2355/isijinternational.44.1931>.
- [219] S.F. Medina, A. Quispe, Improved Model for Static Recrystallization Kinetics of Hot Deformed Austenite in Low Alloy and Nb/V Microalloyed Steels, *ISIJ Int.* 41 (2001) 774–781. <https://doi.org/10.2355/isijinternational.41.774>.
- [220] M. Ji, C. Davis, M. Strangwood, Effect of Grain Size Distribution on Recrystallisation Kinetics in an Fe-30Ni Model Alloy, *Metals (Basel)*. 9 (2019) 369.
- [221] E. Orowan, Zur kristallplastizität. iii, *Zeitschrift Für Phys.* 89 (1934) 634–659.
- [222] G.I. Taylor, The mechanism of plastic deformation of crystals. Part I.-Theoretical, *Proc. R. Soc. London. Ser. A, Contain. Pap. a Math. Phys. Character.* 145 (1934) 362–387.
<https://doi.org/10.1098/rspa.1934.0106>.
- [223] M. Polanyi, Über eine Art Gitterstörung, die einen Kristall plastisch machen könnte, *Zeitschrift Für Phys.* 89 (1934) 660–664. <https://doi.org/10.1007/BF01341481>.
- [224] I.L. Dillamore, C.J.E. Smith, T.W. Watson, Oriented Nucleation in the Formation of Annealing Textures in Iron, *Met. Sci. J.* 1 (1967) 49–54.
<https://doi.org/10.1179/msc.1967.1.1.49>.
- [225] W.T. Read, *Dislocations in crystals*, McGraw-Hill, 1953.
- [226] N. Rajmohan, Y. Hayakawa, J.A. Szpunar, J.H. Root, Neutron diffraction method for stored energy measurement in interstitial free steel, *Acta Mater.* 45 (1997) 2485–2494.
[https://doi.org/https://doi.org/10.1016/S1359-6454\(96\)00371-0](https://doi.org/https://doi.org/10.1016/S1359-6454(96)00371-0).
- [227] I. Baker, L. Liu, D. Mandal, The effect of grain size on the stored energy of cold work as a function of strain for polycrystalline nickel, *Scr. Metall. Mater. States*. 32 (1995).
[https://doi.org/10.1016/S0956-716X\(99\)80031-4](https://doi.org/10.1016/S0956-716X(99)80031-4).
- [228] L.M. Clarebrough, M.E. Hargreaves, M.H. Loretto, The influence of grain size on the stored energy and mechanical properties of copper, *Acta Metall.* 6 (1958) 725–735.
[https://doi.org/https://doi.org/10.1016/0001-6160\(58\)90048-8](https://doi.org/https://doi.org/10.1016/0001-6160(58)90048-8).
- [229] W. Oliferuk, W.A. Świątnicki, M.W. Grabski, Effect of the grain size on the rate of energy storage during the tensile deformation of an austenitic steel, *Mater. Sci. Eng. A.* 197 (1995) 49–58. [https://doi.org/https://doi.org/10.1016/0921-5093\(94\)09766-6](https://doi.org/https://doi.org/10.1016/0921-5093(94)09766-6).

- [230] M.F. Ashby, F.J. Humphreys, C.M. Sellar, H.R. Shercliff, M.J. Stowell, F.J. Humphreys, P.B. Prangnell, J.R. Bowen, A. Gholinia, C. Harris, Developing stable fine-grain microstructures by large strain deformation, *Philos. Trans. R. Soc. London. Ser. A Math. Phys. Eng. Sci.* 357 (1999) 1663–1681. <https://doi.org/10.1098/rsta.1999.0395>.
- [231] C.S. Lee, B.J. Duggan, Deformation banding and copper-type rolling textures, *Acta Metall. Mater.* 41 (1993) 2691–2699. [https://doi.org/10.1016/0956-7151\(93\)90138-I](https://doi.org/10.1016/0956-7151(93)90138-I).
- [232] A.A. Ridha, W.B. Hutchinson, Recrystallisation mechanisms and the origin of cube texture in copper, *Acta Metall.* 30 (1982) 1929–1939. [https://doi.org/http://dx.doi.org/10.1016/0001-6160\(82\)90033-5](https://doi.org/http://dx.doi.org/10.1016/0001-6160(82)90033-5).
- [233] A. Korbel, J.D. Embury, M. Hatherly, P.L. Martin, H.W. Erbsloh, Microstructural aspects of strain localization in Al-Mg alloys, *Acta Metall.* 34 (1986) 1999–2009. [https://doi.org/10.1016/0001-6160\(86\)90259-2](https://doi.org/10.1016/0001-6160(86)90259-2).
- [234] K. Ushioda, S. Nakanishi, T. Morikawa, K. Higashida, Y. Suwa, K. Murakami, Evolution of Heterogeneous Deformation Structure and Recrystallization Texture of Steel, in: *Recryst. Grain Growth V*, Trans Tech Publications Ltd, 2013: pp. 58–65. <https://doi.org/10.4028/www.scientific.net/MSF.753.58>.
- [235] T. Imamura, Y. Hayakawa, Influence of grain size before cold rolling on development of crystallographically equivalent main texture component in recrystallization texture of 3% Si-Fe, *J. Phys. Conf. Ser.* 1270 (2019) 12008. <https://doi.org/10.1088/1742-6596/1270/1/012008>.
- [236] K. Murakami, M. Sugiyama, K. Ushioda, Deformation, recovery and recrystallization from heterogeneous shear bands in steel sheets, *{IOP} Conf. Ser. Mater. Sci. Eng.* 89 (2015) 12009. <https://doi.org/10.1088/1757-899x/89/1/012009>.
- [237] A. Fenghui, L. Bo, Z. Deqin, L. Jinlong, S. Yuhui, Recrystallization Kinetics of Fe-3%Si after Deformation at High Strain Rate and High Temperature, *Mater. Res.* 22 (2019). http://www.scielo.br/scielo.php?script=sci_arttext&pid=S1516-14392019000800222&nrm=iso.
- [238] S. CS, Grains, Phases, and Interfaces: An Interpretation of Microstructure, *Metall. Mater. Trans. A, Phys.* 41 (2010) 1064–1100.
- [239] L. BÄCKE, Modeling the Effect of Solute Drag on Recovery and Recrystallization during Hot Deformation of Nb Microalloyed Steels, *ISIJ Int.* 50 (2010) 239–247.

- <https://doi.org/10.2355/isijinternational.50.239>.
- [240] E. Ahmad, F. Karim, K. Saeed, T. Manzoor, G.H. Zahid, Effect of cold rolling and annealing on the grain refinement of low alloy steel, in: IOP Conf. Ser. Mater. Sci. Eng., 2014: p. 012029. <https://doi.org/10.1088/1757-899X/60/1/012029>.
- [241] K. Lücke, K. Detert, A quantitative theory of grain-boundary motion and recrystallization in metals in the presence of impurities, *Acta Metall.* 5 (1957) 628–637. [https://doi.org/http://dx.doi.org/10.1016/0001-6160\(57\)90109-8](https://doi.org/http://dx.doi.org/10.1016/0001-6160(57)90109-8).
- [242] M. Hillert, B. Sundman, A treatment of the solute drag on moving grain boundaries and phase interfaces in binary alloys, *Acta Metall.* 24 (1976) 731–743. [https://doi.org/https://doi.org/10.1016/0001-6160\(76\)90108-5](https://doi.org/https://doi.org/10.1016/0001-6160(76)90108-5).
- [243] H. Buken, E. Kozeschnik, A Model for Static Recrystallization with Simultaneous Precipitation and Solute Drag, *Metall. Mater. Trans. A Phys. Metall. Mater. Sci.* 48 (2017) 2812–2818. <https://doi.org/10.1007/s11661-016-3524-5>.
- [244] J. Li, J. Wang, G. Yang, Phase field modeling of grain boundary migration with solute drag, *Acta Mater.* 57 (2009) 2108–2120. <https://doi.org/10.1016/j.actamat.2009.01.003>.
- [245] Y. Huang, F.J. Humphreys, The effect of solutes on grain boundary mobility during recrystallization and grain growth in some single-phase aluminium alloys, *Mater. Chem. Phys.* 132 (2012) 166–174. <https://doi.org/10.1016/j.matchemphys.2011.11.018>.
- [246] M. Calcagnotto, D. Ponge, D. Raabe, On the effect of manganese on grain size stability and hardenability in ultrafine-grained ferrite/martensite dual-phase steels, *Metall. Mater. Trans. A Phys. Metall. Mater. Sci.* 43 (2012) 37–46. <https://doi.org/10.1007/s11661-011-0828-3>.
- [247] Y. Lin, H. Wen, Y. Li, B. Wen, W. Liu, E.J. Lavernia, An analytical model for stress-induced grain growth in the presence of both second-phase particles and solute segregation at grain boundaries, *Acta Mater.* 82 (2015) 304–315. <https://doi.org/10.1016/j.actamat.2014.08.059>.
- [248] P.L.O. Rossi, C.M. Sellars, Quantitative metallography of recrystallization, *Acta Mater.* 45 (1997) 137–148. [https://doi.org/https://doi.org/10.1016/S1359-6454\(96\)00167-X](https://doi.org/https://doi.org/10.1016/S1359-6454(96)00167-X).
- [249] S.P. Chen, D.N. Hanlon, S. Van Der Zwaag, Y.T. Pei, J.T.M. Dehossion, Quantification of the recrystallization behaviour in Al-alloy AA1050, *J. Mater. Sci.* 37 (2002) 989–

995. <https://doi.org/10.1023/A:1014356116058>.
- [250] H. Jazaeri, F.J. Humphreys, Quantifying recrystallization by electron backscatter diffraction, *J. Microsc.* 213 (2004) 241–246. <https://doi.org/10.1111/j.0022-2720.2004.01296.x>.
- [251] S. Dziazyk, E.J. Payton, F. Friedel, V. Marx, G. Eggeler, On the characterization of recrystallized fraction using electron backscatter diffraction: A direct comparison to local hardness in an IF steel using nanoindentation, *Mater. Sci. Eng. A.* 527 (2010) 7854–7864. <https://doi.org/10.1016/j.msea.2010.08.063>.
- [252] P.H. Gerber, J. Tarasiuk, R. Chiron, B. Bacroix, Estimation of the recrystallized volume fraction from local misorientation calculations, *Arch. Metall. Mater.* 50 (2005) 747.
- [253] E. Woldt, D.J. Jensen, Recrystallization kinetics in copper: Comparison between techniques, *Metall. Mater. Trans. A.* 26 (1995) 1717–1724. <https://doi.org/10.1007/BF02670758>.
- [254] J. Tarasiuk, P. Gerber, B. Bacroix, Estimation of recrystallized volume fraction from EBSD data, *Acta Mater.* 50 (2002) 1467–1477. [https://doi.org/https://doi.org/10.1016/S1359-6454\(02\)00005-8](https://doi.org/https://doi.org/10.1016/S1359-6454(02)00005-8).
- [255] G. Benchabane, Z. Boumerzoug, I. Thibon, T. Gloriant, Recrystallization of pure copper investigated by calorimetry and microhardness, *Mater. Charact.* 59 (2008) 1425–1428. <https://doi.org/https://doi.org/10.1016/j.matchar.2008.01.002>.
- [256] F. Sun, A. Zúñiga, P. Rojas, E.J. Lavernia, Thermal stability and recrystallization of nanocrystalline Ti produced by cryogenic milling, *Metall. Mater. Trans. A.* 37 (2006) 2069–2078. <https://doi.org/10.1007/BF02586127>.
- [257] F.J. Humphreys, VMAP is a suite of programmes developed for quantitative analysis of the EBSD data generated by the HKL Channel acquisition system, *It Can Be Made Available Req.* (2000).
- [258] I. Samajdar, B. Verlinden, P.V. Houtte, D. Vanderschueren, γ -Fibre recrystallization texture in IF-steel: an investigation on the recrystallization mechanisms, *Mater. Sci. Eng. A.* 238 (1997) 343–350.
- [259] W.B. Hutchinson, Practical Aspects of Texture Control in Low Carbon Steels, in: *Textures Mater. - ICOTOM 10*, Trans Tech Publications Ltd, 1994: pp. 1917–1928. <https://doi.org/10.4028/www.scientific.net/MSF.157-162.1917>.

- [260] E. Bruder, The effect of deformation texture on the thermal stability of UFG HSLA steel, *J. Mater. Sci.* 47 (2012) 7751–7758. <https://doi.org/10.1007/s10853-012-6518-8>.
- [261] J.R. Davis, CHAPTER 1 Introduction to Tensile Testing, in: *Tensile Testing*, 2nd Ed., ASM International, 2004.
- [262] D.N. Hanlon, S.M.C. van Bohemen, S. Celotto, Critical Assessment 10: Tensile elongation of strong automotive steels as function of testpiece geometry, *Mater. Sci. Technol.* 31 (2015) 385–388. <https://doi.org/10.1179/1743284714Y.0000000707>.
- [263] W. Lüders, *Dinglers polytech, J.* 155 (1860) 1566.
- [264] W. Sylwestrowicz, E.O. Hall, The Deformation and Ageing of Mild Steel, *Proc. Phys. Soc. Sect. B.* 64 (1951) 495–502. <https://doi.org/10.1088/0370-1301/64/6/305>.
- [265] W.M. Lomer, The yield phenomenon in polycrystalline mild steel, *J. Mech. Phys. Solids.* 1 (1952).
- [266] A.H. Cottrell, B.A. Bilby, Dislocation Theory of Yielding and Strain Ageing of Iron, *Proc. Phys. Soc. Sect. A.* 62 (1949) 49. <https://doi.org/10.1088/0370-1298/62/1/308>.
- [267] J. Heslop, N.J. Petch, LXXXVIII. The stress to move a free dislocation in alpha iron, *Philos. Mag.* 1 (1956) 866–873. <https://doi.org/10.1080/14786435608238163>.
- [268] S. Rešković, I. Jandrić, F. Vodopivec, Influence of testing rate on Lüders band propagation in niobium microalloyed steel, *Metalurgija.* 55 (2016) 157–160.
- [269] D.H. Johnson, *Luders bands in RPV Steel*, (2013).
- [270] R. Song, D. Ponge, D. Raabe, Improvement of the work hardening rate of ultrafine grained steels through second phase particles, *Scr. Mater.* 52 (2005) 1075–1080. <https://doi.org/10.1016/j.scriptamat.2005.02.016>.
- [271] A. Arlazarov, *Evolution of microstructure and mechanical properties of medium Mn steels and their relationship*, DISS, Université de Lorraine, 2015.
- [272] J.T. Busby, M.C. Hash, G.S. Was, The relationship between hardness and yield stress in irradiated austenitic and ferritic steels, *J. Nucl. Mater.* 336 (2005) 267–278. <https://doi.org/10.1016/j.jnucmat.2004.09.024>.
- [273] A.E. Tekkaya, Improved relationship between Vickers hardness and yield stress for cold formed materials, *Steel Res.* 72 (2001) 304–310. <https://doi.org/10.1002/srin.200100122>.
- [274] P. Zhang, S.X. Li, Z.F. Zhang, General relationship between strength and hardness,

- Mater. Sci. Eng. A. 529 (2011) 62–73. <https://doi.org/10.1016/j.msea.2011.08.061>.
- [275] J.A. Brinell, Mémoire sur les épreuves á bille en acier, II, Cong. Int. Methodes d Essai, A. Wahlberg, Paris. (1900) 243.
- [276] B.W. Mott, Micro-indentation hardness testing, Butterworths Scientific Publications, 1956.
- [277] D. Tabor, The Hardness of Metals, OUP Oxford, 2000.
- [278] Y. Zayachuk, D.E.J. Armstrong, K. Bystrov, S. Van Boxel, T. Morgan, S.G. Roberts, Nanoindentation study of the combined effects of crystallography, heat treatment and exposure to high-flux deuterium plasma in tungsten, J. Nucl. Mater. 486 (2017) 183–190. <https://doi.org/10.1016/j.jnucmat.2017.01.026>.
- [279] C. Fizanne-Michel, M. Cornen, P. Castany, I. Péron, T. Gloriant, Determination of hardness and elastic modulus inverse pole figures of a polycrystalline commercially pure titanium by coupling nanoindentation and EBSD techniques, Mater. Sci. Eng. A. 613 (2014) 159–162. <https://doi.org/10.1016/j.msea.2014.06.098>.
- [280] W.C. Oliver, G.M. Pharr, An improved technique for determining hardness and elastic modulus using load and displacement sensing indentation experiments, J. Mater. Res. 7 (1992) 1564–1583. [https://doi.org/DOI: 10.1557/JMR.1992.1564](https://doi.org/DOI:10.1557/JMR.1992.1564).
- [281] A.C. Fischer-Cripps, Nanoindentation, Springer New York, 2011.
- [282] T.S. Jun, D.E.J. Armstrong, T.B. Britton, A nanoindentation investigation of local strain rate sensitivity in dual-phase Ti alloys, J. Alloys Compd. 672 (2016) 282–291. <https://doi.org/10.1016/j.jallcom.2016.02.146>.
- [283] K. Seto, Y. Funakawa, S. Kaneko, Hot rolled high strength steels for suspension and chassis parts “NANO HITEN” and “BHT® Steel,” JFE Tech Rep. 10 (2007) 19–25.
- [284] W. Bleck, K. Phiu-on, Effects of Microalloying in Multi Phase Steels for Car Body Manufacture, in: A. Haldar, S. Suwas, D. Bhattacharjee (Eds.), Microstruct. Texture Steels, Springer London, London, 2009: pp. 145–163.
- [285] V.N. Surovova, A.G. Ivanov, A. V Salautin, B.M. Ovsyannikov, Influence of sulfur on the microstructure and impact strength of 17G1S steel, Met. Sci. Heat Treat. 23 (1981) 636–639. <https://doi.org/10.1007/BF00712598>.
- [286] C. Revilla, B. López, J.M. Rodríguez-Ibabe, Carbide size refinement by controlling the heating rate during induction tempering in a low alloy steel, Mater. Des. 62 (2014) 296–304. <https://doi.org/https://doi.org/10.1016/j.matdes.2014.05.053>.

- [287] EBSD - Electron Backscatter Diffraction, Oxford Instruments. (2017). <https://www.oxford-instruments.com/products/microanalysis/ebsd> (accessed April 27, 2017).
- [288] O. Instruments, Oxford Instruments HKL Channel 5 user manual, 2007. https://doi.org/https://caf.ua.edu/wp-content/uploads/docs/JEOL-7000F-Oxford_Channel_5_User_Manual.pdf.
- [289] D.I. Kim, K.H. Oh, H.C. Lee, Statistical analysis of the development of recrystallization texture in IF steel, *Mater. Sci. Forum.* 408–412 (2002) 839–844.
- [290] H.J. Bunge, *Mathematical methods of texture analysis*, Akad. Berlin. (1969).
- [291] S. Chen, J. Butler, S. Melzer, Effect of asymmetric hot rolling on texture, microstructure and magnetic properties in a non-grain oriented electrical steel, *J. Magn. Mater.* 368 (2014) 342–352. <https://doi.org/10.1016/j.jmmm.2014.05.054>.
- [292] P. Van Houtte, *MTM-FHM Software Manual*, Katholieke Univ. Leuven, Belgium. (1995).
- [293] GATAN, Murano and Microtest In-Situ Stages, (2018).
- [294] S. Clark, V. Janik, A. Rijkenberg, S. Sridhar, Analysis of the extent of interphase precipitation in V-HSLA steels through in-situ characterization of the γ/α transformation, *Mater. Charact.* 115 (2016) 83–89. <https://doi.org/10.1016/j.matchar.2016.03.021>.
- [295] C. Wu, H. Yang, H.W. Li, Simulated and experimental investigation on discontinuous dynamic recrystallization of a near- α TA15 titanium alloy during isothermal hot compression in β single-phase field, *Trans. Nonferrous Met. Soc. China (English Ed.)* 24 (2014) 1819–1829. [https://doi.org/10.1016/S1003-6326\(14\)63259-3](https://doi.org/10.1016/S1003-6326(14)63259-3).
- [296] X. Huang, D. Juul Jensen, N. Hansen, Effect of grain orientation on deformation structure and recrystallization behaviour of tensile strained copper, in: S.H.G. Sakai T. (Ed.), *4th Int. Conf. Recryst. Relat. Phenom.*, Japan Institute of Metals, 1999: pp. 161–166.
- [297] C. Moussa, M. Bernacki, R. Besnard, N. Bozzolo, About quantitative EBSD analysis of deformation and recovery substructures in pure Tantalum, *IOP Conf. Ser. Mater. Sci. Eng.* 89 (2015). <https://doi.org/10.1088/1757-899X/89/1/012038>.
- [298] T.B. Britton, *High Angular Resolution EBSD (HR-EBSD)*, 2016. <https://drive.google.com/file/d/0BzcVPW0PZrI9X2NvcWtzakVsSTA/view>.

- [299] C.A. Schneider, W.S. Rasband, K.W. Eliceiri, NIH Image to ImageJ: 25 years of image analysis, *Nat. Methods*. 9 (2012) 671. <https://doi.org/10.1038/nmeth.2089>.
- [300] A.M. Page, Quantifying Precipitate Size and Distribution in Aluminum Alloy Friction Stir Welds for Aerospace Structures, (2014).
- [301] A. Karmakar, S. Mukherjee, S. Kundu, D. Srivastava, R. Mitra, D. Chakrabarti, Effect of composition and isothermal holding temperature on the precipitation hardening in Vanadium-microalloyed steels, *Mater. Charact.* 132 (2017) 31–40. <https://doi.org/10.1016/j.matchar.2017.08.003>.
- [302] TA instruments, DIL 805A/D/T, (2019).
- [303] M. Materials, NanoTest Xtreme, (2019).
- [304] Buehler, (2017). <https://www.buehler.co.uk/hardness-testing.php> (accessed April 27, 2017).
- [305] I.L. Dillamore, J.G. Roberts, A.C. Bush, Occurrence of shear bands in heavily rolled cubic metals, *Met. Sci.* 13 (1979) 73–77. <https://doi.org/10.1179/msc.1979.13.2.73>.
- [306] J.L. Bocos, E. Novillo, M.M. Petite, A. Iza-Mendia, I. Gutierrez, Aspects of orientation-dependent grain growth in extra-low carbon and interstitial-free steels during continuous annealing, *Metall. Mater. Trans. A.* 34 (2003) 827. <https://doi.org/10.1007/s11661-003-0117-x>.
- [307] D. Zhuang, L. Wang, Y. Huang, X. Li, H. Zhang, D. Ren, Microstructure and texture evolution during recrystallization of low-carbon steel sheets, *J. Iron Steel Res. Int.* 24 (2017) 84–90. [https://doi.org/10.1016/S1006-706X\(17\)30012-2](https://doi.org/10.1016/S1006-706X(17)30012-2).
- [308] F.M. Castro Cerda, F. Verduyck, T.N. Minh, L. Kestens, A. Monsalve, R. Petrov, The Effect of Heating Rate on the Recrystallization Behavior in Cold Rolled Ultra Low Carbon Steel, *Steel Res. Int.* 88 (2017) 1–9. <https://doi.org/10.1002/srin.201600351>.
- [309] A. Laasraoui, J.J. Jonas, Recrystallization of austenite after deformation at high temperatures and strain rates—Analysis and modeling, *Metall. Trans. A.* 22 (1991) 151–160. <https://doi.org/10.1007/BF03350957>.
- [310] A.D. Rollett, D.J. Srolovitz, R.D. Doherty, M.P. Anderson, Computer simulation of recrystallization in non-uniformly deformed metals, *Acta Metall.* 37 (1989) 627–639. [https://doi.org/https://doi.org/10.1016/0001-6160\(89\)90247-2](https://doi.org/https://doi.org/10.1016/0001-6160(89)90247-2).
- [311] I. Samajdar, B. Verlinden, P. Van Houtte, D. Vanderschueren, Recrystallisation kinetics in IF-steel: A study on the sluggish recrystallisation behaviour, *Scr. Mater.* 37

- (1997) 869–874. [https://doi.org/10.1016/S1359-6462\(97\)00185-1](https://doi.org/10.1016/S1359-6462(97)00185-1).
- [312] H. Réglé, Mechanisms of microstructure and texture evolution during recrystallization of ferritic steels sheets, in: G. Gottstein, D.A. Molodov (Eds.), First Jt. Int. Conf. Recryst. Grain Growth, Springer-Verlag, Berlin, 2001: pp. 707–717.
- [313] C.W. Sinclair, F. Robaut, L. Maniguet, J.D. Mithieux, J.H. Schmitt, Y. Brechet, Recrystallization and Texture in a Ferritic Stainless Steel: an EBSD Study, *Adv. Eng. Mater.* 5 (2003) 570–574. <https://doi.org/10.1002/adem.200300377>.
- [314] D. Raabe, K. Lücke, Rolling and Annealing Textures of BCC Metals, in: *Textures Mater. - ICOTOM 10*, Trans Tech Publications, 1994: pp. 597–610. <https://doi.org/10.4028/www.scientific.net/MSF.157-162.597>.
- [315] M.R. Toroghinezhad, A.O. Humphreys, E. Essadiqi, F. Ashrafizadeh, A. Najafizadeh, J.J. Jonas, Effect of chromium, boron and manganese additions on the deformation and recrystallization textures of warm rolled low carbon steels, *ISIJ Int.* 43 (2003) 1842–1850. <https://doi.org/10.2355/isijinternational.43.1842>.
- [316] M. Holscher, D. Raabe, K. Lucke, Rolling and recrystallization textures of bcc steels, *Steel Res.* 62 (1991).
- [317] S. Vervynckt, K. Verbeken, P. Thibaux, M. Liebeherr, Y. Houbaert, Austenite Recrystallization–Precipitation Interaction in Niobium Microalloyed Steels, *ISIJ Int.* 49 (2009) 911–920. <https://doi.org/10.2355/isijinternational.49.911>.
- [318] S. Vervynckt, K. Verbeken, B. Lopez, J.J. Jonas, Modern HSLA steels and role of non-recrystallisation temperature, *Int. Mater. Rev.* 57 (2012) 187–207. <https://doi.org/10.1179/1743280411Y.0000000013>.
- [319] C.N. Homsher, Determination of the non-recrystallization Temperature (T_{nr}) in multiple Microalloyed steels, (2013).
- [320] F. Boratto, R. Borbasa, S. Yue, J.J. Jonas, Thermomechanical processing of steels and other materials, *Thermec-88*, Tokyo, Japan. (1988) 383–390.
- [321] D.Q. Bai, Effect of rolling parameters on the no-recrystallization temperature (T_{nr}) in Nb-bearing steels, (1993).
- [322] S. Yamasaki, H.K.D.H. Bhadeshia, Modelling and characterisation of V₄C₃ precipitation and cementite dissolution during tempering of Fe - C - V martensitic steel, *Mater. Sci. Technol.* 19 (2003) 1335–1343. <https://doi.org/10.1179/026708303225005971>.

- [323] J.H. Jang, The Effect of Mo or W on TiC Coarsening in HSLA Steel, Pohang University of Science and Technology, 2012.
- [324] F. Perrard, A. Deschamps, P. Maugis, Modelling the precipitation of NbC on dislocations in α -Fe, *Acta Mater.* 55 (2007) 1255–1266. <https://doi.org/10.1016/j.actamat.2006.10.003>.
- [325] K. Xu, Multiphase particle-size-grouping model of precipitation and its application to thermal processing of microalloyed steel, University of Illinois at Urbana-Champaign, 2012.
- [326] M. Mukherjee, U. Prahl, W. Bleck, Modelling the strain-induced precipitation kinetics of vanadium carbonitride during hot working of precipitation-hardened Ferritic–Pearlitic steels, *Acta Mater.* 71 (2014) 234–254. <https://doi.org/https://doi.org/10.1016/j.actamat.2014.03.016>.
- [327] F.S. Medina, M. Gómez, Nucleation rate and number of precipitates in V and Nb-microalloyed steels, *Mater. Sci. Forum.* 783–786 (2014) 1073–1078.
- [328] H. Abe, T. Suzuki, S. Okada, Decomposition of Mn-C Dipoles during Quench-Ageing in Low-Carbon Aluminium-Killed Steels, *Trans. Japan Inst. Met.* 25 (1984) 215–225. <https://doi.org/10.2320/matertrans1960.25.215>.
- [329] V. Massardier, E. Le Patezour, M. Soler, J. Merlin, Mn-C interaction in Fe-C-Mn steels: Study by thermoelectric power and internal friction, *Metall. Mater. Trans. A Phys. Metall. Mater. Sci.* 36 (2005) 1745–1755. <https://doi.org/10.1007/s11661-005-0039-x>.
- [330] H. Numakura, G. Yotsui, M. Koiwa, Calculation of the strength of Snoek relaxation in dilute ternary B.C.C. alloys, *Acta Metall. Mater.* 43 (1995) 705–714. [https://doi.org/https://doi.org/10.1016/0956-7151\(94\)00262-G](https://doi.org/https://doi.org/10.1016/0956-7151(94)00262-G).
- [331] H. Saitoh, K. Ushioda, Influences of Manganese on Internal Friction and Carbon Solubility Determined by Combination of Infrared Absorption in Ferrite of Low-carbon Steels, *ISIJ Int.* 29 (1989) 960–965. <https://doi.org/10.2355/isijinternational.29.960>.
- [332] H. Saitoh, N. Yoshinaga, K. Ushioda, Influence of substitutional atoms on the Snoek peak of carbon in b.c.c. iron, *Acta Mater.* 52 (2004) 1255–1261. <https://doi.org/10.1016/j.actamat.2003.11.009>.
- [333] A.T. Wicaksono, M. Militzer, Interaction of C and Mn in a Σ 3 grain boundary of bcc iron, *IOP Conf. Ser. Mater. Sci. Eng.* 219 (2017) 0–8. [162](https://doi.org/10.1088/1757-</p></div><div data-bbox=)

899X/219/1/012044.

- [334] C.S. Barrett, L.H. Levenson, Analysis of the cold rolling texture of iron, *Trans. Amer. Inst. Min. Metall. Eng.* 145 (1941) 281.
- [335] H. Inagaki, Fundamental Aspect of Texture Formation in Low Carbon Steel, *ISIJ Int.* 34 (1994) 313–321. <https://doi.org/10.2355/isijinternational.34.313>.
- [336] J. Grewen, G. Wassermann, *Textures in research and practice*, Springer, 1969.
- [337] M.Z. Quadir, B.J. Duggan, Deformation banding and recrystallization of α fibre components in heavily rolled IF steel, *Acta Mater.* 52 (2004) 4011–4021. <https://doi.org/10.1016/j.actamat.2004.05.017>.
- [338] B. Hutchinson, Deformation substructures and recrystallisation, *Mater. Sci. Forum.* 558–559 (2007) 13–22. <https://doi.org/10.4028/www.scientific.net/MSF.558-559.13>.
- [339] D.N. Lee, The evolution of recrystallization textures from deformation textures, *Scr. Metall. Mater.* 32 (1995) 1689–1694. [https://doi.org/10.1016/0956-716X\(95\)00256-U](https://doi.org/10.1016/0956-716X(95)00256-U).
- [340] Y. Soda, H.-R. Wenk, Antigorite crystallographic preferred orientations in serpentinites from Japan, *Tectonophysics.* 615–616 (2014) 199–212. <https://doi.org/https://doi.org/10.1016/j.tecto.2013.12.016>.
- [341] R.K. Ray, B. Hutchinson, C. Ghosh, “Back-annealing” of cold rolled steels through recovery and/or partial recrystallisation, *Int. Mater. Rev.* 56 (2011) 73–97. <https://doi.org/10.1179/095066010X12646898728444>.
- [342] F.B. Pickering, *Physical metallurgy and the design of steels*, Applied Science Publishers, 1978.
- [343] H.J. Kestenbach, S.S. Campos, E. V. Morales, Role of interphase precipitation in microalloyed hot strip steels, *Mater. Sci. Technol.* 22 (2006) 615–626. <https://doi.org/10.1179/026708306X81487>.
- [344] J.M. Rodriguez-Ibabe, *Thin Slab Direct Rolling of Microalloyed Steels*, Trans Tech, 2007.
- [345] R.R. Pradhan, Internal report, Bethlehem, PA, USA, 1981.
- [346] H. Hayashi, Sheet metal forming beyond 2000, in: 20th Bienn. [IDDRG] Congr., CRM, Genval, Brussels, Belgium, 1998.
- [347] H. Minami, T. Kobayashi, Y. Funakawa, Cold-rolled and galvanized (GA) ultra-high strength steel sheets for automobile structural parts, *JFE Tech. Rep.* 24 (2019)

23–31.

- [348] G. Dini, A. Najafizadeh, R. Ueji, S.M. Monir-Vaghefi, Improved tensile properties of partially recrystallized submicron grained TWIP steel, *Mater. Lett.* 64 (2010) 15–18. <https://doi.org/10.1016/j.matlet.2009.09.057>.
- [349] W.D. Kenny, N.C. Burlein, D.A. Dether, R. Vlietstra, Development of Ultra-High Strength Galvanized Steel for Automotive Bumper Reinforcements, in: SAE Tech. Pap., SAE International, 1985. <https://doi.org/10.4271/850116>.
- [350] Bumper Project Group, Steel Bumper Systems for Passenger Cars and Light Trucks, 2013.
- [351] Auto/Steel Partnership, High Strength Steel Stamping Design Manual, 2000.
- [352] R.L. Every, M. Hatherly, Oriented Nucleation in Low-Carbon Steels., *Texture.* 1 (1974) 183–194. <https://doi.org/10.1155/TSM.1.183>.
- [353] J. Pak, D.W. Suh, H.K.D.H. Bhadeshia, Displacive phase transformation and surface effects associated with confocal laser scanning microscopy, *Metall. Mater. Trans. A Phys. Metall. Mater. Sci.* 43 (2012) 4520–4524. <https://doi.org/10.1007/s11661-012-1264-8>.
- [354] M.M. Nowell, D.P. Field, S.I. Wright, T.M. Lillo, In-Situ EBSD Investigation of Recrystallization in ECAE Processed Copper, in: *Recryst. Grain Growth*, Trans Tech Publications, 2004: pp. 1401–1406. <https://doi.org/10.4028/www.scientific.net/MSF.467-470.1401>.
- [355] Y. Jin, B. Lin, M. Bernacki, G.S. Rohrer, A.D. Rollett, N. Bozzolo, Annealing twin development during recrystallization and grain growth in pure nickel, *Mater. Sci. Eng. A.* 597 (2014) 295–303. <https://doi.org/10.1016/j.msea.2014.01.018>.
- [356] D. Guan, X. Liu, J. Gao, L. Ma, B.P. Wynne, W.M. Rainforth, Exploring the mechanism of “Rare Earth” texture evolution in a lean Mg–Zn–Ca alloy, *Sci. Rep.* 9 (2019) 1–11. <https://doi.org/10.1038/s41598-019-43415-z>.
- [357] M. Herbig, P. Choi, D. Raabe, Combining structural and chemical information at the nanometer scale by correlative transmission electron microscopy and atom probe tomography, *Ultramicroscopy.* 153 (2015) 32–39. <https://doi.org/10.1016/j.ultramic.2015.02.003>.
- [358] C. Fressengeas, B. Beausir, C. Kerisit, A.-L. Helbert, T. Baudin, F. Brisset, M.-H. Mathon, R. Besnard, N. Bozzolo, On the evaluation of dislocation densities in pure

- tantalum from EBSD orientation data, *Matériaux Tech.* 106 (2018) 604.
- [359] M. Kamaya, Assessment of local deformation using EBSD: Quantification of accuracy of measurement and definition of local gradient, *Ultramicroscopy.* 111 (2011) 1189–1199. <https://doi.org/10.1016/j.ultramic.2011.02.004>.
- [360] T.H. Simm, L. Sun, D.R. Galvin, E.P. Gilbert, D.A. Venero, Y. Li, T.L. Martin, P.A.J. Bagot, M.P. Moody, P. Hill, H.K.D.H. Bhadeshia, S. Biroasca, M.J. Rawson, K.M. Perkins, A SANS and APT study of precipitate evolution and strengthening in a maraging steel, *Mater. Sci. Eng. A.* 702 (2017) 414–424. <https://doi.org/https://doi.org/10.1016/j.msea.2017.07.013>.
- [361] C. Zhu, K. Kaufmann, K. Vecchio, Automated Reconstruction of Spherical Kikuchi Maps, *Microsc. Microanal.* 25 (2019) 912–923. <https://doi.org/DOI:10.1017/S1431927619000710>.
- [362] A.J. Wilkinson, D. Randman, Determination of elastic strain fields and geometrically necessary dislocation distributions near nanoindentations using electron back scatter diffraction, *Philos. Mag.* 90 (2010) 1159–1177. <https://doi.org/10.1080/14786430903304145>.
- [363] C. Moussa, M. Bernacki, R. Besnard, N. Bozzolo, Statistical analysis of dislocations and dislocation boundaries from EBSD data, *Ultramicroscopy.* 179 (2017) 63–72. <https://doi.org/https://doi.org/10.1016/j.ultramic.2017.04.005>.
- [364] J. Jiang, T.B. Britton, A.J. Wilkinson, Measurement of geometrically necessary dislocation density with high resolution electron backscatter diffraction: Effects of detector binning and step size, *Ultramicroscopy.* 125 (2013) 1–9. <https://doi.org/https://doi.org/10.1016/j.ultramic.2012.11.003>.
- [365] O. Instruments, AZtec Hints and Tips 1 Users meeting 2019, 2019. <https://doi.org/https://nano.oxinst.com/assets/uploads/NanoAnalysis/Users%20Meeting%202019%20AZtec%20Hints%20and%20Tips%201.pdf>.